# ELECTRONIC SPECTROSCOPY OF MASS-SELECTED PROTONATED POLYCYCLIC AROMATIC HYDROCARBONS IN NEON MATRICES

Inauguraldissertation

zur
Erlangung der Würde eines Doktors der Philosophie
vorgelegt der
Philosophisch-Naturwissenschaftlichen Fakultät
der Universität Basel

von

IRYNA ROTH GARKUSHA

aus Kyiw, Ukraine

Basel, 2014

Genehmigt von der Philosophisch-Naturwissenschaftlichen Fakultät
auf Antrag von

Dissertationsleiter: Prof. Dr. John P. Maier
Korreferent: Prof. Dr. Markus Meuwly

Basel, den 22. Mai 2012

Prof. Dr. Martin Spiess
Dekan

*To my parents and sister*

# ACKNOWLEDGMENTS

I am very grateful to Prof. John P. Maier for giving me the opportunity to work in his group and for providing me with excellent experimental instruments and financial support necessary for carrying out and completing my dissertation.

I thank Prof. Markus Meuwly for being the co-referee of my thesis and Prof. Thomas Pfohl, who kindly agreed to chair my Ph.D. defence.

A very special thank of mine goes to Dr. Ivan Shnitko† who taught me many of the essentials of the experimental set up and matrix isolation technique in general. Dr. Anton Batalov is thanked for his support during my first steps in the group.

I want to express my deep appreciation to Dr. Adam Nagy with whom I worked the most time of my PhD studies. For all your assistance, collaboration and support through thick and thin—thank you Adam!

Many thanks are also addressed to Prof. Jan Fulara for sharing his deep knowledge on matrix isolation, continuous help during experiments and his theoretical calculations.

I specially thank Dr. Corey Rice for his ideas and advices, explanations, readiness to help with all kinds of problems and for proofreading of my thesis. Varun Gupta is specially thanked for his invaluable support at the time before my defence.

I am very grateful to the people who were technically involved in the experiment for their friendly help and assistance. Grischa Martin, Dieter Wild, Franz Häfeli, Yannick Schmidli and Philipp Knöpfel from the mechanical workshop are cordially thanked for planning and constructing much of the essential parts of the experimental set-up. Georg Holderied is thanked for his support with electronic equipments and Jacques Lecoultre for synthesizing the necessary chemicals. I am also grateful to Jean-Pierre Ramseyer for technical support, in particular for preparing sample rods, and to Dr. Anatoly Johnson for help with LabView programming.

Ester Stalder, Daniela Tischhauser and Maya Greuter from the secretary office are thanked for taking care of all administrative matters.

Prof. P. J. Sarre, Prof. M. F. Rode and Prof. A. L. Sobolewski are kindly acknowledged for collaborations.

The Swiss National Science Foundation and the University of Basel are thanked for their financial support.

I would like to thank the rest of the group for the friendly atmosphere, for nice time we had in- and outside the university. I wish you all the best and good success for the future.

Finally, I would like to thank cordially my parents, my sister and her husband, my nephew and Tobias for their love, strength, encouragement and moral support.

Saint-Louis, August 2012

# CONTENTS

1 THESIS INTRODUCTION ........ 13

2 THE AROMATIC ISM ........ 17
- 2.1 Introduction ........ 18
- 2.2 Unidentified IR emission ........ 19
- 2.3 Diffuse interstellar absorption bands ........ 21
- 2.4 Protonated PAHs as carriers of DIBs ........ 24
- 2.5 Formation of protonated PAHs in the ISM ........ 25
- Bibliography ........ 27

3 METHODOLOGY ........ 33
- 3.1 Matrix Isolation technique: an overview ........ 34
  - 3.1.1 Guest-host interactions and their influence on the spectral features ........ 35
- 3.2 Apparatus Description ........ 36
- 3.3 Production of molecules to be studied ........ 38
  - 3.3.1 Ion sources ........ 38
  - 3.3.2 Production of H-PAH$^+$ cations ........ 42
  - 3.3.3 Direct deposition and ionization „In situ“ ........ 45
- 3.4 Measurements ........ 46
  - 3.4.1 UV-Vis: absorption and emission ........ 46
  - 3.4.2 IR Region ........ 48
- 3.5 Spectral identification ........ 49
  - 3.5.1 Electron scavenger and photoneutralization ........ 50
  - 3.5.2 Selective irradiation of sample ........ 51
- 3.6 Quantum-chemical calculations ........ 52
- Bibliography ........ 53

4 PROTONATED BENZENE AND FULVENE AND NEUTRAL $C_6H_7$ ISOMERS ........ 57
- 4.1 Introduction ........ 58
- 4.2 Observations ........ 59
  - 4.2.1 $C_6H_7^+$ Cations ........ 59
  - 4.2.2 $C_6H_7$ Neutrals ........ 61
- 4.3 Computational results ........ 65
- 4.4 Discussions ........ 69

4.4.1 $C_6H_7^+$ Cations 69
4.4.2 $C_6H_7$ Neutrals 70
4.5 Conclusions 73
Bibliography 74

5 PROTONATED ANTHRACENE AND PHENANTHRENE 77
5.1 Methodology 78
5.2 Results and discussion 78
5.2.1 Protonated Anthracene 78
5.2.2. Protonated Phenanthrene 86
5.3 Relevance of H-An$^+$ and H-Ph$^+$ to DIBs 90
Bibliography 91

6 PROTONATED PYRENE AND CORONENE: ABSORPTION AND FLUORESCENCE 95
6.1 Introduction 96
6.2 Protonated Pyrene 96
6.2.1 Absorption 96
6.2.2 Fluorescence 102
6.3 Protonated Coronene 105
6.3.1 Absorption 105
6.3.2 Fluorescence 110
6.4 Astronomical comparison 112
Bibliography 114

7 PROTONATED NAPHTHALENES AND THEIR REVERSIBLE PHOTOISOMERIZATION 117
7.1 Introduction 118
7.2 Methods 118
7.2.1 Production of ions 118
7.2.2 Computations 120
7.3 Observations 122
7.3.1 Visible spectral region 122
7.3.2 UV spectral region 128
7.3.3 $\alpha$-HN$^+$ ↔ $\beta$-HN$^+$ photoisomerization 129
7.3.4 Fluorescence studies 133
7.3.5 Other $C_{10}H_9^+$ and $C_{10}H_9$ isomers 135
7.4 Computational results 137
7.4.1 Electronic transitions of $C_{10}H_9^+$ and $C_{10}H_9$ isomers 137
7.4.2 Electronic states and photophysics of HN$^+$ 140
7.5 Conclusions 144
Bibliography 145

APPENDIX 149

A.1 Ring-Chain cations: $C_6H_5{-}C_{2n}H^+$, n=1–4 ....150
  A.1.1 Introduction ....150
  A.1.2 $C_8H_6^+$ ....150
  A.1.3 $C_{10}H_6^+$ isomers ....151
  A.1.4 $C_{12}H_6^+$ and $C_{14}H_6^+$ ....154
A.2 "Indene" series ....156
  A.2.1 $C_9H_7^+$ ....156
  A.2.2 $C_9H_8^+$ ....158
  A.2.3 $C_9H_9^+$ ....160
A.3 $C_{10}H_7^+$ ....164
A.4 $TiO_2$ ....165
A.5 $TiO_3/TiC_4$ ....168
Bibliography ....169

CONCLUSIONS ....171

CURRICULUM VITAE ....174
List of publications ....175

# CHAPTER 1

## THESIS INTRODUCTION

Polycyclic aromatic hydrocarbons PAHs have been of great scientific attention for many years due to their ubiquitous presence on Earth and in space. They are found in air, water, soils and are formed during combustion and pyrolytic processes from anthropogenic and natural sources. These are, for example, coal processing or incomplete combustion of organic compounds, motor vehicle exhaust or cigarette smoke. Amongst natural sources of PAH emission are forest fires, volcanoes, hydrothermal processes and others. Many of these species are known to be mutagenic and carcinogenic [1-3]. Astrophysically, PAHs and their numerous derivatives are viewed as a common constituent of the interstellar and circumstellar environments because of the widespread detection of the unidentified IR emission bands, which are produced by PAH related material "heated" by the absorption of UV radiation [4]. It is believed, that PAH related species contribute to astronomical spectral features in the whole range — from the UV to the radio region.

In the protonated form (H-PAH$^+$s) PAHs represent a fundamental class of organic ions. H-PAH$^+$s are the intermediates in electrophillic substitution reactions and several acid-catalyzed transformations of aromatic rings [5, 6]. Great effort has been devoted, therefore, since the 1960s for elucidating their chemical and physical properties [7]. Among other polycyclic arene derivatives, H-PAH$^+$s may also play a role as short-lived intermediates toward soot formation in flames and combustion environments [8-10]. Direct spectroscopic monitoring of such processes would require the knowledge of their electronic properties and structure.

The topic of H-PAH$^+$s has been revived recently in the context of their possible role in the ISM [11-14]. It is believed that this class of PAH derivatives may be responsible for some of the Diffuse Interstellar and Unidentified Infrared emission bands and even for some of the Red Rectangle emission features [14-16]. A number of experimental and computational results have been reported since then; the main focus, however, was on their IR spectral characterization. According to the PAH hypothesis, all the astronomical spectral features above imply electronic absorption and intramolecular dynamics such as electronic relaxation and IVR. However, experimental data that are of direct relevance for the identification of interstellar or circumstellar H-PAH$^+$s are rather scarce. Laboratory electronic spectra of isolated H-PAH$^+$s in the gas phase or in cryogenic matrices, are missing in the literature, mainly due to the experimental challenges in their production and spectral detection.

The main part of this work was devoted, therefore, to the production and spectroscopic characterization of protonated PAHs. The approach utilized is a combination of mass-selection with matrix isolation spectroscopy. Ions of interest were embedded in solid neon and investigated by means of electronic absorption and emission spectroscopy in the 1100–250 nm spectral range. The results of the present matrix studies provide information on the structure of H-PAH$^+$s, their ground and excited states electronic properties, wavelengths and relative intensities of the bands of these species, which can be used as a starting point for gas-phase measurements and for evaluating their astrophysical relevance.

This thesis is structured in the following way:

*Chapter 2* provides a short description of the ISM and the unidentified interstellar spectral features. A brief history, characteristics and the problem of the diffuse interstellar bands are described. An overview of chemical properties of PAHs and their role in the ISM, with the main point on the protonated species, is also given.

*Chapter 3* provides an insight into the matrix isolation technique in general, a description of the experimental set up successfully employed for the studies on H-PAH$^+$s, as well as other unstable and/or reactive compounds of astrophysical relevance. A number of methods tested for their production are detailed along with difficulties encountered during these studies.

In the next chapters of the manuscript results of the matrix isolation studies on the protonated PAHs and respective neutrals, ranging from benzene to coronene, are presented. The interpretations of the spectra observed are supported by the computational data; the relevance of the studied species is discussed.

*Chapter 4* describes the studies on $C_6H_7^+$ and neutral $C_6H_7$ isomers. Direct spectroscopic characterization of two structural isomers of this cation, which have been postulated in the earlier gas-phase reactivity studies are presented. One of the isomers is confirmed to be protonated benzene, whereas the second, less stable isomer of $C_6H_7^+$ is identified as $\alpha$-protonated fulvene and is characterized spectroscopically for the first time. Their electronic transitions lie in the UV range and overlap. After neutralization of the cations, the electronic transitions of cyclohexadienyl and $\alpha$-hydrogenated fulvene radicals are identified. Upon excitation of cyclohexadienyl to the $B\ ^2B_1$ state, photoisomerization to an open-chain structure and $\alpha$-hydrogenated fulvene radical was observed.

*Chapter 5:* several isomers of protonated anthracene and phenanthrene are detected; they have moderately intense absorption systems in the 400–550 nm range, where a number of broad DIBs are found. Corresponding neutrals were observed in the UV. The present spectroscopic studies on these two species allow a direct comparison of their transition intensities with the ones of the parent anthracene$^+$ and phenanthrene$^+$ cations. The near IR electronic transitions of parent PAH cations are by an order of magnitude stronger than the visible absorptions of the protonated species.

*Chapter 6* describes the results of investigations on protonated pyrene and coronene, which are often considered as a model of PAHs in the discussions of their role in the ISM. Three electronic transitions of the most stable isomer of protonated pyrene and four of protonated coronene were observed for the first time. The strongest, $S_1 \leftarrow S_0$ transitions, are in the visible region, with onset at 487.5 nm for protonated pyrene and 695.6 nm for protonated coronene. The fluorescence spectra were also recorded: protonated pyrene and coronene once electronically excited decay radiatively. The strongest, visible absorption and fluorescence bands of cations were compared with astronomical spectra for evaluating their relevance.

*Chapter 7: Alpha*- and *beta*-protonated naphthalenes were investigated by electronic absorption and fluorescence spectroscopy in matrices. The absorption spectra revealed $S_1/S_2 \leftarrow S_0$ transitions in the optical and UV domains with onsets at 502.1 and 396.1 nm in the case of $\alpha$-HN$^+$, and 534.5 and 322.3 nm for $\beta$-HN$^+$. Wavelength-dispersed fluorescence was observed for $\alpha$-HN$^+$. Another $C_{10}H_9^+$ isomer was also detected in the UV and identified as 2-indenylmethylium. Corresponding neutral $C_{10}H_9$ radicals were also characterized. The intramolecular proton transfer leading to the $\alpha$-HN$^+ \leftrightarrow \beta$-HN$^+$ photoisomerization was observed and is reversible: wavelength-selective irradiation of the $S_2 \leftarrow S_0$ absorption of $\alpha$-HN$^+$ leads to the $\alpha$-HN$^+ \rightarrow \beta$-HN$^+$ isomerization, whereas $\beta$-HN$^+$ relaxes rapidly into the more stable $\alpha$-HN$^+$ either *via* quantum tunneling of the "excess" hydrogen or, upon $S_1 \leftarrow S_0$

excitation of the $\beta$-HN$^+$, through one of the two out-of-plane, chair-like $S_1/S_0^{\alpha}$ or $S_1/S_0^{\beta}$, conical intersection geometries.

In the last part of this thesis (*Appendix*) results of several other (secondary) projects are briefly summarized. Among them are electronic spectra of $C_6H_5{-}C_{2n}H^+$ (n=1-4) ions in neon matrices and preliminary results on the structure of the cations; reactions pathway between benzene / phenylacetylene and $HC_2H$ / $HC_4H$ are discussed. Substituted benzene cations in general are expected to bare large oscillator strengths; their electronic transitions are predicted to fall in the visible and near IR regions due to the open-shell electronic structure. These species can, therefore, be considered as possible carriers of DIBs.

## CHAPTER 2

# THE AROMATIC ISM

The presence of polycyclic aromatic hydrocarbons and their numerous derivatives in the interstellar medium is evidenced almost exclusively from their infrared emission spectra — the so-called "unidentified" infrared (UIR) emission bands. However, it is very difficult to identify an individual PAH from these spectra as these emission features are typical for groups of molecules rather than for a specific molecule; in contrast to infrared spectra, electronic spectra (as well as rotational) are distinct characteristics of the molecular structure and provide essential information on the individual molecules present in space.

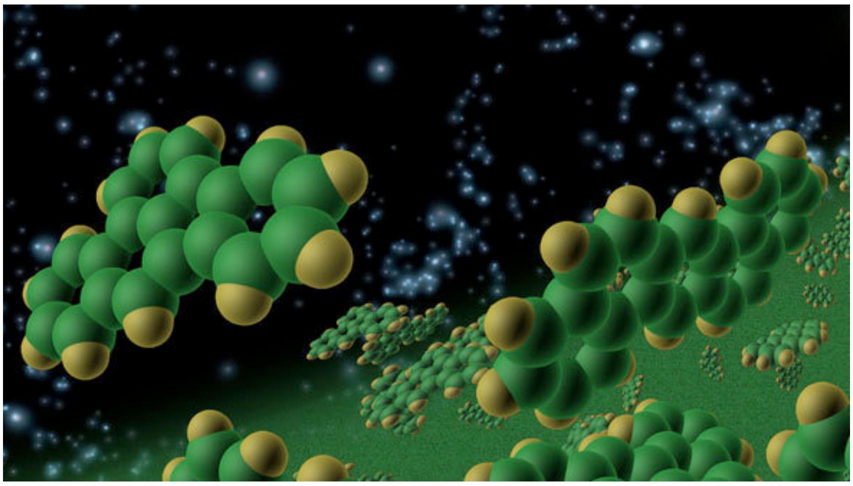

Illustration: NASA/JPL/Caltech/T-Pyle/SSC

## 2.1 INTRODUCTION

The space between stars is not completely empty. It contains gas (99%) and dust (1%), which coexist under different physical conditions. The most abundant elements of the IS gas are hydrogen and helium, which are a result of the Big Bang nucleosynthesis. Less than 2% of atoms are elements heavier than hydrogen or helium, are a result of the processes of stellar evolution. IS gas and dust aggregate to form interstellar clouds, differing in temperature ($10–10^4$ K) and densities ($100–10^6$ H atoms in $cm^{-3}$). Stars are formed in the darkest regions of the ISM – in dense molecular clouds. The most abundant and chemically reactive elements of ISM are carbon, nitrogen and oxygen. Other heavier elements are synthesized deep within the stars and are expelled into the surroundings during the intense mass-loss at the end of their lifecycle through stellar winds, planetary nebulae and supernovae. If the abundance of carbon exceeds that of oxygen in such outflows, a wide variety of organic material is formed. Ejected material disperses then through the ISM enriching it with the atomic and/or molecular carbonaceous material. In the ISM, these compounds are further processed through a different chemical and physical processes such as gas-phase and grain-surface chemistry, UV radiation, destruction by cosmic rays or shock waves and others.

Since the beginning of the 20th century, the study of the physics and chemistry of interstellar gas has played a dominant role in astrophysics. Most of the work at that time was focused on observations of the absorption lines coming from diffuse interstellar medium, which does not completely obscure the light of background stars. These lines are known now as Diffuse Interstellar Bands (DIBs). More than seven decades ago the first diatomic species CH, CN and $CH^+$ have been detected in such low-density regions of ISM through their UV-optical transitions. Development of millimetre-wave telescopes in the 1970s switched most of the laboratory effort to the dense regions, dark molecular clouds, where a rich chemistry happens. Up to now, more than 150 gas-phase molecules have been observed in space. Among them are organics such as nitriles, aldehides, alcohols, acids, as well as many long-chain hydrocarbon compounds. Almost all have been detected in dense clouds or circumstellar regions by rotational and ro-vibrational spectroscopy in the radio-frequency up to far-infrared regions.

Diffuse interstellar medium remains, however, until now much less understood. Besides the first diatomics, other simple molecules were later identified in the UV (CO and $H_2$) and in the near IR regions ($C_2$, $H_2$, $H_3^+$). The smallest polyatomic carbon chain, $C_3$, has been identified in interstellar clouds in the optical [17] and far IR [18]. On top of that, a large and diverse set of organic compounds is believed to be found in the diffuse ISM and contribute to the main unidentified spectral features observed in diffuse/translucent clouds. These are the UV bump at 217 nm, UIRs between 3 and 15 μm and DIBs in the visible, 400–1100 nm. Whereas the former two are generally attributed to a solid organic compounds and PAH derivatives, respectively (and can not be identified by a single carrier), DIBs are the numerous (resolved) spectral features of individual molecules present in space, representing until now the most intriguing challenges of astronomical spectroscopy.

Diffuse interstellar bands are detected from the ISM regions with temperatures in the range of 50–100 K and particle densities of 10–$10^3$ $cm^{-1}$. Since their first observation in 1922 [19], more than 600 absorption lines have been discovered [20]. A number of molecular carriers were suggested, but either disproved after careful laboratory studies or are still awaiting their laboratory spectral characterization. It is widely assumed that the DIB carriers are composed of cosmically most abundant elements, H, C, O, and N. Moreover, they are “organic” in nature, because of carbon’s ability to form a great diversity of molecules to support the wide variety of individual species probably needed to explain the DIBs [21].

Much of the recent discussions about possible carriers of these interstellar absorption lines (or in general to be interstellar) has been focused on PAHs and related species. Such discussions have been provoked by the fact, that they are widely accepted to be the carriers of “aromatic” IR emission, which is observed from a large variety of astronomical objects, in particular from the diffuse interstellar medium. There are an extensive number of reviews on the role of PAHs (and related compounds) in astrophysical environments [21-27]. The most prominent aspects of these proposals are briefly summarized in Sections 2.2 and 2.3.

## 2.2 UNIDENTIFIED IR EMISSION

The astrophysical importance of PAHs is closely linked with the UIR emission bands. This spectrum is dominated by a series of broad features at 3030, 1610, 1280, 1150 and 890 $cm^{-1}$ (3.3, 6.2, 7.7, 8.6 and 11.2 μm) as well as number of minor bands and continuum (Figure 2.1).

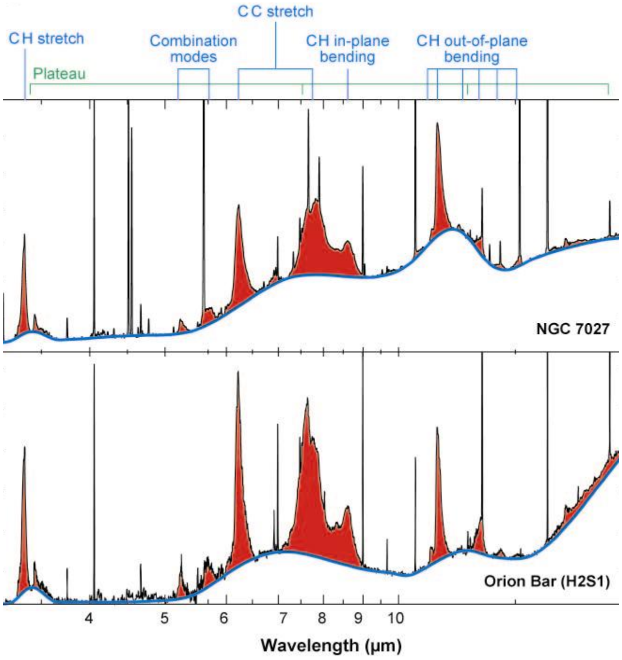

**Figure 2.1:** The mid-infrared spectra of the photodissociation region in the Orion Bar and in the planetary nebulae NGC 7027 are dominated by a rich set of emission features. These features are labeled with the vibrational modes of polycyclic aromatic hydrocarbon molecules at the top. Figure taken from [28].

These are characteristic of vibrations in $sp^2$-hybridized hydrocarbons, as in aromatic molecules. The UIRs are found in a variety of astronomical sources, including diffuse ISM, circumstellar environments and even from extragalactic sources. They are normally observed toward regions in which dust and gas are illuminated with UV light from a nearby star. The mechanism suggested to explain the UIRs is that a gas-phase PAH molecule absorbs Vis/UV light from a nearby star, relaxes electronically through internal conversion or intersystem crossing. This is followed by internal vibrational redistribution faster than fluorescence, and afterward emits IR radiation [23, 29, 30].

Neutral and ionized PAHs were not able to reproduce the intensity ratio and the correlation observed between different lines from different sources. Consequently, many complex PAH derivatives, such as dehydrogenated and hydrogenated, nitrogen- and silicon-containing, methyl-substituted PAHs and their metal complexes have been considered. Recently, protonated PAH molecules have been put forward as possible UIR carriers. Their calculated IR spectra identify H-PAH$^+$s as promising candidates for UIR band carriers [14]. Since then a number of H-PAH$^+$s have been studied in the gas phase using single-photon IR photodissociation spectroscopy by the messenger atom method, or by IR multiphoton dissociation using free-electron lasers [31-36]. The largest molecule studied so far is protonated coronene, whose IR spectrum closely resembles the astronomical UIR features [36].

Numerous absorption and emission experiments on different classes of PAHs, in either noble gas matrices or in the gas phase failed, however, to characterize with certainty the UIR features. It has been concluded that the general characteristics – profile and position – of UIRs are reproduced by nearly all larger species studied, making individual identification in the mid-IR difficult. In the far-IR range PAHs exhibit vibrations in-plane deformation of the PAH skeleton, which produce very distinct/characteristic spectral features. Hence, far-IR spectral signatures of interstellar PAHs, which may become available with Herschel spectroscopic studies, might provide key information on the individual PAHs present in space [37].

## 2.3 DIFFUSE INTERSTELLAR ABSORPTION BANDS

Diffuse interstellar bands (Figure 2.2) are absorption lines seen in spectra of stars and produced by the absorption of stellar light by species present in diffuse or translucent clouds, as is evident from the constant spectral position respective to the stellar atomic lines. Despite several identified (mostly in UV) atomic and molecular electronic absorptions (Section 2.1), their origin remains unclear [39-41]. The strongest evidence has been presented recently for the linear $CCCH_2$ being responsible for a series of DIBs [42]. Matrix isolation spectra of the mass-selected $C_3H_2$ and $C_3D_2$ were used as a guide for the identification of the bands in the gas phase using CRD experiments; both were recorded in this group.

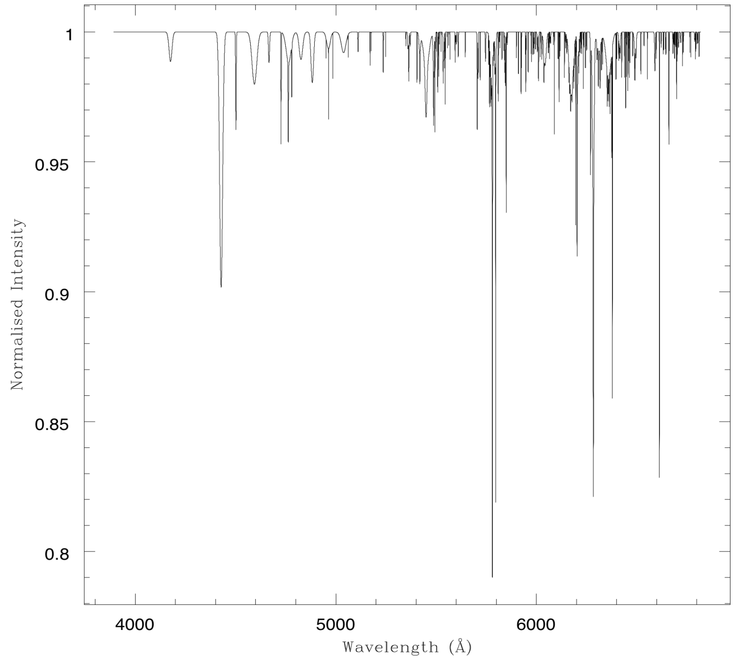

**Figure 2.2:** Synthetic spectrum of 226 DIBs confirmed towards BD+63° 1964 between 3906 Å and 6812 Å. This object is cited as a prototype for the DIB spectrum (taken from [38]).

A short overview of the observational properties and behavior of DIBs is given below.

- Correlation between DIB strengths and the star-light reddening is observed for many of DIBs, but the shape and width of individual DIB appear to be constant, irrespective of the sight line. These characteristics should vary if solid-state transitions were responsible, thus providing evidence for free, gas-phase molecules being carriers of the absorption features.
- Interstellar grains are known to align due to the interstellar magnetic field. None of the studied DIBs of different strengths and widths exhibit a polarised absorption spectrum, neither for the dense (efficient grain alignment) nor for the diffuse clouds [43, 44]. Thus, the carriers are not related to large grains and grain impurities, but to gas-phase molecules.
- The DIB's width and shape is assumed to be due to close lying unresolved rotational lines or the fast intramolecular vibrational relaxation. High-resolution observations of DIBs revealed a fine structure in the profiles of many sharper diffuse bands, whereas the broader have a smooth profile [40, 45]. The observed fine structure is typical of

rotational contours of large gas-phase molecules. The profiles were found to vary with temperature of the surrounding [46, 47].

- No correlation found between DIB strength and UV bump, which is also believed to arise from organic interstellar material and for which a line polarization is observed.
- Only a few DIBs were found to exhibit a reasonable correlation with each other (one of the examples are the 6196 and 6613 Å DIBs) thus indicating that the majority of the DIBs have different, possibly physically/chemically related carriers. Such correlation-search studies are based on several assumptions: DIBs are vibronic bands of gas-phase molecules; transitions occur from their ground vibrational state; intensities of the bands with a common carrier are fixed, as they do not depend on temperature and density. Additionally, several DIB families can be distinguished. One of such families is a number of strong DIBs, which correlate with atomic hydrogen much stronger than with $H_2$, and that the DIBs are weak (relative to reddening) in dense clouds. Another set of DIBs appears to be abundant in diffuse molecular clouds. The DIB carriers are likely fairly large molecules and the breadth of the bands is likely due to unresolved rotational structure and/or intramolecular vibrational relaxation (IVR) [21, 47].

It has been proposed that PAHs contribute to some of the DIBs right after the mechanism explaining the UIR emission appeared [23, 30]. This gave birth to the so-called PAH-DIB hypothesis, which in turn stimulated extensive experimental studies, in noble gas matrices and in the gas phase. Apart from having their electronic transitions in the UV, optical and near IR spectral ranges, PAH compounds are also resistant to UV radiation as is required for the DIB carrier.

According to numerous experimental data, the strongest (first) electronic transitions of neutral PAHs lie in the UV region. Due to their low ionization potential, around 5–9 eV depending on their size and geometry, neutral PAHs are ionized by UV radiation in the ISM, in regions close to stars or in the diffuse interstellar clouds. Resulting $PAH^+$ cations are strong absorbers of visible and near-IR photons, where DIBs are found, and gained significant attention for that reason. The transitions tend to redshift with increasing in size of the cation. Several attempts have been made to compare available spectral data of a range of neutral and ionized PAHs with DIBs. Among them are coronene and ovalene and their cations [48]; fulerene $C_{60}^+$ spectrum recorded in neon matrix showed a reasonable correlation with four of the DIB lines in the 935–965 nm region [27].

Such a match is, however, not conclusive due to the matrix-to-gas phase spectral shift. Gas-phase data are not available till now.

Naphthalene and anthracene cations have been proposed to be the carriers of a number of DIBs as a result of direct comparisons of observations with gas-phase data [49, 50]. The hypothesis was, however, disproved; several further observations failed to detect interstellar absorptions at wavelengths of the laboratory spectra [51, 52]. Moreover, they will probably dissociate and loose H atom or $C_2H_2$. The spectra of several cold, gas-phase neutral PAHs have been compared with an extensive number of astronomical spectra of reddened, early-type stars. The observations show, that neutral PAHs exhibit band profiles similar to the profile of the narrow DIBs. This indicates that the carriers of the narrow DIBs may have close molecular structure and characteristics [53].

## 2.4 PROTONATED PAHS AS CARRIERS OF DIBS

H-PAH$^+$s represent a specific group of prospective DIB carriers. Several laboratory measurements demonstrated that they can be readily formed through attachment of H-atoms to PAH$^+$ radical cations [11, 12, 54], whereas no significant reaction was observed for the formed H-PAH$^+$s. These results are explained in terms of the electronic structure of the two cationic species. PAH$^+$ has an open-shell electronic structure and reacts readily (and rapidly [11, 54]) with a hydrogen atom, which has an unpaired electron too. The resulting species, H-PAH$^+$, possess a more favorable closed-shell configuration and is, therefore, also much less reactive with another hydrogen atom.

Protonation does not alter the electron number of the molecule. The electronic structure of H-PAH$^+$s is related to that of the parent neutrals, retaining a system of conjugated $\pi$ electrons. The proton is, however, covalently bound to a carbon moiety forming an aliphatic $sp^3$-hybridized carbon atom. This reduces the aromaticity of the PAH, its symmetry and the HOMO-LUMO gap, and these altogether changes the electronic spectrum of parent aromatic molecule. The most significant result is the occurrence of allowed electronic transitions at much lower energies, in the visible and near IR regions, as has been also confirmed by computations [15]. On the other hand, calculated HOMO-LUMO energy differences of small H-PAH$^+$s are close to their dissociation energies, which are around 2.2–3.5 eV for a H atom or $H_2$ loss [55]. Thus, in the absence of IVR, this makes them unstable in the ISM. However, as the size of PAH gets larger, IVR process may play a profound role in their stabilization. As for protonated coronene, calculations predict the electronic absorption at around 1.7 eV and the calculated dissociation energy is ca. 4.4 eV.

## 2.5 FORMATION OF PROTONATED PAHS IN THE ISM

Presence of H-PAH$^+$s in the ISM assumes the presence of neutral and/or ionized PAHs in these environments. Their direct formation in the diffuse ISM has not been considered in models dealing with the gas-phase chemistry. There are several other regions of ISM, where PAHs could be formed. One possibility is that they are "born" in circumstellar envelopes/outflows of carbon-rich stars [56]. In such environments PAHs may be formed in quantities, sufficient to contribute for the UIRs and DIBs. Many formation models have been reported, which originate from numerous combustion chemistry studies.

In these models, the first step towards PAH formation is the closure of the first aromatic ring, which may result in formation of either benzene (c-$C_6H_6$) or phenyl radical (c-$C_6H_5$). In early studies on "acetylenic" flames, the $C_6$-ring formation is observed in reactions of vinylic $C_4H_3$ and $C_4H_5$ radicals with acetylene directly involving chemically activated isomerization channels [57, 58]:

$$1\text{-}C_4H_3 + C_2H_2 \rightarrow C_6H_5$$

$$1\text{-}C_4H_5 + C_2H_2 \rightarrow C_6H_6 + H$$

Another, prevalent formation route involves the recombination of two propargyl radicals [59-61]:

$$C_3H_3 + C_3H_3 \rightarrow C_6H_6$$

$$C_3H_3 + C_3H_3 \rightarrow C_6H_5 + H$$

The propargyl reactions lead to several intermediates such as, for example, fulvene (an isomer of benzene). Direct formation of benzene dominates.

Several routes have been proposed for the formation of larger PAH molecules. The most extensively studied (experimentally as well as theoretically) is the so-called "HACA mechanism" – where a stepwise acetylation along with hydrogen abstraction results in a formation of the next fused ring [62-64]. In combination with the Diels–Alder-type mechanism (dominant in methane combustion), where the acetylene molecule closes "empty spaces" in such PAHs as biphenyl, phenanthrene, it is the way of producing larger, more compact PAH species (Figure 2.3) [65, 66].

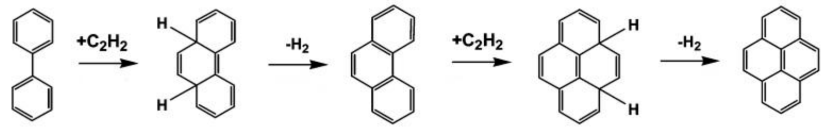

**Figure 2.3:** Schematic presentation of Diels–Alder type formation mechanism of phenanthrene and pyrene [65].

PAH could also be formed during sputtering of graphitic and/or carbonaceous grains under harsh environmental conditions, such as interstellar shocks, thereby resulting in PAHs as fragmentation products. When a graphitic grain is destroyed in a shock, the fragment will be a planar, fused-ring species, which may react with H atoms and result in PAHs [24]. If carbonaceous dust is taken into account, their processing may result in chemical structures, that are much more complex than thought, consisting of aromatic and aliphatic fragments linked together (section A.1).

Another possibility is the formation of PAHs in dense molecular clouds. Recently, crossed molecular beam experiments along with theoretical studies reported gas-phase naphthalene formation via a barrierless and exoergic reaction of phenyl radical ($C_6H_5$) and vinyl-acetylene ($CH_2=CH-C\equiv CH$) [67]. These studies have shown, that PAH-formation may occur not only in high temperature environments such as combustion systems, but also implies that low temperature chemistry can initiate the synthesis of the very first PAH in the interstellar medium, such as cold molecular clouds.

Neutral PAHs, once formed, will be ionized by UV radiation in the ISM, as their ionization potentials are rather low (around 6-9 eV depending on their size and geometry). Alternatively, absorption of a UV photon may lead to unimolecular reaction resulting in an H atom loss. The PAH species created may react with highly abundant atomic and/or molecular hydrogen to form protonated PAHs. The relevant reaction rates have been measured in selected-ion flow tube experiments for benzene, naphthalene, pyrene and coronene [11, 12, 68]. PAH cations reacted readily with atomic hydrogen, dehydrogenated $PAH^+$ with $H_2$ molecules, both at almost the same rate. Reaction rate constants for the reactions above were found to be in the range 2.5–1.4 $10^{-10}$ $cm^3$ $s^{-1}$ and independent on size of PAH cations. The association of protonated PAHs with atomic hydrogen was found to be much slower. At high-density conditions, such association reactions proceed by collisional stabilisation, while at low density they proceed by radiative stabilization. The radiative association with H was shown to be efficient for larger PAH species, and the $H_2$ loss dissociation channel for protonated species is not likely to be important in such reactions [13]. Thus, H-PAH$^+$s could be formed in ISM regions with a high ionization rate and hydrogen atom abundance, such as diffuse or translucent clouds.

Another source of protonated PAHs in the ISM may be the proton transfer from species such as $H_3^+$ or $H_3O^+$, abundant in the ISM, to a neutral PAH [69, 70]. Reaction rate studies of proton transfer to a range of various organic compounds in a flowing afterglow-selected ion flow tube experiment found that for smaller hydrocarbons including cyclic species the dissociative proton transfer is usually observed if the exothermicity of a particular channel exceeds 100 kJ mol$^{-1}$ [71]. Larger aromatic hydrocarbons, on the other hand, should experience only non-dissociative proton transfer, forming protonated PAHs, as the excess energy in so formed H-PAH$^+$s will be distributed among many vibrational modes.

## BIBLIOGRAPHY

[1] D. Poster, M. Schantz, L. Sander, S. Wise. Analysis of polycyclic aromatic hydrocarbons (PAHs) in environmental samples: a critical review of gas chromatographic (GC) methods. *Analyt. Bioanalyt. Chem.,* 386 (2006) 859-881.

[2] T. Wenzl, R. Simon, E. Anklam, J. Kleiner. Analytical methods for polycyclic aromatic hydrocarbons (PAHs) in food and the environment needed for new food legislation in the European Union. *Trends Analyt. Chem.,* 25 (2006) 716-725.

[3] R. Simon, J. Gomez Ruiz, C. von Holst, T. Wenzl, E. Anklam. Results of a European inter-laboratory comparison study on the determination of EU priority polycyclic aromatic hydrocarbons (PAHs) in edible vegetable oils. *Analyt. Bioanalyt. Chem.,* 391 (2008) 1397-1408.

[4] A.G.G.M. Tielens. 25 years of PAH hypothesis, in: *PAHs and the Universe*; C. Joblin, A.G.G.M. Tielens, Eds.; *EAS Publications Series*, 46 (2011) 3-10.

[5] G.A. Olah. Aromatic Substitution .28. Mechanism of Electrophilic Aromatic Substitutions. *Acc. Chem. Res.,* 4 (1971) 240-248.

[6] G.A. Olah, C.U. Pittman, R. Waack, M. Doran. ELECTRONIC SPECTRA OF CARBONIUM IONS IN STRONGLY ACIDIC SOLUTIONS. *J. Am. Chem. Soc.,* 88 (1966) 1488-1495.

[7] G.A. Olah, J.S. Staral, G. Asencio, G. Liang, D.A. Forsyth, G.D. Mateescu. Stable carbocations. 215. $^{13}$C nuclear magnetic resonance spectroscopic study of the benzenium, naphthalenium, and anthracenium ions. *J. Am. Chem. Soc.,* 100 (1978) 6299-6308.

[8] P. Weilmuenster, A. Keller, K.H. Homann. Large molecules, radicals, ions, and small soot particles in fuel-rich hydrocarbon flames: Part I: positive ions of polycyclic aromatic hydrocarbons(PAH) in low-pressure premixed flames of acetylene and oxygen. *Combust. Flame,* 116 (1999) 62-83.

[9] A.B. Fialkov, J. Dennebaum, K.H. Homann. Large molecules, ions, radicals, and small soot particles in fuel-rich hydrocarbon flames part V: Positive ions of polycyclic aromatic hydrocarbons (PAH) in low-pressure premixed flames of benzene and oxygen. *Combust. Flame,* 125 (2001) 763-777.

[10] A. Kiendler, F. Arnold. First composition measurements of positive chemiions in aircraft jet engine exhaust: detection of numerous ion species containing organic compounds. *Atmosph. Env.,* 36 (2002) 2979-2984.

[11] V. Le Page, Y. Keheyan, V.M. Bierbaum, T.P. Snow. Chemical constraints on organic cations in the interstellar medium. *J. Am. Chem. Soc.,* 119 (1997) 8373-8374.

[12] T.P. Snow, V. Le Page, Y. Keheyan, V.M. Bierbaum. The interstellar chemistry of PAH cations. *Nature,* 391 (1998) 259-260.

[13] E. Herbst, V. Le Page. Do H atoms stick to PAH cations in the interstellar medium? *Astron. Astrophys.,* 344 (1999) 310-316.

[14] D.M. Hudgins, C.W. Bauschlicher, L.J. Allamandola. Closed-shell polycyclic aromatic hydrocarbon cations: a new category of interstellar polycyclic aromatic hydrocarbons. *Spectrochim. Acta, Part A,* 57 (2001) 907-930.

[15] A. Pathak, P.J. Sarre. Protonated PAHs as carriers of diffuse interstellar bands. *Mon. Not. Roy. Astron. Soc.,* 391 (2008) L10-L14.

[16] M. Hammonds, A. Pathak, P.J. Sarre. TD-DFT calculations of electronic spectra of hydrogenated protonated polycyclic aromatic hydrocarbon (PAH) molecules: implications for the origin of the diffuse interstellar bands? *Phys. Chem. Chem. Phys.,* 11 (2009) 4458-4464.

[17] J.P. Maier, N.M. Lakin, G.A.H. Walker, D.A. Bohlender. Detection of C3 in Diffuse Interstellar Clouds. *Astrophys. J.,* 553 (2001) 267-273.

[18] J. Cernicharo, J.R. Goicoechea, E. Caux. Far-infrared Detection of $C_3$ in Sagittarius B2 and IRC+10216. *Astrophys. J. Lett.,* 534 (2000) L199.

[19] M.L. Heger. The spectra of certain class B stars in the regions 563-668 and 328-338 nm. *Lick Observatory bulletin,* 337 (1922) 141-147.

[20] L.M. Hobbs, D.G. York, T.P. Snow, T. Oka, J.A. Thorburn, M. Bishof, S.D. Friedman, B.J. McCall, B. Rachford, P. Sonnentrucker, D.E. Welty. A catalog of Diffuse Interstellar bands in the spectrum of HD 204827. *Astrophys. J.,* 680 (2008) 1256.

[21] T.P. Snow, B.J. McCall. Diffuse Atomic and Molecular Clouds. *Annu Rev Astron Astr,* 44 (2006) 367-414.

[22] F. Salama, E.L.O. Bakes, L.J. Allamandola, A.G.G.M. Tielens. Assessment of the polycyclic aromatic hydrocarbon-diffuse interstellar band proposal. *Astrophys. J.,* 458 (1996) 621-636.

[23] J.L. Puget, A. Leger, F. Boulanger. Contribution of large polycyclic aromatic molecules to the infrared emission of the interstellar medium. *Astron. Astrophys.,* 142 (1985) L19-L22.

[24] A.G.G.M. Tielens. Interstellar Polycyclic Aromatic Hydrocarbon molecules. *Annu. Rev. Astron. Astrophys.,* 46 (2008) 289-337.

[25] P. Ehrenfreund, S.B. Charnley. Organic molecules in the interstellar medium, comets, and meteorites: A voyage from dark clouds to the early earth. *Annu Rev Astron Astr,* 38 (2000) 427-483.

[26] F. Salama. PAHs in Astronomy - A Review. *IAU: Organic Matter in Space,* 251 (2008) 357-365.

[27] J. Fulara, J. Krelowski. Origin of diffuse interstellar bands: spectroscopic studies of their possible carriers. *New Astron. Rev.,* 44 (2000) 581-597.

[28] E. Peeters, S. Hony, C. Van Kerckhoven, A. Tielens, L.J. Allamandola, D.M. Hudgins, C.W. Bauschlicher. The rich 6 to 9 mu m spectrum of interstellar PAHs. *Astron. Astrophys.,* 390 (2002) 1089-1113.

[29] A. Leger, L. D'Hendecourt. Are polycyclic aromatic hydrocarbons the carriers of the diffuse interstellar bands in the visible? *Astron. Astrophys.,* 146 (1985) 81-85.

[30] G.P. van der Zwet, L.J. Allamandola. Polycyclic aromatic hydrocarbons and the diffuse interstellar bands. *Astron. Astrophys.,* 146 (1985) 76-80.

[31] N. Solca, O. Dopfer. Protonated benzene: IR spectrum and structure of $C_6H_7^+$. *Angew. Chem.-Int. Edit.,* 41 (2002) 3628-3631.

[32] W. Jones, P. Boissel, B. Chiavarino, M.E. Crestoni, S. Fornarini, J. Lemaire, P. Maitre. Infrared fingerprint of protonated benzene in the gas phase. *Angew. Chem.-Int. Edit.,* 42 (2003) 2057-2059.

[33] U.J. Lorenz, N. Solca, J. Lemaire, P. Maitre, O. Dopfer. Infrared spectra of isolated protonated polycyclic aromatic hydrocarbons: Protonated naphthalene. *Angew. Chem.-Int. Edit.,* 46 (2007) 6714-6716.

[34] H. Knorke, J. Langer, J. Oomens, O. Dopfer. Infrared spectra of isolated protonated polycyclic aromatic hydrocarbon molecules. *Astrophys. J. Lett.,* 706 (2009) L66-L70.

[35] A.M. Ricks, G.E. Douberly, M.A. Duncan. The infrared spectrum of protonated naphthalene and Its relevance for the Unidentified Infrared bands. *Astrophys. J.,* 702 (2009) 301-306.

[36] O. Dopfer. Laboratory Spectroscopy of Protonated PAH Molecules Relevant For Interstellar Chemistry, in: *PAHs and the Universe*; C. Joblin, A.G.G.M. Tielens, Eds.; *EAS Publications Series*, 46 (2011) 103-108.

[37] C. Joblin, G. Mulas, G. Malloci, E. Bergin. Search for far-IR PAH bands with Herschel: modelling and observational approaches, in: *PAHs and the Universe*; C. Joblin, A.G.G.M. Tielens, Eds.; *EAS Publications Series*, 46 (2011) 123-130.

[38] S.O. Tuairisg, J. Cami, B.H. Foing, P. Sonnentrucker, P. Ehrenfreund. A deep echelle survey and new analysis of diffuse interstellar bands. *Astron. Astrophys. Suppl. Ser.,* 142 (2000) 225-238.

[39] W.H. Smith, T.P.J. Snow, D.G. York. Comments on the origins of the diffuse interstellar bands. *Astrophys. J.,* 218 (1977) 124-132.

[40] J.R. Miles, P.J. Sarre. On the diffuse interstellar bands. *J. Chem. Soc., Faraday Transact.,* 89 (1993) 2269-2276.

[41] L.M. Hobbs, D.G. York, J.A. Thorburn, T.P. Snow, M. Bishof, S.D. Friedman, B.J. McCall, T. Oka, B. Rachford, P. Sonnentrucker, D.E. Welty. Studies of the Diffuse Interstellar Bands. III. HD 183143. *Astrophys. J.,* 705 (2009) 32.

[42] J.P. Maier, G.A.H. Walker, D.A. Bohlender, F.J. Mazzotti, R. Raghunandan, J. Fulara, I. Garkusha, A. Nagy. Identification of $H_2CCC$ as a Diffuse Interstellar Band Carrier. *Astrophys. J.,* 726 (2011) 41.

[43] N.L.J. Cox, N. Boudin, B.H. Foing, R.S. Schnerr, L. Kaper, C. Neiner, H. Henrichs, J.F. Donati, P. Ehrenfreund. Linear and circular polarisation of diffuse interstellar bands. *Astron. Astrophys.,* 465 (2007) 899-906.

[44] N.L.J. Cox, P. Ehrenfreund, B.H. Foing, L. d'Hendecourt, F. Salama, P.J. Sarre. Linear and circular spectropolarimetry of diffuse interstellar bands. *Astron. Astrophys.,* 531 (2011) A25.

[45] P.J. Sarre, J.R. Miles, S.M. Scarrott. Molecular Diffuse Interstellar Band Carriers in the Red Rectangle. *Science,* 269 (1995) 674-676.

[46] J. Cami, F. Salama, J. Jimenez-Vicente, G.A. Galazutdinov, J. Krelowski. The rotational excitation temperature of the lambda 6614 diffuse interstellar band carrier. *Astrophys. J.,* 611 (2004) L113-L116.

[47] N.L.J. Cox. The Diffuse Interstellar Bands: an Elderly Astro-Puzzle Rejuvenated, in: *The molecular Universe*; J. Cernicharo, R. Bachiller, Eds.; *IAU Symposium Preceed. Series*, 7 (2011) 162-176.

[48] P. Ehrenfreund, L. D'Hendecourt, L. Verstraete, A. Leger, W. Schmidt, D. Defourneau. Search for the 4430 Å DIB in the spectra of coronene cation and neutral ovalene. *Astron. Astrophys.,* 259 (1992) 257-264.

[49] S. Iglesias-Groth, A. Manchado, D.A. García-Hernández, J.I.G. Hernández, D.L. Lambert. Evidence for the Naphthalene Cation in a Region of the Interstellar Medium with Anomalous Microwave Emission. *Astrophys. J. Lett.,* 685 (2008) L55.

[50] S. Iglesias-Groth, A. Manchado, R. Rebolo, J.I.G. Hernández, D.A. García-Hernández, D.L. Lambert. A search for interstellar anthracene toward the Perseus anomalous microwave emission region. *Mon. Not. Roy. Astron. Soc.,* 409 (2010) 880-880.

[51] J.M. Searles, J.D. Destree, T.P. Snow, F. Salama, D.G. York, J. Dahlstrom. Searching for Naphthalene Cation Absorption in the Interstellar Medium. *Astrophys. J.,* 732 (2011) 50.

[52] G. Galazutdinov, B.-C. Lee, I.-O. Song, M. Kazmierczak, J. Krełowski. A search for interstellar naphthalene and anthracene cations. *Mon. Not. Roy. Astron. Soc.,* 412 (2011) 1259-1264.

[53] F. Salama, G.A. Galazutdinov, J. Krelowski, L. Biennier, Y. Beletsky, I.-O. Song. Polycyclic Aromatic Hydrocarbons and the Diffuse Interstellar Bands: A Survey. *Astrophys. J.,* 728 (2011) 154.

[54] B. Eichelberger, T. Snow, P., C. Barckholtz, V. Bierbaum, M. . Reactions of H, N, and O Atoms with Carbon Chain Anions of Interstellar Interest: An Experimental Study. *Astrophys. J.,* 667 (2007) 1283.

[55] V. Kapinus. Photophysical properties of protonated aromatic hydrocarbons. *Ph.D Thesis*, California Institute of Technology, 2005.

[56] I. Cherchneff. The formation of Polycyclic Aromatic Hydrocarbons in evolved circumstellar environments, in: *PAHs and the Universe*; C. Joblin, A.G.G.M. Tielens, Eds.; *EAS Publications Series*, 46 (2011) 177-189.

[57] M. Frenklach, J.R. Warnatz. Detailed Modeling of PAH Profiles in a Sooting Low-Pressure Acetylene Flame. *Comb. Sci. Tech.,* 51 (1987) 265-283.

[58] P.R. Westmoreland, A.M. Dean, J.B. Howard, J.P. Longwell. Forming benzene in flames by chemically activated isomerization. *J. Phys. Chem.,* 93 (1989) 8171-8180.

[59] J.A. Miller, C.F. Melius. Kinetic and thermodynamic issues in the formation of aromatic compounds in flames of aliphatic fuels. *Combustion and Flame,* 91 (1992) 21-39.

[60] J.A. Miller, S.J. Klippenstein. The Recombination of Propargyl Radicals: Solving the Master Equation. *J. Phys. Chem. A,* 105 (2001) 7254-7266.

[61] W. Tang, R.S. Tranter, K. Brezinsky. An Optimized Semidetailed Submechanism of Benzene Formation from Propargyl Recombination. *J. Phys. Chem. A,* 110 (2006) 2165-2175.

[62] M. Frenklach, H. Wang. Detailed modeling of soot particle nucleation and growth. *Int. Symp. Comb.,* 23 (1991) 1559-1566.

[63] H. Wang, M. Frenklach. Calculations of Rate Coefficients for the Chemically Activated Reactions of Acetylene with Vinylic and Aromatic Radicals. *J. Phys. Chem.,* 98 (1994) 11465-11489.

[64] J. Appel, H. Bockhorn, M. Frenklach. Kinetic modeling of soot formation with detailed chemistry and physics: laminar premixed flames of $C_2$ hydrocarbons. *Comb. Flame,* 121 (2000) 122-136.

[65] V.V. Kislov, N.I. Islamova, A.M. Kolker, S.H. Lin, A.M. Mebel. Hydrogen abstraction acetylene addition and Diels-Alder mechanisms of PAH formation: A detailed study using first principles calculations. *J. Chem. Theor. Comp.,* 1 (2005) 908-924.

[66] V.V. Kislov, A.M. Mebel, S.H. Lin. Ab initio and DFT study of the formation mechanisms of polycyclic aromatic hydrocarbons: The phenanthrene synthesis from biphenyl and naphthalene. *J. Phys. Chem. A,* 106 (2002) 6171-6182.

[67] D.S.N. Parker, F. Zhang, Y.S. Kim, R.I. Kaiser, A. Landera, V.V. Kislov, A.M. Mebel, A.G.G.M. Tielens. Low temperature formation of naphthalene and its role in the synthesis of PAHs (Polycyclic Aromatic Hydrocarbons) in the interstellar medium. *PNAS,* 109 (2012) 53-58.

[68] N.B. Betts, M. Stepanovic, T.P. Snow, V.M. Bierbaum. Gas-phase study of coronene cation reactivity of interstellar relevance. *Astrophys. J.,* 651 (2006) L129-L131.

[69] T.R. Geballe, T. Oka. Detection of H+3 in interstellar space. *Nature,* 384 (1996) 334-335.

[70] P. Drossart, J.P. Maillard, J. Caldwell, S.J. Kim, J.K.G. Watson, W.A. Majewski, J. Tennyson, S. Miller, S.K. Atreya, J.T. Clarke, J.H. Waite, R. Wagener. Detection of $H_3^+$ on Jupiter. *Nature,* 340 (1989) 539-541.

[71] D.B. Milligan, P.F. Wilson, C.G. Freeman, M. Meot-Ner, M.J. McEwan. Dissociative Proton Transfer Reactions of $H_3^+$, $N_2H^+$, and $H_3O^+$ with Acyclic, Cyclic, and Aromatic Hydrocarbons and Nitrogen Compounds, and Astrochemical Implications. *J. Phys. Chem. A,* 106 (2002) 9745-9755.

# CHAPTER 3

# METHODOLOGY

Spectroscopic studies of ions and radicals encounter several essential problems. These are the production of species in sufficient concentrations, the availability of a sensitive detection technique to record their spectra and the ability to identify the observed spectral features. Despite the remarkable progress made in the last decades towards overcoming these difficulties, the *Matrix Isolation* approach remains to be a valuable tool for investigation of spectroscopic properties of transient species. Trapped in a solid cryogenic matrix of inert material, such molecules can be studied spectroscopically by a variety of methods over a wide energy range in a relatively short time. Combination of the matrix isolation with *Mass Selection* enhances further the capability of this method. The apparatus developed in this laboratory is equipped with several ion sources, capable to generate copious amounts of specific ions and combined with a quadrupole mass-filter. The ions and their neutral counterparts are examined by means of *UV-Vis absorption and emission* as well as *IR spectroscopy*. Even despite the main limitations of the matrix isolation technique – spectral shifts and line broadening – the present setup is a unique instrument in producing a variety of transients, performing studies on their structural and spectral properties, providing the basis for high-resolution, gas-phase measurements.

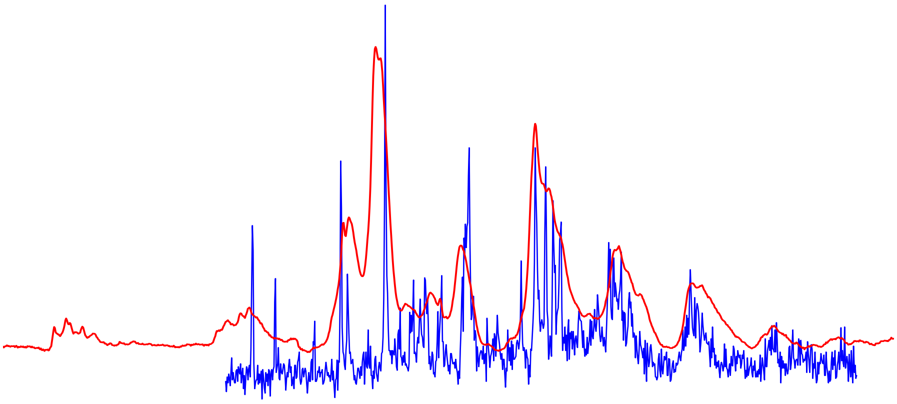

Electronic spectra of $C_4H_3Cl^+$ recorded in Matrix Isolation (red) and 22-pole Ion Trap (blue) Laboratories, University of Basel

S. Chakrabarty et al., *Mol.Phys.,* **110** (24), 3077-3084, 2012

## 3.1 MATRIX ISOLATION TECHNIQUE: AN OVERVIEW

The term “matrix isolation” is commonly used nowadays to describe a well-established technique of trapping atoms, molecules or reactive species in rare gas (Ne, Ar, Kr, Xe) solids at cryogenic temperatures. It has its origins in the development of methods to liquefy gases by Michael Faraday in the early 19th century. In the 1850s James Joule and William Thompson found that the adiabatic expansion of gases resulted in their cooling. The “Joule-Thompson” effect was used to liquefy $O_2$, $N_2$ and CO in the 1870s and later on led to the construction by Carl von Linde in 1895 of the first closed-cycle refrigeration system. James Dewar, who succeeded first in liquefying and then solidifying hydrogen in 1899, further developed the cryogenic technique [1, 2].

The first experiments on matrix isolation spectroscopy date back to L. Vegard’s studies in the 1920s, when organic glasses were used as a host environment. The idea of using rare gases to form cryogenic matrices emerged in the 1950’s by George Pimentel and co-workers [3, 4]. The lack of diffusion of the isolated species in the low temperature matrices and high achievable host-to-guest ratios ($10^6$–$10^8$) allow the stabilization of reactive species. Moreover, due to the high ionization energies and low polarizability of noble gases, the host-guest interactions are rather small. It is, however, not negligible: spectral band splitting and small transition energy shifts (1% of the transition energy [5, 6]) in respect to those in the gas phase are typical for matrix experiments (section 3.5.1).

Rare-gas matrices are transparent to radiation from the far-IR to vacuum-UV. In the IR only the lattice frequencies appear, and these are below 100 $cm^{-1}$, while their lowest-energy electronic transitions occur below 147 nm as for Xe, for Ne it is at 74 nm. The trapped molecules can be subsequently studied by various spectroscopic methods: IR, UV/Vis absorption and emission, ESR, EPR, Raman, and magnetic circular dichroism. Vibrational and electronic absorption spectroscopies are the most established/traditional methods used in combination with matrix isolation. At low temperatures of the experiment the molecules in the sample are quenched to their lowest electronic and vibrational states and no transitions from thermally populated excited states, the so-called “hot bands” are observed. Furthermore, the rigid host matrix limits rotation of most molecules (smaller ones, like $H_2O$, CO, CH can still rotate in the matrix). These features simplify the absorption spectra and may be helpful in the interpretation of gas-phase data.

### 3.1.1 GUEST-HOST INTERACTIONS AND THEIR INFLUENCE ON THE SPECTRAL FEATURES

Although the guest-host interactions are rather weak for solid rare gas matrices, they induce several characteristic changes in the spectral features compared to the gas phase. One of them is that the electronic and vibrational absorptions in matrices are shifted in comparison with gas phase observations – the so-called "matrix shift". The chemically inert matrix environment does not really change the electronic configuration of a guest molecule; its electronic excited state, however, is stabilized in a different way as in the gas phase due to weak electromagnetic fields of the neighbors. Matrix shift is different for each guest, host and site of trapping; the magnitude and even the sign of the shift are difficult to predict. Neon matrix shifts are normally less than 1% of the transition energy, as was reported for vibrational and electronic transitions [5, 6].

The shape and width of electronic absorption bands in matrices are also different from that in the gas phase. Usually the bands are broader, and may have a complex structure (so-called "site structure"). Such a structure arises if molecules occupy different positions in the matrix lattice. Due to these, line broadening or multiple band structures are often observed where only a single band is expected. The appearance of the multiplets may depend on the method of production of the trapped species, the number and population of different sites is temperature dependent. Moreover, bands belonging to the same (and often different) electronic transition of a molecule exhibit the same site structure; this is helpful in the assignment of the spectra if several electronic transitions overlap. Due to shifts and broadening it is impossible to make direct comparison between the absorptions measured in matrix and in the gas phase, only the band maxima are then taken into account. Another characteristic of matrix absorption bands arises due to the coupling of the guest molecule to lattice vibrations of the host. This will produce a wide phonon side band in absorption lines. In cases where coupling between the phonons and electronic states is weak (weak interactions with the host and/or Franck-Condon factors), an intense and well-resolved zero-phonon line (ZPL) will be observed. Usually, electronic absorption and fluorescence spectra of matrix-isolated species overlap and cross at wavelength, which correspond to the position of the ZPL of the electronic transition. This is then a much more precise energy for the band origin and can be compared to the gas phase data if available.

Interaction of guest molecules with the host, results not only in the line-form changes, but also new processes of relaxation become allowed additional to emission of radiation. Matrix isolated molecules may relax non-radiatively to lower states, dissipating the energy in the host lattice. Vibrational relaxations of matrix-isolated molecules depend on the density of vibrational states. For vibrationally excited large molecules with a high density of states, a fast relaxation into the vibrational ground state of an electronic state is observed, from which the most intense emission occurs. Electronic relaxations, as for example internal conversion and intersystem crossing, proceed in matrices also much more effective than in the gas phase. The internal conversion between two states of the same multiplicity is more pronounced, when vibrational levels of the two electronic states are in the proximity of each other. Also the probability of the spin-forbidden inter-system crossing increases drastically in matrices [1].

## 3.2 APPARATUS DESCRIPTION

A general scheme of the experimental apparatus used during these studies is shown in Figure 3.1. Developed in this laboratory more than two decades ago, continuously updated and improved by graduate students and research collaborators, this machine is a unique and most versatile tool in producing and characterizing transients [7-10]. It consists of four main parts—ion source compartment, quadrupole electrostatic bender, quadrupole mass-selection system and cold matrix section—which are linked with each other by means of electrostatic lenses serving for ion extraction, focusing and guidance.

Positive or negative ions are produced in an appropriate ion source (hot-cathode discharge or Cs-sputter source, section 3.3.1), and then extracted using a set of electrostatic lenses and guided further to the quadrupole bender, which is used to separate ions from neutral species. It consists of four 90° sectors of a metal cylinder, which are turned inside out in a way as is illustrated on Figure 3.1. The opposite electrodes are electrically connected with each other and static potentials are applied to them. There are then two independent voltages, which give two degrees of freedom corresponding to the deflection angle and horizontal displacement of an ion beam.

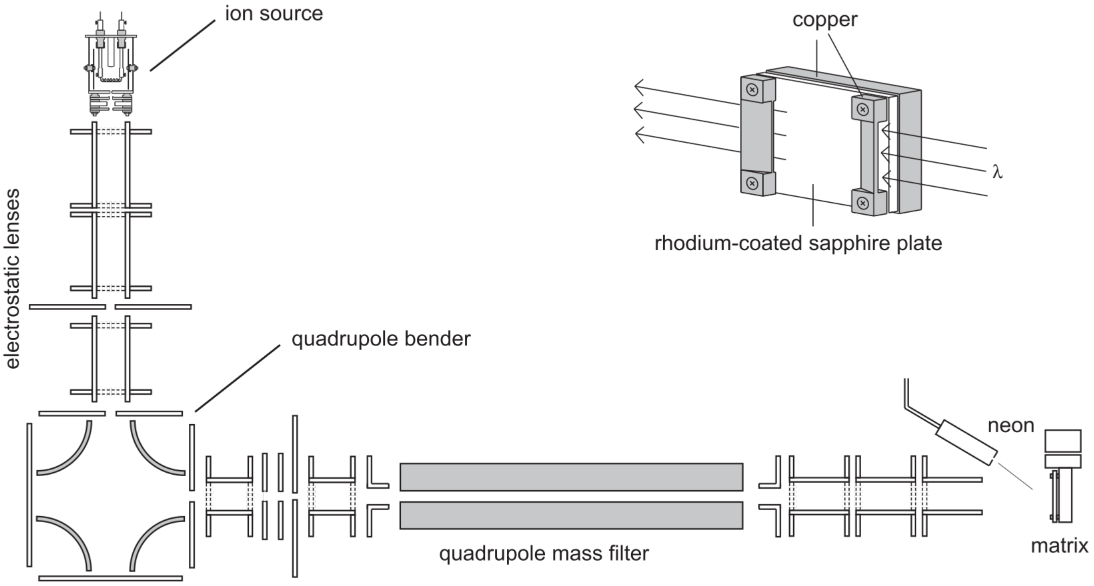

**Figure 3.1:** Scheme of the mass-selective matrix isolation apparatus.

The ion beam is then guided into the quadrupole mass filter (commercial model from "Extrel"). It consists of four 211 mm long 19 mm in diameter metal rods. In combination with the High-Q head models 14 and 15 (Extranuclear Lab.), it allows for a working mass-range of 10–350 amu/charge with unity mass resolution. The opposing rods are connected electrically in pairs, on which the following electrical potentials are applied:

$$\Phi = B \pm (U + V \cdot \cos(2\pi \cdot f \cdot t)),$$

where f = 1.35/1.75 MHz (depending on a High-Q head model), B – reference potential, V – radio frequency amplitude, U – DC voltage, t – time. Ions of a certain $m/z$ ratio will have stable trajectories, oscillating along the quadrupole axis at the given U/V ratio. Other ions will have unstable trajectories and will not pass the quadrupole, ending up on the rods or outside the mass-filter on the vacuum chamber walls. In order to achieve a unity mass resolution it is useful to slow down the ions by applying the reference potential B (~10–40 V). Subsequently, the mass-selected ion beam is guided to the surface of the matrix substrate by means of several cylindrical lenses, where it is condensed with matrix gas (Ne), introduced via a separate inlet compartment.

The matrix substrate is attached to the second (last) stage of the closed-cycle helium cryostat from "Sumitomo/Janis" (RDK-305D, 1.0 Watt @ 4.2 K). The substrate consists of a copper holder to which a sapphire plate is attached, and two copper slits.

Copper is used due to its high thermal conductance. The sapphire plate is coated by rhodium, which has a good reflectivity in the UV region down to 200 nm. Matrix substrate is cooled down to 5.8–6.7 K. The temperature is measured with a silicon-diode sensor, which is mounted in-between the cold-finger and the substrate holder in a separate copper block. The substrate temperature is adjusted with a dual 50 Ohm heaters (connected in parallel, 25 Ohm – 100 W) and controlled by the "LakeShore"-330 temperature controller. The whole cryogenic part is mounted on a rotatable around the vertical axis flange, to allow the optical access from several viewports on the vacuum chamber. Production of the ions is monitored by measuring the current between the matrix substrate and the ground. This allows the optimization of the ion source and the potentials on the lenses for the highest output with respect to a particular ion.

All the parts are mounted inside of differentially pumped high vacuum chambers. In order to maintain an oil-free vacuum system, all oil diffusion pumps have been replaces by turbo-molecular pumps (Pfeiffer). The source and deflector chambers are evacuated to ~$10^{-6}$ mbar by two turbo-pumps with the pumping speed of 230 l $s^{-1}$, the QMS compartment is evacuated by one with the 170 l $s^{-1}$ speed and the vacuum $10^{-7}$ mbar is achieved; matrix chamber is kept at the pressure $10^{-8}$–$10^{-9}$ mbar at room temperature and is supported with a 230 l $s^{-1}$ turbo pump. All of them are pumped out by rotary pumps. The ion source and bender chambers are of standard ISO-K systems and rubber (O-rings) sealing is used. The QMS and matrix chambers are of conflate flanges (CF) type, with OFC gaskets. Pressures inside the chambers are measured using Pfeiffer Vacuum Compact Cold Cathode Gauges. The backing pressure is monitored using a Pirani Gauge.

## 3.3 PRODUCTION OF MOLECULES TO BE STUDIED

### 3.3.1 ION SOURCES

There are three ion sources available in the laboratory and have been used during present studies. These are the two hot-cathode discharge sources for anions and cations as well as a cesium (Cs) sputter source for anions. The one used for production of cations is schematically shown in Figure 3.2.

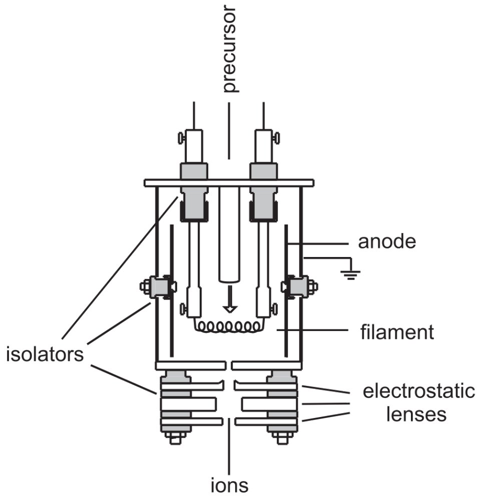

**Figure 3.2:** Hot-cathode discharge source for production of cations.

The precursor gas mixture is introduced into the central part of the source, close to a tungsten filament, which is heated by 6–9 A current (one leg is grounded, other is kept at ~5 V). Filament is mounted inside of two coaxial cylinders. The outer cylinder is grounded, the inner one is kept at positive potential of 50 V and serves as an anode. An electrical discharge created between the anode and ground, and sustained by electrons emitted from the filament, ionizes and fragments sample inside the source. Depending on source conditions, the species formed may experience many collisions before the field of the first electrostatic lens will extract them. By varying such parameters as concentration of precursor mixture and/or its pressure inside the source, discharge current and/or anode and extraction potential, the hole spectrum of ions – small fragments, parent ions and larger, cluster ions in a size of up to 5–10 parent molecules can be produced. A standard example for this is the use of diacetylene/He mixtures in a concentrations ranging from 1:6 to 1:1 used for production of linear $C_nH_m^+$ ions with n = 4–7, m = 1–3 [11]. Recently, small-sized $AH^+$ ions have been observed in the mass spectrum of 2,4-hexadiyne (section A.2 and [12]). These have been spectroscopically identified as phenylacetylene$^+$, naphthalene$^+$, indene derivatives and benzotropylium. $HC_2H/HC_4H$ premixed with benzene / phenylacetylene vapours is another example of rich chemistry in this ion source (Figure 3.3), resulting in a growth of ring-chain species differing in chain size, position on a ring and hydrogenation. Some such species have been isolated in matrices and their electronic spectra recorded; preliminary results along are given (Appendix A.1).

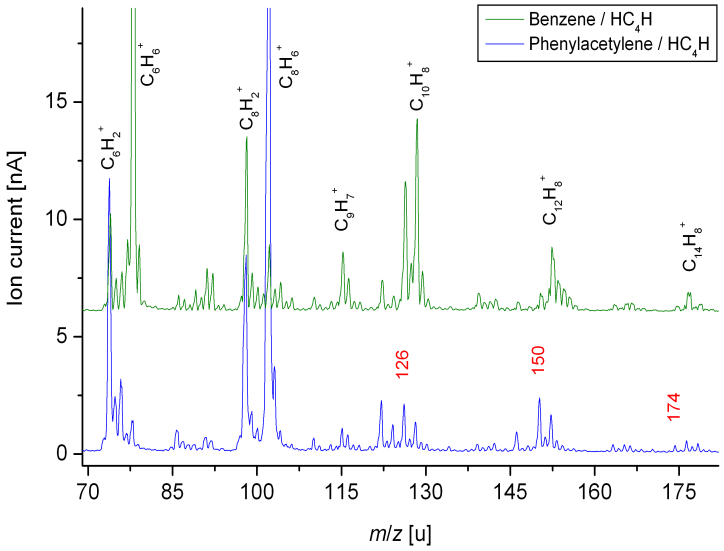

**Figure 3.3:** Mass spectra of ions produced in a hot cathode discharge source from 1,2-dihydronaphthalene (blue) and in the reaction of naphthalene vapour with protonated methanol (red). Spectra are recorded as optimized for $C_{10}H_9^+$ (m/z=129) and are scaled to the same intensity of this peak.

One of the advantages is the possibility of using not only gaseous samples or volatile liquids. Non-volatile liquids may be used by “bubbling” the carrier gas though the sample, whereas solids may be placed into the gas-inlet-tube and resistively heated, or directly into the source chamber in an oven just before the filament.

Another hot-cathode discharge source is used for the production of negative ions (Figure 3.4). Inside the source a filament, which is mounted on a cathode floated at a negative potential of ~200–400 V, emits free electrons when heated by 9–10 A current. By monitoring the discharge between the cathode and the extraction plate, which is held under about –100 V, one regulates the degree of ionization inside the source. A sample (if solid – graphite or aluminium *etc.*) together with the ceramic cylinder (or metal) and the extraction plate build a small volume where the collisions and ion formation happen. In case if gaseous sample is used as a precursor, a metal (separation) disc/grid is placed between the metal and ceramic cylinders. Created in this volume species are extracted through a small opening in the first electrode. This source has been employed for production of sulfur $S_n^-$ anions (n=2–4) using solid (sulfur powder) as well as gaseous (vapour of liquid $CS_2$) samples [10, 13].

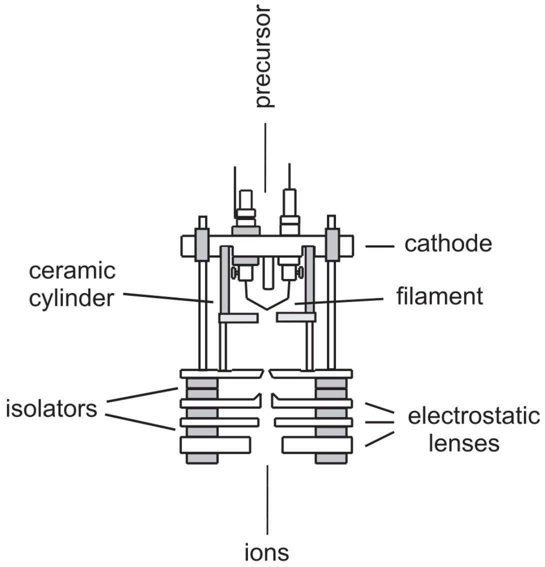

**Figure 3.4:** Hot-cathode discharge source for production of anions.

The other ion source produces negative ions from solid (conductive or semi-conductive) precursors by means of sputtering with high-energy cesium cations ($Cs^+$). The Cs sputter source is schematically shown in Figure 3.5 and consists of an ionizer, a sample, an extractor, a Cs reservoir (outside the source chamber) and tube (inside) for introducing its vapour into the source. The Cs reservoir and tube are heated up to ~300° C to evaporate the Cs and introduce it into the source. The ionizer is a hot filament, made of a coaxial tantalum wire, is kept at ~1000–2000 V. The Cs vapour is ionized, $Cs^+$ are repelled from the ionizer and bombard the sample rod ejecting different species in the so-called sputter manner. The sample (or target) is located above the ionizer, kept at ~40–70 V and is made of a conductive or semi-conductive material as carbon or silicon, or, for example, $TiO_2$/carbon or $TiO_2$/silver composite rods *etc.* can also be used. The ions are extracted from the source in the same way as in the case of two previous sources. It is possible to introduce different gaseous samples inside the source to induce a more complicated chemistry. This ion source has been successfully implemented in the past for producing numerous carbon chain anions [14, 15], small silicon and boron species [16, 17], and during present studies for studies on titanium oxides $TiO_n$ (n=1–3) (see Appendix A.4-5, [18]).

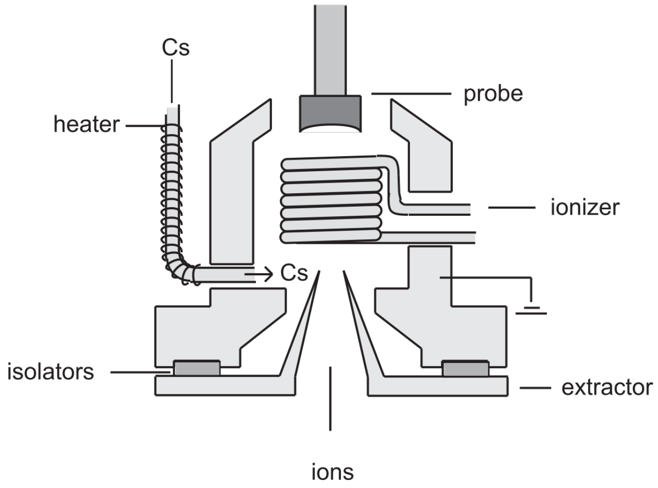

**Figure 3.5:** The cesium sputter ion source for production of anions.

### 3.3.2 PRODUCTION OF H-PAH$^+$ CATIONS

Protonated PAHs studied in our laboratory were produced in a hot-cathode discharge ion source using two approaches. In the first, smaller H-PAH$^+$ (protonated benzene, naphthalene, anthracene and phenanthrene) were produced from the respective dihydro-PAHs diluted with helium. The H-PAH$^+$ cations were formed through ionization of the parent neutral and a subsequent removal of an H atom from one of the $CH_2$ groups, as is typically observed in similar type ion sources or in under electron impact conditions. Strong fragmentation and isomerisation of ions were, however, observed in such experiments as is seen from the mass spectrum on the example of 1,2-dihydro-naphthalene (Figure 3.6, blue trace) and is discussed in detail in Chapter 7. These strongly complicated the interpretation of the recorded spectra. Moreover, larger dihydrogenated PAH samples, like for example $H_2$-Cor, were not commercially available; therefore, another production method was needed.

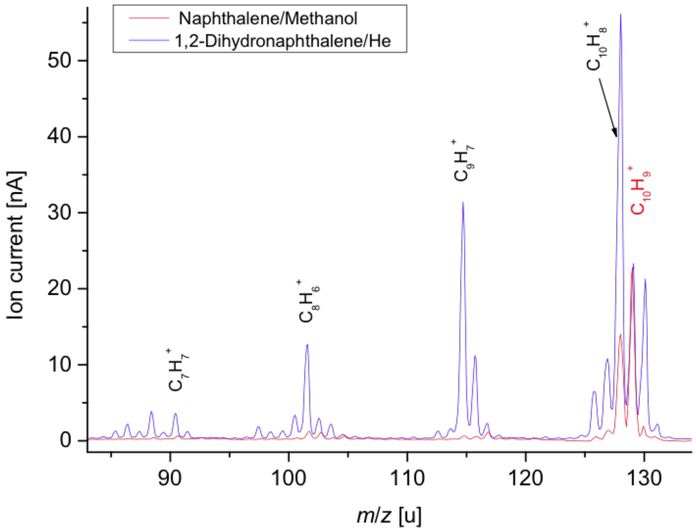

**Figure 3.5:** Mass spectra of ions produced in a hot cathode discharge source from 1,2-dihydronaphthalene (blue) and in the reaction of naphthalene vapour with protonated methanol (red). Spectra are recorded after optimization for $C_{10}H_9^+$ (m/z=129) and are scaled to the same intensity of this mass peak.

Chemical ionization and proton transfer are energetically milder ionization methods [19], frequently used in mass-spectrometric studies. PAHs have relatively high proton affinities (PAs) [20]; therefore, their protonated analogues may be generated in proton transfer reactions. This has been achieved for small PAHs and some heterocyclic aromatics using $CH_5^+$ or $C_2H_5^+$ as proton donors [21, 22]. A similar method was applied during the present studies for the generation of protonated PAHs. Protonated anthracene (H-An$^+$) was used as a test molecule. It is relatively large PAH, thus much less fragmentation is expected, and moreover, its PA (877 kJ mol$^{-1}$) is similar to that of pyrene and coronene (869 and 861 kJ mol$^{-1}$), for which no dihydro-precursors were available. A number of experiments were undertaken in the course of this study using anthracene (An) and several possible proton donors to evaluate and to compare the proton transfer approach to the formation of H-PAH$^+$ from dihydro-compounds.

In the reaction of An with $H_3^+$ or $CH_5^+$ no protonation of the PAH was observed and only parent An$^+$ were present in the mass spectrum. Although the PAs of $H_2$ (424 kJ mol$^{-1}$) and $CH_4$ (536 kJ mol$^{-1}$) [20] are much lower than that of An and thus proton donation is energetically feasible, the excess energy in the reaction appears to be too high to be dissipated *via* internal vibrational relaxation and the formation of PAH$^+$ is favoured. Protonated ethanol $EtOH_2^+$ was chosen as the next proton donor because the PA of the parent EtOH (776 kJ mol$^{-1}$) is higher than those of the reagents above, but still lower than that of An.

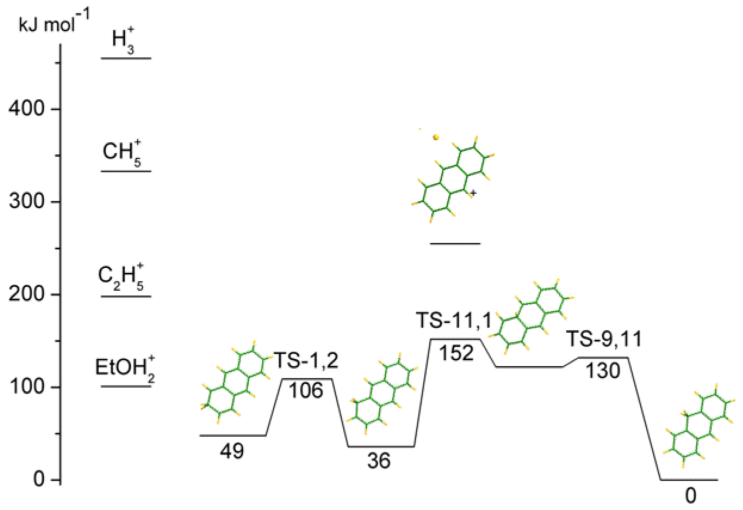

**Figure 3.6:** Potential energy surface of H-An$^+$ calculated with DFT at the B3LYP/6-311G(d,p) level of theory. Energies are corrected for zero-point energy. Experimental excess energies for protonation of An with selected donors are given on the left side of the scheme.

Mass spectra of the anthracene/ethanol system obtained using different conditions in the ion source are shown in Figure 3.7. At a low pressure of ethanol in the source, both substances are ionized by electrons (Figure 3.7, green trace). The mass spectrum is characterized by the parent cation ($m/z$=178) of An (inset b) and, in the low-mass range, by the fragment of ethanol with $m/z$=45 (inset a), as is in agreement with the data obtained using electron ionisation [23]. At higher pressures in the source, $EtOH_2^+$ is formed and the simultaneous growth of the $m/z$=179 cation, H-An$^+$, is observed (blue trace); further increase of the pressure results in more efficient production of both protonated species (red trace). An$^+$ ions are still present (insets b and c; the spectra are normalized to the same intensity of An$^+$), but the high intensity of H-An$^+$ indicates the efficiency of protonation in the ion source under described conditions.

As will be demonstrated in Chapters 5–7 and is seen in Figures 3.5 and 3.7, the PAH can be protonated efficiently in a proton transfer reaction of parent PAH with suitable donors, as simple alcohols. PT reactions ensure energetically much milder conditions with respect to the ionization and fragmentation of the respective dihydro-precursors (Figure 3.7). Moreover, the preferential formation of the lowest-energy isomers of H-PAH$^+$s was observed for the studied cases.

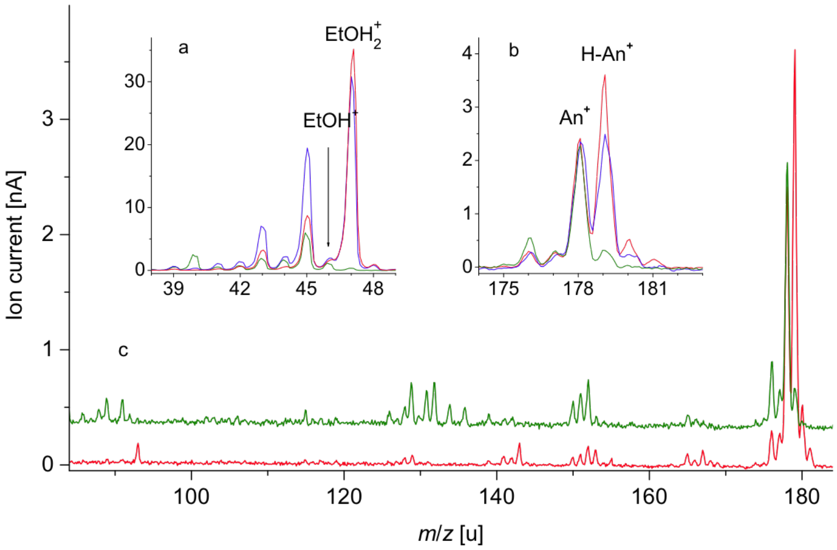

**Figure 3.7:** Mass spectra of ions produced in the reaction of anthracene with protonated ethanol in a hot cathode discharge source at different pressures of ethanol: green trace—low; blue—intermediate conditions; red—highest ethanol pressure, optimized for maximum intensity of protonated anthracene. Insets show increase of a) protonated ethanol and b) protonated anthracene with increasing ethanol pressure, whereas c) displays the influence of ethanol on the fragmentation of anthracene. All spectra are normalized to the same intensity of An$^+$.

### 3.3.3 DIRECT DEPOSITION AND IONIZATION „IN SITU“

There are several other possibilities of generation the species of interest, commonly used if no ion source and/or mass selection is coupled to the matrix isolation setup. Reactive species can then be synthesized *in situ* by photolysis, diffusion, ionization or neutralization or some other reactions of any vaporizable substance [1, 2, 24]. During present studies several such methods were used. Thus, for example, electronic absorption spectrum of neutral naphthalene has been obtained by premixing its vapour with neon and depositing it to form a matrix. Larger PAHs have much lower vapour pressure and need to be heated to allow such a study. For this, a resistively heated quartz oven (by J. Fulara) can be used. It is placed in front of the matrix holder, opposite to the neon inlet tube, thus resulting in a “uniform” deposition. This is, however, technically mach more complicated: replacing the sample, for example, requires opening the matrix chamber, which is under vacuum of ~$10^{-8}$ mbar and needs at least 2–4 days of evacuating.

It was found, that deposition of $Ar^+$ or $Ne^+$ cations produced in the source into a PAH/neon matrix results in the ionization of the PAH. The ionization happens probably inside the matrix sample as a result of a charge/hole migration processes, and may be even stimulated further by irradiating the matrix. Such experiments may be helpful in the identification of spectral carriers. Additionally, reactions of $H^+$ and $H_3^+$ with PAHs trapped in neon matrices have been investigated. $H^+$ and $H_3^+$ were produced from $H_2$ in the hot-cathode discharge source and co-deposited with a PAH/neon mixture onto the matrix substrate. Under conditions, when no electron scavenger used (see section 3.5.2), $H^+$ cations will be neutralized by electrons. $H_3^+$ will recombine with electrons and dissociate to form H and $H_2$. Resultant hydrogen atoms are not affected by the so-called cage-effect; they are mobile and reactive in solid neon. Addition of hydrogen atom to PAH has an energy barrier of ~10–20 kJ $mol^{-1}$, and it can be overcome due to the ability of hydrogen to tunnel through the reaction barrier. At low temperatures such reactions are likely even barrierless. These experiments were found to result in a formation of singly hydrogenated species, as is discussed in Chapters 4 and 7. If electron scavenger is used during deposition, a much more complicated chemistry was observed, and involved probably its fragments.

## 3.4 MEASUREMENTS

### 3.4.1 UV-VIS: ABSORPTION AND EMISSION

Electronic absorption spectra of the trapped matrix species are measured using the following arrangement (Figure 3.8). Xenon arc and halogen lamps are used as light sources for the spectral regions of 225–390 nm and 360–1100 nm, respectively. White light is focused onto the first slit of the matrix substrate by two quartz lenses and propagates through a 150 μm thin and 20 mm long neon matrix in a "wave-guide" manner [25]. Since the light path is long it is possible to obtain electronic absorption spectra even for low concentrations of trapped species. The beam coming out of the second (exit) slit is focused onto a bundle of 50 quartz fibers, which transmits the light exiting the matrix to the entrance slit of a 0.303 m Czerny-Turner spectrograph (Shamrock SR-303i from "Andor"). It is equipped with three rotatable gratings, 1200 and 600 lines/mm blazed at 300 nm and 1200 lines/mm at 500 nm, dispersing the light onto an open-electrode or a back-illuminated CCD camera.

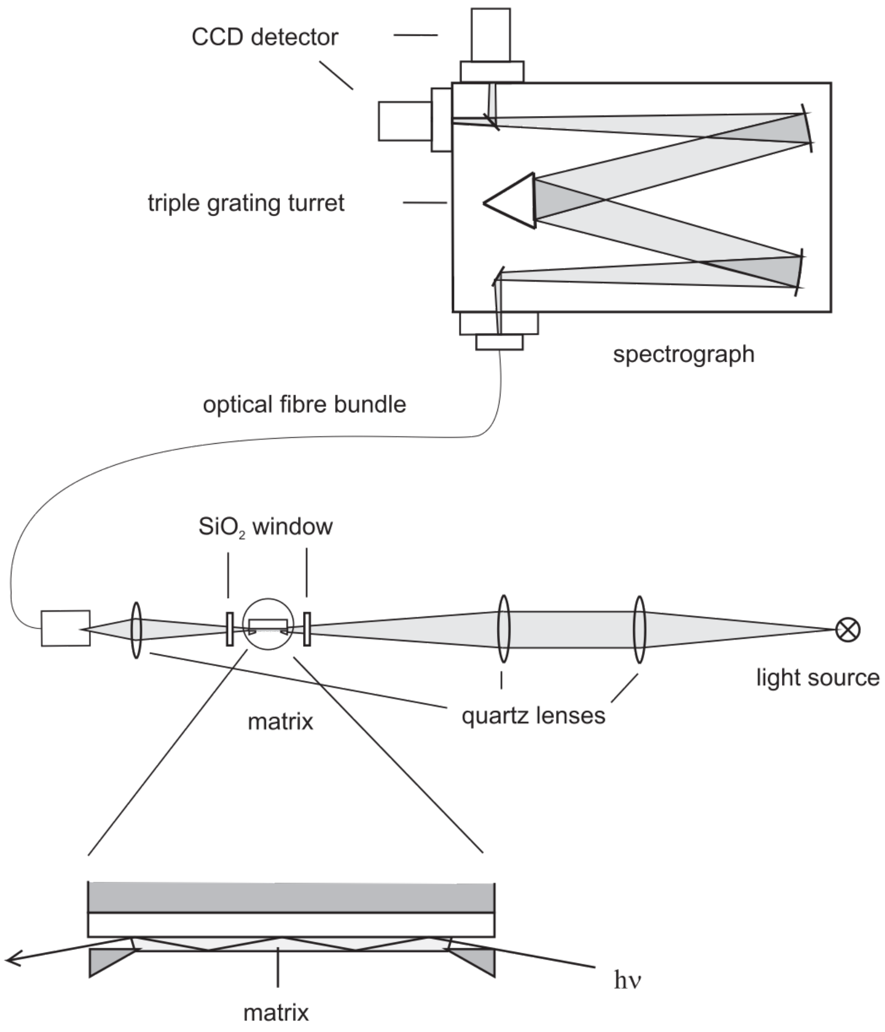

**Figure 3.8:** Scheme of the experimental setup used for recording absorption spectra.

The absorption spectra are recorded in several 55–70 nm long sections covering the 220–1100 nm range. The spectral resolution is defined by the grating used, the width of the spectrograph's input slit and by the number and size of pixels available to process the signal and is 0.1 nm with the 1200 lines/mm grating and 100 μm input slit.

Because of the intensity of the broadband light, care is taken to reduce photo-conversion of the species during the recordings—measurements are started from the longest wavelength using appropriate cut-off filters and continued into the UV. To test whether the isolated species photo-converted during measurements, the procedure is repeated.

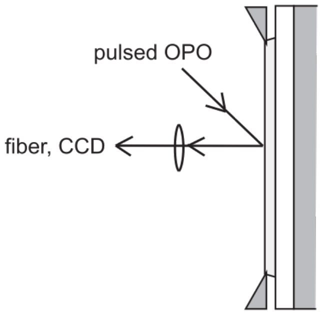

**Figure 3.9:** Schematic of the light pathway as used for the measurements of emission spectra.

Fluorescence spectra can be obtained from the same matrix sample using the same apparatus. For that, matrix is turned by 90° from the position used for deposition and absorption measurements (Figure 3.1, 3.8). The trapped species are excited with a pulsed, ~5 $cm^{-1}$ bandwidth, tunable optical parametric oscillator laser, pumped by $Nd^{3+}$:YAG [12]. The emission data are collected perpendicular to the matrix surface and 45° to the incident laser beam (Figure 3.9). The signal is transmitted to the same spectrograph and cameras, which are used for the absorption measurements. It is accumulated for ~1000 shots of energy 2–30 mJ exciting distinct bands seen in the absorption spectra. Scans are started from the longest-wavelength absorptions, 2–5 nm upwards the excitation wavelength to avoid overexposure of the CCDs with laser scatter. Every recorded section is calibrated using atomic emission lines of several (Ar/Hg, Xe, Ne/Hg) pen-ray lamps.

### 3.4.2 IR REGION

It is possible to record the IR absorption spectra using the same matrix sample when it is rotated 135° away from the position used for deposition and absorption measurements. A Fourier-transform spectrometer (Bruker IFS66v/s) is used for studies. A combination of broadband light sources (glow bar or halogen/tungsten lamps), beam splitters (KBr, $CaF_2$ and $SiO_2$) and detectors (MCT, InSb and Si diode) allow for the covering the 600–25000 $cm^{-1}$ spectral range. A double reflection technique is applied, where an additional concave mirror is placed in the matrix chamber and allows the light beam to pass twice through the sample (Figure 3.10). Thus one obtains several times better sensitivity than with a usually used single reflection scheme, but much lower, however, than would be introducing the wave-guide method for the IR measurements.

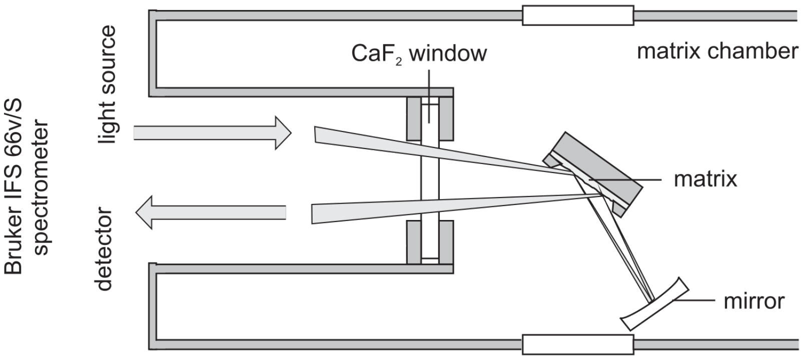

**Figure 3.10:** Schematic of the light pathway as used for the measurements of IR spectra using a Fourier-transform spectrometer.

## 3.5 SPECTRAL IDENTIFICATION

According to experimental experience, a matrix sample does not contain exclusively the ions that were mass selected. Most of the ions are neutralized upon deposition onto the matrix surface. Deposited cations charge the matrix and the ones arriving subsequently are repelled from its surface. They hit metal parts of the vacuum chamber releasing electrons. The latter are attracted to the matrix and captured by the cations neutralizing them. If the electron affinity of the formed neutrals is high, they can accept an additional electron, thus resulting in the anions. This has been observed in experiments with $C_{60}$. A mixture of $C_{60}^+$ and $C_{60}^-$ ions was observed upon irradiation of neon isolated neutral $C_{60}$ with vacuum UV photons [26]. Electron affinity of $C_{60}$ is 2.68 eV and is much higher than for the PAH studied (~0.1–0.5 eV). In addition, fragmentation may take place upon impact with the substrate surface. Thus for example, $C_6H_2^+$ or $C_3H$ and $C_3$ cations have been observed when studying the $C_8H_6^+$, $C_6H_7^+$ and $C_3H_2$. For larger species like the PAHs studied, only (if even this) H loss was observed ($H_2$ was seen for indene series), which is their lowest fragmentation channel [27]. To summarise, the matrix sample contains normally a mixture of ionic and neutral forms of deposited species and even (rarely) their fragments. An example of such a mixture is illustrated in Figure 3.11 [28]. Besides these, several electronic transitions of one absorbing species can be observed, each with its own vibrational pattern. All of the features mentioned lead sometimes to quite complex absorption spectra. There are several experimental procedures, which significantly help with the spectral assignment.

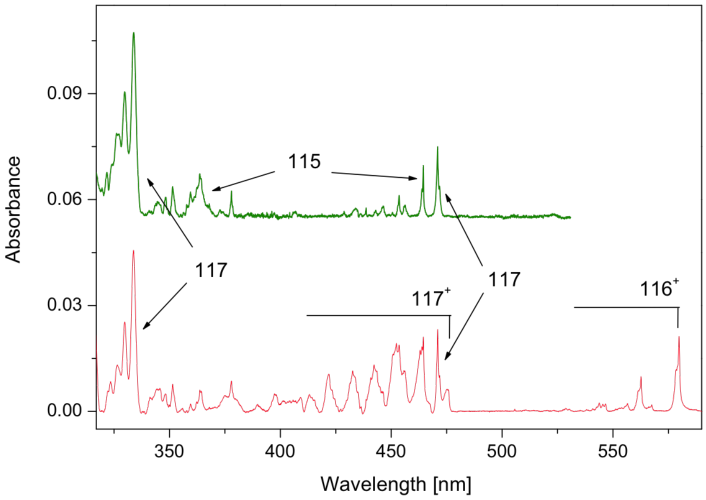

**Figure 3.11:** Electronic absorption spectra recorded after mass-selective deposition of $C_9H_9^+$ cations (*m*/*z*=117) produced from indane/He mixture into a neon matrix with admixture (red) and without electron scavenger (green). Absorption bands of the $C_9H_9^+$ cations, respective neutrals, and several fragments, identified as indene cation ($116^+$) and neutral dehydro-indene radical (115) are observed.

### 3.5.1 ELECTRON SCAVENGER AND PHOTONEUTRALIZATION

Cations can be trapped in the matrix efficiently if their charge is balanced with counter ions. The neutralization of ions in matrices can be suppressed if free electrons present in matrix are captured by an impurity or other species trapped in matrix. For this purpose, molecules with high electron affinity, electron scavengers, are added to neon. They easily capture electrons preventing their recombination with ions. Thus, the matrices formed with electron scavenger will contain orders of magnitude more cationic species than those without and vice versa: the matrices without admixture of such molecules will show absorption of mainly neutrals. In earlier studies [9, 10] carbon tetrachloride ($CCl_4$) was mixed for this purpose with neon in typical concentrations of 1:300. This, however, perturbed the spectrum as the anion formed has a broad absorption feature in the 350 nm range. Presently, chloromethane, $CH_3Cl$, normally added to the neon in the ratio 1:20 000, was found to be a more suitable scavenger. Chloromethane has a high electron affinity, around ~3 eV, and captures electrons efficiently forming thereby $Cl^-$ ions and $CH_3$ radicals [29]. The latter remain in matrix cages and due to the very low concentration they do not interfere with trapped cations. $Cl^-$ anions reduce the space charge, thus allowing more efficient accumulation of mass-selected cations. Moreover, neither of the $CH_3Cl$, $CH_3$ and $Cl^-$ species has absorption in the 200–1100 nm spectral range.

UV irradiation of the matrix induces neutralization of the trapped cations by electrons released from the $Cl^-$ counter ions. This is valid if the photon energy exceeds the detachment threshold of $Cl^-$, whereby the electron affinity of Cl is 3.6 eV in the gas phase, corresponding to photon wavelengths $\lambda < 343$ nm. However, the detachment threshold of $Cl^-$ in a neon matrix is higher than in the gas phase due to the surrounding neon atoms and require photons of higher energy, with $\lambda < 300$ nm. Typically, medium pressure mercury lamp mpHg (5.4 eV) is used as a source of the radiation; cut-off filters can be applied to restrict the energy range. A most pronounced effect was observed when full UV radiation of the mpHg lamp was used. In case of anions, the neutralization goes directly by detachment of the electrons by photons having energies higher than the electron affinities of the species under study.

### 3.5.2 SELECTIVE IRRADIATION OF SAMPLE

Another very useful strategy in the spectral identification is irradiation of a sample at selected wavelengths to selectively bleach one or another absorbing species of a mixture. It is usually started by irradiating at the longest wavelength, where the absorption is observed, in order to avoid simultaneous bleaching of several ions or neutrals in the matrix. If irradiation of the first absorption band does not provide sufficient energy to affect it, then the procedure is moved to shorter wavelength. By using different cut-off and band-pass filters, it is often possible to find a wavelength where at least one species is photobleached, which allows the absorption bands to be distinguished. The so induced changes in the spectra are often easier to discern by taking the difference spectra, that is, the results of subtraction of a spectrum taken after bleaching from that taken before. To properly obtain such a difference spectra it is crucial to assure a highly reproducible sample position, so that the light beam always probes exactly the same part of the matrix.

Besides these, the implementation of laser induced fluorescence (LIF) technique during these studies, provide an additional, complementary tool to identify and characterize molecules spectroscopically. In contrast to absorption spectra, which contain spectral features of all trapped species, LIF allows the selective excitation of single species.

An allowed electronic transition is resonantly excited and the induced fluorescence may be observed, providing information on the lower/ground electronic states.

## 3.6 QUANTUM-CHEMICAL CALCULATIONS

Past and present work from our laboratory showed that the structure of ions is not always foretold by the geometry of the precursor used and several isomers of a certain $m/z$ ratio can be produced in a discharge source and trapped subsequently in neon. The relative population of these isomers depends then on the kinetics of processes and/or ion-molecule reactions happening in the source, as well as on the energetics of ions. Therefore, in order to select a suitable precursor, support the interpretation of the observed spectra and the assignment of the electronic transitions, quantum-chemical calculations are needed. With the help of calculated optimized structures, harmonic frequencies, some thermodynamic properties and electronic transition energies a full analysis of the species can be drawn.

However, due to the size of the molecules studied during this work, with almost seventy electrons for the smallest of the studied protonated PAH, the use of highly correlated quantum chemistry methods becomes computationally challenging. The approach chosen for the present studies is hybrid-DFT method (B3LYP exchange-correlation functional) [30, 31] and its time-dependent extension TD DFT, which are based on a modelling of electron correlation through general functions of electron density and incorporates a portion of exact exchange from the Hartree-Fock theory. In the last years (TD) DFT has been widely applied for the calculation of ground- and excited electronic state properties of medium sized and large molecules; many of them have focused on neutral, closed-shell cations, radical cations, neutral radicals, and other particular classes of PAHs, in particular due to the effective balance of cost and accuracy of the method. The scaling of DFT with molecular size is relatively low — comparable to its Hartree-Fock counterpart — and usually yields accurate geometries for closed-shell molecules [32-37]. Moreover, TD DFT has been used recently to calculate electronic transition energies and oscillator strengths of larger H-PAH$^+$s, coronene and ovalene [37], and the present experimental studies may be used to evaluate their reliability directly.

Calculations were done using Gaussian03 program package [38]. B3LYP exchange functional hybrid DFT method [30, 31] and Dunning's correlation-consistent polarized valence-only double(triple)-zeta (cc-pVD(T)Z, depending on size of the molecule) basis set were used to describe the systems [39].

Besides these, the experimental data are compared throughout the work with the higher level *ab initio* calculations done by J. Fulara. In these, vertical electronic excitation energies have been determined with second-order approximated coupled-cluster (CC2) method [40, 41]. The preceding geometry optimization of the molecular systems in their ground electronic state was done with the MP2 and cc-pVDZ basis set. All MP2 and CC2 calculations were carried out with the *Turbomole* package [42], making use of the resolution-of-the-identity approximation for the evaluation of the electron repulsion integrals [43].

In Chapter 7 presented computational results on the protonated naphthalene isomers were carried out by Profs. M. Rode and A. Sobolewski form the Institute of Physics of Polish Academy of Sciences (Warsaw, Poland).

## BIBLIOGRAPHY

[1] B. Meyer, Low Temperature Spectroscopy, Elsevier, New York, 1971.

[2] I.R. Dunkin, Matrix-Isolation Technique, Oxford University Press, Oxford, 1998.

[3] E. Whittle, D.A. Dows, G.C. Pimentel. Matrix Isolation Method for the Experimental Study of Unstable Species. *J. Chem. Phys.,* 22 (1954) 1943-1943.

[4] E.D. Becker, G.C. Pimentel. Spectroscopic Studies of Reactive Molecules by the Matrix Isolation Method. *J. Chem. Phys.,* 25 (1956) 224-228.

[5] M.E. Jacox. Comparison of the ground state vibrational fundamentals of diatomic molecules in the gas phase and in inert solid matrices. *J. Mol. Spectr.,* 113 (1985) 286-301.

[6] M.E. Jacox. Comparison of the electronic energy levels of diatomic molecules in the gas phase and in inert solid matrices. *J. Mol. Struct.,* 157 (1987) 43-59.

[7] D. Forney. Optische spektroskopie von kationen in neonmatrizen. *Ph.D Thesis*, University of Basel, 1990.

[8] M. Jakobi. Elektronische und vibratorische spektroskopie an den Fullerenen $C_{60}$, $C_{70}$ und deren ionen in edelgasmatrizen. *Ph.D Thesis*, University of Basel, 1994.

[9] A. Batalov. Absorption spectroscopy of mass-selected hydrocarbon and boron species in 6 K neon matrices. *Ph.D Thesis*, University of Basel, 2006.

[10] I. Shnitko. Absorption spectroscopy of carbon and sulfur chains in 6 K neon matrices. *Ph.D Thesis*, University of Basel, 2008.

[11] J. Fulara, M. Grutter, J.P. Maier. Higher excited electronic transitions of polyacetylene cations $HC_{2n}H^+$ n = 2–7 in neon matrixes. *J. Phys. Chem. A,* 111 (2007) 11831-11836.

[12] A. Nagy, J. Fulara, J.P. Maier. Formation of aromatic structures from chain hydrocarbons in electrical discharges: absorption and fluorescence study of $C_{11}H_9^+$ and $C_{11}H_9$ isomers in neon matrices. *J. Am. Chem. Soc.,* 133 (2011) 19796-19806.

[13] I. Shnitko, J. Fulara, I. Garkusha, A. Nagy, J.P. Maier. Electronic transitions of $S_2^-$ and $S_3^-$ in neon matrixes. *Chem. Phys.,* 346 (2008) 8-12.

[14] P. Freivogel, M. Grutter, D. Forney, J.P. Maier. Infrared bands of mass-selected carbon chains $C_n$ (n = 8-12) and $C_n^-$ (n = 5-10, 12) in neon matrices. *Chem. Phys.,* 216 (1997) 401-406.

[15] M. Tulej, J. Fulara, A. Sobolewski, M. Jungen, J.P. Maier. Electronic transitions of $C_3^-$ above the photodetachment threshold. *J. Chem. Phys.,* 112 (2000) 3747-3753.

[16] J. Fulara, P. Freivogel, M. Grutter, J.P. Maier. Electronic absorption spectra of Sin and $Si_n^-$ (n = 2-4) in neon matrices. *J. Phys. Chem.,* 100 (1996) 18042-18047.

[17] E. Riaplov. Spectroscopy of mass selected carbon and boron species in solid neon. *Ph.D Thesis*, University of Basel, 2002.

[18] R. Middleton, J. Klein. Production of metastable negative ions in a cesium sputter source: Verification of the existence of $N_2^-$ and $CO^-$. *Phys. Rev. A,* 60 (1999) 3786-3799.

[19] M.S.B. Munson, F.H. Field. Chemical Ionization Mass Spectrometry. I. General Introduction. *J. Am. Chem. Soc.,* 88 (1966) 2621-2630.

[20] E.P.L. Hunter, S.G. Lias. Evaluated gas phase basicities and proton affinities of molecules: An update. *J. Phys. Chem. Ref. Data,* 27 (1998) 244.

[21] U.J. Lorenz, J. Lemaire, P. Maitre, M.-E. Crestoni, S. Fornarini, O. Dopfer. Protonation of heterocyclic aromatic molecules: IR signature of the protonation site of furan and pyrrole. *Int. J. Mass Spectrom.,* 267 (2007) 43-53.

[22] U.J. Lorenz, N. Solca, J. Lemaire, P. Maitre, O. Dopfer. Infrared spectra of isolated protonated polycyclic aromatic hydrocarbons: Protonated naphthalene. *Angew. Chem.-Int. Edit.,* 46 (2007) 6714-6716.

[23] http://webbook.nist.gov, NIST Mass Spectrom. Data Center, 1990.

[24] L. Andrews, M. Moskovits, Chemistry and Physics of Matrix-Isolated Species, Elsevier, Amsterdam., 1989.

[25] R. Rossetti, L.E. Brus. Wave-Guide Propagation in Frozen Gas Matrices. *Rev. Sci. Instrum.,* 51 (1980) 467-470.

[26] J. Fulara, M. Jakobi, J.P. Maier. Electronic and Infrared-Spectra of $C_{60}^{+}$ and $C_{60}^{-}$ in Neon and Argon Matrices. *Chem. Phys. Lett.,* 211 (1993) 227-234.

[27] O. Dopfer. Laboratory spectroscopy of protonated PAH molecules relevant for interstellar chemistry, in: *PAHs and the Universe*; C. Joblin, A.G.G.M. Tielens, Eds.; *EAS Publications Series*, 46 (2011) 103-108.

[28] A. Nagy. Electronic spectroscopy of open chain and aromatic hydrocarbon cations in neon matrices. *PhD Thesis*, University of Basel, 2012.

[29] Z.Y. Zhou, Y.M. Xing, H. Gao. Studies on the bond-breaking reaction of the $CH_3$–X bond for DFT calculations in electron transfer. *J. Mol. Struct.: THEOCHEM,* 542 (2001) 79-87.

[30] R. Bauernschmitt, R. Ahlrichs. Stability analysis for solutions of the closed shell Kohn-Sham equation. *J. Chem. Phys.,* 104 (1996) 9047-9052.

[31] A.D. Becke. Density-functional thermochemistry. III. The role of exact exchange. *J. Chem. Phys.,* 98 (1993) 5648-5652.

[32] J.L. Weisman, T.J. Lee, M. Head-Gordon. Electronic spectra and ionization potentials of a stable class of closed shell polycyclic aromatic hydrocarbon cations. *Spectrochim Acta A,* 57 (2001) 931-945.

[33] S. Hirata, M. Head-Gordon, J. Szczepanski, M. Vala. Time-dependent density functional study of the electronic excited states of polycyclic aromatic hydrocarbon radical ions. *J. Phys. Chem. A,* 107 (2003) 4940-4951.

[34] D.L. Kokkin, T.W. Schmidt. On the electronic properties of dehydrogenated polycyclic aromatic hydrocarbons. *J. Phys. Chem. A,* 110 (2006) 6173-6177.

[35] J.L. Weisman, T.J. Lee, F. Salama, M. Head-Gordon. Time-dependent density functional theory calculations of large compact polycyclic aromatic hydrocarbon cations: Implications for the diffuse interstellar bands. *Astrophys. J.,* 587 (2003) 256-261.

[36] T.M. Halasinski, F. Salama, L.J. Allamandola. Investigation of the ultraviolet, visible, and near-infrared absorption spectra of hydrogenated polycyclic aromatic hydrocarbons and their cations. *Astrophys. J.,* 628 (2005) 555-566.

[37] A. Pathak, P.J. Sarre. Protonated PAHs as carriers of diffuse interstellar bands. *Mon. Not. Roy. Astron. Soc.,* 391 (2008) L10-L14.

[38] M.J. Frisch, e. al. *Gaussian 03 (Revision C.01),* (2004) Gaussian, Inc., Wallingford, CT.

[39] D.E. Woon, J.T.H. Dunning. Gaussian basis sets for use in correlated molecular calculations. III. The atoms aluminum through argon. *J. Chem. Phys.,* 98 (1993) 1358-1371.

[40] O. Christiansen, H. Koch, P. Jørgensen. The second-order approximate coupled cluster singles and doubles model CC2. *Chem. Phys. Lett.,* 243 (1995) 409-418.

[41] C. Hättig, F. Weigend. CC2 excitation energy calculations on large molecules using the resolution of the identity approximation. *J. Chem. Phys.,* 113 (2000) 5154-5161.

[42] R. Ahlrichs, M. Bär, M. Häser, H. Horn, C. Kölmel. Electronic structure calculations on workstation computers: The program system Turbomole. *Chem. Phys. Lett.,* 162 (1989) 165-169.

[43] F. Weigend, M. Häser. RI-MP2: first derivatives and global consistency. *Theor. Chem. Acc.: Theor., Comp. Model.,* 97 (1997) 331-340.

# CHAPTER 4

## PROTONATED BENZENE AND FULVENE AND NEUTRAL $C_6H_7$ ISOMERS

The present investigations on $C_6H_7^+$ trapped in a neon matrix provide a direct spectroscopic characterization of two structural isomers of this cation, which have been postulated in earlier gas-phase mass spectrometric studies. Electronic transitions of protonated benzene ($A\ ^1B_2 \leftarrow X\ ^1A_1$, origin at 325 nm) and $\alpha$-protonated fulvene ($A\ ^1A' \leftarrow X\ ^1A'$, at 335 nm) have been detected. The cations were produced from several different precursors, mass selected and codeposited with neon. After neutralization of the cations, the electronic transitions of cyclohexadienyl (onsets at 549 and 310 nm) and $\alpha$-hydrogenated fulvene (532 and 326 nm) radicals were identified. Upon excitation of cyclohexadienyl to the $B\ ^2B_1$ state, photoisomerisation to an open-chain structure and $\alpha$-hydrogenated fulvene radical was observed.

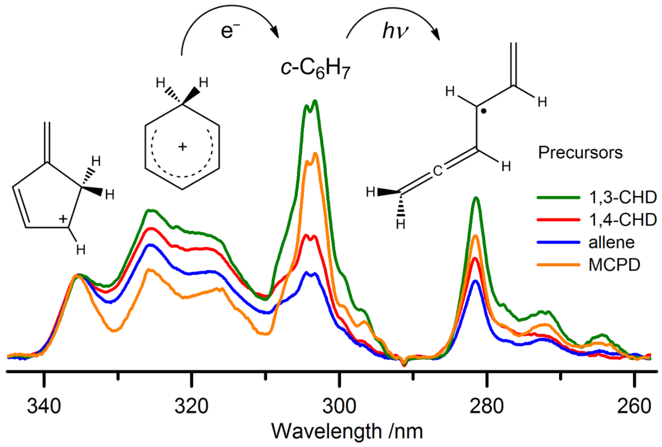

*Electronic transitions of protonated benzene and fulvene, and of $C_6H_7$ isomers in neon matrices*
Iryna Garkusha, Jan Fulara, Adam Nagy, John P. Maier
*J. Am. Chem. Soc.*, **132** (42), 14979–14985, 2010.

## 4.1 INTRODUCTION

Benzene is a building unit of polycyclic aromatic hydrocarbons. Though PAHs are believed to be widespread throughout the ISM, benzene is the only member of the family detected so far. It has been identified in the circumstellar medium in the direction of the proto-planetary nebula CRL 618 [1]. It has been also detected by mass spectrometry in the ionosphere of Titan in its protonated form, $C_6H_7^+$ [2].

The benzenium ion is the most stable isomer of $C_6H_7^+$ and represents a fundamental class of organic ions. $C_6H_7^+$ ions have been studied as complexes with noble gas atoms by IR dissociation (IRPD) spectroscopy [3, 4]. These investigations have provided frequencies of several fundamentals of $C_6H_7^+$: Rg (rare gas) dimers in the range 750–3400 $cm^{-1}$. A group of bands near 2800 $cm^{-1}$ was attributed to the aliphatic C–H stretches of the methylene group of the benzenium ion [3]. Due to the weak interaction between $C_6H_7^+$ and noble gas atoms, the obtained IR frequencies should not differ much from those of the isolated ions.

Multiphoton IRPD spectra of $C_6H_7^+$ cations [5], which undergo $H_2$ loss, differ from the spectra mentioned above. The observed bands are broadened and red-shifted, and vary in intensity from single photon dissociation data, which could be explained by the nature of the multiphoton fragmentation process. These IR studies in combination with *ab initio* calculations have confirmed that benzenium ion in its $^1A_1$ electronic ground state ($C_{2v}$ symmetry) is the favored form of $C_6H_7^+$. The structure is planar with the exception of the $CH_2$ hydrogens, which lie in a plane perpendicular to the benzene ring.

Electronic spectroscopy on protonated benzene is limited to absorption in superacidic solutions [6] and low-resolution UV photodissociation investigations [7]. The gas-phase spectrum revealed two broad, structureless transitions around 330 and 245 nm, which differ significantly from the solution spectra. Interpretation based on early quantum-chemical calculations were given [7]. Recent *ab initio* calculations on excited electronic states provide an assignment for the UV spectrum of this ion. [8]

Not much is known about other isomers of $C_6H_7^+$. A number of investigations, mainly mass spectrometric, have been reported on the structures of $C_6H_7^+$ cations. Besides protonated benzene, all predict at least three additional geometries of interest. The next two most stable forms of this ion, *α*- and *β*-protonated fulvenes, were found based mainly on the proton affinities. The former lies 0.4 and the latter 1.3 eV above the benzenium ion according to calculations [9, 10]. The most stable open-chain isomer is located even higher (by 1.7 eV) [10]. Formation of protonated fulvene, in addition to benzenium ion, likely occurs upon dissociative ionization of a number of $C_6H_8$ isomers [11, 12], or by ion-molecule reactions involving allene, propyne [12, 13], butadiene [14], allyl bromide [15], vinyl chloride [16] and others. Also, isomerisation of protonated benzene into protonated fulvene was suggested to take place in photodissociation studies [15].

There are no spectroscopic data on other isomers of $C_6H_7^+$. In this contribution electronic transitions of $C_6H_7^+$ trapped in neon matrices were investigated. The setup used is as described. $C_6H_7^+$ cations were produced in a hot-cathode discharge source from a number of precursors mixed with helium: 1,3- and 1,4-cyclohexadiene (1,3-CHD and 1,4-CHD), allene, propyne, 1,3,5-hexatriene and methylcyclopentadiene dimer (MCPD). All samples were outgassed by freeze-pump-thaw cycles before use and later mixed with He in the ratio 1:4 for CHD and 1:1 for allene or propyne as precursor. Additionally, reactions of $H_3^+$ with benzene trapped in a neon matrix have been investigated. $H_3^+$ was produced from $H_2$ in an ion source and was codeposited with a benzene/Ne mixture onto the matrix substrate. The ratio of $C_6H_6$/Ne was 1:9000 and the deposited charge of $H_3^+$ was around 1 mC. Besides protonated benzene, the $A\ ^1A' \leftarrow X\ ^1A'$ transition of α-protonated fulvene was observed for the first time. Several isomers of neutral $C_6H_7$, produced by neutralization of $C_6H_7^+$, are characterized by spectroscopic means. Photoinduced isomerization of $C_6H_7$ to an open chain species and $\alpha$-hydrogenated fulvenyl radical was also observed.

## 4.2 OBSERVATIONS

### 4.2.1 $C_6H_7^+$ CATIONS

The UV part of the absorption spectrum recorded after deposition of mass-selected $C_6H_7^+$ species produced from a mixture of 1,3-CHD/He is presented in Figure 4.1 (blue line). It is characterized by three distinct absorption systems (K, L and M). The K system is a broad, structured absorption with an onset at 335 nm. Band systems L and M with onsets at 310 and 282 nm are much narrower. The K and L absorptions decrease, though to a different extent, upon UV irradiation of the matrix with a medium pressure Hg lamp equipped with water and a $\lambda \geq 293$ nm cut-off filters. System M gains intensity under these conditions, which is indicative of its neutral origin (Figure 4.1, red line).

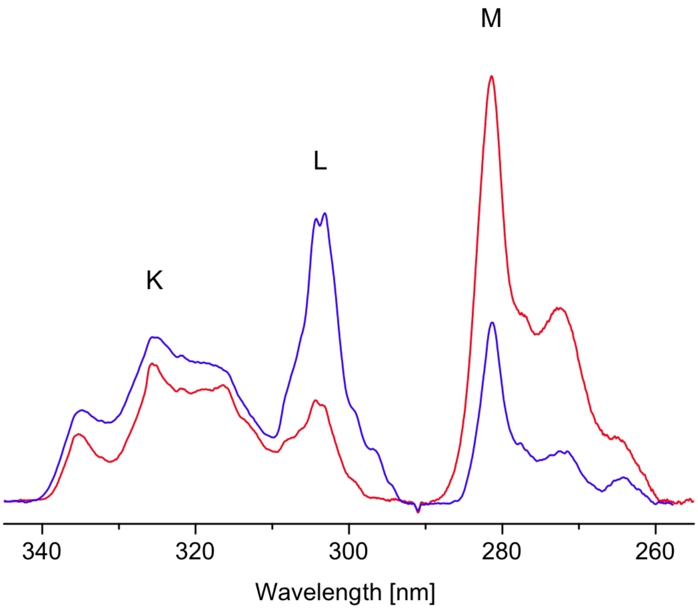

**Figure 4.1:** UV part of the absorption spectrum recorded after deposition of $C_6H_7^+$ cations produced from 1,3-cyclohexadiene in a neon matrix with $CH_3Cl$ electron scavenger (blue line), and after photobleaching with UV photons (red). K represents absorption of $C_6H_7^+$ isomers; L and M belong to different isomers of neutral $C_6H_7$.

Absorptions K and L could originate from $C_6H_7^+$ cations or from photo-unstable $C_6H_7$ neutrals, which could convert to other isomers. UV irradiation of the matrix causes neutralization of the trapped cations by released electrons from the $Cl^-$ counterions. This process is only operative if the photon energy exceeds the detachment threshold of $Cl^-$, whereby the electron affinity of Cl is 3.61 eV in the gas phase [17], corresponding to photon wavelengths $\lambda < 343$ nm. However, the detachment threshold of $Cl^-$ in a neon matrix is higher than in the gas phase due to the surrounding neon atoms and require photons with $\lambda < 300$ nm. Consequently, cations were neutralized using a $\lambda \geq 293$ nm cut-off filter. A more pronounced effect was observed when full UV radiation of the MpHg lamp was used.

In order to ascertain whether K and L come from $C_6H_7^+$ or from photo-unstable $C_6H_7$ neutrals, the cations were also deposited without an electron scavenger. In such experiments free electrons neutralize cations during growth of the matrix. The UV section of the spectrum obtained is shown in Figure 4.2 (blue trace). The K system is absent, while L and M are still present. Therefore, absorption K originates from $C_6H_7^+$ cations and L belongs to a photosensitive $C_6H_7$ neutral.

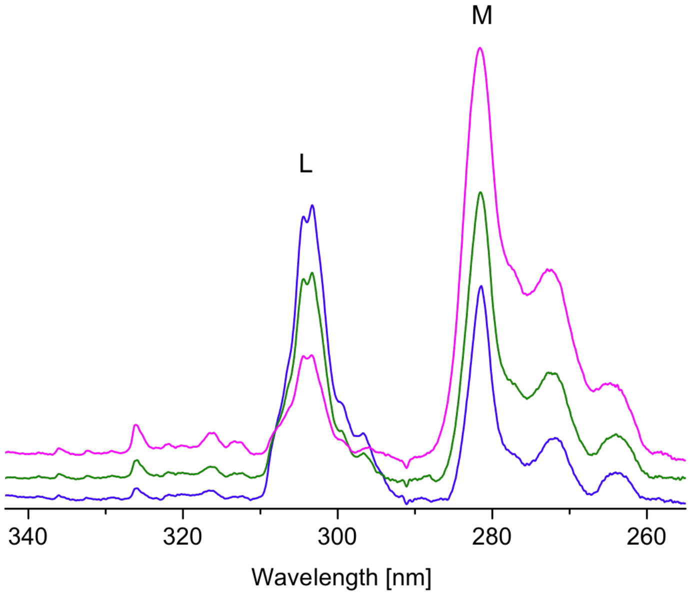

**Figure 4.2:** UV part of the absorption spectrum recorded after deposition of $C_6H_7^+$ cations produced from 1,4-cyclohexadiene in a pure neon matrix (blue line); after 5 (green) and 20 min (magenta) irradiation with a high-pressure Xe lamp using a λ ≥ 305 nm cut-off filter. Isomer L of $C_6H_7$ converts to isomer M upon photobleaching with UV photons.

The structure of the cation responsible for the K system was proven by using several precursors for the production and deposition of the $m/z = 79$ ions. These were 1,4-CHD, allene, propyne, 1,3,5-hexatriene and MCPD. In all cases the K system was present together with the L and M absorptions of neutrals. However, the relative intensities of the bands, constituting the K system, change slightly, depending on the precursor used. To illustrate this better, the spectra were normalized to the same intensity of the first band of K (Figure 4.3). This allows two absorption systems originating from two isomers of $C_6H_7^+$ to be distinguished. Their onsets are labeled as $K_1$ and $K_2$ with wavelengths given in Table 4.1. The $C_6H_7^+$ isomer, which is responsible for the $K_2$ system, is more efficiently produced from 1,3- and 1,4-CHD, while the $K_1$ system is more pronounced in the experiments where allene, propyne and MCPD were utilized.

### 4.2.2 $C_6H_7$ NEUTRALS

As explained above, absorptions L and M (Figure 4.1) originate from two isomers of $C_6H_7$. Besides these, several weaker bands are seen on the long-wavelength side of system L. System L decays in a regular way after 5 and 15 min irradiation of the matrix with a high-pressure Xe lamp equipped with a $\lambda \geq 305$ nm cut-off filter (Figure 4.2). Parallel to this M and the weak feature in the 310–340 nm range increase. This indicates that isomer L of $C_6H_7$ photoconverts to isomer M and to another neutral, which is responsible for the weak band system.

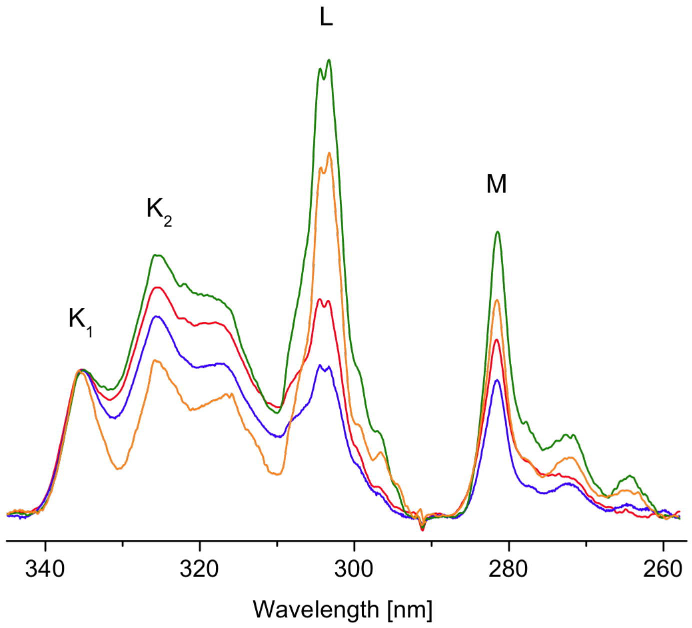

**Figure 4.3:** Comparison of absorption spectra recorded following deposition of $C_6H_7^+$ cations produced from different precursors: 1,3-cyclohexadiene (green line), 1,4-cyclohexadiene (red), allene (blue), and methylcyclopentadiene dimer (orange). $K_1$ – is assigned to α-protonated fulvene, $K_2$ – protonated benzene, L – c-$C_6H_7$, M – to (E)-1.4.5-hexatrien-3-yl radical.

Deposition of $C_6H_7^+$ produced from 1,4-CHD into a pure neon matrix resulted not only in the appearance of the UV absorptions seen in Figure 4.2, but also in the weak 510–550 nm system D. In order to show the relative intensities of the observed features, the visible and UV sections of the spectrum were scaled by appropriate factors in Figure 4.4 (trace a). The spectrum measured after UV irradiation of the matrix is depicted in trace a’. Band D with an onset at 549 nm decays after UV irradiation in a similar manner as absorption L and simultaneously, a weak band at 532 nm grows in intensity.

All the absorptions shown in Figure 4.4 (trace a) were also observed in the spectrum recorded following deposition of $H_3^+$ ions into a matrix containing benzene and neon in the ratio 1:9000. The resulting absorption is trace b of Figure 4.4 and b’ after UV irradiation. Traces a and b are similar, even the multiplet structure of the origin band at 549 nm is well reproduced (insert of Figure 4.4).

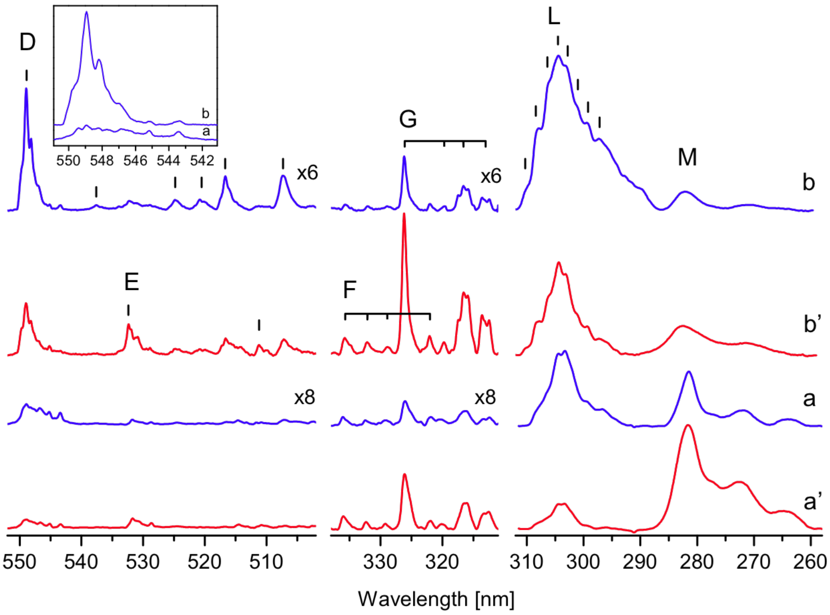

**Figure 4.4:** Absorption spectra recorded after deposition of $C_6H_7^+$ into neon matrix without an electron scavenger. Trace a – after deposition of $C_6H_7^+$ from 1,4-cyclohexadiene; b – after codeposition of $H_3^+$ ions with benzene/Ne = 1:9000; a' and b' – recorded after photobleaching with λ ≥ 293 nm. Bands D and L are assigned to *c*-$C_6H_7$; E and G to α-hydrogenated fulvene radical; F – methyl-hydrogenated fulvene radical; and M – to (E)-1.4.5-hexatrien-3-yl radical.

All the band systems but M are much stronger than in the experiment carried out with mass-selected $C_6H_7^+$. No electron scavenger was used in the experiment with $H_3^+$ ions and the deposited charge was several times larger than in the case of $C_6H_7^+$. Under such conditions only neutral molecules should be present in the matrix, because without an electron scavenger $H_3^+$ should be completely neutralized. The dissociative electron recombination of $H_3^+$ leads to formation of H and $H_2$. Hydrogen atoms are mobile and reactive even in solid neon at 6 K. One could expect that the main reaction product of H with benzene is the cyclohexadienyl radical, *c*-$C_6H_7$. Addition of the first hydrogen atom to benzene has an energy barrier around 16 kJ mol$^{-1}$ [18, 19]; it can be overcome due to the ability of hydrogen to tunnel through the reaction entrance barrier. Electronic transitions of *c*-$C_6H_7$ have been reported [20-23]. According to these, absorption systems L and D with origins at 549 nm and 310 nm can be assigned to the $A\,^2A_2 \leftarrow X\,^2B_1$ and $B\,^2B_1 \leftarrow X\,^2B_1$ electronic transitions of *c*-$C_6H_7$ ($C_{2v}$ symmetry).

**Table 4.1** Observed absorption band maxima (±0.1 nm) of electronic transitions of $C_6H_7^+$ and their neutrals in neon matrices and their assignment

| Species | $\lambda_{Ne}$ / nm | $\tilde{\nu}$ / cm$^{-1}$ | $\Delta\tilde{\nu}$ / cm$^{-1}$ | Assignment $^b$ | |
|---|---|---|---|---|---|
| $\alpha$-HF$^+$ | 335.3 | 29 822 | 0 | $0_0^0$ | $A\ ^1A' \leftarrow X\ ^1A'$ |
| HB$^+$ | 325.4 | 30 727 | 0 | $0_0^0$ | $A\ ^1B_2 \leftarrow X\ ^1A_1$ |
| | 316.3 | 31 619 | 892 | $\nu_{11}$ | |
| $\alpha$-HF | 532.4 | 18 782 | 0 | $0_0^0$ | |
| | 511.2 | 19 560 | 778 | $\nu_{20}$ | |
| | 326.1 | 30 661 | 0 | $0_0^0$ | |
| | 319.7 | 31 283 | 622 | $\nu_{21}$ or $5\nu_{14}$ of MHF | |
| | 316.6 | 31 584 | 923 | $\nu_{17}$ | |
| | 313.6 | 31 886 | 1225 | $\nu_{13}$ | |
| | 312.3 | 32 017 | 1356 | $\nu_{11}$ | |
| MHF | 335.7 | 29 789 | 0 | $0_0^0$ | |
| | 332.1 | 30 111 | 322 | $\nu_{14}$ | |
| | 328.9 | 30 403 | 614 | $2\nu_{14}$ | |
| | 322.0 | 31 055 | 394 | $4\nu_{14}$ | |
| *E*-HT | 281.5 | 35 524 | 0 | $0_0^0$ | |
| | 272.3 | 36 718 | 1194 | $\nu_{19}$ | |
| | 263.6 | 37 930 | 2406 | $2\nu_{19}$ | |
| $c$-$C_6H_7$ | 548.9 | 18 217 | 0 | $0_0^0$ | $A\ ^2A_2 \leftarrow X\ ^2B_1$ |
| | 537.6 | 18 602 | 385 | $2\nu_{23}$ | |
| | 524.8 | 19 056 | 839 | $\nu_{11}$ | |
| | 520.5 | 19 212 | 995 | $\nu_{10}$ | |
| | 516.7 | 19 355 | 1138 | $\nu_8$ | |
| | 507.3 | 19 714 | 1497 | $\nu_5$ | |
| | 310.3 | 32 225 | 0 | $0_0^0$ | $B\ ^2B_1 \leftarrow X\ ^2B_1$ |
| | 308.4 | 32 430 | 205 | $2\nu_{23}$ | |
| | 306.4 | 32 642 | 417 | $4\nu_{23}$ | |
| | 304.5 | 32 843 | 618 | $6\nu_{23}$ | |
| | 302.8 | 33 021 | 796 | $\nu_{11}$ | |
| | 301.0 | 33 222 | 997 | $\nu_{11} + 2\nu_{23}$ | |
| | 299.2 | 33 427 | 1202 | $\nu_{11} + 4\nu_{23}$ | |
| | 297.2 | 33 647 | 1422 | $\nu_{11} + 6\nu_{23}$ | |

[a] $\tilde{\nu} = 1/\lambda_{Ne}$. [b] Vibrational assigments in the excited states of $C_6H_7^+$ and their neutrals are based on ground-state fundamentals calculated with DFT at the B3LYP/cc-pVTZ level of theory, and listed in Table 4.4.

## 4.3 COMPUTATIONAL RESULTS

A number of structural isomers of $C_6H_7^+$ are possible. Theoretical calculations predict that the most stable is protonated benzene ($HB^+$) and higher in energy are protonated fulvenes ($HF^+$) and open-chain structures [9, 10]. We considered six lowest energy isomers of $C_6H_7^+$: $HB^+$, $\alpha$- and $\beta$-$HF^+$, methyl-protonated fulvene ($MHF^+$) and two open-chain forms, (*Z*)- and (*E*)-1,4,5-hexatrien-3-ylium (*Z*-$HT^+$ and *E*-$HT^+$) (Figure 4.5). Geometries were optimized at the DFT/B3LYP/cc-pVTZ level of theory using Gaussian 03 program suite [24]. Vibrational analysis was done to ensure that all isomers are local minima on the $C_6H_7^+$ $S_0$ potential energy surface. In all cases real minima were found (no imaginary frequencies). All the considered $C_6H_7^+$ except $MHF^+$ have singlet electronic ground state. For the latter, calculations predict triplet ground state, similar to the cyclopentadienyl cation ($C_5H_5^+$) [25], locating it 3.1 kJ mol$^{-1}$ lower than the singlet state. The global minimum on the potential energy surface of $C_6H_7^+$ is the $X\,^1A_1$ state of $HB^+$. The next lowest energy isomer $\alpha$-$HF^+$ lies 39 kJ mol$^{-1}$ higher. $\beta$-$HF^+$ was found 108 kJ mol$^{-1}$ above $HB^+$. These data can be compared with the energies 40 and 103 kJ mol$^{-1}$ calculated for $\alpha$- and $\beta$-$HF^+$ at a higher level of theory, G2(MP2) [9]. The other three ions, $MHF^+$, *Z*-$HT^+$ and *E*-$HT^+$, are located at 137, 137 and 147 kJ mol$^{-1}$ above $HB^+$. The $C_6H_7$ radicals, which can be obtained by neutralization of the above discussed cations, have been studied by the DFT/B3LYP/cc-pVTZ method. Again, the lowest energy isomer is the neutral (*c*-$C_6H_7$) derived from protonated benzene. The relative energies of the other isomers of $C_6H_7$ in their doublet ground state with respect to the $X\,^2B_1$ state of *c*-$C_6H_7$ are indicated in Figure 4.5.

The electronic excitation energies were calculated between the singlet manifolds of the $C_6H_7^+$ cations using a time-dependent (TD) DFT method and the geometries of the ions were optimized using the B3LYP functional and the cc-pVTZ basis set. The calculations predict two allowed electronic transitions at 4.2 and 5.4 eV for $PB^+$ with oscillator strengths 0.11 and 0.004. These results agree well with more advanced *ab initio* methods (4.09 and 5.71 eV, $f$ = 0.14 and 0.096) [8]. The TD DFT excitation energies for the considered isomers of $C_6H_7^+$ are collected in Table 4.2. One can expect that these transition energies are predicted with comparable accuracy as for $PB^+$. A striking difference between the calculated oscillator strengths of the UV transition of different isomers of $HF^+$ is apparent in Table 4.2. These indicate a strong transition at 4.35 eV for $\alpha$-$HF^+$ and a weak one in this region for $\beta$-$HF^+$ and $MHF^+$.

**Table 4.2** Excited-state symmetries, vertical excitation energies $\Delta E_V$ and oscillator strengths $f$ for the most stable $C_6H_7^+$ isomers calculated with two different methods and a comparison to experimental data.

| Exc. state | $\Delta E_V$ /eV | $f$ | Exp. / eV |
|---|---|---|---|
| **HB$^+$**, $X\,^1A_1$ | | | |
| $^1B_2$ | **4.17** / 4.36 | 0.11 | 3.81 (325) |
| $^1A_2$ | **5.05** / 5.33 | 0 | |
| $^1B_1$ | **5.41** / 8.10 | 0.004 | |
| **$\alpha$-HF$^+$**, $X\,^1A'$ | | | |
| $^1A'$ | **4.35** / 4.58 | 0.29 | 3.70 (335) |
| $^1A''$ | **4.96** / 5.04 | 0 | |
| $^1A'$ | **5.21** / 7.97 | 0.056 | |
| **$\beta$-HF$^+$**, $X\,^1A'$ | | | |
| $^1A'$ | **2.06** / 2.47 | 0.009 | |
| $^1A''$ | **4.58** / 5.70 | 0 | |
| $^1A''$ | **5.09** / ... | 0.002 | |
| **MHF$^+$**, $X\,^3A''$ | | | |
| $^3A''$ | **3.45** / 3.58 | 0.018 | |
| $^3A'$ | **3.72** / 3.79 | 0.048 | |
| $^3A'$ | **4.03** / 6.53 | 0 | |
| ***Z*-HT$^+$**, $X\,^1A'$ | | | |
| $^1A''$ | **3.11** / 4.48 | 0 | |
| $^1A'$ | **4.26** / 5.44 | 0.60 | |
| $^1A''$ | **5.36** / 8.22 | 0 | |
| ***E*-HT$^+$**, $X\,^1A'$ | | | |
| $^1A''$ | **3.14** / 4.74 | 0 | |
| $^1A'$ | **4.43** / 5.48 | 0.86 | |
| $^1A''$ | **5.40** / 8.37 | 0 | |

[a] Excitation energies were calculated with TD DFT at the B3LYP/cc-pVTZ (**bold**) and CAS(4, 6)/6-311G(d, p) (normal font) level of theory.

**Table 4.3** Excited-state symmetries, vertical excitation energies $\Delta E_V$ and oscillator strengths $f$ for the most stable $C_6H_7$ isomers calculated with two different methods and a comparison to experimental data.

| Exc. state | $\Delta E_V$ /eV | $f$ | Exp. / eV |
|---|---|---|---|
| ***c*-C$_6$H$_7$**, $X\,^2B_1$ | | | |
| $^2A_2$ | **2.79** / 2.69 | 0.001 | 2.26 (549) |
| $^2B_1$ | **4.02** / 4.27 | 0.08 | 4.00 (310) |
| $^2B_1$ | **4.96** / 6.11 | 0.001 | |
| $^2A_1$ | **5.06** | 0.004 | |
| **$\alpha$-HF**, $X\,^1A''$ | | | |
| $^2A'$ | **2.92** / 2.70 | 0.001 | 2.33 (532) |
| $^2A'$ | **4.30** / 4.16 | 0.15 | 3.80 (326) |
| $^2A'$ | **4.47** / 6.56 | 0.091 | |
| $^2A'$ | **5.15** | 0.004 | |
| **$\beta$-HF**, $X\,^1A''$ | | | |
| $^2A'$ | **2.88** / 2.88 | 0.003 | |
| $^2A'$ | **3.64** / 4.51 | 0.003 | |
| $^2A'$ | **4.03** / 6.01 | 0.05 | |
| $^2A'$ | **5.46** | 0.03 | |
| **MHF**, $X\,^2A''$ | | | |
| $^2A'$ | **0.97** / 0.96 | 0 | |
| $^2A'$ | **4.16** / 4.13 | 0.024 | 3.69 (336) |
| $^2A''$ | **4.69 /** 6.66 | 0 | |
| $^2A'$ | **5.32** / | 0.003 | |
| ***Z*-HT**, $X\,^2A''$ | | | |
| $^2A'$ | **2.98** / 2.76 | 0.0004 | |
| $^2A''$ | **3.63** / 4.26 | 0 | |
| $^2A''$ | **3.89** / 6.82 | 0 | |
| $^2A'$ | **4.39** / | 0.01 | |
| $^2A'$ | **4.58** / | 0.43 | |
| $^2A'$ | **4.63** | 0.18 | |
| ***E*-HT**, $X\,^2A''$ | | | |
| $^2A'$ | **3.08** / 2.83 | 0.002 | |
| $^2A''$ | **3.68** / 4.23 | 0 | |
| $^2A''$ | **3.93** | 0 | |
| $^2A'$ | **4.41** | 0.01 | |
| $^2A'$ | **4.64** | 0.04 | |
| $^2A'$ | **4.84** | 0.87 | 4.39 (282) |

[a] Excitation energies were calculated with TD DFT at the B3LYP/cc-pVTZ (**bold**) and CAS(5,6)/6-311G(d, p) (normal font) level of theory.

The excitation energies of the $C_6H_7^+$ isomers were calculated using the complete active space self-consistent field method (CASSCF) and the 6-311G(d, p) basis set. The active space consisted of four valence electrons distributed on six orbitals (CAS(4, 6)). CASSCF calculations for $C_6H_7^+$ cations were carried out in order to compare the excitation energies with those from TD DFT. The CASSCF method provides a crude approximation to the excited state energy, as it takes into account only a static electron correlation effect. The general excitation pattern obtained by the CASSCF and TD DFT methods is comparable; however, energies predicted by the former are higher than from the latter.

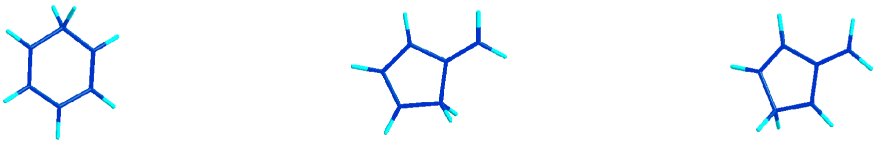

**protonated benzene (PB$^+$, $^1A_1$)**
**0**
cyclohexadienyl radical (*c*-$C_6H_7$, $^2B_1$)
0

**$\alpha$-protonated fulvene ($\alpha$-PF$^+$, $^1A'$)**
**39.3**
$\alpha$-hydrogenated fulvene ($\alpha$-HF, $^2A''$)
19.0

**$\beta$-protonated fulvene ($\beta$-PF$^+$, $^1A'$)**
**108.4**
$\beta$-hydrogenated fulvene ($\beta$-HF, $^2A''$)
44.1

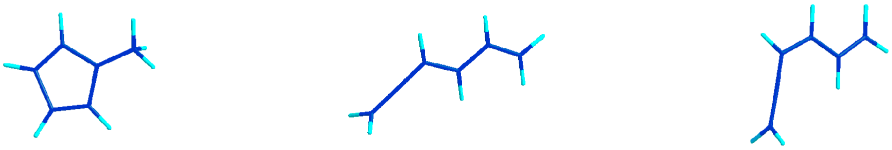

**methyl-protonated fulvene (MPF$^+$, $^3A''$)**
**133.5**
methyl-hydrogenated fulvene (MHF, $^2A'$)
16.9

**(*E*)-1,4,5-hexatrien-3-ylium (*E*-HT$^+$, $^1A'$)**
**136.8**
(*E*)-1,4,5-hexatrien-3-yl radical (*E*-HT, $^2A''$)
112.1

**(*Z*)-1,4,5-hexatrien-3-ylium (*Z*-HT$^+$, $^1A'$)**
**146.9**
(*Z*)-1,4,5-hexatrien-3-yl radical (*Z*-HT, $^2A''$)
118.4

**Figure 4.5:** Schematic representation of the $C_6H_7^+$ cations and their neutral counterparts. Relative energies with respect to the most stable isomer are given in kJ mol$^{-1}$. Ground-state geometries were optimized with DFT at the B3LYP/cc-pVTZ level of theory.

Similarly, TD DFT and CASSCF calculations were carried out for $C_6H_7$ neutrals. Five π valence electrons distributed on six orbitals formed the active space (CAS(5, 6)). The CAS(5, 6)/6-311G(d, p) calculations predict for *c*-$C_6H_7$ two dipole-allowed electronic transitions at 2.69 and 4.27 eV, which can be compared with 2.26 and 4.0 eV from the experimental data. The excitation energies for all the considered $C_6H_7$ isomers are collected in Table 4.3.

## 4.4 DISCUSSIONS

### 4.4.1 $C_6H_7^+$ CATIONS

$PB^+$ is the most stable form of $C_6H_7^+$ and the absorptions of $c$-$C_6H_7$ resulted from the neutralization of $HB^+$ in a neon matrix; therefore, it can be expected that one of the systems $K_1$ or $K_2$ seen in Figures 4.1 and 4.3 originates from $HB^+$ cation. The onsets of these transitions in a neon matrix lie at 3.7 and 3.8 eV, respectively, which are close to the 4.17 eV excitation calculated by the TD DFT method and the more advanced *ab initio* level of theory (4.09 eV) [8]. Both methods predict a strong transition of $HB^+$ in the UV region with an oscillator strength of 0.11 (TD DFT) and 0.14 (*ab initio*). Hence, one of these absorptions ($K_1$ or $K_2$) must originate from $HB^+$.

The gas-phase kinetic studies on $C_6H_7^+$ produced from different precursors have revealed at least two isomers, which differ in reactivity towards conjugate bases; the more reactive is $HB^+$. The highest relative abundance of non-benzenium ions was observed when $C_6H_7^+$ ions were generated from 1,4-CHD and the abundance decreased in the precursor series: allene, propyne and 1,3-CHD [12]. The mechanism of $C_6H_7^+$ production from various precursors is likely to be different. In the case of CHDs, $C_6H_7^+$ is formed by removing one hydrogen atom. The aromatic ring should stay intact and the resulting cation should possess the benzenium ion structure. One could expect formation of some non-cyclic cation from allene or propyne in a following reaction:

$$C_3H_3^+ + C_3H_4 \rightarrow C_6H_7^+,$$

because $C_3H_3^+$ dominates the mass spectrum. MCPD should give rise to ions containing a five-membered ring.

The structure of ions is not always foretold by the geometry of the precursor used. The relative population of $C_6H_7^+$ isomers depends on the kinetics of ion-molecule reactions involved in the source, as well as on the energetics of ions. Energy barriers are overcome in the source and may lead to isomerization.

The relative intensities of band systems $K_1$ and $K_2$ change with the precursor used (Figure 4.3). The strongest relative absorption of the $K_2$ system was observed when 1,3-CHD was used. The highest population of the $PB^+$ cations has been seen in the kinetic gas-phase studies carried out with this precursor [12]. Therefore, the $K_2$ system is assigned to the $A\ ^1B_2 \leftarrow X\ ^1A_1$ transition of this cation. The position of this absorption agrees well with the gas-phase photodissociation spectrum of $HB^+$. [7] The band lying ~890 $cm^{-1}$ above the origin can be assigned to the excitation of the $\nu_{11}$ vibrational mode in the $A\ ^1B_2$

state. In the earlier PD experiments, a much weaker absorption of $HB^+$ was detected at ~245 nm [7] and the recent theoretical calculations predict two excited states, $^1A_1$ and $^1B_1$, in this region, which are dipole accessible from the ground state [8]. However, the oscillator strengths of these transitions are much weaker (0.096 and 0.005, respectively) than to the $A\,^1B_2$ state. This transition was not observed in these measurements due to low transmittance in this region caused by scattered light.

The $K_1$ band system can be assigned to $\alpha$-$HF^+$ for the following reasons. The highest intensity ratio of the absorption $K_1$ to $K_2$ was observed with the MCPD precursor (Figure 4.3, bottom trace), in which a five-membered ring could survive the conditions in the ion source. Among the protonated fulvenes, $\alpha$-$HF^+$ is the most stable structure and TD DFT calculations predict a strong electronic transition only for $\alpha$-$HF^+$ (at 4.35 eV) close to the observed $K_1$ system (3.7 eV). The oscillator strength of the UV transitions of $\alpha$-$HF^+$ is ca. three times larger than for $HB^+$ and is about two orders of magnitude higher than for the other protonated fulvenes ($\beta$-$HF^+$ and $MHF^+$).

### 4.4.2 $C_6H_7$ NEUTRALS

The deposition of mass-selected $C_6H_7^+$ with all the precursors used has resulted in the appearance of the strong 310 nm band system and the weaker one with onset at 549 nm of neutral cyclohexadienyl radical, $c$-$C_6H_7$. This radical was observed as a result of partial neutralization of $C_6H_7^+$, even in the experiments when an electron scavenger was added into the matrix. The origin band of $c$-$C_6H_7$ at 549 nm is sharp and a multiplet structure is apparent. Two modes of energy 27 and 71 $cm^{-1}$ form this pattern. These frequencies are too low to be assigned to any vibration of this molecule; they are due to phonon coupling of the neon lattice to the electronic state of $c$-$C_6H_7$. The $A\,^2A_2 \leftarrow X\,^2B_1$ transition of $c$-$C_6H_7$ with onset at 549 nm has a well-evolved vibrational structure that is formed by the excitation of several totally symmetric fundamental modes in the upper electronic state. The lowest energy vibrational band observed in the spectrum is located ~385 $cm^{-1}$ above the origin and is assigned to the double excitation of the $\nu_{23}$ mode of $b_1$ symmetry. Wavelengths of the observed absorptions of $c$-$C_6H_7$ and their assignments are collected in Table 4.1.

The absorption L of $c$-$C_6H_7$ at ~310 nm has a multiplet structure too. This pattern is well pronounced in the experiment of $H_3^+$ with benzene trapped in a neon matrix (traces b and b’ in Figure 4.4). Absorption L is much broader than band D and two frequencies, 205 and 796 cm$^{-1}$, with their overtones and combinations form the observed profile of the UV system. In the ground state of *c*-$C_6H_7$ the present calculations predict the lowest energy mode $\nu_{23}$ at 175 cm$^{-1}$ ($b_1$ symmetry), corresponding to the out-of-plane ring deformation with a considerable contribution of the out-of-plane motion of the $CH_2$ group. The single excitation of this mode is forbidden for the $^2B_1 \leftarrow X\,^2B_1$ transition; therefore, the energy of ~205 cm$^{-1}$ must correspond to $2\nu_{23}$. The frequency difference of the $\nu_{23}$ mode in the ground and $B\,^2B_1$ state is large and reflects a geometry change along this coordinate upon electronic excitation. The profile of the absorption at ~310 nm is dominated by the long progression of the 205 cm$^{-1}$ overtone bands and its combination with the ~796 cm$^{-1}$ mode. The frequency of the latter is close to the calculated totally symmetric $\nu_{11}$ (871 cm$^{-1}$) mode.

**Table 4.4** Ground-state vibrational frequencies of considered $C_6H_7$ species calculated with DFT at the B3LYP/cc-pVTZ level of theory.

| Species | Symm. | Frequencies / cm$^{-1}$ |
|---|---|---|
| HB$^+$ | $a_1$ | 3213, 3193, 3182, 2950, 1642, 1485, 1277, 1216, 1017, 1008, 901, 597 |
| | $a_2$ | 1152, 1019, 808, 334 |
| | $b_1$ | 2943, 1080, 1055, 852, 663, 419, 216 |
| | $b_2$ | 3211, 3192, 1576, 1487, 1423, 1368, 1209, 1153, 990, 591 |
| $\alpha$-HF$^+$ | $a'$ | 3246, 3243, 3214, 3210, 3152, 3018, 1665, 1524, 1474, 1456, 1399, 1368, 1310, 1283, 1133, 1101, 1005, 957, 891, 821, 668, 348 |
| | $a''$ | 3039, 1158, 1075, 1043, 996, 913, 767, 645, 471, 346, 186 |
| c-$C_6H_7$ | $a_1$ | 3196, 3172, 3152, 2918, 1612, 1462, 1436, 1201, 1003, 989, 871, 567 |
| | $a_2$ | 1182, 975, 730, 387 |
| | $b_1$ | 2899, 981, 937, 780, 639, 530, 175 |
| | $b_2$ | 3173, 3154, 1548, 1420, 1376, 1308, 1173, 1111, 969, 595 |
| $\alpha$-HF | $a'$ | 3225, 3222, 3209, 3191, 3140, 3018, 1569, 1513, 1443, 1420, 1400, 1312, 1274, 1259, 1111, 1045, 989, 945, 857, 820, 639, 355 |
| | $a''$ | 3038, 1146, 956, 931, 831, 785, 664, 619, 531, 397, 184 |
| MHF | $a'$ | 3232, 3211, 3059, 2994, 1513, 1482, 1417, 1402, 1296, 1093, 1018, 994, 916 882 721 629 602 213 |
| | $a''$ | 3224, 3203, 3099, 1534, 1466, 1294, 1168, 1056, 953, 901, 713, 528, 497, 329, –79 |
| *E*-HT | $a'$ | 3230, 3163, 3139, 3136, 3119, 3083, 1943, 1563, 1488, 1458, 1387, 1367, 1306, 1198, 1139, 1012, 899, 887, 724, 434, 303, 121 |
| | $a''$ | 3144, 1021, 996, 917, 872, 791, 617, 546, 299, 219, 145 |

UV irradiation of *c*-$C_6H_7$ with a mpHg lamp using a $\lambda \geq 305$ nm cut-off filter leads to decrease of the visible and UV systems of this species and simultaneously increases the strong absorption at ~282 nm and weaker ones in the 310–340 nm and visible ranges (Figure 4.3). It is well established that 1,3-CHD [26, 27] and its cation [28], which are structurally similar to *c*-$C_6H_7$, undergo photoinduced ring-opening reaction leading to 1,3,5-hexatriene or its cation, respectively. In the case of neutral 1,3-CHD, the ring opening takes place in a fraction of a picosecond and the product relaxes to the more stable (*tZt*-hexartiene) form in several tenths of picosecond [26]. The open-chain structure, produced from 1,3-CHD or 1,3-$CHD^+$ by the UV induced ring-opening reaction, absorbs at shorter wavelength than the parent species.

It is expected that a similar process takes place in the case of UV irradiation of *c*-$C_6H_7$ and the strong band system with onset at 282 nm is assigned to the open-chain isomer. CAS(5, 6)/6-311G(d, p) calculations predict two electronic transitions for the two neutral, open chain isomers *E*- and *Z*-HT at ~2.8 and 4.2 eV; the latter transition lies close to the observed M system (4.39 eV). By analogy to the photoisomerization of 1,3-CHD to *tZt*-hexatriene, the M system is assigned to *E*-HT. The relative absorption of *E*-HT (at ~282 nm) with respect to the 310 nm system of *c*-$C_6H_7$ varies with the experimental conditions. The weakest M absorption was observed in the experiment of $H_3^+$ with benzene trapped in the matrix. In this case *E*-HT was present as a result of the ring opening process of the excited *c*-$C_6H_7$ produced in the exothermic (117 kJ mol$^{-1}$) reaction of $C_6H_6$ with H generated by neutralization of $H_3^+$. The M absorption of *E*-HT was also observed following deposition of $C_6H_7^+$ without an electron scavenger. In such experiments *E*-HT was formed by the neutralization of collisionally produced *E*-$HT^+$ from $PB^+$ in a neon matrix.

Though the CAS calculations predict the electronic transition of *E*-HT also in the visible range (~438 nm), near the weak E band system with onset at 532 nm which grows in intensity upon UV irradiation of the matrix, the system E cannot be assigned to *E*-HT because its relative intensity with respect to absorption at ~282 nm varies with the experimental conditions. The intensity of the E system correlates well with the G system, with onset at 326 nm.

After deposition of $C_6H_7^+$ the absorption of $\alpha$-$HF^+$ was detected. Thus neutral $\alpha$-hydrogenated fulvene ($\alpha$-HF) should also be present in the matrix as a result of neutralization of the corresponding ion. CAS calculations predict two transitions at 459 and 298 nm for this neutral, which are quite close to the observed absorptions at 532 and 326 nm. Therefore, the E and G systems (Figure 4.4) are assigned to $\alpha$-HF (Table 4.1). The absorptions at 532 and 326 nm grow in intensity at the expense of $c$-$C_6H_7$ upon UV irradiation. The absorption of UV photons by $c$-$C_6H_7$ leads not only to the ring opening reaction, but to the photoisomerization to $\alpha$-HF. The latter process is feasible as the calculated barrier ~219 kJ mol$^{-1}$ [9] for the isomerization of HB$^+$ to $\alpha$-HF$^+$ should be similar to the neutral one and it can be overcome by the electronic excitation of $c$-$C_6H_7$. The strongest E and G systems are observed in the reaction of $H_3^+$ with benzene in a neon matrix. The G band is stronger than M in this case, which means that the isomerization to $\alpha$-HF dominates over the ring opening reaction.

Apart from the discussed L, M, D, E and G systems in the 330–340 nm range there is a weak F system present which cannot be attributed to $c$-$C_6H_7$, $E$-HT or $\alpha$-HF species, because only one transition is predicted for these species in this range. Therefore, the F system is due to another isomer of $C_6H_7$. CAS calculations predict a transition around 300 nm for methyl-hydrogenated fulvene MHF and slightly lower in energy for $\beta$-HF (275 nm). The F lies close to the literature value for methyl-cyclopentadienyl radical (336 nm) [29, 30]. Also the vibrational pattern of the F system is similar. Therefore absorption F with an onset at 336 nm is assigned to MHF. The excitation of the $\nu_{14}$ mode and its overtones is observed and agrees well with data reported earlier [29, 30].

## 4.5 CONCLUSIONS

The present investigations on $C_6H_7^+$ trapped in a neon matrix provide a direct spectroscopic characterization of two structural isomers of this cation, which have been postulated in the earlier gas-phase reactivity studies [11-16]. One of these isomers is confirmed to be protonated benzene and its electronic spectrum in a neon matrix agrees well with the one obtained in an earlier photodissociation experiment [7]. The second, less reactive isomer of $C_6H_7^+$ reported in earlier gas-phase studies [12], is identified as $\alpha$-protonated fulvene and is characterized spectroscopically for the first time. The electronic transitions $A\ {}^1B_2 \leftarrow X\ {}^1A_1$ of HB$^+$ and $A\ {}^1A' \leftarrow X\ {}^1A'$ of $\alpha$-HF$^+$ lie in the UV range and they overlap. This fact will hinder their future gas-phase spectroscopic observation as both isomers are produced concomitantly from a number of precursors.

Besides cyclohexadienyl radical, three other isomers of $C_6H_7$ are identified following UV induced neutralization of $C_6H_7^+$ and characterized spectroscopically for the first time: $\alpha$-HF, MHF and $E$-HT. Photoinduced isomerization of $c$-$C_6H_7$ to $E$-HT and $\alpha$-HF was also observed.

## BIBLIOGRAPHY

[1] J. Cernicharo, A.M. Heras, A. Tielens, J.R. Pardo, F. Herpin, M. Guelin, L. Waters. Infrared Space Observatory's discovery of $C_4H_2$, $C_6H_2$, and benzene in CRL 618. *Astrophys. J.*, 546 (2001) L123-L126.

[2] J.H. Waite, D.T. Young, T.E. Cravens, A.J. Coates, F.J. Crary, B. Magee, J. Westlake. The process of tholin formation in Titan's upper atmosphere. *Science*, 316 (2007) 870-875.

[3] N. Solca, O. Dopfer. Protonated benzene: IR spectrum and structure of $C_6H_7^+$. *Angew. Chem.-Int. Edit.*, 41 (2002) 3628-3631.

[4] G.E. Douberly, A.M. Ricks, P.V.R. Schleyer, M.A. Duncan. Infrared spectroscopy of gas phase benzenium ions: Protonated benzene and protonated toluene, from 750 to 3400 $cm^{-1}$. *J. Phys. Chem. A*, 112 (2008) 4869-4874.

[5] W. Jones, P. Boissel, B. Chiavarino, M.E. Crestoni, S. Fornarini, J. Lemaire, P. Maitre. Infrared fingerprint of protonated benzene in the gas phase. *Angew. Chem.-Int. Edit.*, 42 (2003) 2057-2059.

[6] H. Perkampus, E. Baumgarten. Proton-Addition Complexes of Aromatic Hydrocarbons. *Angew. Chem.-Int. Edit.*, 3 (1964) 776-783.

[7] B.S. Freiser, J.L. Beauchamp. Photochemistry of organic ions in gas-phase: comparison of gas-phase photodissociation and solution absorption spectra of benzoyl cation, protonated benzene, and protonated mesitylene. *J. Am. Chem. Soc.*, 98 (1976) 3136-3139.

[8] M.F. Rode, A.L. Sobolewski, C. Dedonder, C. Jouvet, O. Dopfer. Computational study on the photophysics of protonated benzene. *J. Phys. Chem. A*, 113 (2009) 5865-5873.

[9] G. Bouchoux, M. Yanez, O. Mo. Isomerization and dissociation processes of protonated benzene and protonated fulvene in the gas phase. *Int. J. Mass Spectrom.*, 187 (1999) 241-251.

[10] T.S. Zyubina, A.M. Mebel, M. Hayashi, S.H. Lin. Theoretical study of multiphoton ionization of cyclohexadienes and unimolecular decomposition of their mono- and dications. *Phys. Chem. Chem. Phys.*, 10 (2008) 2321-2331.

[11] J.L. Franklin, S.R. Carroll. Effect of Molecular Structure on Ionic Decomposition. II. An Electron-Impact Study of 1,3- and 1,4-Cyclohexadiene and 1,3,5-Hexatrien. *J. Am. Chem. Soc.*, 91 (1969) 6564-6569.

[12] S.G. Lias, P. Ausloos. Structures of $C_6H_7^+$ Ions Formed in Unimolecular and Bimolecular Reactions. *J. Chem. Phys.*, 82 (1985) 3613-3624.

[13] M.T. Bowers, D.D. Elleman, R.M. Omalley, K.R. Jennings. Analysis of ion-molecule reactions in allene and propyne by ion cyclotron resonance. *J. Phys. Chem.*, 74 (1970) 2583-2589.

[14] G. Bouchoux, M.T. Nguyen, J.Y. Salpin. Condensation reactions between 1,3-butadiene radical cation and acetylene in the gas phase. *J. Phys. Chem. A*, 104 (2000) 5778-5786.

[15] Z.Q. Zhu, T. Gaumann. Structures of product ions $C_6H_7^+$ and $C_6H_9^+$ of ion–molecule reactions with allyl bromide. *Org. Mass Spectrom.*, 28 (1993) 1111-1118.

[16] J.A. Herman, K. Herman, T.B. McMahon. Formation of $C_6H_7^+$ ions in ion-molecule reactions in vinyl-chloride. *Can. J. Chem.-Rev. Can. Chim.*, 69 (1991) 2038-2043.

[17] J.D.D. Martin, J.W. Hepburn. Determination of bond dissociation energies by threshold ion-pair production spectroscopy: An improved $D_0$ (HCl). *J. Chem. Phys.*, 109 (1998) 8139-8142.

[18] R. Knutti, R.E. Buhler. Kinetics of the hydrogen atom reactions with benzene, cyclohexadiene and cyclohexene: hydrogenation mechanism and ring cleavage. *Chem. Phys.*, 7 (1975) 229-243.

[19] J.M. Nicovich, A.R. Ravishankara. Reaction of hydrogen atom with benzene. Kinetics and mechanism. *J. Phys. Chem.*, 88 (1984) 2534-2541.

[20] T. Shida, I. Hanazaki. Electronic structures and electronic absorption spectra of cyclohexadienyl and related radicals produced by gamma-irradiation *Bull. Chem. Soc. Japan*, 43 (1970) 646-651.

[21] M. Krauss, R. Osman. Electronic-Spectra of H and OH adducts to benzene. *Chem. Phys. Lett.*, 239 (1995) 258-262.

[22] T. Imamura, W.J. Zhang, H. Horiuchi, H. Hiratsuka, T. Kudo, K. Obi. Laser-induced fluorescence of cyclohexadienyl ($c$-$C_6H_7$) radical in the gas phase. *J. Chem. Phys.*, 121 (2004) 6861-6867.

[23] M. Nakajima, T.W. Schmidt, Y. Sumiyoshi, Y. Endo. Rotationally-resolved excitation spectrum of the jet-cooled cyclohexadienyl radical. *Chem. Phys. Lett.*, 449 (2007) 57-62.

[24] M.J. Frisch, e. al. *Gaussian 03 (Revision C.01)*, (2004) Gaussian, Inc., Wallingford, CT.

[25] H.J. Wörner, F. Merkt. Photoelectron spectroscopic study of the first singlet and triplet states of the cyclopentadienyl cation. *Angew. Chem.-Int. Edit.*, 45 (2006) 293-296.

[26] N. Kuthirummal, F.M. Rudakov, C.L. Evans, P.M. Weber. Spectroscopy and femtosecond dynamics of the ring opening reaction of 1,3-cyclohexadiene. *J. Chem. Phys.*, 125 (2006).

[27] J.B. Schonborn, J. Sielk, B. Hartke. Photochemical ring-opening of cyclohexadiene: Quantum wavepacket dynamics on a global *ab initio* potential energy surface. *J. Phys. Chem. A*, 114 (2010) 4036-4044.

[28] T. Shida, T. Kato, Y. Nosaka. Photoinduced isomerization of ion radicals. The conversion from 1,3-Cyclohexadiene to 1,3,5-Hexatriene cation radicals. *J. Phys. Chem.*, 81 (1977) 1095-1103.

[29] L.F. Dimauro, M. Heaven, T.A. Miller. Lifetimes of the lowest excited states of the cyclopentadienyl and the monomethylcyclopentadienyl radicals. *Chem. Phys. Lett.*, 124 (1986) 489-492.

[30] L. Yu, D.W. Cullin, J.M. Williamson, T.A. Miller. Rotationally resolved laser spectroscopy of the jet-cooled methylcyclopentadienyl radical ($CH_3$-$C_5H_4$ and $CD_3$-$C_5H_4$). *J. Chem. Phys.*, 95 (1991) 804-812.

# CHAPTER 5

# PROTONATED ANTHRACENE AND PHENANTHRENE

Electronic spectra of protonated anthracenes and phenanthrenes have been detected in 6 K neon matrices following deposition of mass-selected $m/z$=179 cations, which were produced from dihydro-anthracene or -phenanthrene, and for anthracene in the proton transfer reaction with protonated ethanol in an ion source. The cations exhibit moderately intense band systems in the 400–550 nm range. Corresponding neutrals were observed in the UV. The absorptions are assigned to specific isomers of the protonated species on the basis of observations and computational results. The astrophysical relevance of protonated anthracenes and phenanthrenes as candidates for carriers of diffuse interstellar bands is discussed.

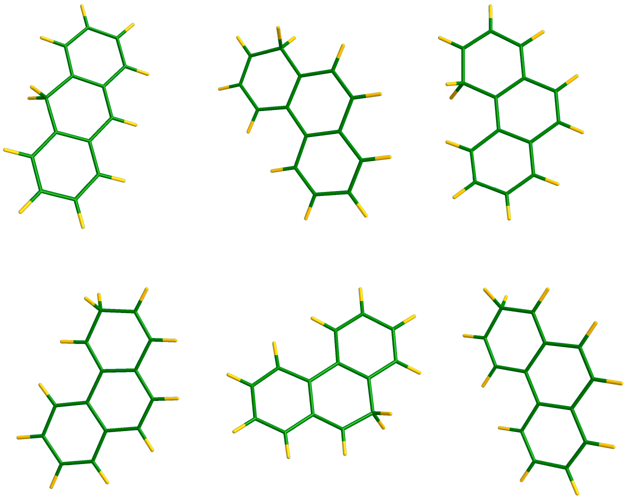

*Electronic absorption spectra of protonated anthracenes and phenanthrenes, and their neutrals in neon matrices*

Iryna Garkusha, Jan Fulara, Adam Nagy, John P. Maier

*Astrophys. J.*, **728**(2), 131/1–7, 2011.

## 5.1 METHODOLOGY

Protonated anthracene (H-An$^+$) and phenanthrene (H-Ph$^+$) cations were produced in a hot cathode discharge source from 9,10-dihydro-anthracene (9,10-DHAn) and 9,10-dihydro-phenanthrene (9,10-DHPh) vapours seeded in helium. Besides these, several experiments have been undertaken to find another way of generating protonated PAHs. The reasons (need) for that was isomerisation of ions in a source, which complicated the assignment of spectra. In addition, this other method was needed to study larger H-PAH$^+$ species, as corresponding dihydrogenated substances ware not commercially available. Anthracene was chosen as a test molecule because of less isomers possible for its protonated form, they are of distinct relative ground-state energies and, therefore, produce significantly less congested spectrum. The results have been summarised already in the experimental part of this thesis. It has been found, that anthracene molecules are efficiently protonated in the ion source in the reaction with protonated ethanol. The relatively small difference in the proton affinities of ethanol and anthracene ensures generation of H-An$^+$ with less fragmentation of the precursor in an ion source, as was shown (Figure 3.5 of experimental part) and a high yield of protonated species.

In order to support the assignment of the spectra observed, geometries of the possible isomers of protonated PAH cations were optimized and their ground-state harmonic frequencies were computed with DFT at the B3LYP / 6-311G(d,p) level of theory. Vertical excitation energies were obtained with time-dependent (TD) DFT at the same level of theory.

## 5.2 RESULTS AND DISCUSSION

### 5.2.1 PROTONATED ANTHRACENE

Deposition of $m/z$=179 cations produced from 9,10-DHAn into a neon matrix resulted in a number of moderately strong absorption systems in the visible range (Figure 5.1, trace a). Known absorptions of anthracene cation (An$^+$) in the near infrared and UV [1], and weak ones of phenanthrene cation (Ph$^+$) in the near IR [2, 3] are also present in the spectrum. The reason for this could be partial fragmentation of the H-An$^+$ cations upon deposition. Weak bands of Ph$^+$ in the near IR may likely be observed due to contamination of 9,10-DHAn with 9,10-DHPh; isomerization of H-An$^+$/An$^+$ in the ion source resulting in H-Ph$^+$/Ph$^+$ can not be ruled out.

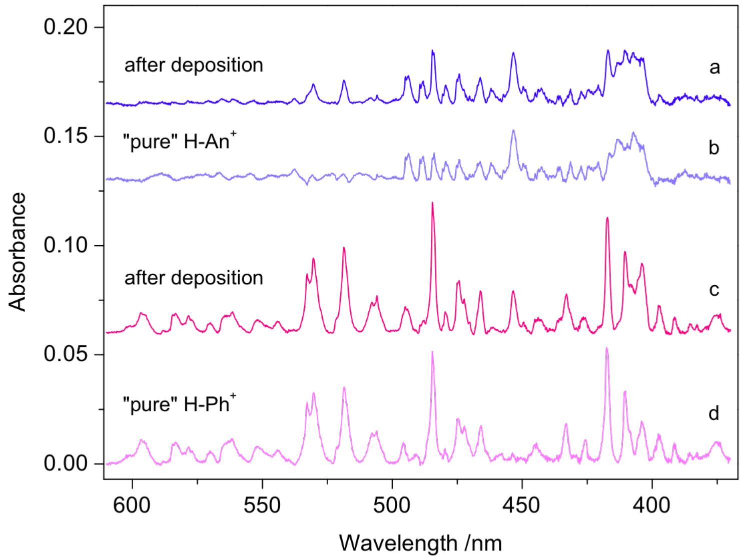

**Figure 5.1:** Electronic absorption spectra recorded in a 6 K neon matrix after deposition of *m*/*z*=179 cations produced from: a) 9,10-dihydro-anthracene and c) 9,10-dihydro-phenenthrene; b) spectrum of protonated anthracenes obtained after scaling trace c to the same intensity of the distinct absorption at 532 nm and subtracting it from trace a; d) spectrum of protonated phenanthrenes obtained after scaling trace a to the same intensity of the absorption at 453 nm and subtracting it from trace c.

In order to test whether the new absorptions seen in Figure 5.1 (trace a) are of H-An$^+$, mass-selected H-Ph$^+$ generated from 9,10-DHPh were deposited and the spectrum recorded (Figure 5.1,trace c). Comparison of the two spectra reveals some similarity. The strongest bands of H-Ph$^+$ are also seen, although weakly, in the spectrum of H-An$^+$, indicating that in the H-An$^+$ experiment H-Ph$^+$ cations were also formed; and vice versa, the H-An$^+$ are formed simultaneously with H-Ph$^+$. To separate absorptions of the two species, H-Ph$^+$ and H-An$^+$, the spectrum of the former was subtracted from that of the latter after proper scaling the spectra so, that the distinct, intense bands of H-Ph$^+$ would have the same intensity in both traces (Figure 5.1, trace b). Similarly, after proper scaling (band at 453 nm) and subtracting the H-An$^+$ spectrum from the H-Ph$^+$ one, the "pure" H-Ph$^+$ trace has been obtained (Figure 5.1, trace d).

The "pure" spectrum of H-An$^+$ is redrawn in Figure 5.2 (green). It is compared to the "raw" spectra observed when dihydro-anthracene was used as a precursor (Figure 5.2, blue) and to the one observed when anthracene/ethanol mixture was used (red). As is seen, it resembles closely the lower one, obtained in the proton transfer reaction of An with H-Eth⁺, which thus in turn shows only the H-An⁺ features. The upper spectrum contains not only the absorptions of H-An⁺, but also the bands of protonated phenanthrene (H-Ph⁺), which likely are present as a result of isomerisation in the ion source.

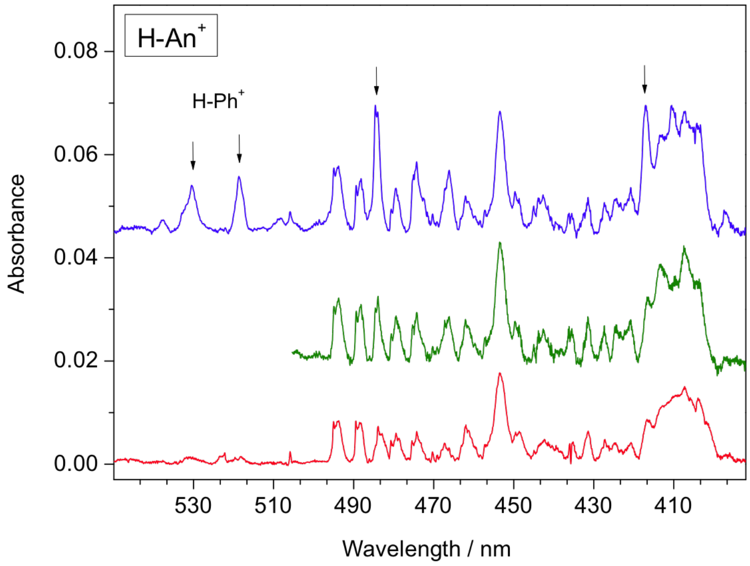

**Figure 5.2:** Electronic spectrum of $C_{14}H_{11}^+$ (m/z=179) cations produced from 9,10-dihydroanthracene as a precursor (blue) compared to the one observed in the reaction of anthracene with protonated ethanol (red). The absorption bands of protonated phenanthrene (ind. with arrows) are present in the former case as a result of isomerisation in the source under discharge conditions. The middle trace is the "clean" spectrum of protonated anthracene after correcting for the absorptions of protonated phenanthrene.

The intensities of the bands decrease after UV irradiation of the matrix, confirming its ionic origin. Three band systems are distinguished and the wavelengths of the maxima are collected in Table 5.1. The first one with onset at 493.8 nm shows a long vibrational progression. The bands constituting this system are easy to distinguish: each of them has a sharp long-wavelength shoulder, which is spaced from the maximum of the band by ~50 cm⁻¹. This is the zero phonon line, often observed in spectra of matrix-isolated species. The strong band at 453.5 nm is the origin of the second system; several weaker bands are tentatively assigned to it. The third system is a group of broad absorptions centred around 410 nm. The baseline was not corrected in this region and may contain a broad bump underneath the absorptions, which could be artificial—due to light interference upon probing the matrix.

Several decades ago H-An$^+$ was studied in strong acidic solutions [4-7] and melted salts [8, 9], and its electronic spectrum was reported. The anthracenium ion H-An$^+$ exhibits a strong, broad absorption with maximum around 410–430 nm in these environments, in the region where the broad feature observed in present matrix study. This, however, can not be compared to the neon matrix data because of the strongly perturbing media of the experiment above.

According to calculations, H-An$^+$ has tree distinct stable isomers. The lowest energy was found for the one, which has the proton attached at position 9 of anthracene (9H-An$^+$) (Figure 5.3). The other two isomers, 1H-An$^+$ and 2H-An$^+$, lie 36.4 and 49.3 kJ mol$^{-1}$ higher. All these are planar with exception of the two out-of-plane hydrogens of the aliphatic $CH_2$ group, resulting in $C_{2v}$ symmetry for 9H-An$^+$ and $C_s$ for 1H-An$^+$ and 2H-An$^+$. The values are corrected for zero-point vibrational energies. As was discussed in Chapter 3, the excess energy from the protonation of An in the reaction with $EtOH_2^+$ makes generation of all three isomers feasible.

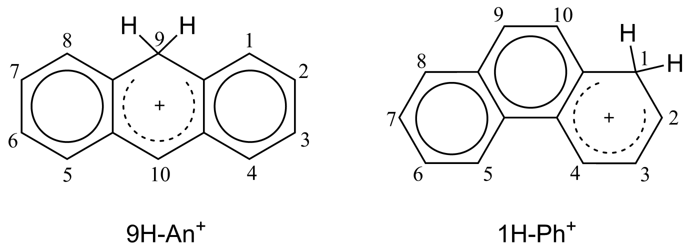

**Figure 5.3:** The lowest energy isomers of protonated anthracene and phenanthrene.

If the energetically less favourable 2H-An$^+$ is formed in the source in the reaction with $EtOH_2^+$, it may possess sufficient energy to overcome the transition state barrier, which separates this isomer from its neighbouring, more stable 1H-An$^+$ (see Chapter 3). This barrier for the 2,1-H shift of the excess proton (H-bridged transition state with the excess proton located above the molecular plane) is rather low, predicted to be ~45 kJ mol$^{-1}$ high [10], and thus, suggesting facile isomerisation towards the lower 1H-An$^+$. 1H-An$^+$ and 9H-An$^+$ isomers, in turn, are separated from each other by relatively high barriers of ~120–130 kJ mol$^{-1}$ and an intermediate “ring-fusion” isomer (Figure 3.6).

Therefore, it is anticipated that the 1H-An$^+$ and 9H-An$^+$ ones formed in the ion source will be kinetically trapped in their potential wells due to the high isomerisation barriers. If this is the case in the present study, 1H-An$^+$ and 9H-An$^+$ should be present in the matrix.

**Table 5.1** Observed band maxima (±0.1 nm) and their assignments of protonated anthracenes and their neutrals in a neon matrix.

| $\lambda_{Ne}$ / nm | $\tilde{\nu}$ / cm$^{-1}$ | $\Delta\tilde{\nu}$ / cm$^{-1}$ | Assignment |
|---|---|---|---|
| **Protonated anthracenes** | | | |
| 493.8 | 20 251 | 0 | $0_0^0$ $A\,^1\mathrm{A}_1 \leftarrow X\,^1\mathrm{A}_1$ 9H-An$^+$ |
| 488.2 | 20 483 | 232 | $\nu_{24}$ |
| 484.0 | 20 661 | 410 | $2\nu_{24}$ |
| 479.4 | 20 859 | 608 | $3\nu_{24}$ |
| 474.2 | 21 088 | 837 | $\nu_{19}$ |
| 466.1 | 21 455 | 1204 | $\nu_{15}$ |
| 462.0 | 21 645 | 1394 | $\nu_{11\text{–}12}$ |
| 448.7 | 22 286 | 2035 | $\nu_{19} + \nu_{15}$ |
| 443.7 | 22 538 | 2287 | $\nu_{19} + \nu_{11\text{–}12}$ |
| 442.7 | 22 589 | 2338 | $2\nu_{15}$ |
| 420.8 | 23 764 | 0 | $0_0^0$ $C\,^1\mathrm{B}_2 \leftarrow X\,^1\mathrm{A}_1$ |
| 416.5 | 24 010 | 246 | $\nu_{24}$ |
| 413.3 | 24 195 | 431 | $2\nu_{24}$ |
| 407.2 | 24 558 | 794 | |
| 453.5 | 22 051 | 0 | $0_0^0$ $B\,^1\mathrm{A}' \leftarrow X\,^1\mathrm{A}'$ 1H-An$^+$ |
| 431.4 | 23 180 | 1130 | $\nu_{17}$ |
| 427.4 | 23 397 | 1347 | $\nu_{12}$ |
| 424.5 | 23 557 | 1506 | $\nu_9$ |
| **Hydro-anthracenyl radical** | | | |
| 326.4 | 30 637 | 0 | $0_0^0$ H-An |
| 320.7 | 31 182 | 545 | |
| 313.2 | 31 928 | 1291 | |
| 305.7 | 32 712 | 2075 | |

a) $\tilde{\nu} = 1/\lambda_{Ne}$

Excitation energies of the three isomers of H-An$^+$ were calculated using the TD DFT method at the B3LYP/6-311G(d, p) level of theory and are given in Table 5.2. The calculated electronic excitation energies of the three H-An$^+$ isomers differ substantially. As is seen, 2H-An$^+$ isomer does not possess strong (in comparison to the more stable isomers) electronic transitions in the range of experiment. Because of this reason and energetical considerations discussed above, 2H-An$^+$ will be not considered further. The strongest transitions for the 1H-An$^+$ and 9H-An$^+$ isomers are predicted in the 3.2–3.4 eV range, close to the two systems observed at 454 and 420 nm (2.73 and 3.99 eV respectively). Their first allowed transitions, however, are predicted to occur at substantially different energies, around 650 nm (1.92 eV) for 1H-An$^+$ and 450 nm (2.78 eV) for the 9H-An$^+$, respectively. The former is much lower in energy than the first transition observed in the experiment, at 494 nm (2.51 eV) (Figure 5.2); the latter is just ~0.3 eV higher, which is a reasonable overestimate for a vertical energies (for TD DFT and similar sized molecules). Therefore, and because this is the lowest energy isomer, it is concluded that the observed absorption band system at 494 nm is due to the $A\,{}^1A_1 \leftarrow X\,{}^1A_1$ electronic transition of 9H-An$^+$. As a consequence, the broad absorption observed at ~420 nm can be attributed to its strongest, $C\,{}^1B_2 \leftarrow X\,{}^1A_1$ transition. The assignment of individual vibrational bands that form these systems is given in Table 5.1. It is based on calculated ground-state frequencies of the species considered (Table 5.3). In some cases the assignment is not unambiguous, because several modes have frequencies falling within ±30 cm$^{-1}$ of the observed ones.

The other absorption feature observed at 454 nm is tentatively assigned to the strongest, $B\,{}^1A' \leftarrow X\,{}^1A'$ electronic transition of 1H-An$^+$. According to DFT computations, the second transition of the 9H-An$^+$ isomer is within the same 3.2–3.4 eV range. Its oscillator strength is, however, two orders of magnitude lower (0.0002) than that for the first transition. Of cause, this can change with the computational method and level used, depends on the geometry change upon electronic excitation as well.

Recently, high-resolution gas-phase photodissociation spectrum of jet-cooled H-An$^+$ have been reported. The $S_1 \leftarrow S_0$ transition of protonated anthracene was observed at 491.43 nm and assigned to the 9H-An$^+$. This is in agreement with the neon matrix value of 493.8 nm. Several low-energy frequencies in the excited state have been also derived. Among them, the most intense ones at 232 (and its overtones) and 834 cm$^{-1}$ are in agreement with the peaks at 232, 837 cm$^{-1}$ (Table 1, Figure 5.2) above the origin in neon matrix, respectively.

Besides the visible absorptions of H-An$^+$ discussed above, the UV range is also relevant for these species. The 295–385 nm section of the spectrum measured after deposition of H-An$^+$ into a neon matrix is shown in Figure 5.4 (trace b).

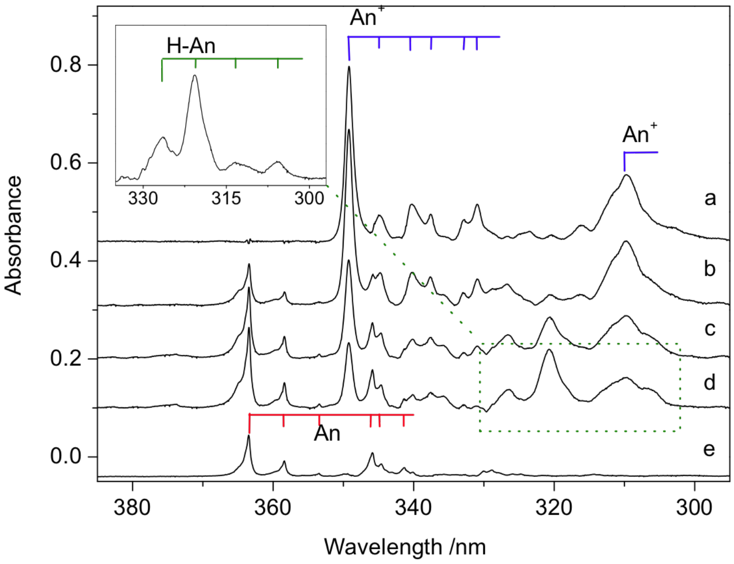

**Figure 5.4:** UV part of the absorption spectra recorded after: b) deposition of $C_{14}H_{11}^+$ cations in a 6 K neon matrix produced from 9,10-dihydro-anthracene, c) 20 min and d) subsequent 25 min irradiation with a medium-pressure Hg lamp; a) and e) are spectra of anthracene cation (An$^+$) and neutral anthracene (An) respectively. The insert shows absorption of hydro-anthracenyl radical (H-An), appearing as a result of photobleaching of the H-An$^+$ cations.

The strongest bands are the absorptions of anthracene cation (trace a) and neutral anthracene (trace e). Neutral anthracene appears in the matrix as a result of the neutralization of An$^+$. After stepwise UV irradiation of the matrix, new absorptions in the 300–340 nm range appeared and grew in intensity (traces c and d). They are shown in the insert of Figure 5.4 where the bands of An$^+$, which remained after UV irradiation, were removed. The system, which has appeared after UV photobleaching of H-An$^+$ cations, is of hydro-anthracenyl radical (H-An).

**Table 5.2** Excited state symmetries, vertical excitation energies $\Delta E_V$ and oscillator strengths $f$ for protonated anthracenes and phenanthrenes calculated with TD DFT at the B3LYP/6-311G(d,p) level of theory. Relative ground-state energies (kJ mol$^{-1}$) with respect to the most stable isomer are given in parentheses.

| Protonated Anthracenes | | | Protonated Phenanthrenes | | |
|---|---|---|---|---|---|
| Exc. state | $\Delta E_V$ / eV | $f$ | Excited state | $\Delta E_V$ / eV | $f$ |
| 9H-An$^+$, $X\,^1A_1$, $C_{2v}$ | (0) | | 1H-Ph$^+$, $X\,^1A'$, $C_s$ | (0) | |
| $^1A_1$ | 2.78 | 0.02 | $^1A'$ | 2.39 | 0.15 |
| $^1B_2$ | 3.13 | 0.0002 | $^1A'$ | 2.64 | 0.02 |
| $^1B_2$ | 3.39 | 0.5 | $^1A'$ | 3.95 | 0.2 |
| $^1B_1$ | 4.73 | 0.0003 | $^1A'$ | 4.33 | 0.005 |
| $^1A_1$ | 4.76 | 0.02 | $^1A''$ | 4.66 | 0 |
| 1H-An$^+$, $X\,^1A'$, $C_s$ | (36.4) | | 9H-Ph$^+$, $X\,^1A'$, $C_s$ | (0.6) | |
| $^1A'$ | 1.92 | 0.05 | $^1A'$ | 2.36 | 0.06 |
| $^1A'$ | 3.17 | 0.3 | $^1A'$ | 2.60 | 0.09 |
| $^1A'$ | 3.69 | 0.006 | $^1A'$ | 3.89 | 0.002 |
| $^1A'$ | 4.35 | 0.04 | $^1A'$ | 4.37 | 0.06 |
| $^1A''$ | 4.56 | 0.0003 | $^1A''$ | 4.56 | 0.0001 |
| 2H-An$^+$, $X\,^1A'$, $C_s$ | (49.3) | | 3H-Ph$^+$, $X\,^1A'$, $C_s$ | (2.4) | |
| $^1A'$ | 1.91 | 0.07 | $^1A'$ | 2.63 | 0.04 |
| $^1A'$ | 3.42 | 0.006 | $^1A'$ | 2.70 | 0.2 |
| $^1A'$ | 3.58 | 0.07 | $^1A'$ | 4.13 | 0.03 |
| $^1A'$ | 4.57 | 0.04 | $^1A'$ | 4.56 | 0.009 |
| $^1A''$ | 4.60 | 0 | $^1A'$ | 4.64 | 0.06 |
| | | | 4H-Ph$^+$, $X\,^1A'$, $C_s$ | (4.4) | |
| | | | $^1A'$ | 2.01 | 0.03 |
| | | | $^1A'$ | 2.96 | 0.2 |
| | | | $^1A'$ | 3.74 | 0.03 |
| | | | $^1A'$ | 4.43 | 0.2 |
| | | | $^1A''$ | 4.49 | 0.0002 |
| | | | 2H-Ph$^+$, $X\,^1A'$, $C_s$ | (9.0) | |
| | | | $^1A'$ | 2.24 | 0.04 |
| | | | $^1A'$ | 3.26 | 0.2 |
| | | | $^1A'$ | 3.80 | 0.03 |
| | | | $^1A''$ | 4.58 | 0 |
| | | | $^1A'$ | 4.63 | 0.5 |

According to TD DFT calculations two isomers of neutral H-An, 9H-An and 1H-An, have strong transition in the UV range around 342 and 337 nm, respectively (Fulara et al. 2010). These are close to the observed band system with onset at 326.4 nm. It is impossible to conclude from the present experimental data which H-An isomer is responsible for the absorptions in this region. It is also not excluded, that both 9H-An and 1H-An contribute to the spectrum in Figure 5.4, as the bands have a peculiar intensity distribution and may belong to two overlapping systems.

### 5.2.2. PROTONATED PHENANTHRENE

The electronic absorption spectrum obtained after mass-selective deposition of $m/z$ = 179 cations produced from 9,10-DHPh is presented in Figure 5.1 (trace c), and after removing the absorptions of H-An$^+$ in trace d. The spectrum is rich in absorption bands, which may belong to several electronic systems of several H-Ph$^+$ isomers. Several irradiation experiments were carried out on a matrix containing H-Ph$^+$ ions. These differed in wavelength domain of the UV radiation and exposure time. Spectra recorded after deposition and some irradiation steps are compared in Figure 5.5 (traces a–e). To indicate the changes in intensity of the bands, two spectra measured after different irradiation steps were subtracted from each other after normalizing them to the same intensity of the specific band (traces f and g).

The spectra in Figure 5.5 reveal several electronic band systems, which behave differently under irradiation conditions; this indicates their different origin. Eight band systems of H-Ph$^+$ could be distinguished after deposition in a neon matrix. Seven systems have ionic origin, because they decrease upon UV irradiation of the matrix with full mpHg lamp. The spectrum is redrawn in Figure 5.6 and the absorptions, which belong to the same isomer of H-Ph$^+$ (which behave in the same way), are marked with specific colour. They belong to different isomers of H-Ph$^+$.

Protonated phenanthrene has been studied in strong acidic solutions and the spectrum exhibits two broad absorptions with maxima at 410 and 520 nm [5, 7]. These electronic systems were tentatively assigned to two isomers: 1H-Ph$^+$ and 9H-Ph$^+$. The spectrum of H-Ph$^+$ in solution covers the same spectral range as in Figure 5.6. Interaction of solvent molecules with dissolved ionic species is much stronger than with neutrals. Therefore, detailed comparison of these two spectra is of no relevance, in contrast to the neutral hydro-phenanthrenyl radical.

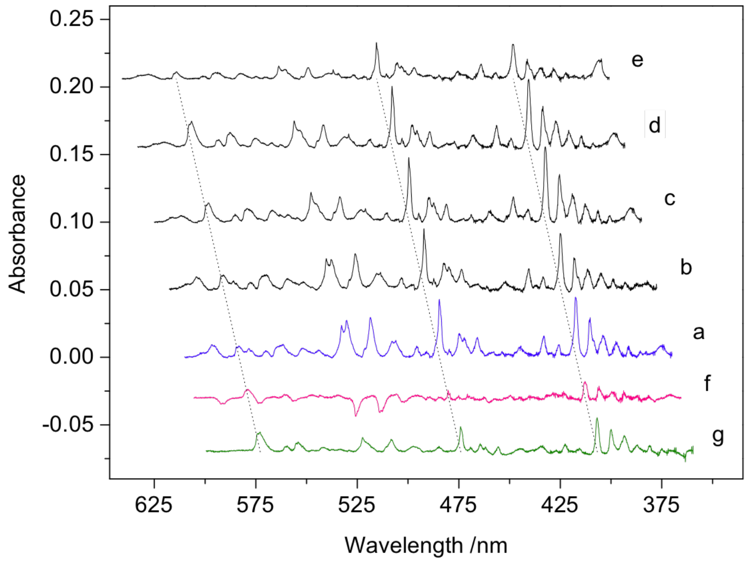

**Figure 5.5:** Absorption spectra recorded after deposition of $C_{14}H_{11}^+$ cations in a 6 K neon matrix produced from 9,10-dihydro-phenanthrene after: a) deposition, b) exposure to the UV radiation of a high-pressure Xe lamp during measurement, c) 30 min and d) additional 30 min photobleaching with $390 > \lambda > 250$ nm, e) subsequent 20 min irradiation with a full medium-pressure Hg lamp; f) = c − a and g) = d − e show changes in the intensities of bands following the irradiation steps.

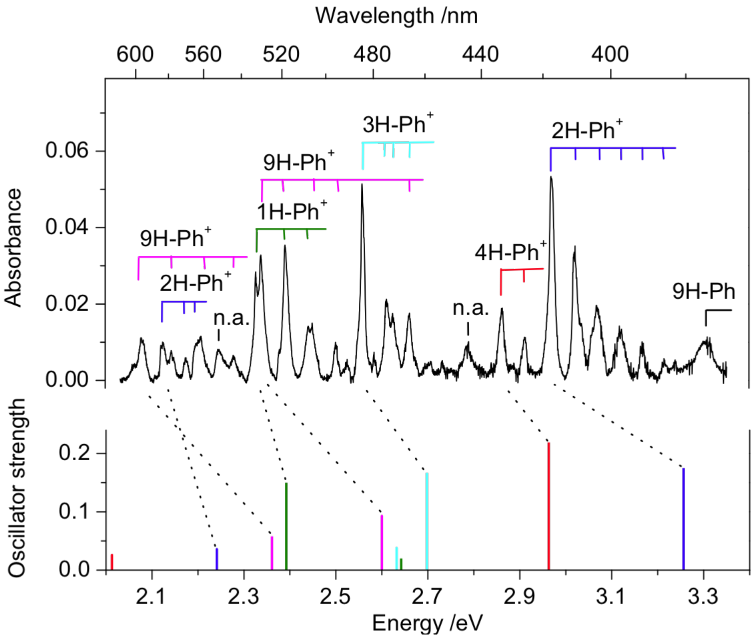

**Figure 5.6:** Electronic absorption spectrum of protonated phenanthrenes compared to the excitation energies of the five considered isomers (stick spectrum), calculated with TD DFT at the B3LYP/6-311G(d,p) level of theory. n.a.—not assigned bands.

All considered isomers, 1H-, 2H-, 3H-, 4H- and 9H-Ph$^+$, have similar electronic ground-state energies spanning only 9 kJ mol$^{-1}$ (Table 5.2). The calculations predict 1H-Ph$^+$ to be the most stable isomer; 9H-Ph$^+$, however, is only by 0.6 kJ mol$^{-1}$ higher. The highest in energy was found to be 2H-Ph$^+$, located 9 kJ mol$^{-1}$ above 1H-Ph$^+$. Because the energy difference of the five isomers is so small, their relative order may change with the level of calculations.

Vertical excitation energies and their oscillator strengths of the five H-Ph$^+$ isomers are collected in Table 5.2 and displayed in Figure 5.6. All H-Ph$^+$ isomers have two allowed electronic transitions in the visible, where the absorptions of protonated phenanthrenes have been detected. As is seen from Figure 5.6, the number of H-Ph$^+$ isomers, their relative energies and density of their electronic transitions in this range complicate the assignment. The only possible assignment of the absorption systems to specific isomers is done by comparing the excitation energy of its strongest transition with the onset of the nearest system (Table 5.3). Individual bands of a given system are assigned using calculated vibrational frequencies of the H-Ph$^+$ isomers in their ground state.

Only one of eight systems increase in intensity after prolonged irradiation with a mpHg lamp (Figure 5.5, trace e) and is, therefore, of neutral nature. It is a single band with an origin at 375 nm. Most likely it is the hydro-phenanthrenyl radical (H-Ph), which appears in the matrix as a result of the neutralization of H-Ph$^+$ cations. The most stable neutral fragment (phenanthrene molecule), which could be formed from the H-Ph$^+$ ions, can be excluded as carrier of this band, because it absorbs at shorter wavelengths [3] and its systems were also detected in this experiment.

In the past, 9-hydro-phenanthrenyl radical (9H-Ph) was studied in organic solutions. It was produced by hydrogen subtraction from 9,10-DHPh [11] or by hydrogen addition to phenanthrene [12, 13] following pulse radiolysis. The spectrum consists of a broad band with maximum at 395 nm. This is not too far from the observed absorption at 375 nm for the neutral product in the present experiment. Therefore, the absorption is assigned to the 9H-Ph radical.

**Table 5.3** Observed band maxima (±0.1 nm) and their assignments of protonated phenanthrenes and their neutrals in a neon matrix.

| $\lambda_{Ne}$ / nm | $\tilde{\nu}$ $^{a)}$ / cm$^{-1}$ | $\Delta\tilde{\nu}$ /cm$^{-1}$ | Assignment |
|---|---|---|---|
| **H-Phenanthrene$^+$** | | | |
| 596.6 | 16 762 | 0 | $0_0^0$ $(1)^1A' \leftarrow X\,^1A'$ 9H-Ph$^+$ |
| 578.2 | 17 295 | 533 | $\nu_{42}$ |
| 561.4 | 17 813 | 1051 | $2\nu_{42}$ |
| 543.7 | 18 392 | 1631 | $\nu_{12}$ |
| 530.3 | 18 857 | 0 | $0_0^0$ $(2)^1A' \leftarrow X\,^1A'$ 9H-Ph$^+$ |
| 518.6 | 19 283 | 425 | $\nu_{44}$ |
| 506.1 | 19 759 | 902 | $\nu_{36}$ or $\nu_{37}$ |
| 495.5 | 20 182 | 1324 | $\nu_{22\text{-}24}$ |
| 465.9 | 21 464 | 2607 | $2\nu_{22\text{-}24}$ |
| 583.3 | 17 144 | 0 | $0_0^0$ $(1)^1A' \leftarrow X\,^1A'$ 2H-Ph$^+$ |
| 570.1 | 17 541 | 397 | $\nu_{45}$ |
| 564.7 | 17 709 | 565 | $\nu_{41}$ |
| 417.4 | 23 958 | 0 | $0_0^0$ $(2)\ A' \leftarrow X\,^1A'$ 2H-Ph$^+$ |
| 410.5 | 24 361 | 403 | $\nu_{44}$ |
| 404.0 | 24 752 | 795 | $2\nu_{44}$ |
| 397.4 | 25 164 | 1206 | $3\nu_{44}$ |
| 391.3 | 25 556 | 1598 | $4\nu_{44}$ |
| 385.5 | 25 940 | 1983 | $5\nu_{44}$ |
| 532.8 | 18 769 | 0 | $0_0^0$ $(1)^1A' \leftarrow X\,^1A'$ 1H-Ph$^+$ |
| 518.6 | 19 283 | 514 | $\nu_{42}$ |
| 507.9 | 19 689 | 920 | $\nu_{36}$ |
| 484.5 | 20 640 | 0 | $0_0^0$ $(2)^1A' \leftarrow X\,^1A'$ 3H-Ph$^+$ |
| 474.6 | 21 070 | 431 | $\nu_{44}$ |
| 472.3 | 21 173 | 533 | $\nu_{42}$ |
| 465.9 | 21 464 | 824 | $2\nu_{44}$ |
| 433.1 | 23 089 | 0 | $0_0^0$ $(2)^1A' \leftarrow X\,^1A'$ 4H-Ph$^+$ |
| 425.8 | 23 485 | 396 | $\nu_{45}$ |
| 551.8 | 18 123 | not assigned | |
| 444.7 | 22 487 | not assigned | |
| **H-Phenanthrene** | | | |
| 375.1 | 26 660 | 0 | $0_0^0$ 9H-Ph |

a) $\tilde{\nu} = 1/\lambda_{Ne}$

## 5.3 RELEVANCE OF H-AN$^+$ AND H-PH$^+$ TO DIBS

Protonated aromatic hydrocarbons are important constituents of the interstellar medium. It has been considered that these species could be carriers of some DIBs [14, 15]. Time-dependent (TD) DFT calculations reveal that some such cations could have strong transitions in the visible domain, where DIBs are detected [16]. They might be responsible also for unidentified infrared emission bands related to the aromatic C–C stretching at 6.2 μm and aliphatic C-H modes of $CH_2$ group observed as a shoulder near the strong aromatic 3.3 μm IR emission band [17]. They may play a catalytic role for the synthesis of $H_2$ [18-20], which likely proceeds in the following steps. The first is formation of H-PAH$^+$ in a reaction of PAH$^+$ with H, followed by attachment of a second H atom to produce $H_2$-PAH$^+$. The latter dissociates leading to $H_2$, and PAH$^+$ is recovered. Protonated PAHs can be formed in the interstellar medium also in ion-molecule reactions of hydrogen-deficient PAH$^+$ cations with $H_2$, of atomic hydrogen with PAH$^+$ or neutral PAHs with highly abundant $H_3^+$. The mechanisms mentioned above assume the presence of PAH$^+$ ions in the ISM; therefore their astrophysical relevance should also be discussed too.

The present spectroscopic studies on protonated anthracene and phenanthrene allow a direct comparison of their transition intensities with the ones of the An$^+$ and Ph$^+$ cations. The near infrared electronic transitions of An$^+$ and Ph$^+$ are by an order of magnitude stronger than the visible absorptions of the protonated species.

The electronic transition of Ph$^+$ in a neon matrix [3] and gas phase, as the Ph$^+$–Ar complex [2], has been already reported. The position of all bands reported [3] agrees well with our studies however the relative intensities of the band systems are different. In the present mass-selective experiment besides Ph$^+$ neutral phenanthrene has also been detected in the UV range. The oscillator strength of the near infrared band system of Ph$^+$ was evaluated to be 0.25 by measuring the change of the intensity of cationic and neutral phenanthrene induced by the UV irradiation of the matrix, and using the experimental oscillator strength of the latter [21]. This value is about four orders of magnitude higher than that reported [3], but is close to the gas-phase value (0.15±0.05) [2]. High oscillator strength of the near infrared transition of $Ph^+$ confined mainly to the origin band at 892 nm makes it favorable for the search of this band in the ISM. $An^+$, similarly to $Ph^+$, has a strong electronic transition in the near infrared region with the onset around 709 nm and about 5 times stronger system around 349 nm (in a Ne matrix), the latter one can be used for a sensitive detection of $An^+$ in the ISM.

The results of the present spectroscopic study on protonated anthracene and phenanthrene isolated in neon matrices reveal that their electronic transitions fall in the 400–550 nm range, where a number of broad DIBs are found [22, 23]. Several isomers of these species have been detected; they have moderately intense absorption systems. The isomers do not differ much in energy. In the case of protonated phenanthrene all five isomers have energies within 9 kJ mol$^{-1}$ of each other. If H-$Ph^+$ is formed in the reaction of neutral phenanthrene with $H_3^+$ in the ISM, then these five isomers should be about equally populated, but their column density in a specific line of sight would be lower than for $Ph^+$. The lower oscillator strength of the visible transition of protonated phenanthrenes in comparison with the near infrared one of $Ph^+$, together with lower concentration of the former resulting from the population of several isoenergetic isomers, could hamper their optical detection in the ISM. Similar arguments apply to the detection of H-$An^+$. More promising are the protonated PAHs which form fewer isomers (e.g. coronene) and if they have a larger oscillator strength.

## BIBLIOGRAPHY

[1] J. Szczepanski, M. Vala, D. Talbi, O. Parisel, Y. Ellinger. Electronic and vibrational spectra of matrix isolated anthracene radical cations: Experimental and theoretical aspects. *J. Chem. Phys.,* 98 (1993) 4494-4511.

[2] P. Brechignac, T. Pino. Electronic spectra of cold gas phase PAH cations: Towards the identification of the Diffuse Interstellar Bands carriers. *Astron. Astrophys.,* 343 (1999) L49-L52.

[3] F. Salama, C. Joblin, L.J. Allamandola. Electronic absorption spectroscopy of matrix-isolated polycyclic aromatic hydrocarbon cations. 2. The phenanthrene cation ($C_{14}H_{10}^+$) and its 1-methyl derivative. *J. Chem. Phys.,* 101 (1994) 10252-10262.

[4] W.I. Aalbersberg, G.J. Hoijtink, E.L. Mackor, W.P. Weijland. The formation of hydrocarbon positive ions in strong proton donors. *J. Chem. Soc.,* (1959) 3049-3054.

[5] G. Dallinga, E.L. Mackor, A.A.V. Stuart. The absorption spectra of aromatic carbonium ions in HF solution. *Mol. Phys.,* 1 (1958) 123-140.

[6] V. Gold, F.L. Tye. The basicity of hydrocarbons. 2. Ultraviolet absorption spectra of conjugated hydrocarbons in sulphuric acid solution *J. Chem. Soc.,* (1952) 2172-2180.

[7] C. Reid. The aromatic carbonium ions. *J. Am. Chem. Soc.,* 76 (1954) 3264-3268.

[8] M. Brigodiot, J.M. Lebas. Infrared spectrum of anthracenium cation. *J. Mol. Struct.,* 32 (1976) 311-323.

[9] S.P. Zingg, A.S. Dworkin, M. Sorlie, D.M. Chapman, A.C. Buchanan, G.P. Smith. Reactivity of anthracene in liquid $SbCl_3$-$AlCl_3$-N-(1-butyl)pyridinium chloride mixtures. *J. Electrochem. Soc.,* 131 (1984) 1602-1608.

[10] V. Kapinus. Photophysical properties of protonated aromatic hydrocarbons. *Ph.D Thesis*, California Institute of Technology, 2005.

[11] H. Koizumi, S. Fukamura, T. Ichikawa, H. Yoshida, J. Kubo. Radical formation in pulse radiolysis of organic solutions of 9,10-dihydrophenanthrene. *Radiat. Phys. Chem.,* 50 (1997) 567-573.

[12] J. Grodkowski, P. Neta, J.F. Wishart. Pulse radiolysis study of the reactions of hydrogen atoms in the ionic liquid methyltributylammonium bis[(trifluoromethyl)-sulfonyl]imide. *J. Phys. Chem. A,* 107 (2003) 9794-9799.

[13] T. Kawakubo. Optical and EPR studies of radiation-induced radicals in phenanthrene single crystals. *Mol. Cryst. Liq. Cryst.,* 62 (1980) 41-58.

[14] E. Herbst, V. Le Page. Do H atoms stick to PAH cations in the interstellar medium? *Astron. Astrophys.,* 344 (1999) 310-316.

[15] V. Le Page, Y. Keheyan, V.M. Bierbaum, T.P. Snow. Chemical constraints on organic cations in the interstellar medium. *J. Am. Chem. Soc.,* 119 (1997) 8373-8374.

[16] A. Pathak, P.J. Sarre. Protonated PAHs as carriers of diffuse interstellar bands. *Mon. Not. Roy. Astron. Soc.,* 391 (2008) L10-L14.

[17] D.M. Hudgins, C.W. Bauschlicher, L.J. Allamandola. Closed-shell polycyclic aromatic hydrocarbon cations: a new category of interstellar polycyclic aromatic hydrocarbons. *Spectrochim. Acta, Part A,* 57 (2001) 907-930.

[18] C.W. Bauschlicher. The reaction of polycyclic aromatic hydrocarbon cations with hydrogen atoms: The astrophysical implications. *Astrophys. J.,* 509 (1998) L125-L127.

[19] M. Hirama, T. Ishida, J.I. Aihara. Possible molecular hydrogen formation mediated by the radical cations of anthracene and pyrene. *J. Comput. Chem.,* 24 (2003) 1378-1382.

[20] M. Hirama, T. Tokosumi, T. Ishida, J. Aihara. Possible molecular hydrogen formation mediated by the inner and outer carbon atoms of typical PAH cations. *Chem. Phys.,* 305 (2004) 307-316.

[21] E. Clar, Polycyclic Hydrocarbons, New York: Academic Press, 1964.

[22] P. Jenniskens, F.-X. Desert. A survey of diffuse interstellar bands (3800–8680 A). *Astron. Astrophys. Suppl. Ser.,* (1994) 39-78.

[23] L.M. Hobbs, D.G. York, T.P. Snow, T. Oka, J.A. Thorburn, M. Bishof, S.D. Friedman, B.J. McCall, B. Rachford, P. Sonnentrucker, D.E. Welty. A catalog of Diffuse Interstellar bands in the spectrum of HD 204827. *Astrophys. J.,* 680 (2008) 1256.

# CHAPTER 6

# PROTONATED PYRENE AND CORONENE: ABSORPTION AND FLUORESCENCE

Protonated pyrene and coronene have been isolated in 6 K neon matrices. Three electronic transitions of the most stable isomer of protonated pyrene and four of protonated coronene were recorded. The strongest, $S_1 \leftarrow S_0$ transitions, are in the visible region, with onset at 487.5 nm for protonated pyrene and 695.6 nm for protonated coronene. The corresponding neutrals were also characterized. The absorptions were assigned on the basis of *ab initio* coupled-cluster and time-dependent DFT calculations. Their fluorescence spectra in solid neon were also observed. Laser excitation of the $S_n \leftarrow S_0$ transitions of the cations resulted in an extended, vibrationally-resolved $S_1 \rightarrow S_0$ fluorescence with onset at 487.8 and 695.4 nm for protonated pyrene and coronene, respectively. The astrophysical relevance of protonated polycyclic aromatic hydrocarbons is discussed.

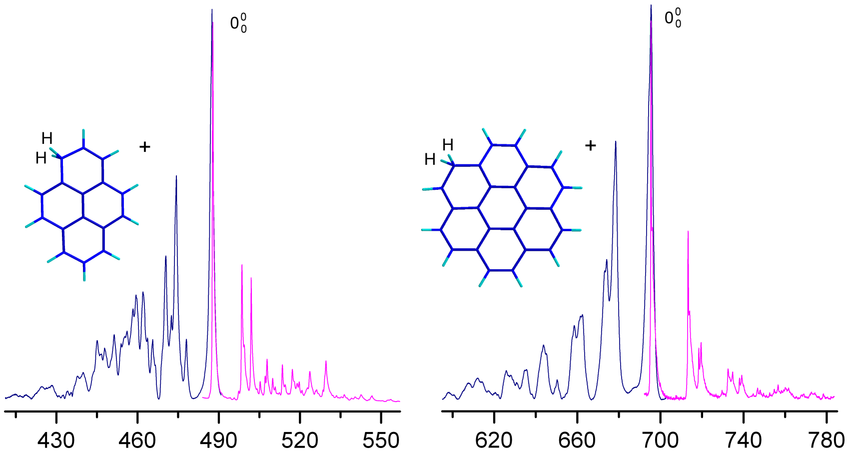

*Electronic absorption spectra of protonated pyrene and coronene in neon matrices*
Iryna Garkusha, Jan Fulara, Peter J. Sarre, John P. Maier
*J. Phys. Chem. A*, 115(40), 10972–10978, 2011.

*Fluorescence of protonated pyrene and coronene in neon matrices*
Iryna Garkusha, Jan Fulara, John P. Maier
*J. Mol. Struct.*, **1025**, 147–150, 2012

## 6.1 INTRODUCTION

Pyrene and coronene are prototypical PAH molecules. They are often considered as astrophysical models for studying their formation mechanisms, reactions with astrophysically relevant molecules and atoms, or their possible role as the synthesis of $H_2$ in the ISM. Recently, their protonated counterparts (H-PAH$^+$s) became the topic of quantum-chemical as well as experimental interest because of their role as possible carriers of unidentified infrared emission bands (UIRs) [1] and diffuse interstellar bands (DIBs) [2-4]. Protonated coronene is the largest molecule so far studied in the IR region in gas phase. Its IR multiphoton dissociation spectrum resembles to some extent astronomical UIR features [5].

Electronic transitions of protonated pyrene and coronene, calculated recently with TD DFT, should give rise to strong absorption features in the DIB region [4]. Electronic transitions of a number of protonated PAHs have been studied in strong acidic solutions, however, they are strongly perturbed by the liquid environment. Among them is also protonated pyrene (H-Py$^+$), for which two broad electronic absorption bands were observed at around 475 and 380 nm [6-8]. No electronic spectra of H-Cor$^+$ have been found in the literature.

In this chapter, electronic absorption and fluorescence spectra of prototypical H-PAH species, namely H-Py$^+$ and H-Cor$^+$, and their neutral radical counterparts, H-Py and H-Cor, isolated in 6 K neon matrices are presented. The experimental set-up used has been described. H-Py$^+$ and H-Cor$^+$ were produced in a hot cathode discharge source in a proton transfer reaction (PT) between protonated ethanol (EthOH$_2^+$) and an appropriate aromatic hydrocarbon. Pyrene and coronene samples were resistively heated to get an appropriate vapour pressure. The ion current achieved for H-PAH$^+$s was in the range 5–20 nA, and resulted in a total accumulated charge of ~42 μC for H-Py$^+$ and ~60 μC for H-Cor$^+$.

## 6.2 PROTONATED PYRENE

### 6.2.1 ABSORPTION

The electronic spectrum of $m/z$ = 203 cations produced in the reaction of Py with EtOH$_2^+$ and deposited in a neon matrix is dominated by two absorption features located at 487 and 389 nm (Figure 6.1, blue line). Besides these, the strongest known bands of $Py^+$ and Py are weakly seen in the spectrum at 360 and 323 nm, respectively [9, 10].

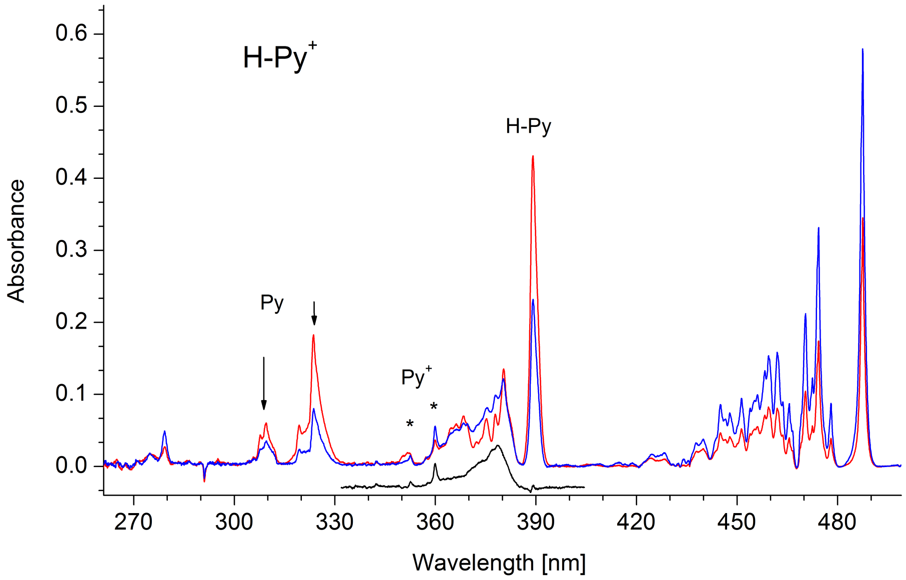

**Figure 6.1:** Absorption spectra recorded after deposition of $C_{16}H_{11}^+$ ($m/z = 203$) cations into a neon matrix (blue) and after photobleaching with UV photons (red). Weak bands of neutral pyrene and its radical cation are indicated with arrows and asterisks, respectively. The black, bottom trace shows weak absorption of protonated pyrene, obtained after scaling the red trace to the intensity of the absorption at 389 nm and subtracting it from the blue one.

After irradiation of the matrix with a medium-pressure Hg lamp, the 487 nm system decreases and the other at 389 nm gains intensity (Figure 6.1, red line). The known bands of $Py^+$ behave in the same manner—they decrease in intensity after irradiation and give rise to the absorptions of Py. No new bands appear in the spectrum. Upon irradiation, the trapped cations are neutralized by electrons, which are released from an electron scavenger present in the matrix. These are $Cl^-$ anions, formed when $CH_3Cl$ molecules capture electrons released during deposition [11]. Thus, the 487 nm system is due to $H\text{-}Py^+$ and the one at 389 nm belongs to the corresponding neutral H-Py radical. The two systems are characterized by strong, sharp origin bands followed by similar, complex vibrational structures showing excitations in the same vibrational fundamentals. For instance, the 570/591 and 747/762 $cm^{-1}$ modes are active in the excited states of $H\text{-}Py^+$ and its neutral, respectively. Wavelengths of the maxima of the observed bands are given in Table 6.1.

**Table 6.1** Absorption band maxima (±0.1 nm) observed for the electronic transitions of protonated pyrene and corresponding neutral in a neon matrix and the calculated vertical excitation energies $\Delta E_V$ (**bold** – MP2/CC2/cc-pVDZ, *italics* – TD DFT/BLYP/TZVP). Relative integrated intensities of observed systems are given in parentheses.

| $\lambda$ / nm | $\Delta E_V$ / eV | $\tilde{\nu}$ $^{a)}$ / cm$^{-1}$ | $\Delta\tilde{\nu}$ / cm$^{-1}$ | Assignment $^{b)}$ | |
|---|---|---|---|---|---|
| **1H-Py$^+$** | | | | | |
| 487.5 (1) | **2.80 /** *2.61* | 20 513 | 0 | $0^0_0$ | (1)$^1$A′←$X$ $^1$A′ |
| 478.0 | | 20 919 | 406 | 406 | |
| 474.3 | | 21 083 | 570 | 570 | |
| 472.5 | | 21 165 | 652 | 652 | |
| 470.4 | | 21 260 | 747 | 747 | |
| 466.6 | | 21 432 | 919 | 919 | |
| 465.6 | | 21 478 | 965 | 570+406 | |
| 463.6 | | 21 568 | 1055 | 1055 | |
| 462.1 | | 21 639 | 1126 | 2×570 | |
| 459.5 | | 21 761 | 1248 | 570+652 | |
| 458.3 | | 21 819 | 1306 | 570+747 | |
| 456.1 | | 21 925 | 1412 | | |
| 455.0 | | 21 979 | 1466 | | |
| 453.9 | **3.03** / *2.77* | 22 032 | 1519 | | (2)$^1$A′←$X$ $^1$A′ |
| 451.3 | | 22 157 | 1644 | 3×570 | |
| 447.8 | | 22 333 | 1820 | | |
| 445.0 | | 22 470 | 1957 | | |
| 439.9 | | 22 735 | 2222 | | |
| 437.7 | | 22 848 | 2335 | | |
| 428.3 | | 23 347 | 2834 | | |
| 424.4 | | 23 560 | 3047 | | |
| 378.6 (0.21) | **3.53 /** *3.21* | 26 414 | | $0^0_0$ | (3)$^1$A′←$X$ $^1$A′ |
| 279.2 (0.068) | **4.46 /** *4.41* | 35 812 | 0 | $0^0_0$ | (4)$^1$A′←$X$ $^1$A′ |
| 274.7 | | 36 406 | 594 | 594 | |
| **1H-Py** | | | | | |
| 389.1 | **3.85** | 25 702 | 0 | $0^0_0$ | (4)$^2$A′←$X$ $^2$A″ |
| 380.3 | | 26 293 | 591 | 591 | |
| 377.9 | | 26 464 | 762 | 762 | |
| 375.2 | | 26 653 | 951 | 951 | |
| 372.1 | | 26 871 | 1169 | 2×591 or 1169 | |
| 368.4 | | 27 147 | 1445 | 1445 | |
| 366.2 | | 27 310 | 1608 | 951+591 or 1608 | |
| 364.5 | | 27 435 | 1733 | 951+762 | |

$^{a)}$ $\tilde{\nu} = 1/\lambda_{Ne}$. $^{b)}$ Vibrational assignment is based on the a′ modes in the electronic ground state of 1H-Py$^+$ and corresponding neutral obtained with DFT/BLYP/cc-pVDZ: 445, 578, 667, 779, 925 and 1071 cm$^{-1}$ for 1H-Py$^+$; 574, 775, 968, 1181, 1452 and 1615 cm$^{-1}$ for 1H-Py.

Two other bands of cationic origin are also assigned to H-Py$^+$. The first one is a weak system originating at 279 nm (Figure 6.1). The second is a band hidden by the strong 389 nm absorption of H-Py. It is seen better when the spectrum recorded after irradiation is subtracted from the one recorded after deposition, scaled to the intensity of the strong 389 nm peak. It is the broad band centered at 378 nm (Figure 6.1, black trace). In the past, H-Py$^+$ has been studied in strong acidic solutions [6, 7] and in H$^+$-zeolites [8]. Two broad electronic absorption bands of H-Py$^+$ were observed at around 475 and 380 nm. The wavelengths of these absorptions are close to the ones observed presently.

Pyrene has three non-equivalent protonation sites located at carbon atoms 1, 2 and 4 (Scheme 6.1). In order to assign the observed absorptions of H-Py$^+$ to a specific isomer theoretical calculations are needed. The ground state energies of these isomers have been computed with the *ab initio* RI-MP2 method using the cc-pVDZ basis set. Additionally, RI-DFT calculations [12] with the BLYP [13, 14] functional and the TZVP basis set [15] have been carried out on the H-Py$^+$ isomers.

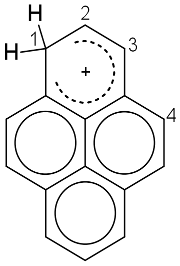

**Scheme 6.1:** Lowest energy isomer of protonated pyrene.

The relative energies obtained with the two methods are similar (Table 6.2). The lowest energy isomer is 1H-Py$^+$ ($C_s$ symmetry, $^1A'$ ground state). The other two, 4H-Py$^+$ and 2H-Py$^+$, are predicted to be 45 and 67 kJ mol$^{-1}$ higher in energy according to the calculations at the MP2 level. Thus, the excess energy of ~120 kJ mol$^{-1}$, which is the difference of the PAs of the two reactants in the reaction of Py with EtOH2+$^+$, is sufficient to give rise to any of these isomers.

Vertical excitation energies have been determined for all three isomers with CC2/cc-pVDZ and TD DFT/BLYP/TZVP; the results are compared in Table 6.2. The TD DFT method gives the electronic transitions of the H-Py$^+$ isomers ~0.3 eV higher in energy than CC2. Small differences in the oscillator strengths are seen, but the general pattern is similar.

**Table 6.2** Excited state symmetries, vertical excitation energies and oscillator strengths for protonated pyrenes obtained with TD DFT at the BLYP/TZVP level of theory and with the MP2/CC2 method and the cc-pVDZ basis set. Relative ground-state energies (kJ mol$^{-1}$) with respect to the most stable isomer are given in parentheses.

| TD DFT/BLYP/TZVP | | | MP2/CC2/cc-pVDZ | | |
|---|---|---|---|---|---|
| Exc. state | $\Delta E_V$ / eV | $f$ | Exc. state | $\Delta E_V$ / eV | $f$ |
| 1H-Py$^+$, $X\,^1$A′, $C_s$ (0) | | | (0) | | |
| $^1$A′ | 2.61 | 0.04 | $^1$A′ | 2.8 | 0.18 |
| $^1$A′ | 2.77 | 0.20 | $^1$A′ | 3.03 | 0.21 |
| $^1$A′ | 3.21 | 0.08 | $^1$A′ | 3.53 | 0.16 |
| $^1$A′ | 3.79 | 0.001 | $^1$A′ | 4.46 | 0.02 |
| $^1$A′ | 4.41 | 0.01 | $^1$A′ | 5.12 | 0.03 |
| $^1$A′ | 4.71 | 0.01 | $^1$A′ | 5.18 | 0.02 |
| 4H-Py$^+$, $X\,^1$A′, $C_s$ (43.3) | | | (44.8) | | |
| $^1$A′ | 1.40 | 0.02 | $^1$A′ | 1.87 | 0.05 |
| $^1$A′ | 2.24 | 0.06 | $^1$A′ | 2.53 | 0.11 |
| $^1$A′ | 2.97 | 0.005 | $^1$A′ | 3.62 | 0.002 |
| $^1$A′ | 3.58 | 0.01 | $^1$A′ | 4.22 | 0.01 |
| $^1$A′ | | | $^1$A′ | 4.44 | 0.07 |
| | | | $^1$A′ | 4.61 | 0.19 |
| 2H-Py$^+$, $X\,^1$A$_1$, $C_{2v}$ (57.2) | | | (66.8) | | |
| $^1$B$_2$ | 1.8 | 0.04 | $^1$B$_2$ | 2.02 | 0.07 |
| $^1$A$_1$ | 2.81 | 0.004 | $^1$A$_1$ | 3.19 | 0.04 |
| $^1$A$_1$ | 2.82 | 0.001 | $^1$A$_1$ | 3.48 | 0.0001 |
| $^1$B$_2$ | 3.64 | 0.03 | $^1$B$_2$ | 4.11 | 0.03 |
| $^1$A$_1$ | 3.94 | 0.63 | $^1$A$_1$ | 4.40 | 0.96 |
| $^1$B$_2$ | 3.96 | 0.006 | $^1$B$_2$ | 4.67 | 0.006 |
| $^1$B$_2$ | 4.24 | 0.01 | $^1$B$_2$ | 4.98 | 0.04 |
| $^1$B$_2$ | 4.26 | 0.02 | $^1$A$_1$ | 5.40 | 0.34 |
| $^1$A$_1$ | 4.56 | 0.04 | | | |
| $^1$A$_1$ | 4.83 | 0.12 | | | |

The electronic excitation energies of the three H-Py$^+$ isomers differ substantially. The three strongest transitions for the most stable isomer 1H-Py$^+$ obtained by the CC2 method are predicted in the 2.8–3.5 eV range, close to the two systems observed at 487 and 378 nm (2.54 and 3.27 eV respectively). The other two isomers are predicted to absorb strongly in the UV; furthermore, their first allowed transitions are at around 680–620 nm (1.8–2.0 eV). These are much lower in energy than the first transition assigned here to H-Py$^+$. Therefore and because this is the lowest energy isomer, it is concluded that the observed absorption bands are due to 1H-Py$^+$.

The lowest energy transition of 1H-Py$^+$ is predicted at 475 nm (2.61 eV) by TD DFT and at 443 nm (2.80 eV) by the CC2 method. Thus, the 487 nm absorption system is attributed to the $(1)^1A' \leftarrow X\,^1A'$ transition of 1H-Py$^+$. The CC2 calculations overestimate its energy by 0.25 eV (Table 6.2). Taking such a shift into account, the observed system at 378 nm is assigned to the $(3)^1A' \leftarrow X\,^1A'$ transition of this isomer. Both the CC2 and the TD DFT methods predict an additional absorption system of 1H-Py$^+$ around 440–450 nm (~2.8 eV) due to the $(2)^1A' \leftarrow X\,^1A'$ transition. As is seen from Figure 6.1, there is a congestion of vibrational bands of the $(1)^1A' \leftarrow X\,^1A'$ system in this region. It is difficult to conclude from the present experimental data whether there is an additional electronic absorption band in this range. The highest energy electronic transition observed at 279 nm is due to the $(4)^1A' \leftarrow X\,^1A'$ excitation of the same isomer. Tentative assignment of the vibrational bands of the systems is based on the harmonic ground-state frequencies of 1H-Py$^+$ calculated with DFT/BLYP/cc-pVDZ, that are given in Table 6.1 as footnote.

The strong absorption at 389 nm is of the neutral 1H-Py radical. According to CC2 calculations, 1H-Py has three weak transitions in the 410–350 nm (3–3.5 eV) range (all with oscillator strengths $f$~0.002) followed by a strong one at around 330 nm (3.85 eV) with $f$~0.28. This is not far from the observed band system. No other bands have been detected in the experiment. 1H-Py has been detected using laser- and flash-photolysis of Py and dihydro-pyrene in amines solutions [16] and by VUV photolysis of Py in CO matrices [17]. The spectra reported show three broad bands starting at around 400 nm. An oscillator strength of ~0.09 for this transition has been derived [17]; it is about 3 times lower than the one predicted by the present calculations. It was possible to estimate the $f$ value of the strongest absorption of 1H-Py$^+$ at 487 nm by adopting the reported one for the 1H-Py radical [17]. This was done by evaluating the integrated intensity change of 1H-Py$^+$ and its neutral absorptions that resulted from UV irradiation. The value obtained is

0.13, if it is assumed that no other process except neutralization is involved. This is close to 0.17 predicted by the CC2 method.

### 6.2.2 FLUORESCENCE

Experiments have also been carried out to detect fluorescence of H-Py$^+$. Laser excitation of any absorption band in the 487.5 nm system of 1H-Py$^+$ (top panel of Figure 6.2) induces fluorescence in the 488–550 nm region. The vibrationally-resolved spectrum obtained after excitation into the 470.4 nm absorption band is shown in Figure 6.2 (magenta trace). Weak features seen above 530 nm are reproducible and they extend to 560 nm. The long-wavelength edge of the absorption overlaps with the short-wavelength one of the fluorescence at 487.5 nm and is the zero-phonon line of the origin band of the $S_1$ ($^1A'$) ← $S_0$ ($^1A'$) transition of 1H-Py$^+$.

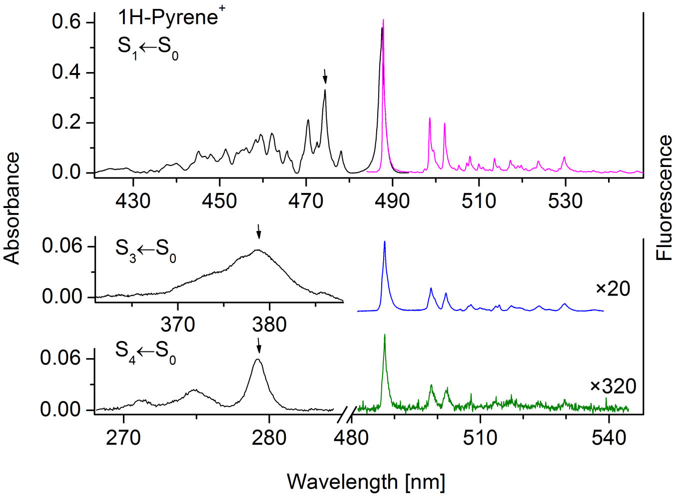

**Figure 6.2**: Electronic absorption (left) and fluorescence (right) spectra of protonated pyrene (1H-Py$^+$ isomer) in a neon matrix. The fluorescence was observed upon laser excitation at the wavelengths indicated with arrows.

A weaker emission was observed following the excitation of two other electronic transitions of 1H-Py$^+$: $S_3$ ← $S_0$ at 378.6 nm and $S_4$ ← $S_0$ at 274.7 nm. The spectra are shown, together with the respective absorptions, in the middle and bottom panels of Figure 6.2. Structured emission has been detected in each case, though a broad absorption band has been excited (middle trace). The position of the bands and their relative intensities in the fluorescence spectra are identical with the ones recorded upon excitation of the first electronic transition of 1H-Py$^+$. The present florescence study confirms our earlier assignment that two UV absorption systems with onsets at 378.6 nm and at 274.7 nm belong to the same molecule as the 487.5 nm one, namely 1H-Py$^+$.

Because the strongest fluorescence band coincides with the origin band of the first absorption system and no other peak has been detected at the shorter wavelength, the emission seen in Figure 6.2 is the transition from the zero vibrational level of the (1) $^1$A' excited state of 1H-Py$^+$ to vibrationally excited levels in the $X$ $^1$A' ground state. A fast internal conversion of the higher electronic states to the (1) $^1$A' state and vibrational relaxation takes place prior to the emission, a common behavior of large molecules.

The positions of the most prominent bands derived from the fluorescence spectrum of 1H-Py$^+$ are collected in Table 6.3. The strongest fluorescence band is the onset of the electronic transition. Two other peaks spaced from the origin by 442 and 579 cm$^{-1}$ dominate the emission. Their overtones and combinations are also apparent. In order to assign the transitions, calculations of the frequencies of the normal modes of 1H-Py$^+$ using density functional theory (DFT) with the B3LYP functional and the cc-pVDZ basis set were carried out. The cation has 50 totally symmetric normal modes (a' symmetry), which can be active in the fluorescence. The calculated frequencies are given in the footnote of Table 6.3 and are compared, after scaling by 0.98, with the observed ones. The modes of energy above 3000 cm$^{-1}$ are not included, because no fluorescence bands were detected in the corresponding region. The agreement between the calculated and the observed frequencies, particularly for the lowest-energy modes, is good. Somewhat less certain is the assignment of the bands with ground state frequencies > 1000 cm$^{-1}$ due to a congestion of normal modes in this region.

Recently, infrared transitions of a number of protonated polycyclic hydrocarbon cations have been studied in the gas-phase by infrared multiphoton disscociation spectroscopy (IRMPD) by observing H-atom or $H_2$ loss [5, 18]. Protonated pyrene was also among them, with four strong broad bands in the 1100–1600 cm$^{-1}$ range and two weaker ones below 1100 cm$^{-1}$. The observed IR peaks are broad (~30 cm$^{-1}$) mainly due to the multiphoton character of the IRMPD process. In the neon matrix the resolution of the fluorescence bands of 1H-Py$^+$ was around 5 cm$^{-1}$ and more than 20 normal modes are identified in the spectrum. This then provides a large set of vibrational frequencies of 1H-Py$^+$ in its electronic ground state. The neon matrix to gas phase shift should not be larger than 16 cm$^{-1}$ (1% of the transition energy) for the modes below 1600 cm$^{-1}$ [19, 20].

**Table 6.3** Band maxima (±0.1 nm) of the (1) $^1$A' → $X\,^1$A' fluorescence of protonated pyrene, 1-HPy$^+$, in a 6 K neon matrix. Intensity is indicated as strong or medium (all others are weak).

| $\lambda_{\mathrm{Ne}}$ / nm | $\tilde{\nu}$ [a] / cm$^{-1}$ | $\Delta\tilde{\nu}$ / cm$^{-1}$ | a' (calc.) | Assignment [b] |
|---|---|---|---|---|
| 487.8 s | 20 499 | 0 | | $0_0^0$ (1) $^1$A' → $X\,^1$A' |
| 494.3 | 20 229 | 270 | | |
| 495.7 | 20 172 | 327 | 343 | $\nu_{50}$ |
| 497.4 | 20 105 | 394 | 400 | $\nu_{49}$ |
| 498.6 s | 20 057 | 442 | 448 | $\nu_{48}$ |
| 499.4 m | 20 023 | 476 | 486 | $\nu_{47}$ |
| 502.0 s | 19 920 | 579 | 586 | $\nu_{44}$ |
| 504.2 | 19 833 | 666 | 674 | $\nu_{43}$ |
| 505.3 | 19 789 | 710 | 718 | $\nu_{42}$ |
| 507.2 | 19 718 | 781 | 787 | $\nu_{41}$ |
| 507.9 m | 19 691 | 808 | 813 | $\nu_{40}$ |
| 509.9 m | 19 611 | 888 | | $2\nu_{48}$ |
| 510.9 | 19 574 | 925 | 937 | $\nu_{39}$ |
| 513.6 m | 19 472 | 1027 | | $\nu_{48} + \nu_{44}$ |
| 514.6 | 19 433 | 1066 | | $\nu_{47} + \nu_{44}$ |
| 517.2 m | 19 334 | 1165 | 1169 | $\nu_{32}$ or $2\nu_{44}$ |
| 519.0 m | 19 269 | 1230 | 1224 | $\nu_{29}$ |
| 519.7 m | 19 241 | 1258 | 1244 | $\nu_{27}$ |
| 520.8 | 19 201 | 1298 | | |
| 522.8 | 19 127 | 1372 | 1379 | $\nu_{23}$ |
| 523.7 m | 19 095 | 1404 | 1409 | $\nu_{21}$ |
| 525.8 | 19 019 | 1480 | 1490 | $\nu_{17}$ |
| 526.2 | 19 005 | 1494 | 1507 | $\nu_{16}$ |
| 528.5 | 18 920 | 1579 | 1578 | $\nu_{14}$ |
| 529.3 | 18 893 | 1606 | 1593 | $\nu_{13}$ |
| 529.7 m | 18 880 | 1619 | 1620 | $\nu_{12}$ |
| 536.4 | 18 644 | 1855 | | |
| 542.7 | 18 426 | 2073 | | |
| 546.8 | 18 287 | 2212 | | |

[a] $\tilde{\nu} = 1/\lambda_{Ne}$

[b] Vibrational assignment is based on *a'* modes (cm$^{-1}$) of 1H-Py$^+$ in its electronic ground state: 343, 400, 448, 486, 492, 526, 586, 674, 718, 787, 813, 937, 968, 991, 1083, 1119, 1137, 1153, 1169, 1183, 1197, 1224, 1234, 1244, 1317, 1332, 1359, 1379, 1395, 1409, 1421, 1427, 1450, 1490, 1507, 1547, 1578, 1593, 1620, 1642, 2935, 3127, 3129, 3130, 3131, 3135, 3142, 3145, 3147, 3157 computed with DFT/B3LYP/cc-pVDZ (scaled by 0.98).

## 6.3 PROTONATED CORONENE

### 6.3.1 ABSORPTION

Deposition of $m/z = 301$ cations produced in the reaction of Cor with EtOH2+⁺ into a neon matrix resulted in two strong electronic systems in the visible originating at 695 and 560 nm (Figure 6.3, blue trace). They are of cationic origin because they lose intensity after irradiation with UV photons (Figure 6.3, red line). Besides these, known transitions of $Cor^+$ are seen throughout the measured region starting from ~950 nm [21]. Its electronic spectrum has been measured anew for a direct comparison. Approximately, every fourth Cor molecule contains one $^{13}C$ atom and contributes to the intensity of the $m/z = 301$ peak in the mass spectrum. Fragmentation *via* H loss is the lowest dissociation channel for all smaller H-PAHs⁺ [5] except protonated benzene [22], (where the $H_2$ loss is dominant), and may also be true for Cor. Additionally, the mass resolution for H-$Cor^+$ was worse than for the lighter ions.

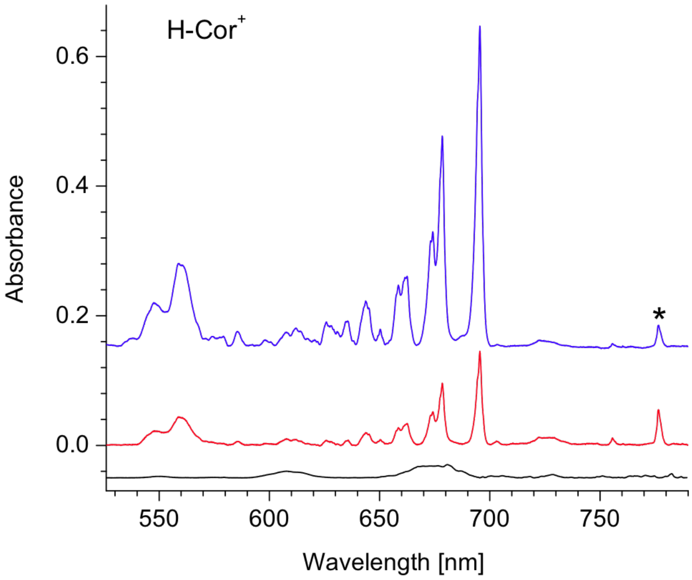

**Figure 6.3:** Long-wavelength part of the electronic absorption spectra recorded after deposition of $C_{24}H_{13}^+$ ($m/z = 301$) cations produced in the reaction of coronene with protonated ethanol into a neon matrix (blue) and after UV irradiation of the matrix (red). The bottom, black trace shows absorptions of coronene cation.

In the spectral range shown in Figure 6.3, $Cor^+$ has two broad, weak bands at 680 and 616 nm (Figure 6.3, black trace). The spectrum is scaled to match the intensity of the distinct bands in the range 800–950 nm of $Cor^+$ that is present in the matrix together with H-$Cor^+$. The $Cor^+$ absorptions are too weak to contribute to the strong bands mentioned above. Therefore, the absorption systems of Figure 6.3 at 695 and 560 nm are of H-$Cor^+$. The first shows a long progression in the ~360 and 457 $cm^{-1}$ modes and their combination bands. Each of the bands has a higher energy shoulder spaced from the sharper maximum by ~24 $cm^{-1}$. The latter are zero-phonon bands followed by side bands, often observed in matrix spectra. The second system consists of three broad bands spaced by ca. 370 $cm^{-1}$. Wavelengths of the observed bands are given in Table 6.4.

The short-wavelength part of the spectrum contains a number of overlapping systems of cationic and neutral species (Figure 6.4, green trace). It is dominated by a strong band at 470 nm, which is due to a neutral because it grows after UV irradiation. $Cor^+$ is also seen in this region; its absorption is hidden underneath the strong one of a neutral. A part of the $Cor^+$ spectrum is shown as black trace in Figure 6.4, normalized to the same intensity as described. The blue trace was recorded after deposition of H-$Cor^+$ and subtraction of the bands of $Cor^+$, thus representing part of the “pure” spectrum of H-$Cor^+$ and the neutral H-Cor. The same procedure was applied for the spectrum recorded after UV irradiation of the matrix (Figure 6.4, red trace). The band centred at 447 nm is lower in intensity after photobleaching and therefore corresponds to the third transition of H-$Cor^+$. It is obscured by the strong absorption system originating at 470 nm, and can be seen better after scaling and subtracting the spectrum recorded after deposition from the one after irradiation (inset of Figure 6.4). Additionally, a weak absorption of H-$Cor^+$ was detected in the UV at 346 nm. It is not shown because of the presence of bands of neutral and cationic coronene in its vicinity.

The system with origin at 470 nm and a broad one centred at 401 nm (Figure 6.4) are of neutral origin. In addition, a weak vibronic system at 776 nm was detected. These belong to H-Cor, which is formed by neutralization of H-$Cor^+$ upon UV irradiation of the matrix. The bands do not coincide with known absorptions of neutral Cor, which could also be formed under such conditions.

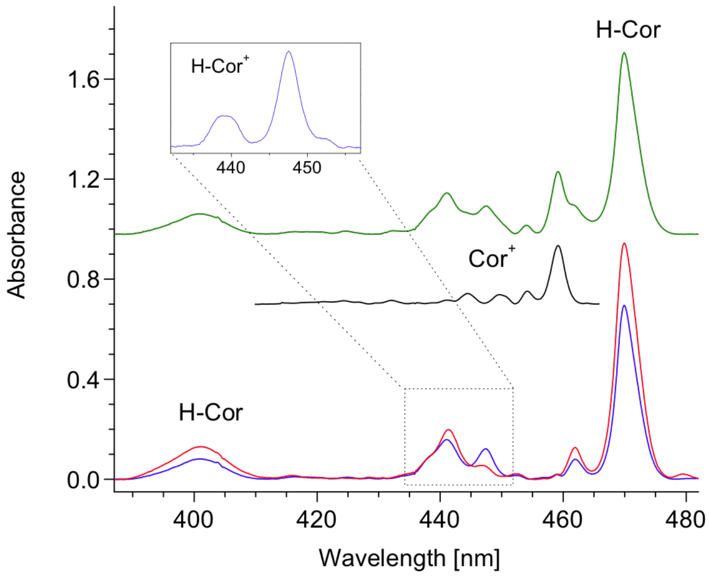

**Figure 6.4:** Short-wavelength part of the electronic absorption spectrum recorded after deposition of $C_{24}H_{13}^+$ ($m/z = 301$) cations into a neon matrix (green trace). Spectral features due to protonated coronene, corresponding neutral radical and coronene cation are present. The blue and red traces were observed on deposition and after photobleaching, respectively, and after subtracting the absorption bands of coronene cation (black trace). The $(3)^1A' \leftarrow X\ ^1A'$ transition of protonated coronene is shown in the inset, obtained after downscaling the red trace to the intensity of the absorption at 469 nm on the blue one and subtracting from it.

To support the assignment of the observed electronic transitions of H-Cor$^+$ and H-Cor, excitation energies have been calculated using two approaches. All the protonation sites of Cor are equivalent taking only the periphery of the carbon skeleton into account; therefore, only one isomer of H-Cor$^+$ and of its neutral counterpart was considered. The geometry has been optimized at the RI-MP2/def2-SVP and DFT/BLYP/TZVP level of theory. CC2 with the def2-SVP basis set [23] and TD DFT at BLYP/TZVP level have been applied to calculate the excitation energies. The computational results are given in Table 6.4.

As is seen, CC2 calculations overestimate the excitation energies for H-Cor$^+$ by around 0.2 eV, whereas the TD DFT method underestimates them by ~0.15 eV. The assignment of the observed transitions of H-Cor$^+$ in a neon matrix is based on theoretical predictions and is given in Table 6.4. Less accurate are the calculated intensities. The oscillator strength of the first electronic transition of H-Cor$^+$ is 0.11, whereas the second one is predicted to be stronger with $f$~0.18 according to the CC2 calculations (Table 6.4).

TD DFT gives the *f* values for these transitions of 0.04 and 0.1 respectively. Similar intensities for electronic transitions of H-Cor$^+$ were obtained when calculated with TD DFT using same BLYP functional in conjunction with the 6-311G** basis set [4]. Hence, they do not strongly depend on the method and the basis set used. The strongest observed absorption system is assigned to the $(1)^1A' \leftarrow X\,^1A'$ transition observed at 695 nm, followed by the ~2 times weaker one at 560 nm.

Excitation energies of H-Cor have been calculated using MP2/CC2/def2-SVP. Its strongest electronic transition $(3)^2A' \leftarrow X\,^2A''$ is predicted around 365 nm (3.4 eV; $f \sim 0.23$), higher by 0.8 eV from the observed one. The lowest electronic excitation is calculated to occur at 443 nm (2.8 eV) and is two orders of magnitude less intense. Its energy is 1.2 eV higher than the band system observed at 776 nm and the integrated intensity is about 50 times less than that of the 469 nm system. The calculated excitation energies for H-Cor show less good agreement with the observations than for H-Cor$^+$. This is not surprising due to the open-shell electronic structure of H-Cor. The computational results are given in Table 6.4 along with the assignment of the observed electronic bands. The vibrational assignment is based on the computed harmonic frequencies in the $^2A''$ ground state of H-Cor.

**Table 6.4** Observed band maxima (±0.1 nm) and their assignments for protonated coronene and the corresponding neutral coronenyl radical in a neon matrix, and the calculated vertical excitation energies $\Delta E_V$

| λ / nm | $\Delta E_V$ / eV | $\tilde{\nu}$ [a)] / $cm^{-1}$ | $\Delta\tilde{\nu}$ / $cm^{-1}$ | Assignment | |
|---|---|---|---|---|---|
| **H-Cor$^+$** | | | | | |
| 695.6 (1) | **2.0 /** 1.70 | 14377 | 0 | $0_0^0$ | $(1)^1A'\leftarrow X\ ^1A'$ |
| 678.5 | | 14738 | 361 | 361 | |
| 674.1 | | 14834 | 457 | 457 | |
| 662.5 | | 15095 | 718 | 2 × 361 | |
| 658.5 | | 15186 | 809 | 457 + 361 | |
| 650.2 | | 15379 | 1002 | 3 × 361 | |
| 645.2 | | 15499 | 1122 | 457 + 2 × 361 | |
| 643.7 | | 15534 | 1157 | | |
| 638.4 | | 15664 | 1287 | 4 × 361 | |
| 635.6 | | 15732 | 1355 | 1355 | |
| 630.8 | | 15854 | 1477 | 457 + 3 × 361 | |
| 628.1 | | 15921 | 1544 | | |
| 625.7 | | 15981 | 1604 | | |
| 614.3 | | 16280 | 1903 | | |
| 611.8 | | 16344 | 1967 | | |
| 607.5 | | 16462 | 2085 | | |
| 585.5 | | 17078 | 2701 | 2 × 1355 | |
| 559.8 (0.56) | **2.41 /** 2.11 | 17865 | 0 | $0_0^0$ | $(2)^1A'\leftarrow X\ ^1A'$ |
| 548.4 | | 18235 | 370 | 370 | |
| 537.4 | | 18607 | 742 | 2 × 370 | |
| 447.6 (0.22) | **3.03 /** 2.62 | 22341 | 0 | $0_0^0$ | $(3)^1A'\leftarrow X\ ^1A'$ |
| 439.1 | | 22773 | 432 | | |
| 346.3 (0.29) | **3.79 /** 3.14 | 28876 | 0 | $0_0^0$ | $(5)^1A'\leftarrow X\ ^1A'$ |
| **H-Cor** | | | | | |
| 776.5 (0.02) | **2.78** | 12878 | 0 | $0_0^0$ | $(1)^2A'\leftarrow X\ ^2A''$ |
| 755.6 | | 13235 | 357 | | |
| 479.3 (1) | **3.44** | 20863w | | | |
| 469.9 | | 21279 | 0 | $0_0^0$ | $(3)^2A'\leftarrow X\ ^2A''$ |
| 462.0 | | 21646 | 367 | 367 | |
| 447.1 | | 22367 | 1088 | | |
| 441.3 | | 22661 | 1382 | | |
| 401.2 (0.37) | **3.72** | 24928 | 0 | $0_0^0$ | $(5)^2A'\leftarrow X\ ^2A''$ |

[a)] $\tilde{\nu} = 1/\lambda_{Ne}$

### 6.3.2 FLUORESCENCE

Laser excitation into any absorption band of the $S_1 \leftarrow S_0$ electronic system of H-Cor$^+$ results in emission in the near infrared. The fluorescence spectrum obtained after excitation at 678.5 nm, where a strong absorption band next to the origin is located, is shown in top panel of Figure 6.5 together with the respective absorptions.

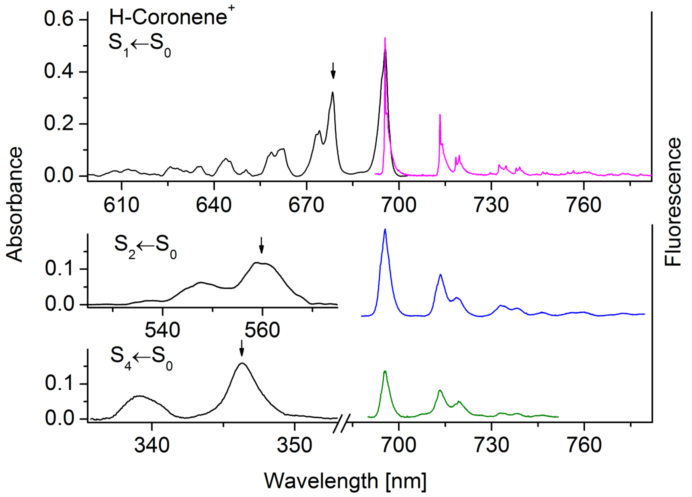

**Figure 6.5:** Electronic absorption (left) and fluorescence (right) spectra of protonated coronene in a neon matrix. The fluorescence was observed upon laser excitation at the wavelengths indicated with arrows.

The spectrum is characterized by a well resolved vibrational structure which is a mirror image of the absorption system. The strongest band is the origin and it partially overlaps with the onset of the absorptions. Almost equally strong emission was detected once the onsets of the $S_n \leftarrow S_0$ (n=2–4) transitions have been excited. The resulting fluorescence spectra are shown in bottom panel of Figure 6.5. The fluorescence observed upon excitation to the $S_n$ states of H-Cor$^+$ indicates that the main relaxation channel is internal conversion to $S_1$. In the case of 1H-Py$^+$ the intensity of the fluorescence decreases with the excitation to the higher electronic states ($S_3$, $S_4$) which subsequently decay nonradiatively to $S_0$ faster than to $S_1$.

Several fundamental vibrations have been derived from the fluorescence spectrum of H-Cor$^+$ and are gathered in Table 6.5. The assignment of the vibrations given there is based on the calculated frequencies of the normal modes using the DFT method with

B3LYP functional and cc-pVDZ basis set. The agreement between the observed frequencies and calculated ones after scaling by 0.98 is a quite good. The assignment in the 1000–1250 cm$^{-1}$ range is tentative, because there are many calculated modes in this range with frequencies within 20–30 cm$^{-1}$ of the observed values.

Protonated coronene has also been studied in the gas phase by the IRMPD method [5]. The obtained spectrum is composed of several broad bands, as was the case with 1H-Py$^{+}$. Not all vibrations observed in the gas phase have counterparts in the fluorescence spectrum of H-Cor$^{+}$. For some of the modes the difference between the gas-phase and neon matrix is as large as 30 cm$^{-1}$. The frequencies in the gas phase, due to the broadness of the peaks in the spectrum, were determined with a large error. On the other hand the neon matrix fluorescence data bear a random shift in comparison to the gas-phase values.

**Table 6.5** Band maxima (±0.1 nm) and the vibrational assignment of the (1) $^1$A' → $X$ $^1$A' fluorescence of protonated coronene, H-Cor$^{+}$, in a 6 K neon matrix.

| $\lambda_{Ne}$ / nm | $\tilde{\nu}$ / cm$^{-1}$ a) | $\Delta\tilde{\nu}$ / cm$^{-1}$ | a′ (calc) | Assignment b) |
|---|---|---|---|---|
| 695.4 | 14 381 | 0 | | $0_0^0$ (1) $^1$A′ → $X$ $^1$A′ |
| 713.4 | 14 018 | 363 | 357 / 360 | $\nu_{70}$ [or $\nu_{69}$] |
| 718.5 | 13 918 | 463 | 462 | $\nu_{66}$ |
| 719.5 | 13 898 | 483 | 484 / 484 | $\nu_{64}$ [or $\nu_{63}$] |
| 729.6 | 13 707 | 674 | 670 /671 | $\nu_{59}$ [or $\nu_{58}$] |
| 732.4 | 13 654 | 727 | | $2\nu_{70/69}$ |
| 734.5 | 13 615 | 766 | 761 | $\nu_{56}$ |
| 737.9 | 13 552 | 829 | | $\nu_{70/69}+\nu_{66}$ |
| 738.9 | 13 533 | 848 | | $\nu_{70/69}+\nu_{64/63}$ |
| 746.8 | 13 390 | 991 | 977 /980 | $\nu_{52/51}$ |
| 748.1 | 13 368 | 1013 | 1006 | $\nu_{50}$ |
| 752.6 | 13 288 | 1093 | | $3\nu_{70/69}$ |
| 754.4 | 13 255 | 1126 | 1129 | $\nu_{48}$ |
| 756.3 | 13 222 | 1159 | 1153 | $\nu_{44}$ |
| 759.7 | 13 163 | 1218 | 1215 | $\nu_{41}$ |
| 761.3 | 13 135 | 1246 | 1243 | $\nu_{37}$ |
| 768.0 | 13 021 | 1360 | 1355 | $2\nu_{59/58}$ or $\nu_{32}$ |
| 772.6 | 12 943 | 1438 | 1441 | $\nu_{25}$ |
| 774.1 | 12 919 | 1462 | 1464 | $4\nu_{70/69}$ or $\nu_{23}$ |
| 778.1 | 12 852 | 1529 | 1526 | $\nu_{20}$ |
| 783.9 | 12 756 | 1625 | 1624 /1636 | $\nu_{14/13}$ |

a) $\tilde{\nu}$ =1/ $\lambda_{Ne}$ b) Vibrational assignment is based on the a' modes in the electronic ground state of protonated coronene obtained with DFT/B3LYP/cc-pVDZ (scaled by 0.98): 357, 360, 371, 377, 462, 473, 484, 484, 546, 620, 658, 670, 671, 751, 761, 788, 807, 911, 977, 980, 1006, 1062, 1129, 1140, 1144, 1148, 1153, 1186, 1200, 1215, 1222, 1226, 1229, 1243, 1306, 1313, 1318, 1355, 1365, 1378, 1388, 1397, 1404, 1418, 1425, 1441, 1459, 1464, 1484, 1518, 1526, 1543, 1561, 1593, 1610, 1618, 1624, 1636 cm$^{-1}$.

## 6.4 ASTRONOMICAL COMPARISON

Coronene and pyrene are often considered as a model of PAHs in the discussions of their role in the ISM. One of the motivations for this study was to explore whether electronic transitions of protonated PAHs are relevant to the diffuse interstellar absorption bands (DIBs). First discussed as a possibility over ten years ago [2, 3, 24], this has been studied recently through TD DFT calculations of electronic transitions of H-Cor$^+$ and protonated ovalene [4]. An interesting characteristic of H-PAH$^+$s is the existence of allowed electronic transitions in the visible part of the spectrum where most of the DIBs are found. Protonated PAHs are not unique in this respect as large PAH neutrals, radicals, radical cations and anions can also possess bands falling in the general region of DIBs. This has been illustrated in the experiments reported here and in other studies [25]. Nevertheless, H-PAH$^+$s are generally closed-shell molecules which makes them good candidates from the perspective of interstellar chemistry.

The present neon matrix data provide an improved basis for comparison with astronomical spectra, although one that still falls far short of the required laboratory gas-phase spectra. Based on the behaviour of small systems and comparison with a range of similar molecules for which both, gas-phase and matrix values are available [19, 20], it is anticipated that the wavenumbers for the gas-phase transitions of H-PAH$^+$ systems will lie within 200 cm$^{-1}$ of the neon matrix values, while the band separations deduced from the vibrational band structure should be about two orders of magnitude better.

Taking first H-Cor$^+$, there is a strong, narrow electronic transition at 695.6 nm with extended vibrational band structure and weaker, broader ones at 559.8 nm and 447.6 nm. For H-Cor$^+$ to be considered as a DIB candidate, there must be a reasonable correspondence in wavelength, overall spectral pattern and relative band intensity between laboratory and astronomical data. From the matrix measurements, it is expected that the origin band of the $(1)^1A' \leftarrow X\,^1A'$ transition will fall in the ~685–705 nm range. Examination of published diffuse band data for, *e.g.*, HD 183143 and HD 204827 [26, 27] shows that the most prominent narrow unidentified absorption within this range is the λ6993 DIB, which has an asymmetric profile [26]. Using the measured spectral intervals listed in Table 7.3, the strongest additional gas-phase bands of the $(1)^1A' \leftarrow X\,^1A'$ system would then be expected in the region of 682.1, 677.7, 665.9 and 661.9 nm, where the first listed should have an intensity around 2/3 of the origin band. We are not able to identify DIBs that satisfy these criteria; the situation is made particularly complicated because of the high number of narrow DIBs falling in the 670–690 nm region. Given the uncertainties in predicting gas-phase transition wavenumbers and the high DIB density in this region, the chances of an accidental "match" are high.

For H-Py$^+$, the origin band of the $(1)^1\mathrm{A}'\leftarrow X\,^1\mathrm{A}'$ system falls at 487.5 nm in the neon matrix, and so likely between 483 and 493 nm in the gas phase; only one DIB in HD 183143 falls within this range ($\lambda$4882 with a FWHM of ~1.1 nm); a search for the next two bands in the series reveals no candidates. In HD 204827 weaker narrower DIB candidates fall within the wavelength range of interest but do not have plausible features at higher frequency.

Another point of this study was the relevance of protonated PAHs to the UIRs. According to one hypothesis, protonated PAHs can be the carriers of the UIR bands observed in emission from many astronomical objects [1]. Another hypothesis states that above a certain size the protonated PAHs "lose identity" and their IR spectra are similar and closely resemble UIRs [18]. Therefore experimental data on the vibrations of protonated pyrene and coronene are desirable.

The wavelength-dispersed fluorescence spectra of protonated pyrene and coronene isolated in 6 K neon matrices provide a better set of vibrational frequencies in the ground state than the IRMPD spectra recorded in the gas phase. In order to compare the vibrations of these two cations their fluorescence spectra are plotted on a wavenumber scale with their origins shifted to the same position (Figure 6.6). The spectra differ particularly in the low frequency range, where two bands dominate. These originate from an in-plane deformation of the PAH skeleton. Higher frequencies are observed for these vibrations in the case of 1H-Py$^+$. They are 442 and 579 cm$^{-1}$, the latter is the ring-breathing mode. In the case of H-Cor$^+$ the lowest frequency vibrations lie at 363 and 483 cm$^{-1}$ and the latter is the ring-breathing mode.

The fluorescence spectra of 1H-Py$^+$ and H-Cor$^+$ measured experimentally are compared with the positions of UIR bands marked with vertical broken lines in Figure 6.6. The vibration around 1620 cm$^{-1}$ is observed for both cations and it coincides with the 6.2 µm UIR band. Though the fluorescence spectra provide frequencies of many normal modes of the cations, the intensities derived from these spectra can differ from those, measured with IRMPD technique in the middle infrared region. In the former case they reflect the geometry change upon electronic excitation of the cation and depend on the Franck-Condon factors. In the IRMPD spectra these are dependent on the multiphoton and the action character of the method used.

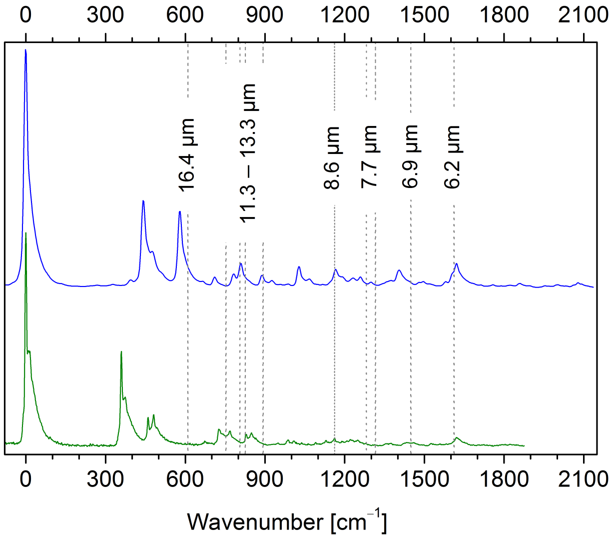

**Figure 6.6:** Comparison of the vibrational frequencies derived from the fluorescence spectra of protonated pyrene (blue) and protonated coronene (green) in neon matrices. The origin bands are shifted to the same position. The spectral positions of several UIR bands are indicated with dashed lines.

And the last point is the electronic relaxation of PAHs. UIR bands are assumed to result from the electronic excitation of PAHs$^+$ and/or H-PAHs$^+$ by UV light of the nearby stars. The cations subsequently decay nonradiatively to high vibrational levels of the electronic ground state, which relax radiatively in the IR and may cause the UIR bands. The present studies show, however, that protonated PAHs (1H-Py$^+$, H-Cor$^+$) once electronically excited decay radiatively.

## BIBLIOGRAPHY

[1] D.M. Hudgins, C.W. Bauschlicher, L.J. Allamandola. Closed-shell polycyclic aromatic hydrocarbon cations: a new category of interstellar polycyclic aromatic hydrocarbons. *Spectrochim. Acta, Part A,* 57 (2001) 907-930.

[2] V. Le Page, Y. Keheyan, V.M. Bierbaum, T.P. Snow. Chemical constraints on organic cations in the interstellar medium. *J. Am. Chem. Soc.,* 119 (1997) 8373-8374.

[3] T.P. Snow, V. Le Page, Y. Keheyan, V.M. Bierbaum. The interstellar chemistry of PAH cations. *Nature,* 391 (1998) 259-260.

[4] A. Pathak, P.J. Sarre. Protonated PAHs as carriers of diffuse interstellar bands. *Mon. Not. Roy. Astron. Soc.,* 391 (2008) L10-L14.

[5] H. Knorke, J. Langer, J. Oomens, O. Dopfer. Infrared spectra of isolated protonated polycyclic aromatic hydrocarbon molecules. *Astrophys. J. Lett.,* 706 (2009) L66-L70.

[6] G. Dallinga, E.L. Mackor, A.A.V. Stuart. The absorption spectra of aromatic carbonium ions in HF solution. *Mol. Phys.,* 1 (1958) 123-140.

[7] C. Reid. The aromatic carbonium ions. *J. Am. Chem. Soc.,* 76 (1954) 3264-3268.

[8] X.S. Liu, K.K. Iu, J.K. Thomas, H.Y. He, J. Klinowski. Spectroscopic studies of protonated aromatic species and radical cations in $H^+$-zeolites. *J. Am. Chem. Soc.,* 116 (1994) 11811-11818.

[9] F. Salama, L.J. Allamandola. Neutral and ionized polycyclic aromatic hydrocarbons, diffuse interstellar bands and the ultraviolet extinction curve. *J. Chem. Soc., Faraday Trans.,* 89 (1993) 2277-2284.

[10] M. Vala, J. Szczepanski, F. Pauzat, O. Parisel, D. Talbi, Y. Ellinger. Electronic and vibrational spectra of matrix-isolated pyrene radical cations: Theoretical and experimental aspects. *J. Phys. Chem.,* 98 (1994) 9187-9196.

[11] J. Fulara, A. Nagy, I. Garkusha, J.P. Maier. Higher energy electronic transitions of $HC_{2n+1}H^+$ (n=2-7) and $HC_{2n+1}H$ (n=4-7) in neon matrices. *J. Chem. Phys.,* 133 (2010) 024304.

[12] M. Sierka, A. Hogekamp, R. Ahlrichs. Fast evaluation of the Coulomb potential for electron densities using multipole accelerated resolution of identity approximation. *J. Chem. Phys.,* 118 (2003) 9136-9148.

[13] A.D. Becke. Density-functional exchange-energy approximation with correct asymptotic behavior. *Phys. Review A,* 38 (1988) 3098.

[14] C. Lee, W. Yang, R.G. Parr. Development of the Colle-Salvetti correlation-energy formula into a functional of the electron density. *Phys. Review B,* 37 (1988) 785.

[15] A. Schäfer, C. Huber, R. Ahlrichs. Fully optimized contracted Gaussian basis sets of triple zeta valence quality for atoms Li to Kr. *J. Chem. Phys.,* 100 (1994) 5829-5835.

[16] T. Okada, T. Mori, N. Mataga. Hydrogen atom transfer in the quenching of pyrene fluorescence by amines. *Bull. Chem. Soc. Japan,* 49 (1976) 3398-3402.

[17] J. Bouwman, H.M. Cuppen, A. Bakker, L.J. Allamandola, H. Linnartz. Photochemistry of the PAH pyrene in water ice: the case for ion-mediated solid-state astrochemistry. *Astron. Astrophys.,* 511 (2010) A33.

[18] O. Dopfer. Laboratory spectroscopy of protonated PAH molecules relevant for interstellar chemistry, in: *PAHs and the Universe*; C. Joblin, A.G.G.M. Tielens, Eds.; *EAS Publications Series*, 46 (2011) 103-108.

[19] M.E. Jacox. Comparison of the ground state vibrational fundamentals of diatomic molecules in the gas phase and in inert solid matrices. *J. Mol. Spectr.,* 113 (1985) 286-301.

[20] M.E. Jacox. Comparison of the electronic energy levels of diatomic molecules in the gas phase and in inert solid matrices. *J. Mol. Struct.,* 157 (1987) 43-59.

[21] P. Ehrenfreund, L. D'Hendecourt, L. Verstraete, A. Leger, W. Schmidt, D. Defourneau. Search for the 4430 A DIB in the spectra of coronene cation and neutral ovalene. *Astron. Astrophys.,* 259 (1992) 257-264.

[22] W. Jones, P. Boissel, B. Chiavarino, M.E. Crestoni, S. Fornarini, J. Lemaire, P. Maitre. Infrared fingerprint of protonated benzene in the gas phase. *Angew. Chem.-Int. Edit.,* 42 (2003) 2057-2059.

[23] A. Schäfer, H. Horn, R. Ahlrichs. Fully optimized contracted Gaussian basis sets for atoms Li to Kr. *J. Chem. Phys.,* 97 (1992) 2571-2577.

[24] E. Herbst, V. Le Page. Do H atoms stick to PAH cations in the interstellar medium? *Astron. Astrophys.,* 344 (1999) 310-316.

[25] M. Hammonds, A. Pathak, A. Candian, P.J. Sarre. Spectroscopy of protonated and deprotonated PAHs, in: *PAHs and the Universe*; C. Joblin, A.G.G.M. Tielens, Eds.; *EAS Publications Series*, 46 (2011) 373-379.

[26] L.M. Hobbs, D.G. York, T.P. Snow, T. Oka, J.A. Thorburn, M. Bishof, S.D. Friedman, B.J. McCall, B. Rachford, P. Sonnentrucker, D.E. Welty. A catalog of Diffuse Interstellar bands in the spectrum of HD 204827. *Astrophys. J.,* 680 (2008) 1256.

[27] L.M. Hobbs, D.G. York, J.A. Thorburn, T.P. Snow, M. Bishof, S.D. Friedman, B.J. McCall, T. Oka, B. Rachford, P. Sonnentrucker, D.E. Welty. Studies of the Diffuse Interstellar Bands. III. HD 183143. *Astrophys. J.,* 705 (2009) 32.

# CHAPTER 7

# PROTONATED NAPHTHALENES AND THEIR REVERSIBLE PHOTOISOMERIZATION

*Alpha*- and *beta*-protonated naphthalenes were investigated by electronic absorption and fluorescence spectroscopies in 6 K neon matrices using a mass-selected $C_{10}H_9^+$ ($m/z = 129$) ion beam. The absorption spectra revealed $S_1/S_2 \leftarrow S_0$ transitions in the optical and UV domains with onsets at 502.1 and 396.1 nm in the case of $\alpha$-HN$^+$, and 534.5 and 322.3 nm for $\beta$-HN$^+$. Wavelength-dispersed fluorescence was observed from $S_1$ state of $\alpha$-HN$^+$, starting at 504.4 nm. Another $C_{10}H_9^+$ isomer, 2-indenylmethylium, was also detected in the UV, the absorption origin band being at 377.8 nm. Corresponding neutral $C_{10}H_9$ radicals were also characterized. Light-induced $\alpha$-HN$^+ \rightarrow \beta$-HN$^+$ isomerization was observed upon $S_2 \leftarrow S_0$ excitation of $\alpha$-HN$^+$, whereas the resulting $\beta$-HN$^+$ relaxed rapidly back into the more stable $\alpha$-HN$^+$ either *via* quantum tunnelling of a liable hydrogen or upon $S_1 \leftarrow S_0$ excitation of $\beta$-HN$^+$. The intramolecular proton transfer leading to the $\alpha$-HN$^+ \leftrightarrow \beta$-HN$^+$ photoisomerization has a reversible character. The observations are explained with the support of theoretical calculations.

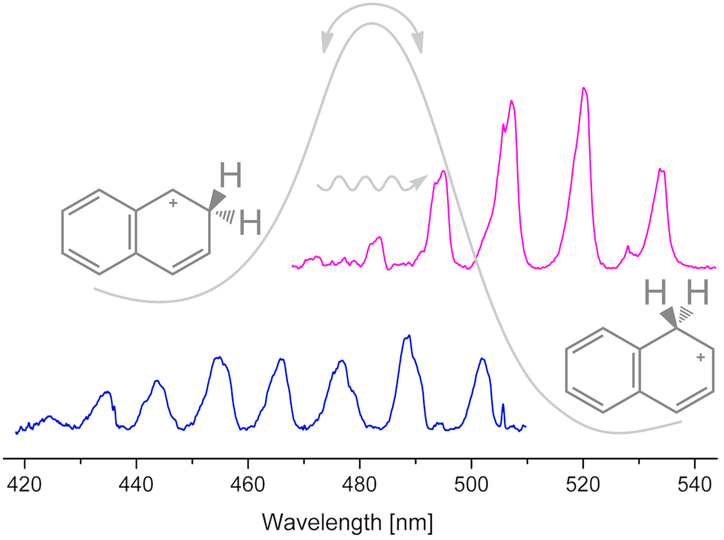

Manuscript in preparation:

*Electronic spectra and reversible photoisomerization of protonated naphthalenes in solid neon*

I. Garkusha, A. Nagy, J. Fulara, M. F. Rode,[a] A. L. Sobolewski[a] , and J. P. Maier
[a] *Institute of Physics, Polish Academy of Sciences, Al. Lotników 32/46, PL–02668 Warsaw, Poland*

## 7.1 INTRODUCTION

Naphthalene is the simplest of the PAHs. In its protonated form it has been the focus of investigations with different spectroscopic techniques and theoretical approaches for over a half a century; however, the information obtained is limited. First of all, the structure of its isomers, *alpha* and *beta*-protonated naphthalene ($\alpha$- and $\beta$-$HN^+$), has been shown by NMR in superacidic solutions to be $\sigma$-complex of the "excess" hydrogen and the aromatic ring [1, 2]. Secondly, ground-state vibrational spectra and electronic excitation energies have been calculated and the results used to make a comparison with UIRs and DIBs [3-5].

In the gas phase, the focus has been on IR spectroscopy. For that, different experimental methods have been employed. In one, the IR multiphoton dissociation spectrum of $HN^+$ was recorded using an ion cyclotron resonance mass spectrometer coupled to a free-electron laser. The cations have been produced in chemical ionization of the parent PAH using $CH_5^+$ or $C_2H_5^+$ as proton donor [6]. In another, a discharge was coupled with a supersonic expansion of PAHs seeded into a $H_2$/Ar mixture. Naphthalenes were thus protonated by $H_3^+$, followed by condensation with argon in a cold expansion. The resulting mass-selected $HN^+\cdot Ar$ complexes have been studied by means of single IR photodissociation using a tunable IR OPO laser system [7].

As for electronic spectroscopy, a few condensed-phase measurements are available [8-11]. Two papers on the $(1)^1A' \leftarrow \tilde{X}\,^1A'$ transition of $\alpha$-$HN^+$ in the gas phase appeared a short ago [12, 13]. This study presents electronic transitions of $C_{10}H_9^+$ isomers, $\alpha$- and $\beta$-$HN^+$, and 2-indenylmethylium, as well as of their neutrals in the visible and UV ranges. A reversible photoinduced proton transfer was observed between $\alpha$- and $\beta$-$HN^+$ and is explained with the support of theoretical calculations.

## 7.2 METHODS

### 7.2.1 PRODUCTION OF IONS

In the present study, the two methods described in Chapter 3 were used for the generation of protonated naphthalenes. In the first, $C_{10}H_9^+$ cations were produced from 1,2-dihydro-naphthlene (1,2-DHN) or 2-methyl-indene (2-MetI) in a hot-cathode discharge source. The fragment ion of $m/z = 129$ is one of the most intense in the mass spectrum of DHN obtained under such conditions. In the second, $C_{10}H_9^+$ was generated in a proton transfer reaction (PT) between protonated methanol ($MeOH_2^+$) and naphthalene (Naph) in the same source. The proton affinity (PA) of MeOH (754 kJ mol$^{-1}$) is lower than that of Naph (803 kJ mol$^{-1}$) [14] thus, the PT is energetically feasible. With a low pressure of the alcohol, both initial substances are ionized by electrons and mainly their parent and fragment ions are formed (Figure 7.1, A and B, green). At higher pressures, the protonated species $MeOH_2^+$ and $HN^+$ start to form (blue); further increase of the MeOH pressure leads to an efficient protonation of Naph (red). The $HN^+$ yield is higher comparing to that of the first method; moreover, the fragmentation becomes much less pronounced (Figure 7.1, C).

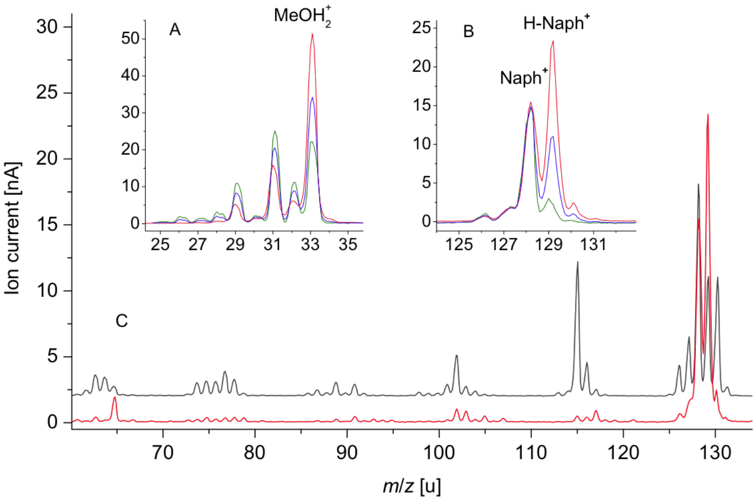

**Figure 7.1:** Mass spectra of ions produced in the reaction of naphthalene with protonated methanol ($MeOH_2^+$) in a hot-cathode discharge source at different pressures of methanol: green trace—low, blue—intermediate conditions, red—highest alcohol pressure, as optimized to reach a maximum intensity of protonated naphthalene ($HN^+$, $m/z = 129$). The inset panels show gains of A) protonated methanol and B) protonated naphthalene with increasing methanol pressure. Panel C) is a comparison of the mass spectra of ions produced from 1,2-dihydro-naphthalene (black) and in the protonation reaction above under optimum conditions (red). All spectra are normalized to the same intensity of naphthalene cation ($m/z = 128$).

As was previously demonstrated with protonated anthracene and larger H-PAH$^+$s (Chapters 5,6), the PT reaction ensures energetically “milder” conditions with respect to the ionization and H-loss of the respective dihydro-compounds, with the preferential formation of the most stable H-PAH$^+$ isomers. $MeOH_2^+$ was found to be the only suitable protonation agent of Naph among the reactants tested: $H_3^+$, $CH_5^+$, $H_3O^+$, $MeOH_2^+$ and protonated ethanol ($EtOH_2^+$), listed in an order of increasing proton affinity of the corresponding neutral precursor (422, 544, 691, 754 and 779 kJ mol$^{-1}$) [14]. Though in the case of $EtOH_2^+$ the PT is energetically feasible, no $HN^+$ was seen in the mass spectrum.

A possible reason why $HN^+$ was also not formed using other proton donors is a too large difference between their PAs and that of Naph. Even if $HN^+$ was formed initially, a large excess energy led to its dissociation. The optimal difference between PAs of the proton donor and acceptor was found to be ~50 kJ/mol, as was used for the proton donor selection for the other studied PAHs.

Several complementary experiments have been conducted. These include the recording the electronic spectra of Naph and $Naph^+$, $C_{10}H_7^+$, $C_{10}H_{10}^+$; direct deposition of naphthalene vapor with concurrent deposition of $H^+/H_3^+/Ar^+$ produced in the ion source. Electronic absorption and fluorescence spectra of all species were obtained using a mass-selective matrix isolation technique as described. In order to efficiently trap the cations, chloromethane was mixed into the neon in a ratio 1:20 000. To produce matrices containing the highest possible concentration of neutral species with respect to cations, $C_{10}H_9^+$ were also trapped in neon without an electron scavenger. In such experiments, most cations are neutralized with electrons ejected from metal surfaces; resulting neutral species are structurally identical with the cations.

### 7.2.2 COMPUTATIONS

Discharge conditions of experiment are favourable for isomerization to take place; therefore, a number of isomeric structures have to be considered for theoretical exploration. An extended search for the most stable isomers was carried out using DFT with the B3LYP functional and cc-pVDZ basis set. The results are collected in Figure 7.2. Vibrational analysis was done to ensure that all these isomers are minima on the $C_{10}H_9^+$ $S_0$ potential energy surface (PES). The geometry of the four most stable $C_{10}H_9^+$ isomers was then re-optimized using a larger basis set, cc-pVTZ, as well as with the MP2 at the cc-pVDZ level. The relative ground-state energies obtained using these methods are compared in Figure 7.2.

According to the DFT calculations and results of earlier studies [3, 6], the global minimum on the $C_{10}H_9^+$ potential energy surface is $\alpha$-$HN^+$. The other isomers, $\beta$-$HN^+$, 1-azulenium (1-$HAz^+$) and the 2-indenyl-methylium cation (2-$IMe^+$), lie 13, 22 and 36 kJ mol$^{-1}$ above it, respectively. The energetic order of $\beta$-$HN^+$ and 1-$HAz^+$ is reversed at the MP2/cc-pVDZ level: they lie 16 and 9 kJ mol$^{-1}$ above $\alpha$-$HN^+$. These four cations are planar, with the exception of the $CH_2$ group, which lies in the plane perpendicular to the aromatic rings ($C_s$ symmetry). Other possible $C_{10}H_9^+$ isomers are significantly higher in energy and were not considered further.

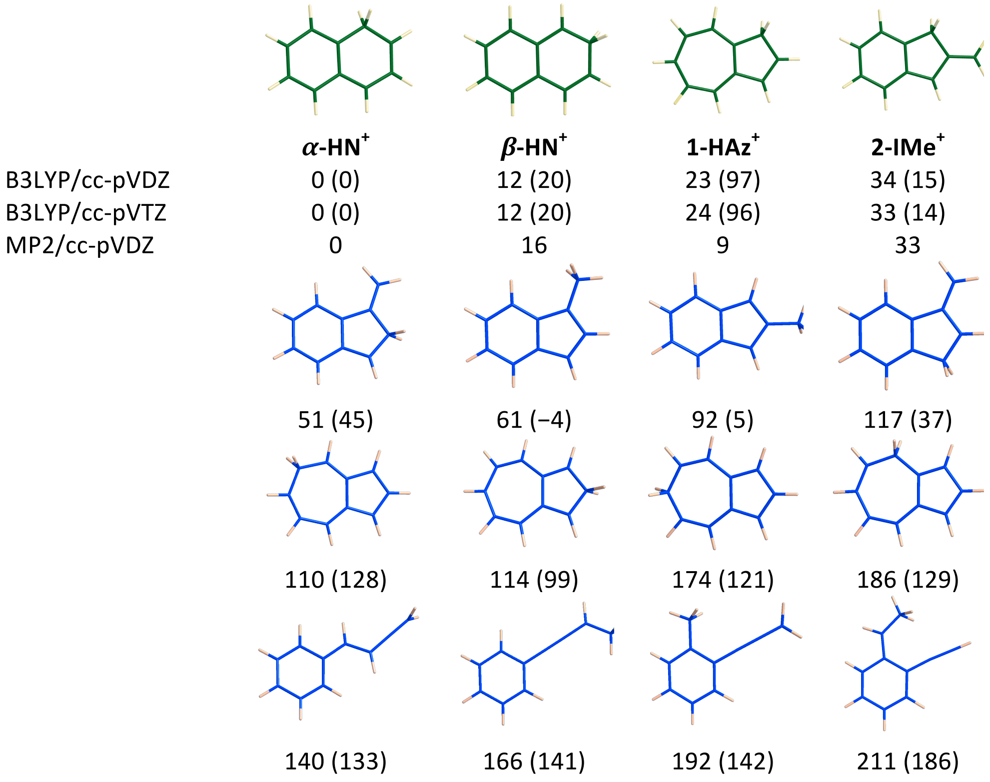

**Figure 7.2:** Relative ground-state energies (kJ mol$^{-1}$, corrected for zero-point vibrations) of the four most stable $C_{10}H_9^+$ isomers and corresponding $C_{10}H_9$ neutral radicals (parentheses) obtained with DFT at the B3LYP/cc-pVTZ level of theory and with MP2/cc-pVDZ. Energies of other possible geometries shown were obtained only with B3LYP/cc-pVDZ.

To support the assignment of the observed electronic transitions, excitation energies of the four most stable $C_{10}H_9^+$ isomers and their $C_{10}H_9$ neutrals were computed with time-dependent (TD) DFT and an *ab initio* second-order approximate coupled-cluster (CC2) method. In the latter case the equilibrium geometries of the lowest-lying excited states were determined with the CC2 method using implemented analytic gradients; the preceding geometry optimization of the molecular systems in their ground electronic state was done with the MP2 and cc-pVDZ basis set.

Additional calculations for $\alpha$- and $\beta$-HN$^+$ were carried out. In order to determine barriers for their photophysically relevant reactions, minimum-energy profiles along the reaction coordinates in the ground $S_0$ and excited $S_1$ and $S_2$ states were determined by

MP2 and CC2, respectively. After choosing a suitable coordinate, all other nuclear degrees of freedom were optimized for a given (frozen) value of this coordinate in the construction of the path. The conical intersection (CI) geometries between $S_1$ and $S_0$ for the two isomers were optimized with the complete active space self-consistent field (CASSCF) method along with the cc-pVDZ basis set, with the active space comprising two electrons in two orbitals.

## 7.3 OBSERVATIONS

### 7.3.1 VISIBLE SPECTRAL REGION

Deposition of $m/z = 129$ cations produced with either of the two described methods (section 7.2.1) into neon matrices revealed several electronic absorptions of different strength and width in the 250–700 nm spectral range. The strongest known systems of naphthalene radical cation (Naph$^+$, $m/z = 128$), the $D_2 \leftarrow D_0$ and $D_5 \leftarrow D_0$ electronic transitions around 675 and 306 nm, respectively [15, 16], were also observed in the spectrum. The presence of Naph$^+$ is the result of partial fragmentation of $C_{10}H_9^+$ upon deposition and/or due to natural $^{13}C$ isotopologue distribution. The absorption of Naph$^+$ was remeasured for the present study for a direct comparison with the electronic spectra in the $C_{10}H_9^+$ experiment. For that, Naph$^+$ was produced in the ion source from naphthalene diluted with helium, mass selected and embedded in neon containing a small amount of $CH_3Cl$; its spectrum is shown in Figure 7.3.

The visible part of the spectrum recorded after deposition of mass-selected $C_{10}H_9^+$ ions produced in the reaction of naphthalene with $MeOH_2^+$ is characterized by a new, extended series of broad absorption features starting around 502 nm as well as a weaker, sharper single band at ~528 nm (Figure 7.4, trace a). The former was not observed in the experiment conducted without an electron scavenger in neon, whereas the latter was stronger (trace b). Under such conditions (Section 7.2.1), cations are neutralized in a matrix and their absorptions are weaker or, as in this case, absent in the spectrum, and those of neutral species appear stronger. Therefore, the 502 nm system is of cationic, whereas the band at 528 nm is of neutral origin.

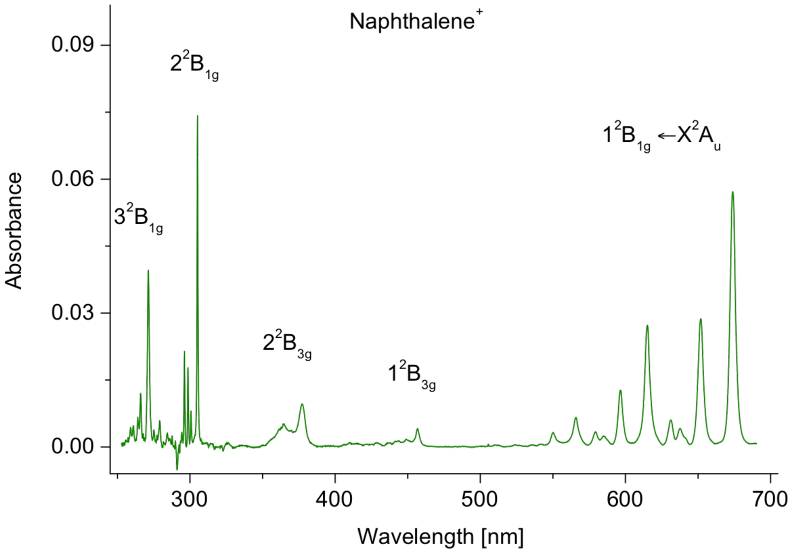

**Figure 7.3:** Electronic spectrum of naphthalene radical cation recorded after mass-selective deposition of $C_{10}H_8^+$ produced from naphthalene into a neon matrix. The spectrum is identical to the published in refs. 26, 27. Indicated assignment of the observed transitions is taken from ref. 27.

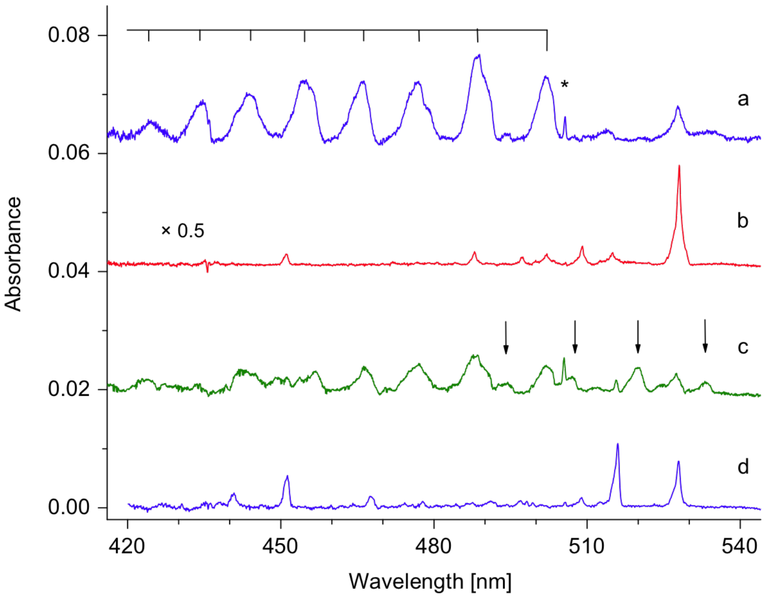

**Figure 7.4:** Visible part of the electronic absorption spectra recorded after deposition of $C_{10}H_9^+$ cations produced from (a) a naphthalene/MeOH mixture and (c) 1,2-dihydro-naphthalene into a $CH_3Cl$/neon matrix. Traces b and d were obtained from the same two precursors in experiments without $CH_3Cl$. All spectra are scaled to the same deposited charge of $C_{10}H_9^+$. Cationic bands are marked by their vibrational progression or arrows.

Significantly lower in intensity was the 502 nm absorption system when $C_{10}H_9^+$ was produced from 1,2-DHN and deposited into a neon matrix containing $CH_3Cl$ (Figure 7.4, trace c); however, an additional weak absorption was observed (indicated by arrows). It originates at 535 nm and partially overlaps with the 502 nm system. It is absent in the spectrum obtained from the same precursor but without an electron scavenger (trace d) and is, therefore, of cationic nature. Comparison of the spectra shown in traces b and d of Figure 7.4 reveals that the latter comprises two systems with onsets at 528 and 516 nm, which belong to two isomers of neutral $C_{10}H_9$.

According to observations, two absorptions of $C_{10}H_9^+$ are observed when 1,2-DHN was used as a precursor, whereas only one, with onset at 502 nm, is prominent in the spectrum of $C_{10}H_9^+$ generated from $MeOH_2^+$ and Naph. It is attributed to the most stable $C_{10}H_9^+$ isomer, namely α-HN⁺, because this method provides the mildest production conditions, as was shown on the protonated pyrene system (Chapter 6). The bands constituting the 502 nm system are located 576, 1026, 1557, 2057, 2627 and 3110 cm⁻¹ above the origin (Figure 7.4, trace a; Table 7.1). Absorptions of other $C_{10}H_9^+$ isomer with onset at ~535 nm are not seen in this spectrum. Furthermore, absorptions of neutrals formed by neutralization of these cations in a pure neon matrix originate then from one isomer of $C_{10}H_9$, $\alpha$-HN, with probably a minor contribution of the other form (Figure 7.4, trace b).

The use of 1,2-DHN as a precursor suggests formation of the two isomers of protonated naphthalene upon the removal of a H atom from one of the $CH_2$ groups of the dihydrogenated molecule. These species should be responsible for the two cationic systems with onsets at 502 and 535 nm in the spectrum of $C_{10}H_9^+$ produced from 1,2-DHN (Figure 7.4, trace c). According to theoretical calculations, $\beta$-HN⁺ lies ~16 kJ mol⁻¹ higher in energy than $\alpha$-HN⁺. Though 1-HAz⁺ in the ground state has a similar energy to $\beta$-HN⁺ ones, it can be excluded from further considerations, due to large rearrangements of the structure needed to form this ion. Therefore, the carrier of the 535 nm system is $\beta$-HN⁺. Several bands belonging to this absorption are distinguishable, they form a regular progression built on a ~490 cm⁻¹ mode (Figure 7.4, trace c; Table 7.1). Likewise, two $C_{10}H_9$ neutrals are formed in a pure neon matrix followed neutralization of $C_{10}H_9^+$ generated from the 1,2-DHN precursor. The first system with onset at 528 nm was the most prominent one obtained upon neutralization of $\alpha$-HN⁺. The second one starting at 516 nm is associated with neutralization of $\beta$-HN⁺ and is, therefore, of $\beta$-HN radical.

The two neutral systems at 528 and 516 nm are confirmed to be the $D_1 \leftarrow D_0$ and $D_2 \leftarrow D_0$ transitions of $\alpha$- and $\beta$-hydronaphthyl radicals, respectively. Their electronic spectra are known from earlier studies on irradiated naphthalene crystals and solutions [17, 18]. Recently, they have also been observed in the gas phase by a mass-resolved resonant two-photon ionization technique [19]. In the latter experiments, the two isomers were produced from 1,2-DHN, whereas only $\alpha$-HN was seen from 1,4-dihydro-naphthalene. Transitions of the two radicals overlap; they were separated and assigned employing hole-burning spectroscopy and calculations. The onset of the $D_1 \leftarrow D_0$ transition of $\alpha$-HN in the gas phase is at 527.7 nm. Several excited-state frequencies were obtained (e.g., 475, 564, 747, 965 and 1050 cm$^{-1}$); they are close to those derived for the 528 nm system in neon (Table 7.2). The origin band of the $\beta$-HN system in the gas phase (516.4 nm) is spaced 414 cm$^{-1}$ from that of $\alpha$-HN; this separation is close to 448 cm$^{-1}$ observed between the corresponding systems in a neon matrix. Thus, it is concluded that the $\alpha$- and $\beta$-HN isomers are seen in experiments of the present study starting with the 1,2-DHN precursor, whereas only $\alpha$-HN is in the spectrum when naphthalene/MeOH is used. Furthermore, as neutral $C_{10}H_9$ radicals are formed by neutralization of $C_{10}H_9^+$ in the matrix retaining the cationic structure, the identification of spectral features of $\alpha$- and $\beta$-HN in these matrices provides further conformation of the assignment of 502 and 535 nm absorptions to the $\alpha$- and $\beta$-HN$^+$ isomers, respectively.

In the course of this study on protonated naphthalenes, two papers on the electronic spectrum of jet-cooled $\alpha$-HN$^+$ using photodissociation spectroscopy have appeared. The origin band of the $(1)\,^1A' \leftarrow X\,^1A'$ transition is reported at 503.36 nm in the gas phase [13], in agreement with the neon matrix value of 502 nm. Vibrational assignment of this system was given and several low-energy frequencies in the excited state derived [12]. Among them, the most intense ones at 335, and 481 and 575 cm$^{-1}$ correspond well to the peak at 315 cm$^{-1}$ (Table 7.1) and with the asymmetric profile of the band 576 cm$^{-1}$ above the origin in neon (Figure 7.4, trace a), respectively.

**Table 7.1** Absorption band maxima (±0.1 nm) of electronic transitions of $C_{10}H_9^+$ cations observed in 6 K neon matrices and assignment

| $\lambda_{\mathrm{Ne}}$ /nm | $\tilde{\nu}$ [a)] /cm$^{-1}$ | $\Delta\tilde{\nu}$ /cm$^{-1}$ | Assignment [b)] |
|---|---|---|---|
| **$\alpha$-HN$^+$** | | | |
| 502.1 | 19 916 | 0 | $0_0^0$ (1)$^1\mathrm{A}' \leftarrow \tilde{X}\,^1\mathrm{A}'$ |
| 494.3 | 20 231 | 315 | $\nu_{34}$ |
| 488.0 | 20 492 | 576 | $\nu_{31}$ |
| 477.5 | 20 942 | 1026 | $\nu_{26}$ |
| 475.2 | 21 044 | 1128 | $\nu_{24}$ |
| 465.7 | 21 473 | 1557 | $\nu_{11}$ |
| 455.1 | 21 973 | 2057 | $2\nu_{26}$ |
| 443.6 | 22 543 | 2627 | $2\nu_{26} + \nu_{31}$ |
| 434.3 | 23 026 | 3110 | $\nu_{47}$ |
| 424.5 | 23 557 | 3641 | $3\nu_{26}$ |
| 396.1 | 25 246 | 0 | $0_0^0$ (2)$^1\mathrm{A}' \leftarrow \tilde{X}\,^1\mathrm{A}'$ |
| 386.2 | 25 893 | 647 | $\nu_{30}$ |
| 377.1 | 26 518 | 1272 | $2\nu_{30}$ |
| **$\beta$-HN$^+$** | | | |
| 534.5 | 18 709 | 0 | $0_0^0$ (1)$^1\mathrm{A}' \leftarrow \tilde{X}\,^1\mathrm{A}'$ |
| 520.8 | 19 201 | 492 | $\nu_{32}$ |
| 507.7 | 19 697 | 988 | $2\nu_{32}$ |
| 495.4 | 20 186 | 1477 | $3\nu_{32}$ |
| 483.8 | 20 670 | 1961 | $4\nu_{32}$ |
| 472.2 | 21 177 | 2468 | $5\nu_{32}$ |
| 322.3 | 31 028 | 0 | $0_0^0$ (2)$^1\mathrm{A}' \leftarrow \tilde{X}\,^1\mathrm{A}'$ |
| 317.8 | 31 467 | 439 | $\nu_{32}$ |
| 313.4 | 31 909 | 881 | $2\nu_{32}$ |
| 309.1 | 32 348 | 1320 | $3\nu_{32}$ |
| 305.0 | 32 789 | 1761 | $4\nu_{32}$ |
| **2-IMe$^+$** | | | |
| 377.8 | 26 469 | 0 | $0_0^0$ (2)$^1\mathrm{A}' \leftarrow \tilde{X}\,^1\mathrm{A}'$ |
| 374.0 | 26 738 | 269 | $\nu_{34}$ |
| 371.2 | 26 940 | 471 | $\nu_{32}$ |
| 367.2 | 27 233 | 764 | $\nu_{34} + \nu_{32}$ or $\nu_{29}$ |
| 364.8 | 27 412 | 943 | $2\nu_{32}$ or $\nu_{26}$ |
| 362.9 | 27 556 | 1087 | $\nu_{24}$ |
| 360.1 | 27 770 | 1301 | $\nu_{34} + \nu_{24}$ or $\nu_{19}$ |
| 357.2 | 27 996 | 1527 | 2 × 764 |
| 355.8 | 28 106 | 1637 | $\nu_{9/10}$ |
| 352.1 | 28 401 | 1932 | |

[a)] [a] $\tilde{\nu} = 1/\lambda_{\mathrm{Ne}}$. [b)] Vibrational assigments in the excited states of $C_{10}H_9^+$ are based on ground-state fundamentals calculated with DFT at the B3LYP/cc-pVTZ level of theory, and listed in Table 7.5.

**Table 7.2** Observed absorption band maxima (±0.1 nm) of electronic transitions of neutral $C_{10}H_9$ radicals in neon matrices and assignment

| $\lambda_{Ne}$ /nm | $\tilde{\nu}$ [a] /cm$^{-1}$ | $\Delta\tilde{\nu}$ /cm$^{-1}$ | Assignment [b] |
|---|---|---|---|
| ***α*-HN** | | | |
| 528.1 | 18 936 | 0 | $0_0^0$ (1)$^2$A′ ← $\tilde{X}^2$A″ |
| 515.0 | 19 417 | 481 | $\nu_{33}$ |
| 512.5 | 19 512 | 576 | $\nu_{31}$ |
| 509.1 | 19 643 | 707 | $\nu_{30}$ |
| 502.1 | 19 916 | 980 | $\nu_{26}$ or $\nu_{25}$ |
| 499.9 | 20 004 | 1068 | $\nu_{24}$ |
| 497.2 | 20 113 | 1177 | $\nu_{22}$ |
| 488.0 | 20 492 | 1556 | $\nu_{31}$ + $\nu_{26/25}$ or $\nu_{11}$ |
| 369.2 | 27 088 | 0 | $0_0^0$ (2)$^2$A′ ← $\tilde{X}^2$A″ |
| 363.0 | 27 552 | 464 | $\nu_{33}$ |
| 330.9 | 30 221 | 0 | $0_0^0$ (3)$^2$A′ ← $\tilde{X}^2$A″ |
| 327.6 | 30 525 | 304 | $\nu_{34}$ |
| 325.5 | 30 722 | 501 | $\nu_{32}$ |
| 324.40 | 30826 | 0 | $0_0^0$ (4)$^2$A′ ← $\tilde{X}^2$A″ |
| 323.06 | 30954 | 128 | 2$\nu_{51}$ |
| 320.20 | 31230 | 404 | 2$\nu_{50}$ |
| 318.84 | 31364 | 538 | 2$\nu_{50}$ + 2$\nu_{51}$ |
| 317.50 | 31496 | 670 | 2$\nu_{50}$ + 4$\nu_{51}$ |
| 314.50 | 31797 | 971 | |
| 311.60 | 32092 | 1266 | |
| ***β*-HN** | | | |
| 516.2 | 19 372 | 0 | $0_0^0$ (2)$^2$A′ ← $\tilde{X}^2$A″ |
| **2-IMe** | | | |
| 451.2 | 22 163 | 0 | $0_0^0$ (1)$^2$A′ ← $\tilde{X}^2$A″ |
| 440.8 | 22 686 | 523 | $\nu_{31}$ |
| 430.5 | 23 229 | 1066 | $\nu_{24}$ |
| 422.4 | 23 674 | 1511 | $\nu_{11}$ |
| 284.1 | 35 199 | 0 | $0_0^0$ (3)$^2$A′ ← $\tilde{X}^2$A″ |
| 279.3 | 35 804 | 605 | $\nu_{30}$ |
| 275.5 | 36 298 | 1099 | $\nu_{23}$ |
| **n.a.**[b] | | | |
| 467.5 | 21 390 | 0 | $0_0^0$ |
| 457.5 | 21 858 | 468 | |
| 443.9 | 22 528 | 1138 | |

[a] $\tilde{\nu} = 1/\lambda_{Ne}$ [b] Vibrational assigments in the excited states of $C_{10}H_9$ are based on ground-state frequencies computed with DFT at the B3LYP/cc-pVTZ level of theory (Table 7.5).

[b] Not assigned.

### 7.3.2 UV SPECTRAL REGION

The UV part of the absorption spectrum recorded after deposition of mass-selected $C_{10}H_9^+$ ions produced in the reaction of naphthalene with $MeOH_2^+$ into a neon matrix containing $CH_3Cl$ is characterized by a number of strong absorptions in the 250–400 nm region (Figure 7.5, trace a). The spectrum obtained when the ions were produced from the same precursor and deposited into a matrix without an electron scavenger is much simpler (Figure 7.5, trace c). Three electronic systems with onsets at 369, 331 and 324 nm are seen in the spectrum (Table 7.2). They correspond to neutral $C_{10}H_9$, namely α-HN, because they were observed in the same matrix as its 528 nm system. Moreover, their relative intensities correlate well with each other and with that of the visible α-HN system in different experiments and with the precursor used. The absorptions of neutral α-HN are also present in trace a as a result of partial neutralization of the cations during growth of the matrix.

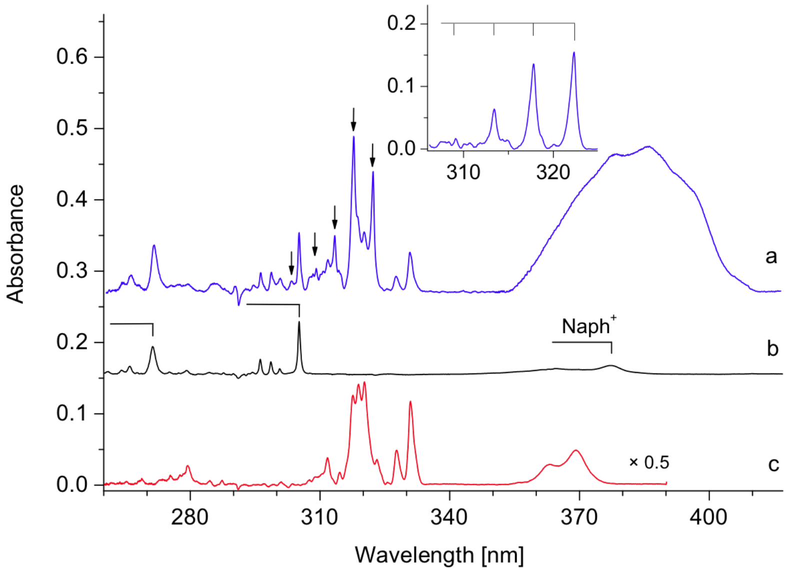

**Figure 7.5:** UV part of the electronic absorption spectra recorded after deposition of $C_{10}H_9^+$ cations produced from naphthalene/MeOH in experiments carried out (a) with and (b) without an electron scavenger. The spectra were normalized to the same accumulated charge of $C_{10}H_9^+$. Bands due to naphthalene radical cation ($Naph^+$) are seen in trace a; trace b is part of the $Naph^+$ spectrum (Figure 7.2), scaled to the same intensity as the origin band at ~670 nm. Inset shows the $S_2 \leftarrow S_0$ transition of *β*-protonated naphthalene obtained by subtracting trace b from trace a after proper intensity scaling; these same absorptions are also marked by arrows on trace a.

Besides these, absorptions of Naph$^+$ weakly contribute to the spectrum of $C_{10}H_9^+$ (Figure 7.5, trace a). They are shown in trace b, which is a UV section of the "pure" Naph$^+$ spectrum (Figure 7.3), downscaled to the intensity of the origin band of its $D_2 \leftarrow D_0$ transition in the 670–650 nm range observed after depositing $C_{10}H_9^+$. The remaining absorptions, the broad one centered at 385 nm and the system of sharp bands starting at 322 nm (seen in trace a, Figure 7.5), are of HN$^+$ cations.

Electronic spectra of HN$^+$ have been studied in the past in acidic solutions. In such media, the HN$^+$ spectrum is characterized by a strong, broad absorption around 390 nm, which has later been assigned to the $\alpha$-HN$^+$ isomer [9, 11]. The 385 nm absorption of $C_{10}H_9^+$ observed in neon (Figure 7.5, trace a) is similar to that. The intensity of this band may be, however, slightly overestimated due to an experimental background artefact in this region. The band is ~40 nm broad, with a barely discernible/unresolved vibrational structure (Table 7.1). This suggests a short lifetime of the cation in this electronic state. A broad absorption was also reported for the $S_1 \leftarrow S_0$ transition of protonated benzene in neon matrix (Chapter 4). For the latter calculations predict a fast decay of $S_1$ via a conical intersection to $S_0$ [20].

The other cationic system with origin at 322 nm (Figure 7.5, trace a, marked with arrows) is well pronounced in the spectrum. It is seen even better in the inset of this figure, for which the spectrum recorded in neon without $CH_3Cl$ (trace b) was subtracted from that when the matrix contained an electron scavenger (trace a) after downscaling the former to the same intensity of the 331 nm neutral peak. Five sharp bands constituting the 322 nm system are identified; they form a vibrational progression built on a ~440 cm$^{-1}$ mode (Table 7.1).

One would expect that these two absorption systems originate from $\alpha$-HN$^+$, because its transition dominates the visible part of the spectrum measured in the same matrix (Figure 7.4, trace a). They belong, however, to two isomers of $C_{10}H_9^+$ because their relative intensities vary with the experimental conditions used.

### 7.3.3 $\alpha$-HN$^+$ ↔ $\beta$-HN$^+$ PHOTOISOMERIZATION

Repetition of the visible scans after UV measurements revealed remarkable changes in the absorption spectrum of $C_{10}H_9^+$ produced from the naphthalene/MeOH mixture. It resulted in the lowering the intensity of the 502 nm system of $\alpha$-HN$^+$ and in appearance of the 535 nm system (Figure 7.6, traces a and b), identical to the one produced from the

1,2-DHN (Figure 7.4, trace c) and assigned to $\beta$-HN$^+$. Prolonged photolysis of the sample with UV radiation of a high pressure xenon lamp equipped with a band-pass filter, transmitting the light in the region where strong broad absorption of $C_{10}H_9^+$ is located ($340 < \lambda < 390$ nm), led to depletion of the 502 nm system of the $\alpha$-HN$^+$ isomer and caused a substantial growth of the 535 nm system of $\beta$-HN$^+$ (Figure 7.6, trace c). However, the strong absorption system at 535 nm appeared to lose intensity during every scan and, after 10 min irradiation with $\lambda > 508$ nm with a halogen lamp, converted back to the initially observed strength of the 502 nm system of $\alpha$-HN$^+$ (Figure 7.6, trace d). Thus, the $\alpha \leftrightarrow \beta$ isomerization process is reversible. The spectrum shown in Figure 7.6 (trace c) was recorded just after UV irradiation of the matrix using the shortest possible exposure time and only a few scan accumulations.

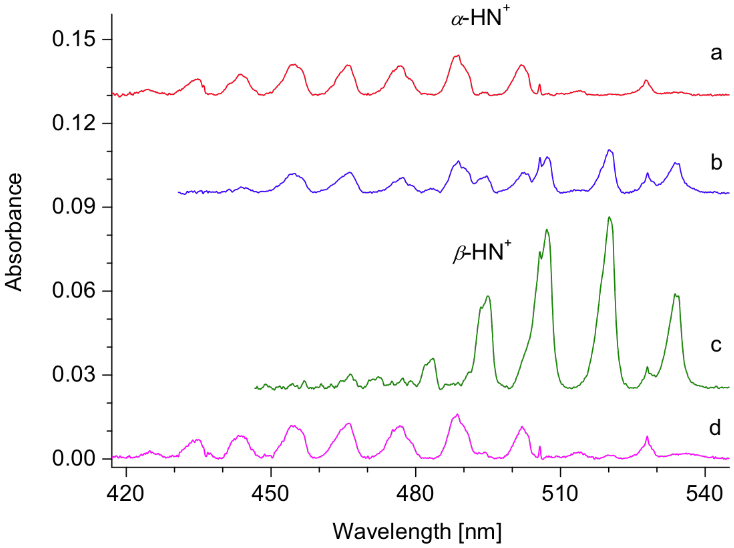

**Figure 7.6:** Electronic absorption spectra of protonated naphthalenes illustrating the observed photophysical processes. Visible part of the spectrum of $C_{10}H_9^+$ cations produced from naphthalene/MeOH mixture and recorded after (a) deposition into a neon matrix with electron scavenger, (b) measurement of the UV region, (c) subsequent 20 min irradiation of the matrix with $390 > \lambda > 340$ nm using a high-pressure xenon lamp and (d) 10 min bleaching of the matrix with $\lambda > 508$ nm using a halogen lamp.

In order to evaluate the behaviour of the UV bands of $C_{10}H_9^+$ upon UV irradiation and elucidate their relation to the visible ones, systematic studies were carried out. The most efficient irradiation steps were applied again to obtain and study matrices containing either purely $\alpha$- or $\beta$-HN$^+$ isomers. Besides these, a number of a stepwise irradiations of the matrix with either 390 > $\lambda$ > 340 or $\lambda$ > 508 nm have been undertaken. The scans were restricted only to the visible and UV regions where the absorptions of $C_{10}H_9^+$ occur. Moreover, spectra were measured using cut-off and band-pass filters, and the number of accumulations was drastically reduced, all in order to prevent photoconversion of the isomers during recording the spectra.

Visible and UV spectral regions of $HN^+$ recorded using the same irradiation scheme are compared in Figure 7.7, panels A and B. First, the matrix was irradiated 10 min with $\lambda$ > 508 nm to convert the $HN^+$ cations to $\alpha$-$HN^+$ (502 nm system as in Figure 7.6, trace d) and the spectrum was measured only in the 420–300 nm range (Figure 7.7 B, red trace). Next, the matrix was exposed to 390 > $\lambda$ > 340 nm radiation for 12 min and the same range was re-measured (Figure 7.7 B, blue). As a result, the broad system around 385 nm became weaker and the sharp one originating at 323 nm grew. This behaviour confirms that these two UV systems belong to different $HN^+$ isomers trapped in neon. The green trace of Figure 7.7 B was recorded after a 20 min long photolysis with 390 > $\lambda$ > 340 nm, and thus corresponds to the highest intensity of the 535 nm system of $\beta$-$HN^+$ and no absorptions of $\alpha$-$HN^+$ (green trace, panel A, same as in Figure 7.6, trace c). As is seen, (Figure 7.7 A and B) the intensity of the 385 nm system correlates well with that at 502 nm; therefore, it is of $\alpha$-$HN^+$. The absorption features at 535 and 323 nm are both produced by prolonged irradiation of the 385 nm system. Moreover, these two systems are destroyed when irradiated by $\lambda$ > 508 nm; hence, they are of common origin and belong to $\beta$-$HN^+$. In fact, the 323 nm system is present in the spectrum recorded after deposition of $C_{10}H_9^+$ from the Naph/MeOH mixture only as a result of (partial) $\alpha \leftrightarrow \beta$ photoconversion during UV measurements. The mechanism of photoconversion is discussed in Section 7.4.

Besides the $\alpha$-$HN^+$ $\leftrightarrow$ $\beta$-$HN^+$ photoisomerization, a spontaneous decay of $\beta$-$HN^+$ was observed in a neon. Figure 7.7 C reproduces the origin band of its 535 nm system recorded using cut-off filters which block the light below ~520 nm (at 523 nm, the position of the first vibrational band of the 535 nm system, the light intensity was ~3.5 % of its initial value used for scanning). The green and magenta traces were measured right after each other; comparison of their intensity illustrates that there is only a modest change caused by exposure to the light used for the absorption measurements. In the orange trace a spectrum is shown after the matrix was left in the dark for ~30 min. A large, nearly complete drop in the strength of the absorption is apparent.

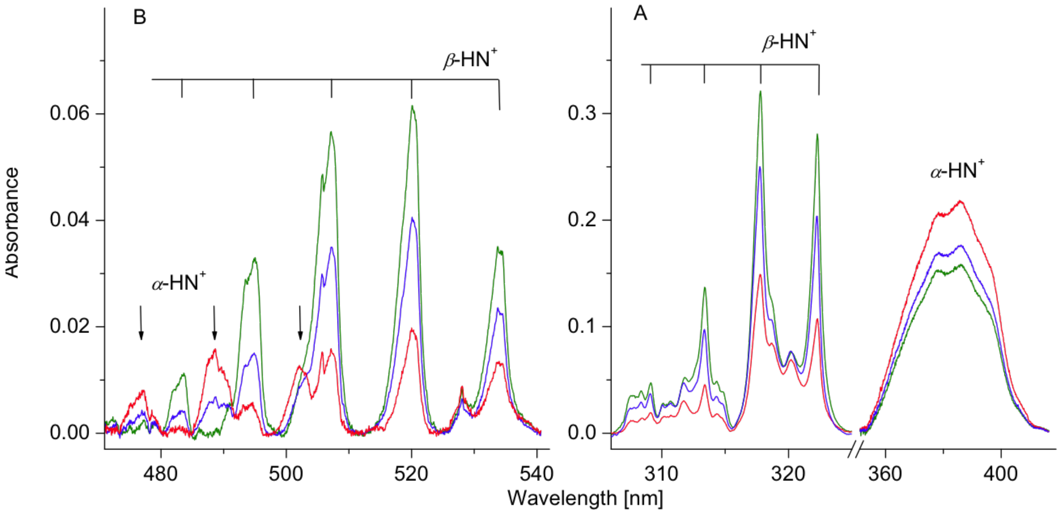

**Figure 7.7:** Electronic absorption spectra of protonated naphthalenes illustrating observed photophysical processes. **Panel A:** Visible section of the spectra of $C_{10}H_9^+$ cations produced from a naphthalene/MeOH mixture and recorded after UV measurements (red trace), and subsequent 12 (blue) and 20 min (green) bleaching of the matrix with $390 > \lambda > 340$ nm radiation. **Panel B:** UV part measured reproducing the irradiation conditions used in panel A.

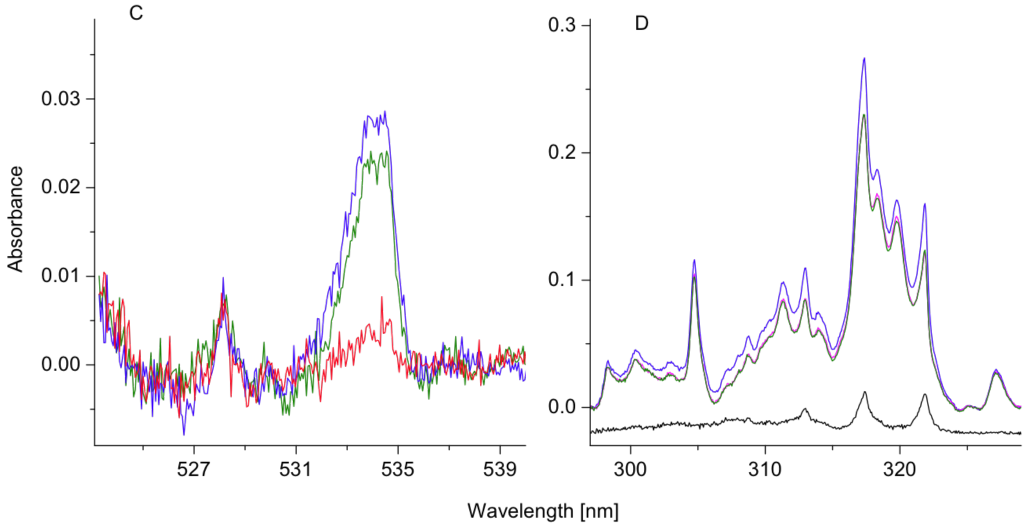

**Panel C:** Origin band of the 535 nm absorption system of $\beta$-protonated naphthalene recorded using cut-off filters blocking the light below ~520 nm. Blue and green traces were measured with ~2 min difference to illustrate the slight intensity decay caused by the excitation, whereas for the red curve the matrix was left for ~30 min without any action taken. **Panel D:** Region of the $S_2 \leftarrow S_0$ transition of the same $\beta$-$HN^+$ isomer. Blue trace was recorded after bleaching of the matrix with $390 > \lambda > 340$ nm radiation, for the red – the matrix was left for ~12 min in the dark; green – was recorded with ~2 min difference illustrating that no decay is caused by the excitation. Black trace is obtained by subtracting the red trace from the blue.

Computational studies have shown that $\alpha$-HN$^+$ requires about 47 kJ mol$^{-1}$ (0.49 eV) to reach and overcome the transition-state barrier for a 1 to 2 proton shift; this value is somewhat lower (32 kJ mol$^{-1}$, ~0.33 eV) for the other, $\beta \rightarrow \alpha$ direction, starting from the less stable $\beta$-HN$^+$. However, the neon matrix temperature of 6 K corresponds only to about 0.5 kJ mol$^{-1}$, which is all the energy that is available for vibrations. This points to a quantum tunnelling of the hydrogen being responsible for the decay of $\beta$-HN$^+$ in solid neon. Similar processes have been observed in low-temperature matrices, among others, for the *cis*/*trans* isomerism of formic acid, HCOOH, by IR [21, 22] and deuterium scrambling in substituted methane radical cations using electron spin resonance [23, 24]. According to the Boltzmann distribution, (nearly) exclusively the $v'' = 0$ state of $\beta$-HN$^+$ is populated at 6 K; the respective wave function has then to be in reasonable overlap with that of an excited vibrational state of $\alpha$-HN$^+$ in its ground electronic state. The probability of finding the simplest model system, the harmonic oscillator, in the classically forbidden region amounts to ~16 %; this value decreases rapidly with increasing v quantum number. Therefore, the $\alpha$-HN$^+$ vibrational state involved in the tunnelling is likely a fundamental vibration or first overtone. A simple backward pumping scheme might be feasible in the $\alpha \rightarrow \beta$ direction with the sole use of an IR laser below or above the isomerization barrier (but without accessing the first electronic excited state of $\alpha$-HN$^+$).

### 7.3.4 FLUORESCENCE STUDIES

Fluorescence measurements have been carried out on a matrix containing $C_{10}H_9^+$ cations produced in the Naph/ $MeOH_2^+$ reaction. Laser excitation into any of the absorption bands of the 502 nm system of $\alpha$-HN$^+$ resulted in a structured emission in the 504–625 nm region. The spectrum is shown in Figure 7.8 (red trace) along with the corresponding absorption scan (blue). All the fluorescence features are to the red of the absorption trace and resemble a mirror image of the latter. Thus, the fluorescence spectrum corresponds to the emission from the (adiabatically relaxed) $S_1$ state of $\alpha$-HN$^+$ to vibrational levels of its ground electronic state. The onsets of the two spectra overlap partially and cross at 503.5 nm, which is then the position of the zero-phonon line of the absorption and emission. This is also a more precise energy for the $0_0^0$ band of the $S_1 \leftarrow S_0$ transition of the $\alpha$-HN$^+$ isomer in neon and the (red) shift is even less (10 cm$^{-1}$) from the recently reported gas-phase value [12, 13] than derived from the origin band maxima.

The 504 nm fluorescence system, though much weaker in intensity, has been also detected upon excitation in the 370–396 nm range, where the strong, broad absorption of $\alpha$-HN$^+$ is located. The observations of the same fluorescence spectrum confirm that the 502 and 385 nm systems belong to the same isomer, $\alpha$-HN$^+$.

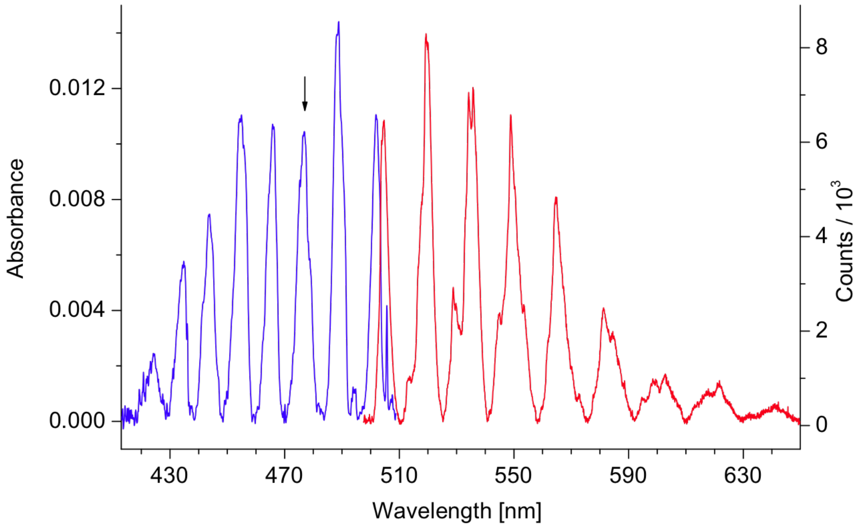

**Figure 7.8:** Electronic absorption (blue trace) and fluorescence (red) spectra recorded after deposition of $C_{10}H_9^+$ cations produced in the reaction of naphthalene vapor with protonated methanol. The emission was obtained upon excitation of the 477.5 nm absorption feature (arrow).

The wavelengths of the band maxima of the observed fluorescence are given in Table 7.3. The spectrum is similar to the 502 nm absorption system. Both contain a weak band spaced by 321 and 315 cm$^{-1}$ from the origin, respectively. This is followed by the second band, strongest in both spectra, located ~580–590 cm$^{-1}$ from the origin. The third emission feature consists of at least four overlapping bands, 915, 955, 1103 and 1162 cm$^{-1}$, and may explain the slight asymmetry of some absorption bands. The vibrational structure in the fluorescence corresponds to the vibrational energy levels in the ground electronic state and can be compared directly to the calculated frequencies (Table 7.5, footnote a).

The matrix sample containing $C_{10}H_9^+$ cations produced in the Naph/ $MeOH_2^+$ reaction was also exposed to prolonged $390 > \lambda > 340$ nm radiation of a xenon lamp to photoconvert the species to $\beta$-HN$^+$; however, no fluorescence was detected upon laser excitation across the 535 nm absorption system. This could be expected in view of the absorption behaviour: $\lambda > 508$ nm irradiation corresponding to the $S_1 \leftarrow S_0$ excitation in

$\beta$-HN$^+$ causes rapid $\beta \rightarrow \alpha$ isomer flip in a non-radiative relaxation process involving surface crossing(s). This will be further elucidated in Section 7.4.2.

**Table 7.3** Fluorescence band maxima (±0.1 nm) and vibrational assignment of the $S_1 \rightarrow S_0$ transition of *alpha*-protonated naphthalene in a 6 K neon matrix

| $\lambda_{Ne}$ /nm | $\tilde{\nu}$ [a] /cm$^{-1}$ | $\Delta\tilde{\nu}$ /cm$^{-1}$ | Assignment [b] |
|---|---|---|---|
| 504.4 | 19 826 | 0 | $0_0^0$ $(1)^1A' \rightarrow \tilde{X}\,^1A'$ |
| 512.7 | 19 505 | 321 | $\nu_{34}$ |
| 517.6 | 19 320 | 506 | $\nu_{33}$ or $\nu_{32}$ |
| 520.1 | 19 227 | 599 | $\nu_{31}$ |
| 528.8 | 18 911 | 915 | $\nu_{34} + \nu_{31}$ or $\nu_{28}$ |
| 529.9 | 18 871 | 955 | $\nu_{27}$ |
| 534.1 | 18 723 | 1103 | $\nu_{33} + \nu_{31}$ or $\nu_{25}$ |
| 535.8 | 18 664 | 1162 | $\nu_{24}$ |
| 544.8 | 18 355 | 1471 | $\nu_{14}$ |
| 548.9 | 18 218 | 1608 | $\nu_{10}$ |
| 550.4 | 18 169 | 1657 | $\nu_9$ |
| 551.8 | 18 123 | 1703 | $\nu_{31}$ + 1103 |
| 553.6 | 18 064 | 1762 | $\nu_{31} + \nu_{24}$ |
| 564.5 | 17 715 | 2111 | $\nu_{27} + \nu_{24}$ |
| 572.9 | 17 455 | 2371 | $\nu_{14}$ + 915 |
| 581.1 | 17 209 | 2617 | $\nu_{27} + \nu_9$ |
| 584.7 | 17 103 | 2723 | $\nu_{10}$ + 1103 |
| 594.7 | 16 815 | 3011 | $\nu_8$ |
| 598.4 | 16 711 | 3115 | $\nu_7$ |
| 602.8 | 16 589 | 3237 | $\nu_1$ |
| 621.8 | 16 082 | 3744 | $\nu_{33/32} + \nu_1$ |

[a] $\tilde{\nu} = 1/\lambda_{Ne}$. [b] The assignments are based on the totally symmetric (a′ in $C_s$) modes in the electronic ground state of $\alpha$-HN$^+$ calculated with DFT at the B3LYP/cc-pVTZ level of theory (unscaled) given in Table 7.5.

### 7.3.5 OTHER $C_{10}H_9^+$ AND $C_{10}H_9$ ISOMERS

Besides absorptions of the two HN$^+$ isomers and respective neutral species, another cationic system is present in the spectrum of $C_{10}H_9^+$ produced from 1,2-DHN. This feature at 377.8 nm is imposed on the broad UV absorption of $\alpha$-HN$^+$ (Figure 7.9). Several relatively sharp bands spaced 269, 471, 764, 943 and 1087 cm$^{-1}$ from the origin contribute to this system (Table 7.1).

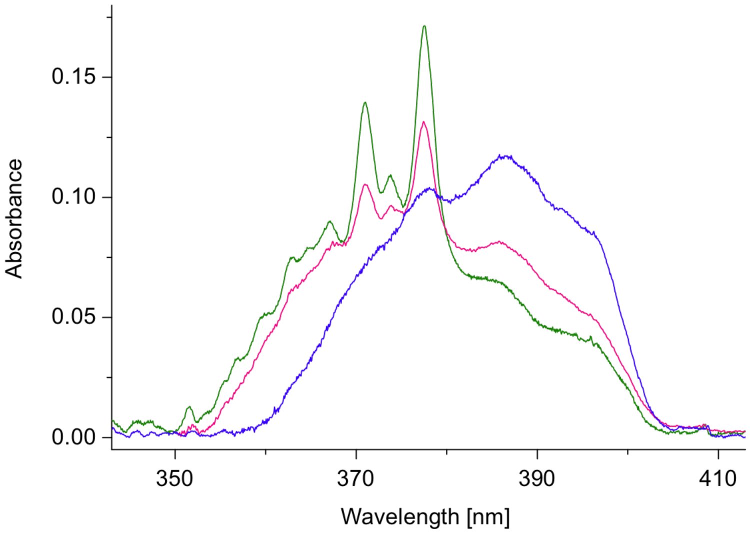

**Figure 7.9:** Part of the electronic absorption spectrum of $C_{10}H_9^+$ produced from a naphthalene/methanol mixture (blue trace), 1,2-dihydro-naphthalene (red) and 2-methyl-indene (green) and deposited in a neon matrix with scavenger. The spectra were normalized to the same accumulated charge of $C_{10}H_9^+$. $S_2 \leftarrow S_0$ transitions of $\alpha$-protonated naphthalene and 2-indenylmethylium overlap.

Previous studies from this laboratory on different aromatic as well as aliphatic hydrocarbons has shown that several isomers of cations of a given $m/z$ can be trapped in neon. This has been demonstrated on the benzotropylium and 2-naphtylmethylium cations [25]. Formation of these bicyclic structures was observed as the preferred channels even if open-chain precursors were used. Two lowest energy isomers of $C_{10}H_9^+$ next to $HN^+$ (Figure 7.2) are considered, therefore, as possible candidates of these new absorptions. These are 1-HAz$^+$ and 2-IMe$^+$.

Protonated naphthalene is, to some extent, a "benzene-fused" analogue of protonated benzene. Numerous experimental studies on $C_6H_7^+$ isomers pointed out the presence of the $\alpha$-protonated fulvene, nearest in energy isomer to protonated benzene [26-28]. Their isomerization was also treated theoretically [29]. Both isomers, protonated benzene and $\alpha$-protonated fulvene were simultaneously trapped in neon under similar experimental conditions to the present study (Chapter 4). Moreover, formation of benzofulvene was found to be an intermediate step in the $^{13}C$-labeled topomerization of naphthalene; production of hydronaphthyl and naphthalene has been observed as products of 2-MetI in a heated shock tubes [30-33].

To test whether the 378 nm absorption system belongs to benzofulvenic $C_{10}H_9^+$ isomer, the $m/z$=129 cations were produced from 2-MetI and deposited into a neon matrix with electron scavenger. Similar spectrum is observed to that using 1,2-DHN. All the visible and UV spectral features of $\alpha$- and $\beta$-HN$^+$ discussed above are present, though much weaker; the one around 378 nm is at the same time stronger (Figure 7.9, blue trace). The spectra shown are normalized to the same deposited charge, but may not reproduce correctly the intensity of the underlying transition of $\alpha$-HN$^+$ due to the hydrogen migration upon the measurements. Nevertheless, the intensity of the 378 nm band remains the same upon irradiation from the scanning. All these mean higher yield of this cation starting from 2-MetI and confirms its benzofulvenic structure. In addition, the carrier of the dominant $m/z$=115 in the mass spectrum of DHN (Figure 7.1) was found to be of indene-like structure (Chapter 9.2).

Calculations predict 2-IMe$^+$ as the most stable structure of $C_{10}H_9^+$ with an indene skeleton, 33 kJ mol$^{-1}$ above $\alpha$-HN$^+$ (Figure 7.2). It can be formed from the 2-MetI precursor by a simple H loss from the methyl group, this being the preferred route for fragmentation. The fourth considered isomer, 1-HAz$^+$, is even lower in energy than 2-IMe$^+$; however, its production from the indene-based precursor is less probable, as it would involve a rearrangement of a six-membered ring breaking its high (aromatic) stability.

Photobleaching of the matrix containing $C_{10}H_9^+$ produced from 1,2-DHN resulted in an increase of the $\alpha$-HN and $\beta$-HN features as well as of the new systems with origins at 451 and 284 nm respectively. The latter were even stronger after photobleaching of $C_{10}H_9^+$ produced from 2-MetI. Therefore, these two systems are assigned to the 2-IMe neutral radical. The wavelengths of the vibrational bands with their assignment based on the calculated frequencies of the normal modes in the ground state of this radical are given in Table 7.1.

## 7.4 COMPUTATIONAL RESULTS

### 7.4.1 ELECTRONIC TRANSITIONS OF $C_{10}H_9^+$ AND $C_{10}H_9$ ISOMERS

TD DFT and CC2 vertical electronic excitation energies from the ground states of the four most stable $C_{10}H_9^+$ isomers of Figure 7.2 and the corresponding $C_{10}H_9$ neutrals are listed in Table 7.4, and compared with experimental data. There are two absorption band systems for a given $C_{10}H_9^+$ species with reasonable oscillator strengths $f$ in the experimentally accessible spectral domain.

**Table 7.4** Excited-state symmetries, vertical excitation energies $\Delta E_\mathrm{V}$ and oscillator strengths $f$ for three considered $C_{10}H_9^+$ isomers and $C_{10}H_9$ neutrals calculated with two different methods, and comparison with experimental data[a]

| | TD DFT//B3LYP/cc-pVDZ | | CC2//MP2/cc-pVDZ | | |
|---|---|---|---|---|---|
| Exc. state | $\Delta E_\mathrm{V}$ /eV | $f$ | $\Delta E_\mathrm{V}$ /eV | $f$ | Expt.[b] /eV |
| **α-HN**$^+$, $X$ $^1$A' | | | | | |
| $^1$A′ | 2.86 | 0.020 | 2.95 | 0.037 | 2.47 |
| $^1$A′ | 3.60 | 0.25 | 3.48 | 0.32 | 3.13 |
| $^1$A″ | 4.75 | 0.0007 | 5.08 | 0.0009 | |
| **β-HN**$^+$, $X$ $^1$A′ | | | | | |
| $^1$A | 2.78 | 0.074 | 2.73 | 0.11 | 2.32 |
| $^1$A′ | 4.36 | 0.075 | 4.42 | 0.17 | 3.85 |
| $^1$A | 4.53 | 0.012 | 4.63 | 0.011 | |
| **2-IMe**$^+$, $X$ $^1$A′ | | | | | |
| $^1$A′ | 2.82 | 0.017 | 2.95 | 0.025 | |
| $^1$A′ | 3.83 | 0.55 | 3.68 | 0.66 | 3.28 |
| $^1$A″ | 4.67 | 0 | 5.08 | 0 | |
| $^1$A′ | 5.03 | 0.028 | 5.17 | 0.033 | |
| **1-HAz**$^+$, $X$ $^1$A′ | | | | | |
| $^1$A′ | 3.69 | 0.011 | 3.91 | 0.19 | |
| $^1$A′ | 3.94 | 0.19 | 4.06 | 0.041 | |
| $^1$A′ | 5.04 | 0.035 | 5.23 | 0.054 | |
| **α-HN**, $X$ $^2$A″ | | | | | |
| $^2$A′ | 2.82 | 0.0014 | 3.45 | 0.0011 | 2.35 |
| $^2$A′ | 3.16 | 0.0013 | 4.05 | 0.0010 | 3.36 |
| $^2$A′ | 3.65 | 0.021 | 4.57 | 0.28 | 3.75 |
| $^2$A′ | 3.84 | 0.20 | 4.65 | 0.0005 | 3.87 |
| $^2$A′ | 4.02 | 0.076 | 4.71 | 0.028 | |
| **β-HN**, $X$ $^2$A″ | | | | | |
| $^2$A′ | 2.42 | 0.0001 | 3.29 | 0.0008 | |
| $^2$A′ | 3.17 | 0.054 | 3.93 | 0.0009 | 2.40 |
| $^2$A′ | 3.33 | 0.0025 | 4.12 | 0.081 | |
| $^2$A′ | 3.56 | 0.0001 | | | |
| $^2$A′ | 4.29 | 0.025 | | | |
| **2-IMe**, $X$ $^2$A″ | | | | | |
| $^2$A′ | 2.89 | 0.015 | 3.46 | 0.026 | 2.75 |
| $^2$A′ | 3.21 | 0.0018 | 4.10 | 0.0025 | |
| $^2$A′ | 3.59 | 0.016 | 4.59 | 0.084 | 4.36 |
| $^2$A′ | 4.00 | 0.039 | 4.63 | 0.070 | |
| $^2$A′ | 4.28 | 0.40 | | | |
| **1-HAz**, $X$ $^2$A″ | | | | | |
| $^2$A′ | 2.79 | 0.0088 | | | |
| $^2$A′ | 3.06 | 0.0004 | | | |
| $^2$A′ | 3.66 | 0.041 | | | |
| $^2$A′ | 3.98 | 0.12 | | | |

**Table 7.5** Ground-state totally symmetric vibrational fundamentals (a' in $C_S$, unscaled) of $C_{10}H_9^+$ cations and $C_{10}H_9$ neutrals calculated with DFT at the BLYP/cc-pVTZ level of theory

| Frequencies /cm$^{-1}$ |
|---|
| **$\alpha$-HN$^+$** |
| 3222, 3221, 3207, 3199, 3194, 3192, 3182, 2981, 1663, 1613, 1590, 1546, 1493, 1463, 1438, 1406, 1370, 1313, 1290, 1259, 1211, 1187, 1181, 1150, 1109, 1050, 974, 922, 796, 751, 607, 502, 501, 355 |
| **$\beta$-HN$^+$** |
| 3222, 3213, 3210, 3200, 3197, 3195, 3183, 2969, 1669, 1645, 1582, 1537, 1506, 1455, 1434, 1422, 1371, 1304, 1284, 1260, 1232, 1190, 1172, 1155, 1049, 1040, 934, 931, 783, 749, 614, 508, 501, 361 |
| **2-IMe$^+$** |
| 3259, 3222, 3211, 3210, 3206, 3196, 3153, 3042, 1666, 1651, 1596, 1534, 1483, 1457, 1427, 1400, 1385, 1361, 1311, 1225, 1206, 1201, 1174, 1133, 1029, 989, 893, 888, 804, 665, 592, 492, 450, 270 |
| **1-HAz$^+$** |
| 3247, 3229, 3203, 3195, 3186, 3178, 3174, 3025, 1647, 1626, 1612, 1574, 1533, 1474, 1468, 1391, 1366, 1349, 1303, 1266, 1261, 1225, 1150, 1122, 1061, 981, 969, 899, 838, 744, 674, 500, 406, 337 |
| **$\alpha$-HN** |
| 3197, 3192, 3182, 3180, 3166, 3162, 3157, 2951, 1639, 1607, 1563, 1514, 1469, 1435, 1415, 1388, 1365, 1324, 1271, 1230, 1201, 1168, 1166, 1134, 1090, 1059, 957, 919, 792, 749, 609, 504, 485, 357 |
| **$\beta$-HN** |
| 3199, 3183, 3177, 3168, 3165, 3163, 3154, 2926, 1686, 1613, 1568, 1504, 1456, 1441, 1415, 1402, 1360, 1355, 1285, 1242, 1201, 1169, 1156, 1134, 1053, 1039, 925, 905, 783, 753, 611, 503, 497, 356 |
| **2-IMe** |
| 3243, 3207, 3198, 3185, 3173, 3167, 3143, 3030, 1635, 1614, 1540, 1502, 1473, 1424, 1408, 1393, 1345, 1326, 1283, 1215, 1192, 1179, 1160, 1114, 1038, 980, 886, 878, 808, 663, 597, 488, 448, 268 |
| **1-HAz** |
| 3227, 3195, 3182, 3170, 3155, 3143, 3137, 3005, 1660, 1623, 1563, 1514, 1458, 1432, 1410, 1380, 1335, 1284, 1252, 1236, 1208, 1124, 1076, 1048, 978, 952, 927, 888, 758, 668, 559, 492, 404, 330 |

TD DFT and CC2 calculations predict, that the two lowest energy electronic transitions ($S_1$ and $S_2$) of $\alpha$-$HN^+$ and $\beta$-$HN^+$ result from the $^1\pi\pi^*$ excitation. Vertical excitation energies calculated for the ground state geometry of the cations are overestimated by 0.3–0.5 eV with respect to the neon matrix data (Table 7.4). The agreement is much better for the adiabatic excitation energies, where geometries of both states involved in the electronic transition were optimized. The calculation predicts also the right order of the electronic systems in the spectra of these cations. In the visible range $\beta$-$HN^+$ absorbs at the longer wavelengths than $\alpha$-$HN^+$, whereas in the UV it is the reverse. Moreover the calculated oscillator strengths qualitatively agree with the observed relative intensities of the $S_1 \leftarrow S_0$ and $S_2 \leftarrow S_0$ transitions of the two cations: an order of magnitude stronger UV transition of $\alpha$-$HN^+$ than the visible one, whereas similar oscillator strengths for $\beta$-$HN^+$. As for the 2-$IMe^+$, calculations predict a weak transition in the visible and much stronger (~50 times, Table 7.4) in the UV. The intensity of the first transition of 2-$IMe^+$ was too low to be observed in the present experiment. In the case of the $C_{10}H_9$ open-shell radicals, the agreement is somewhat worse which may be due to the multi-reference character of their excited states. Further discussion is restricted to the higher-level CC2/MP2 methods and to the two isomers of protonated naphthalene.

### 7.4.2 ELECTRONIC STATES AND PHOTOPHYSICS OF $HN^+$

The ground-state unrestrained optimization of $\alpha$- and $\beta$-$HN^+$ leads to two stable, planar forms, $C_s^{\alpha}(S_0)$ and $C_s^{\beta}(S_0)$, respectively, the latter being ~0.16 eV higher in energy. They are separated from each other by an energy barrier of ~0.49 eV on the ground-state PES (Figure 7.10). The energy landscape of the excited states is more complex. Optimization of the first excited states with the $C_s$ symmetry constrain starting from the ground-state equilibrium geometries leads to almost isoenergetic excited-state geometries, $C_s^{\alpha}(S_1)$ and $C_s^{\beta}(S_1)$, at 2.56 and 2.57 eV above $C_s^{\alpha}(S_0)$ (Table 7.6). While the planar $C_s^{\alpha}(S_1)$ form is the stable $S_1$ minimum of $\alpha$-$HN^+$, $C_s^{\beta}(S_1)$ is unstable with respect to the out-of-plane deformation of the $CH_2^+$ moiety. The unrestrained optimization of this latter geometry results in a $C_1^{\beta}(S_1)$ prefulvenic-like structure of 2.38 eV energy (Figure 7.10 and Table 7.6). The corresponding prefulvenic form of the $C_1^{\alpha}(S_1)$ conformer was also found. Even though its energy (2.50 eV) is slightly lower than that of the $C_s^{\alpha}(S_1)$ conformer these two excited state minima are separated by a small energy barrier of about 0.05 eV (Figure 7.10). The interatomic distance between the two carbon atoms adjacent to the $CH_2^+$ moiety of the two prefulvenic forms is significantly shorter in comparison to the corresponding distance in the planar structures. What both $S_1$-prefulvenic geometries have also in common is the significant raise of the ground state energy for these two geometries, which results in the dramatic decrease of the energy gap between the $S_1$ and $S_0$ electronic states, which could amplify the nonadiabatic coupling between the states and efficient internal conversion to the ground state. The $S_0$ and $S_1$ states become almost degenerate for both $C_1^{\alpha}(S_1)$ and $C_1^{\beta}(S_1)$ geometries as is indicated in Figure 7.10 by overlapping of the solid-red and dashed-black lines.

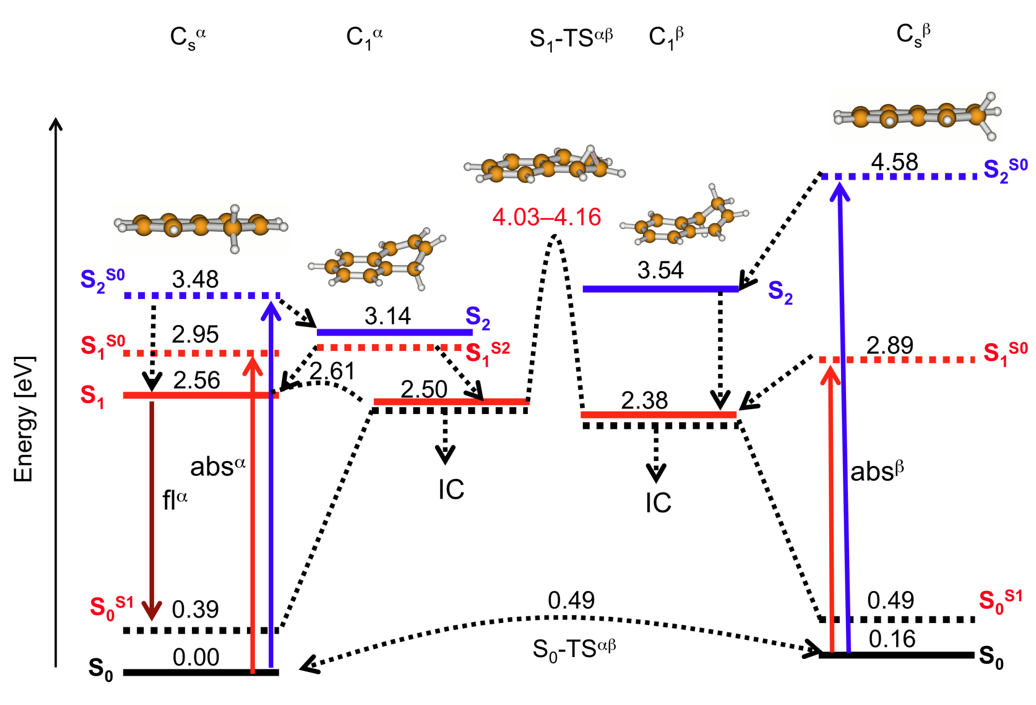

**Figure 7.10:** Vertical (dashed lines) and adiabatic (solid) energies for the $S_1 \leftarrow S_0$ and $S_2 \leftarrow S_0$ transitions of *alpha* and *beta* isomers of protonated naphthalene. Ground-state energy computed at the optimized geometry of the first or second excited-state minimum is denoted as $S_0^{S1}$ or $S_0^{S2}$, respectively. The energy (eV) of a given state is relative to the $C_s^{\alpha}(S_0)$ global minimum. The spectroscopic processes (absorption "abs" and fluorescence "fl") that were observed in the experiments are indicated by solid, colored arrows, whereas the radiationless processes (vibrational relaxation and internal conversion "IC") assumed to play a role are indicated by black, dashed lines.

The $C_s$ symmetry-restricted optimization of the second singlet excited states $S_2$ gives the $C_s^{\alpha}(S_2)$ and $C_s^{\beta}(S_2)$ forms, whose adiabatic electronic excitation energies are 3.25 and 4.39 eV, respectively. Both, however, have an imaginary out-of-plane vibration of the $CH_2^+$ unit; their unconstrained optimization results in two stable minima, $C_1^{\alpha}(S_2)$ and $C_1^{\beta}(S_2)$, at 3.14 and 3.54 eV (Figure 7.11, Table 7.6). The proximity of the $C_1^{\alpha}(S_2)$ and $C_1^{\alpha}(S_1)$ levels (which are separated only by 0.64 eV ) will cause an ultrafast relaxation of $\alpha$-HN$^+$ in the $S_2$ state to the $S_1$ state lying nearby. The fast decay of the $S_2$ state can explain broadness and weakly discerned vibrational structure in the UV absorption band of $\alpha$-HN$^+$ seen in Figure 7.5. The corresponding energy difference for $b$-conformer is 1.16 eV and the cation lives much longer in the $S_2$ state than one vibrational period and the vibrational pattern is well seen in the UV spectrum.

**Table 7.6** Adiabatic energies [relative to the $C_s^{\alpha}(S_0)$ global minimum] for the $S_1 \leftarrow S_0$ and $S_2 \leftarrow S_0$ transitions of protonated naphthalenes calculated at the excited-state minima $S_1$ and $S_2$, ground-state energies at the optimized geometry of the first or second excited-state minima $S_0^{S1}$ or $S_0^{S2}$, and fluorescence energies $\Delta E^{fl}$ for the given $S_1$ minima obtained with the CC2/cc-pVDZ method excited-state equilibrium geometries[a]

| | Forms of the ground state, $S_0$ | | | |
|---|---|---|---|---|
| | **$C_s^{\alpha}(S_0)$** | | | **$C_s^{\beta}(S_0)$** |
| $S_0$ | 0. | | | 0.16 |
| | Forms of the first excited state, $S_1$ | | | |
| | **$C_s^{\alpha}(S_1)$** | **$C_1^{\alpha}(S_1)$** | **$C_1^{\beta}(S_1)$** | **$C_s^{\beta}(S_1)$** |
| $S_1$ | 2.56 | 2.50 | 2.38 | 2.57 |
| $S_0^{S1}$ | 0.39 | 1.92 | 2.37 | 0.49 |
| $\Delta E^{fl}$ | 2.17 | 0.58 | 0.01 | 2.08 |
| | Forms of the second excited state, $S_2$ | | | |
| | **$C_s^{\alpha}(S_2)$** | **$C_1^{\alpha}(S_2)$** | **$C_1^{\beta}(S_2)$** | **$C_s^{\beta}(S_2)$** |
| $S_2$ | 3.25 | 3.14 | 3.54 | 4.39 |
| $S_1^{S2}$ | 2.86 | 2.99 | 2.97 | 2.75 |
| $S_0^{S2}$ | 0.26 | 0.67 | 2.75 | 0.35 |

[a] All values in eV.

The computational results in Figure 7.10 suggest the $S_1 \rightarrow S_0$ internal conversion to be an efficient and fast deactivation process in view of the $S_1$–$S_0$ energy gap. Although the CC2 approach, being a single-reference method, is unable to locate precisely and characterize the conical intersection (CI) between these states, the result strongly suggests the presence of CI in the vicinity of the optimized geometry. A CASSCF search for the lowest-energy CI between the $S_1$ and $S_0$ states starting from the CC2 optimized geometries $C_1^{\alpha}$ and $C_1^{\beta}$ of the $S_1$ state resulted in the location of the chair-like $CI^{\alpha}$ and $CI^{\beta}$ structures (Figure 7.11). Both these have the same motif of the $\beta$-carbon being distorted out of the molecular plane, independently of the location ($\alpha$ or $\beta$) of the proton.

The $C_s^{\alpha}(S_1)$ and $C_s^{\beta}(S_1)$ minima are separated by a barrier of ~1.5 eV or more (Figure 7.10). This practically precludes a PT reaction to take place on the excited-state PES, even considering the excess energy from the (vertical) excitation to the $S_2$. This is in contrast to the situation in the ground state where the two isomers are separated by a much smaller barrier. An explanation of this difference is that in the $S_0$ state the “excess” proton interacts with the neutral molecular frame and, thus, can easily “jump” between carbon atoms. The $S_1 \leftarrow S_0$ excitation of $HN^+$ neutralizes to some extent the positive charge on the protonated ring and the $CH_2^+$ moiety of the ground state adopts in the excited state locally an “alkanic” $CH_2$ character, as it can be seen from the inspection of the molecular orbitals involved (Figure 7.11). The transformation of one isomer into another involves breaking and formation of the (partially) covalent C–H bond, which is reflected by the high barrier on the PES of the $S_1$ state.

The following photophysical scheme of $HN^+$ emerges from the theoretical studies. For the a-$HN^+$ there are two close lying excited state forms, the planar $C_s^{\alpha}(S_1)$ and the non-planar $C_1^{\alpha}(S_1)$ separated by a low barrier (see Figure 7.10). An optical excitation of the $\alpha$-isomer near the “bottom” of the $S_1$ state results in fluorescence from this state because this local minimum is protected by a barrier from the $S_1/S_0$ $CI^{\alpha}$. At higher-energy excitation to this state, or due to an excitation within the $S_2$ manifold, access to the $CI^{\alpha}$ opens and the system may return to the ground state in a radiationless way with little probability for emission from the local minimum of the $S_1$ state. In case of the $\beta$-isomer there is no stable minimum on the $S_1$ PES near the Franck–Condon geometry which could be protected by a barrier from the “abyss” of the CI with the ground state. The relaxation of this planar geometry to its relaxed $CI^{\beta}$ form is exothermic by about 0.5 eV. Thus, the $\beta$-isomer is not expected to fluoresce from $C_s^{\beta}(S_1)$ or $C_1^{\beta}(S_1)$ forms as both are subject to fast non-radiative deactivation to the ground electronic state. In other words, $\beta$-$HN^+$ is expected to deactivate optical excitation *via* the radiationless pathway through the $S_1/S_0$ conical intersection $CI^{\beta}$. These findings are in accord with the experimental observations.

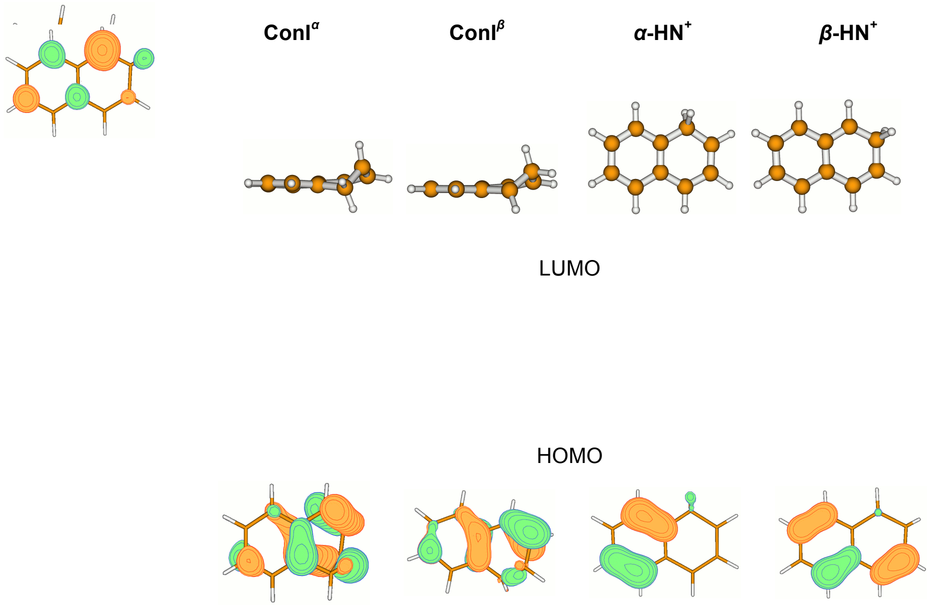

**Figure 7.11:** Left: Geometrical structure of the $S_1/S_0$ conical intersections ("ConIs") determined at the CASSCF(2,2)/cc-pVDZ level for *alpha* and *beta* isomers of protonated naphthalene and the relevant CASSCF natural orbitals. Right: Geometry, and HOMO and LUMO orbitals involved in the S1 ← $S_0$ excitation of the two isomers obtained at the MP2/cc-pVDZ level of theory in $C_s$ symmetry.

Another question regards the mechanism of the photoinduced conversion between the two HN$^+$ isomers. Inspection of Figure 7.10 suggests that a PT process in the excited-state is unlikely to occur in view of a large barrier separating these species; such a reaction can only take place on the ground-state PES, because this state is populated with high excess of vibrational energy due to the $S_1 \rightarrow S_0$ internal conversion at the CIs. This energy is high enough to overcome the ground-sate barrier, and to "thermalize" and cool down (due to the interaction with environment) the molecular system in one of the isomeric minima on the $S_0$ PES. The photoinduced isomerization mechanism sketched above is similar to that suggested previously for protonated benzene.[20] It was predicted that none of the first four lowest-lying excited singlet states of HB$^+$ would show fluorescence but rather undergo a fast non-radiative decay.

## 7.5 CONCLUSIONS

Protonated PAHs are produced efficiently *via* in a proton transfer reaction of parent PAHs with suitable proton donors such as simple alcohols, when the donor's PA is ~50 kJ mol$^{-1}$ lower than the acceptor's. Such a reaction route prefers production of the most stable

H-PAH$^+$ isomer over other alternatives. Whenever available, dihydro-PAHs can also be used as a precursor; they get ionized and fragmented (H loss) in discharge-type environments, and form several structural isomers of the respective (small) H-PAH$^+$.

*Alpha*- and *beta*-protonated naphthalenes possess moderately intense $S_1/S_2 \leftarrow S_0$ transitions in the visible and UV spectral regions (calculated oscillator strengths $f \sim 0.05$–0.3), with origin bands located in a neon matrix at 502.1 and 396.1 nm for $\alpha$-HN$^+$, and 534.5 and 322.3 nm in the case of $\beta$-HN$^+$. $\alpha$-HN$^+$ was observed to fluoresce from its $S_1$ state upon both the excitation to $S_1$ or $S_2$. Another $C_{10}H_9^+$ isomer, 2-indenylmethylium (2-IMe$^+$), was produced from 1,2-DHN and 2-MetI and absorbs in the UV, with onset at 377.8 nm. $C_{10}H_9$ radicals corresponding to the detected cations reveal band systems with origin at 528.1 and 330.9 nm for $\alpha$-, 516.2 nm for $\beta$-hydronaphthyl and 451.2 and 284.1 nm in the case of 2-methylene-indene.

Selective irradiation ($390 > \lambda > 350$ nm) of the $S_2 \leftarrow S_0$ absorption of $\alpha$-HN$^+$ induces intramolecular proton transfer leading to the $\alpha\text{-HN}^+ \rightarrow \beta\text{-HN}^+$ isomerisation. This photoprocess is reversible: $\beta$-HN$^+$ relaxes rapidly into the by ~12 kJ mol$^{-1}$ more stable *alpha* form either *via* quantum tunnelling of the “excess” (liable) hydrogen or, upon $S_1 \leftarrow S_0$ excitation of $\beta$-HN$^+$, through one of the two out-of-plane, chair-like $S_1/S_0^{\alpha}$ or $S_1/S_0^{\beta}$, conical intersection geometries.

Theoretical calculations on the ground- and excited states of the HN$^+$ cations, vertical and adiabatic excitation energies and minimum-energy pathways along the relevant $r$(C–H) and r(C–C) reaction coordinates reveal complexity for even this “simple” H-PAH$^+$ system.

## BIBLIOGRAPHY

[1] G.A. Olah, J.S. Staral, G. Asencio, G. Liang, D.A. Forsyth, G.D. Mateescu. Stable carbocations. 215. 13C nuclear magnetic resonance spectroscopic study of the benzenium, naphthalenium, and anthracenium ions. *J. Am. Chem. Soc.,* 100 (1978) 6299-6308.

[2] G.A. Olah, G.D. Mateescu, Y.K. Mo. Stable carbocations. CXL. Naphthalenium ions. *J. Am. Chem. Soc.,* 95 (1973) 1865-1874.

[3] D.M. Hudgins, C.W. Bauschlicher, L.J. Allamandola. Closed-shell polycyclic aromatic hydrocarbon cations: a new category of interstellar polycyclic aromatic hydrocarbons. *Spectrochim. Acta, Part A,* 57 (2001) 907-930.

[4] A. Pathak, P.J. Sarre. Protonated PAHs as carriers of diffuse interstellar bands. *Mon. Not. Roy. Astron. Soc.,* 391 (2008) L10-L14.

[5] M. Hammonds, A. Pathak, A. Candian, P.J. Sarre. Spectroscopy of protonated and deprotonated PAHs, in: *PAHs and the Universe*; C. Joblin, A.G.G.M. Tielens, Eds.; *EAS Publications Series*, 46 (2011) 373-379.

[6] U.J. Lorenz, N. Solca, J. Lemaire, P. Maitre, O. Dopfer. Infrared spectra of isolated protonated polycyclic aromatic hydrocarbons: Protonated naphthalene. *Angew. Chem.-Int. Ed.,* 46 (2007) 6714-6716.

[7] A.M. Ricks, G.E. Douberly, M.A. Duncan. The infrared spectrum of protonated naphthalene and Its relevance for the Unidentified Infrared bands. *Astrophys. J.,* 702 (2009) 301-306.

[8] A.A.V. Stuart, E.L. Mackor. Electronic spectra of carbonium ions. *J. Chem. Phys.,* 27 (1957) 826-827.

[9] C. Reid. The aromatic carbonium ions. *J. Am. Chem. Soc.,* 76 (1954) 3264-3268.

[10] G. Dallinga, E.L. Mackor, A.A.V. Stuart. The absorption spectra of aromatic carbonium ions in HF solution. *Mol. Phys.,* 1 (1958) 123-140.

[11] H. Perkampus, E. Baumgarten. Proton-addition complexes of aromatic hydrocarbons. *Angew. Chem.-Int. Ed.,* 3 (1964) 776-783.

[12] I. Alata, C. Dedonder, M. Broquier, E. Marceca, C. Jouvet. Role of the charge-transfer state in the electronic absorption of protonated hydrocarbon molecules. *J. Am. Chem. Soc.,* 132 (2010) 17483-17489.

[13] I. Alata, R. Omidyan, M. Broquier, C. Dedonder, O. Dopfer, C. Jouvet. Effect of protonation on the electronic structure of aromatic molecules: naphthalene$H^+$. *Phys. Chem. Chem. Phys.,* 12 (2010) 14456-14458.

[14] E.P.L. Hunter, S.G. Lias. Evaluated gas phase basicities and proton affinities of molecules: An update. *J. Phys. Chem. Ref. Data,* 27 (1998) 244.

[15] F. Salama, L.J. Allamandola. Electronic absorption spectroscopy of matrix-isolated polycyclic aromatic hydrocarbon cations. I. The naphthalene cation ($C_{10}H_8^+$). *J. Chem. Phys.,* 94 (1991) 6964-6977.

[16] T. Bally, C. Carra, M. P. Fulscher, Z. Zhu. Electronic structure of the naphthalene radical cation and some simple alkylated derivatives. *J. Chem. Soc., Perkin Transact. 2,* (1998) 1759-1766.

[17] T. Chong, Y. Shibata, N. Itoh. Luminescence from the hydronaphthyl radicals in naphthalene single crystals. *Physica status solidi,* 27 (1975) 599-604.

[18] T. Nakayama, S.J. Sheng. Optical studies of hydronaphthyl radicals embedded in dihydronaphthalene crystal. *Mol. Cryst. Liq. Cryst.,* 69 (1981) 199-206.

[19] J.A. Sebree, V.V. Kislov, A.M. Mebel, T.S. Zwier. Spectroscopic and thermochemical consequences of site-specific H-atom addition to naphthalene. *J. Phys. Chem. A,* 114 (2010) 6255-6262.

[20] M.F. Rode, A.L. Sobolewski, C. Dedonder, C. Jouvet, O. Dopfer. Computational study on the photophysics of protonated benzene. *J. Phys. Chem. A,* 113 (2009) 5865-5873.

[21] M. Pettersson, E.M.S. Macoas, L. Khriachtchev, J. Lundell, R. Fausto, M. Rasanen. Cis -> trans conversion of formic acid by dissipative tunneling in solid rare gases: Influence of environment on the tunneling rate. *J. Chem. Phys.,* 117 (2002) 9095-9098.

[22] K. Marushkevich, L. Khriachtchev, M. Rasanen. High-energy conformer of formic acid in solid neon: Giant difference between the proton tunneling rates of cis monomer and trans-cis dimer. *J. Chem. Phys.,* 126 (2007) 241102-241104.

[23] L.B. Knight, J. Steadman, D. Feller, E.R. Davidson. Experimental evidence for a $C_{2v}$ (2B1) ground-state structure of the methane cation radical: ESR and ab initio CI investigations of methane cation radicals ($CH_4^+$ and $CD_2H_2^+$) in neon matrixes at 4 K. *J. Am. Chem. Soc.,* 106 (1984) 3700-3701.

[24] M.N. Paddon-Row, D.J. Fox, J.A. Pople, K.N. Houk, D.W. Pratt. Dynamic Jahn-Teller effect in methane radical cation. Location of the transition structures for hydrogen scrambling and inversion. *J. Am. Chem. Soc.,* 107 (1985) 7696-7700.

[25] A. Nagy, J. Fulara, J.P. Maier. Formation of aromatic structures from chain hydrocarbons in electrical discharges: absorption and fluorescence study of $C_{11}H_9^+$ and C11H9 isomers in neon matrices. *J. Am. Chem. Soc.,* 133 (2011) 19796-19806.

[26] S.G. Lias, P. Ausloos. Structures of $C_6H_7^+$ ions formed in unimolecular and bimolecular reactions. *J. Chem. Phys.,* 82 (1985) 3613-3624.

[27] G. Bouchoux, M.T. Nguyen, J.Y. Salpin. Condensation reactions between 1,3-butadiene radical cation and acetylene in the gas phase. *J. Phys. Chem. A,* 104 (2000) 5778-5786.

[28] J.A. Herman, K. Herman, T.B. McMahon. Formation of $C_6H_7^+$ ions in ion-molecule reactions in vinyl-chloride. *Can. J. Chem.-Rev. Can. Chim.,* 69 (1991) 2038-2043.

[29] G. Bouchoux, M. Yanez, O. Mo. Isomerization and dissociation processes of protonated benzene and protonated fulvene in the gas phase. *Int. J. Mass Spectrom.,* 187 (1999) 241-251.

[30] L.T. Scott, M.M. Hashemi, T.H. Schultz, M.B. Wallace. Thermal rearrangements of aromatic compounds. 15. Automerization of naphthalene. New evidence consistent with the intermediacy of benzofulvene. *J. Am. Chem. Soc.,* 113 (1991) 9692-9693.

[31] F. Dubnikova, A. Lifshitz. Ring expansion and isomerization in methyl indene and methylene indene radicals. Quantum chemical and transition-state theory calculations. *Israel J. Chem.,* 43 (2003) 325-338.

[32] A. Lifshitz, C. Tamburu, A. Suslensky, F. Dubnikova. Decomposition, isomerization, and ring expansion in 2-Methylindene: Single-pulse shock tube and modeling study. *J. Phys. Chem. A,* 108 (2004) 3430-3438.

[33] M. Lu, J.A. Mulholland. PAH Growth from the pyrolysis of CPD, indene and naphthalene mixture. *Chemosphere,* 55 (2004) 605-610.

## Chapter 8

# APPENDIX

Polycyclic aromatic hydrocarbon (PAH) cations are of astrophysical interest due to the fact that they are candidates for diffuse interstellar bands as well as for unidentified infrared bands. Although their molecular and electronic structure is relatively well studied, very little is known about their complex chemistry such as isomerization, photostability, dehydrogenation, or fragmentation patterns. Small PAHs are believed to be destroyed under harsh conditions of interstellar medium. Detection of several common fragments in the mass spectra of "smaller" PAHs during the present work encouraged identification of their structure. For this, several most prominent fragment cations and products of their ion-molecule reactions were isolated in neon and their electronic spectra were recorded. Results are presented in this chapter. Some of these results are side projects, some of them will be presented in details in the thesis of A. Nagy.

## A.1 RING-CHAIN CATIONS: $C_6H_5–C_{2N}H^+$, N=1–4

### A.1.1 INTRODUCTION

PAHs and their derivatives are of astrophysical interest as they are candidates for diffuse interstellar bands and for unidentified infrared bands [1-3]. Small unsaturated hydrocarbons $C_mH_n$ ($n$=1,2) are also common compounds in interstellar as well as terrestrial environments [4-6]. Many species, which belong to these classes of molecules were extensively studied by spectroscopic means.

Aromatic rings fused with aliphatic species may arise, under specific conditions, as a result of reactions between molecules of the two classes. Moreover, such "ring-chains" may play an important role as intermediates in the PAH formation processes. Stepwise acetylation of a benzene ring and/or reactions of resonance-stabilized free radicals are examples of such reactions [7, 8]. Furthermore, in space they could be produced during dust grain sputtering under harsh environmental conditions.

Electronic spectra of some such species should exhibit a strong "single" transition in the visible spectral range [9]. Recent experimental studies in conjunction with computational showed this on example of $C_{11}H_9^+$ isomers and correspondent neutrals [10]. To contribute, reactions of benzene/phenylacetylene with $HC_2H$/$HC_4H$ have been investigated (see Figure 3.3) and electronic spectra of some selected ring-chain radical ions in neon matrices were recorded. Preliminary results on their structure are discussed.

### A.1.2 $C_8H_6^+$

Phenylacetylene cation ($PA^+$) is a prototypical product of the reaction of benzene and acetylene. It is identified as one of the most prominent fragment cations formed from small cyclic precursors (such as naphthalene, indene or cyclooctatetraene) and is readily formed in ion-molecule reactions of linear precursor mixtures [10, 11]. It has been studied extensively by different experimental methods in the gas phase [12]. Its electronic spectrum recorded after deposition of $m/z = 102$ cations produced from Phenylacetylene/He onto a neon matrix is presented (Figure A.1). It is characterized by a strong transition in the visible with an origin at ~567 nm. The given assignment of the electronic transition and its vibrational bands are taken from ref. [12].

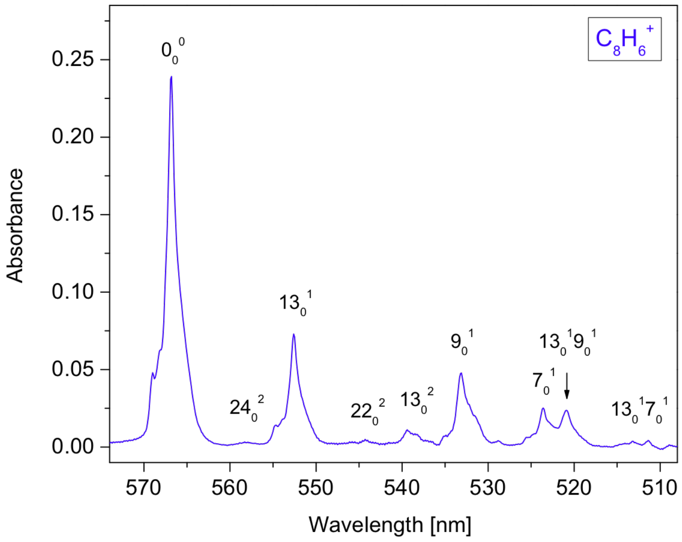

**Figure A.1:** $C\ ^2B_1 \leftarrow X\ ^2B_1$ electronic transition of phenylacetylene$^+$ radical cation as recorded after deposition of the $m/z = 102$ ions produced from phenylacetylene diluted with He into a neon matrix. Assignment is from ref. [12]

### A.1.3 $C_{10}H_6^+$ ISOMERS

Cation of $m/z = 126$ is the next, after PA$^+$, member of the $\Phi$-$C_{2n}H^+$ series. Two strong electronic transitions at around 671 and 378 nm dominate the spectrum of this cation (Figure A.2, blue) if produced in a reaction of PA with $HC_2H$ in an ion source. The first transition is red-shifted by ~100 nm from the known $C\ ^2B_1 \leftarrow X\ ^2B_1$ transition of PA$^+$ [12]. Such a shift may be related to some extent to the size dependent transitions observed for linear carbon chains [13, 14]. The $m/z = 126$ cation differs from the PA$^+$ by an additional $C_2$ unit. One could expect in this case either an elongation of a carbon chain on a ring or, reflecting the nature of electrophilic aromatic substitution reactions, production of ortho/para isomers. To deduce the structure of the $m/z = 126$ cation observed in the experiment above, the ions were also produced from two other precursors—benzene/$HC_4H$ mixture and *para*-diethynylbenzene (*p*-DEB). The spectra recorded after deposition of the respective ions are compared to that of $C_{10}H_6^+$ produced from a PA/$HC_2H$ mixture (Figure A.2). From the spectra is clearly seen, that two isomers of $C_{10}H_6^+$ are formed in the latter reaction. The less populated isomer of $C_{10}H_6^+$ has an identical band system to the parent ion produced from *p*-DEB. The spectrum of the major $m/z = 126$

isomer is identical to the one obtained in reaction of benzene and diacetylene. In the latter, one can expect a preferential formation of phenyldiacetylene cation.

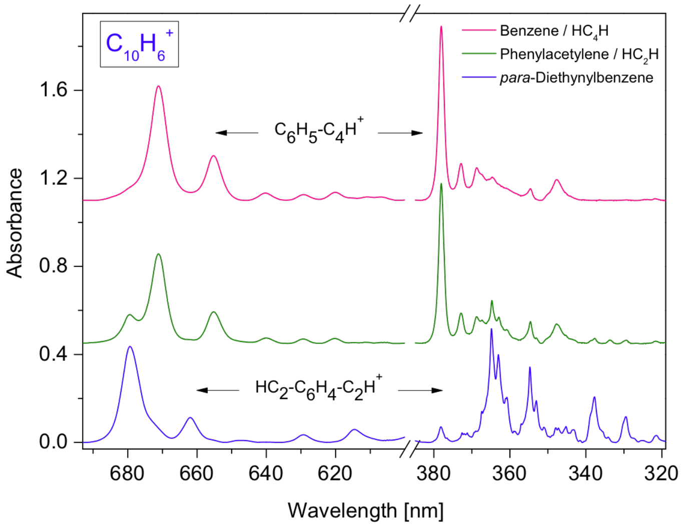

**Figure A.2:** Electronic absorption spectra of $C_{10}H_6^+$ ($m/z$ = 126) cations produced from different precursor mixtures.

Thus, ion-molecule reactions between PA and acetylene in the ion source lead to the formation of two isomers of $C_{10}H_6^+$. The major product is the phenyldiacetylene cation, which is formed by elongation of the acetylenic chain. Much less populated is the *p*-$DEB^+$, which is a product of H atom substitution by acetynyl radical in *para* position of PA.

In order to support the assignment, several isomeric structures of $C_{10}H_6^+$ have been considered for theoretical exploration (Figure A.3). Their ground-state geometry was optimized with DFT method at the B3LYP/6-311G(d,p) level of theory. Vibrational analysis was done to ensure that all the isomers are local minima on the $C_{10}H_6^+$ potential energy surface. Excitation energies were computed with TD DFT at the same level. The results are collected in Table A.1. According to these calculations, the two isomers are the lowest in energy. Calculated transitions energies are in good agreement with experimental observations (Table A.1).

The structure of the $C_{10}H_6^+$ isomers produced in the ion-molecule reactions of PA with $HC_2H$ was also confirmed by the detection of their neutral products, which are formed by photobleaching the cations in the matrix. The strongest absorption of neutrals observed in the UV region is the known band system of phenyldiacetylene [15]. Absorption of *p*-DEB [16] is barely observed in the spectrum of PA/$HC_2H$.

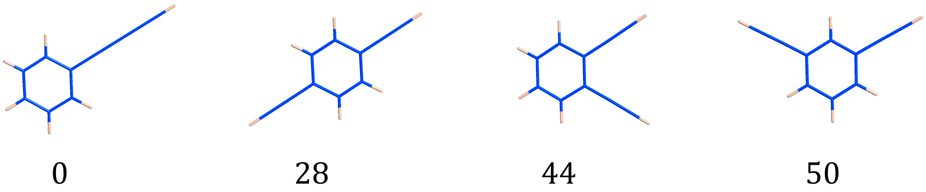

**Figure A.3:** Structures and relative ground-state energies (kJ mol$^{-1}$, corrected for ZPE) of the four considered $C_{10}H_6^+$ isomers obtained with DFT at the B3LYP / 6-311G(d,p) level of theory.

**Table A.1** Vertical excitation energies for $C_{10}H_6^+$ isomers obtained with TD DFT at the B3LYP/6-311G(d,p) level of theory. Relative ground-state energies (kJ mol$^{-1}$) with respect to the most stable isomer are given in parentheses.

| Exc. State | $\Delta E_V$ / eV | $\lambda$ / nm | $f$ | Exp. / eV (nm) |
|---|---|---|---|---|
| 1,1-DiEthBenzene$^+$, $X\,^2B_1$, $C_{2v}$ (0) | | | | |
| $^2A_2$ | 0.86 | 1146 | 0 | |
| $^2B_2$ | 1.21 | 1022 | 0.0004 | |
| $^2A_1$ | 2.16 | 574 | 0.15 | 1.85 (671) |
| $^2A_2$ | 3.35 | 370 | 0 | |
| $^2A_1$ | 3.45 | 359 | 0.12 | 3.28 (378) |
| $^2A_1$ | 3.48 | 356 | 0.0044 | |
| 1,4- DiEthBenzene$^+$, $X\,^2B_{2g}$, $D_{2h}$ (28) | | | | |
| $^2B_{3g}$ | 1.43 | 867 | 0 | |
| $^2A_u$ | 1.61 | 770 | 0 | |
| $^2B_{1g}$ | 1.65 | 751 | 0 | |
| $^2B_{1u}$ | 1.98 | 625 | 0.16 | 1.83 (679) |
| $^2A_g$ | 3.40 | 365 | 0 | |
| $^2B_{1u}$ | 3.78 | 328 | 0.49 | 3.40 (365) |
| $^2B_{1g}$ | 3.89 | 318 | 0 | |
| $^2B_{2u}$ | 4.10 | 302 | 0.0082 | |
| 1,2-DiEthBenzene$^+$, $X\,^2B_1$, $C_{2v}$ (44) | | | | |
| $^2B_2$ | 0.86 | 1448 | 0.0093 | |
| $^2A_2$ | 1.41 | 879 | 0 | |
| $^2B_1$ | 1.59 | 778 | 0 | |
| $^2A_1$ | 2.55 | 486 | 0.064 | |
| $^2B_2$ | 2.69 | 461 | 0.026 | |
| $^2A_1$ | 3.70 | 335 | 0.026 | |
| $^2B_2$ | 3.74 | 332 | 0.12 | |
| $^2B_1$ | 3.82 | 325 | 0.0001 | |
| 1,3-DiEthBenzene$^+$, $X\,^2A_2$, $C_{2v}$ (50) | | | | |

### A.1.4 $C_{12}H_6^+$ AND $C_{14}H_6^+$

Larger members of the Φ-$C_{2n}H^+$ series have been produced from a PA/$HC_4H$ mixture and their spectra were measured in absorption in neon matrices (Figure A.4).

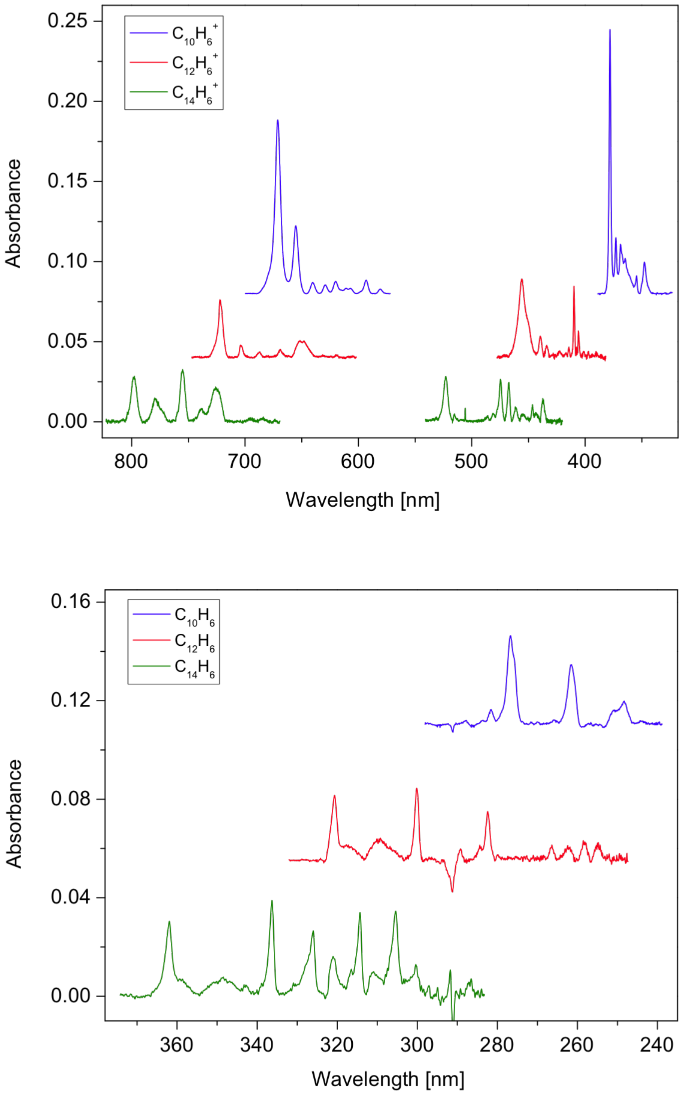

**Figure A.4:** Electronic absorption spectra of Φ-$C_{2n}H^+$ cations (upper panel) and the corresponding neutrals (lower) in neon matrices. $C_{12}H_6^+$ and $C_{14}H_6^+$ have been produced from PA/$HC_4H$/He=(1:4):1 mixture. Absorption spectra of neutral Φ-$C_{2n}H$ species have been recorded after photobleaching the cations.

Two band systems are well discernible in the spectra of $C_{12}H_6^+$ and $C_{14}H_6^+$, similarly as is observed for $C_{10}H_6^+$. Both transitions of the cations shift to the red as the size of the cations increases; the wavelengths of the origin bands does not exhibit a linear dependence as a function of the number of $C_2$ subunits in the linear substituent, as it is known for linear carbon and hydrocarbon chains. After photobleaching the cations, absorptions of neutrals have been detected in the UV range (Figure A.4). The redshift of the origin bands of the neutrals shows linear dependence on the size of the carbon chain, similar to the cations.

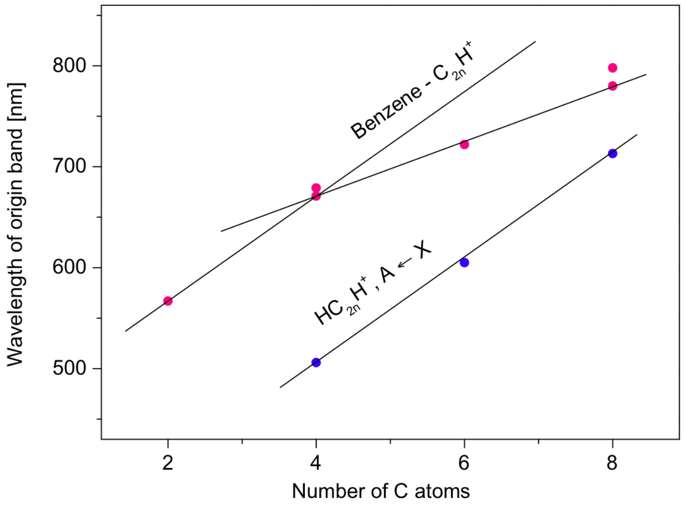

**Figure A.5:** Wavelengths of the origin bands of electronic transitions of $HC_{2n}H^+$ and Φ-$C_{2n}H^+$ (n = 1 – 4), plotted as a function of the number of carbon atoms of the absorbing species (attached to the benzene ring).

## A.2 “INDENE” SERIES

### A.2.1 $C_9H_7^+$

$C_9H_7^+$ (*m*/*e* = 115) is an abundant fragment in the mass spectra of various cyclic precursors (DHN, Naph., biphenyl); it is formed also from a mixture of linear hydrocarbons and many other precursors studied in this laboratory (Chapters 3, 7, [10]). Moreover, its mass is located between such stable ions as *m*/*z*=102 (PA) and 128 (Naph) (CH difference), and is expected then to be the most stable isomer on the $C_9H_7^+$ potential energy surface. From earlier mass spectrometric studies, the cation should be the same as generated from indene by low-energy electron ionization. Theoretical calculations predict that the most stable isomer is 1-indenylium cation; other isomers $C_9H_7^+$ are by 80–130 kJ mol$^{-1}$ higher in energy. In order to confirm this, $C_9H_7^+$ cations were produced from indene and selectively deposited to form a matrix. Two electronic transitions of cationic $C_9H_7^+$ and two of its neutral (stronger after mpHg bleaching) were identified (Figure A.6, Table A.2). The two cationic systems decay at the same rate (as well as the neutrals grow similarly); its stability with varying precursors and the results of calculations, all these point out that the carrier is the 1-indenylium cation. Moreover, the neutral absorptions at 465 nm, which are formed by neutralization of respective cations, are also seen as a fragment ($H_2$ loss) of protonated indene upon deposition and/or UV irradiation (section A.2.3). This provides further conformation of the „indene”-like structure of these species.

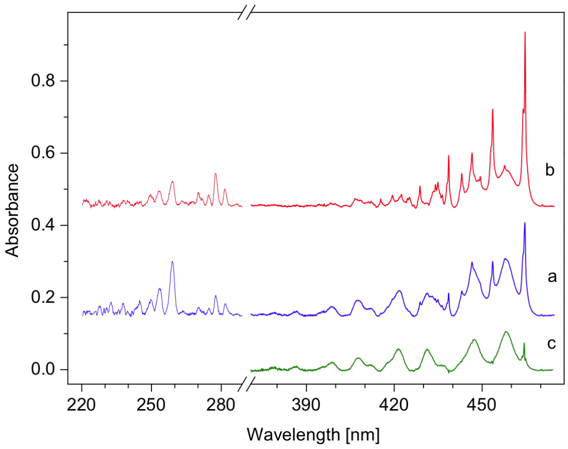

**Figure A.6:** Electronic absorption spectra recorded after (a) mass-selective deposition of $C_9H_7^+$ (*m*/*z* = 115) cations, produced from indene vapour, into a $CH_3Cl$/neon matrix and (b) subsequent 60 min irradiation of the sample with a medium pressure Hg lamp. The cationic features observed in visible are better discernible in trace c, which was obtained by subtracting trace b from a after proper intensity scaling.

**Table A.2** Absorption band maxima ($\lambda_{Ne}$ ± 0.1 nm) of electronic transitions of $C_9H_7^+$ (1-indenylium cation) and its neutral observed in 6 K neon matrices.

| $\lambda_{Ne}$ /nm | $\tilde{\nu}$ /cm$^{-1}$ | $\Delta\tilde{\nu}$ /cm$^{-1}$ | Assignment |
|---|---|---|---|
| **115+** | | | |
| 458.25 | 21 822 | 0 | $0_0^0$ |
| 447.31 | 22 356 | 534 | $\nu_{15}$ |
| 436.51 | 22 909 | 1087 | $\nu_{11}/2\nu_{15}$ |
| 431.29 | 23 186 | 1364 | $\nu_8$ |
| 421.50 | 23 725 | 1903 | $\nu_{15} + \nu_8$ |
| 412.17 sh | 24 262 | 2440 | $\nu_{11}/2\nu_{15} + \nu_8$ |
| 407.70 | 24 528 | 2706 | $2\nu_8$ |
| 398.66 | 25 084 | 3262 | $2\nu_8 + \nu_{15}$ |
| 386.41 | 25 879 | 4057 | $3\nu_8$ |
| | | | |
| 258.93 | 38 620 | 0 | $0_0^0$ |
| 253.55 | 39 440 | 820 | $\nu_{13}$ |
| 249.58 | 40 067 | 1447 | $\nu_7$ |
| 244.94 | 40 827 | 2207 | |
| | | | |
| **115** | | | |
| 464.68 s | 21 520 | 0 | $0_0^0$ |
| 457.67 w | 21 850 | 330 | |
| 453.62 s | 22 045 | 525 | $\nu_{15}$ |
| 449.40 w | 22 252 | 732 | $\nu_{14}$ |
| 446.55 s | 22 394 | 874 | $\nu_{13}$ |
| 443.05 m | 22 571 | 1051 | $2\nu_{15}$ or $\nu_{11}$ |
| 438.58 s | 22 801 | 1281 | n.a. |
| 436.41 | 22 914 | 1394 | $\nu_{15} + \nu_{13}$ |
| 434.88 m | 22 995 | 1475 | $\nu_6$ or |
| 434.07 m | 23 038 | 1518 | n.a. |
| 433.05 | 23 092 | 1572 | $3\nu_{15}$ |
| 428.78 m-s | 23 322 | 1802 | 1281 + $\nu_{15}$ |
| 425.19 | 23 519 | 1999 | |
| 422.48 | 23 670 | 2150 | |
| 419.38 | 23 845 | 2325 | 1281 + $2\nu_{15}$ |
| 415.37 | 24 075 | 2555 | |
| | | | |
| 281.56 | 35 516 | 0 | |
| 277.67 | 36 014 | 498 | |
| 274.61 | 36 415 | 899 | |
| 271.84 | 36 787 | 1271 | |
| 270.15 | 37 017 | 1501 | |

### A.2.2 $C_9H_8^+$

Electronic absorption spectrum of $m/z = 116$ cations produced from indene/helium revealed three new systems of cationic origin (because their intensity decreased after irradiation with an mpHg) (Figure A.6, a). Same set of spectral features was observed when $m/z = 116$ cations were produced from a "linear mixture" (Figure A.6, c), as well as from indane (not shown). The two stronger absorptions are at around 580 and 356 nm, the other at 723 nm is much weaker (Table A.3).

Based on experimental observations (precursor considerations, fragmentation pattern) and theoretical results, it has been concluded that the former, strong transitions are of 1-indene$^+$, the latter – of other, by 12 kJ mol$^{-1}$ less stable indene-type isomer, 2-indene$^+$. Moreover, it was found, that UV irradiation of the matrix with Xe in the 310–390 nm range (Figure A.6, b) induces the 1- → 2-indene$^+$ isomerization, similarly to protonated naphthalene isomers (Chapter 7). As for the "back-pumping", several schemes such as $\lambda > 570$ nm Hlg and Xe, 15 min $\lambda > 480$ nm Xe, 40 min $\lambda > 510$ nm mpHg were tried. Intensity decrease of the 724 nm system is seen, but not much correlation/reversibility could be found as it was with protonated naphthalene.

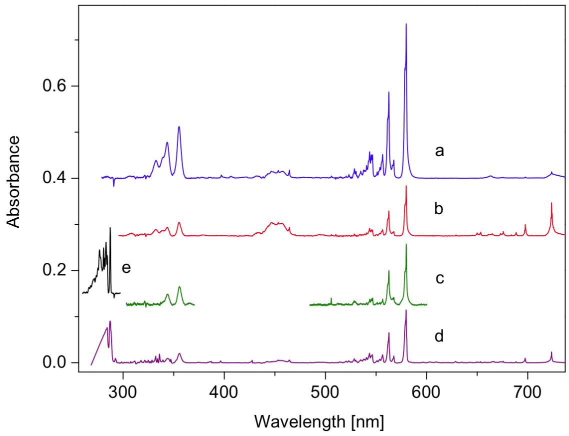

**Figure A.6:** Electronic absorption spectra recorded after (a) mass-selective deposition of $C_9H_8^+$ ($m/z = 116$) cations, produced from indene vapour into a $CH_3Cl$/neon matrix, (b) subsequent 15 min, $308 < \lambda < 390$ nm irradiation of the sample with a xenon lamp. In (c) $C_9H_8^+$ was produced from a mixture of linear hydrocarbon precursors in the ion source (scaled), whereas for d) in a mass-selected $CH_2^+$ (normalized to 25 µC deposited charge) deposition into an indene/neon matrix (ionization reaction taking place upon matrix formation). The black trace – recorded after direct deposition of indene vapor mixed with neon.

**Table A.3** Electronic absorption band maxima ($\lambda_{Ne}$ ± 0.1 nm) of $C_9H_8^+$ cations observed in 6 K neon matrices and the assignment.

| $\lambda_{Ne}$ /nm | $\tilde{\nu}$ /cm$^{-1}$ | $\Delta\tilde{\nu}$ /cm$^{-1}$ | Assignment |
|---|---|---|---|
| 2-indene$^+$ | | | |
| 723.6 | 13 819 | 0 | $0_0^0$ |
| 703.2 vw | 14 220 | 401 | |
| 697.6 | 14 334 | 515 | $\nu_{16}$ |
| 688.6 | 14 523 | 704 | $\nu_{15}$ |
| 683.6 | 14 628 | 809 | 2 × 401 or $\nu_{14}$ |
| 675.9 | 14 795 | 976 | |
| 673.2 | 14 854 | 1035 | $2\nu_{16}$ |
| 664.8 | 15 042 | 1223 | $\nu_{16} + \nu_{15}$ or $\nu_{10}$ |
| 661.1 | 15 126 | 1307 | $\nu_{16} + \nu_{14}$ or $\nu_9$ |
| 657.0 | 15 221 | 1402 | $2\nu_{15}$ or $\nu_7$ |
| 653.5 | 15 303 | 1484 | $\nu_{16}$ + 976 or $\nu_6$ |
| 650.1 | 15 383 | 1564 | |
| 645.0 | 15 504 | 1685 | $\nu_{15}$ + 976 |
| 1-indene$^+$ | | | |
| 579.7 | 17 249 | 0 | $0_0^0$ |
| 567.6 | 17 619 | 370 | $\nu_{30}$ |
| 562.7 | 17 771 | 522 | $\nu_{29}$ |
| 556.5 | 17 970 | 721 | $\nu_{27}$ |
| 553.7 | 18 059 | 810 | $\nu_{26}$ |
| 551.0 | 18 149 | 900 | $\nu_{30} + \nu_{29}$ |
| 546.4 | 18 303 | 1054 | $\nu_{22}$ |
| 545.1 | 18 344 | 1095 | $\nu_{30} + \nu_{27}$ or $\nu_{21}$ |
| 543.5 | 18 399 | 1150 | $\nu_{20}$ |
| 540.4 | 18 503 | 1254 | $\nu_{29} + \nu_{27}$ or $\nu_{17}$ |
| 538.6 | 18 566 | 1317 | $\nu_{29} + \nu_{26}$ ?? |
| 537.7 | 18 598 | 1349 | $\nu_{15}$ |
| 534.6 | 18 705 | 1456 | |
| 531.1 | 18 829 | 1580 | $\nu_{29} + \nu_{22}$ |
| 529.9 | 18 870 | 1621 | $2\nu_{26}$ or $\nu_{30}$ + 1254 or $\nu_8$ |
| 528.4 | 18 925 | 1676 | $\nu_{29} + \nu_{20}$ |
| 525.6 | 19 026 | 1777 | $\nu_{29}$ + 1254 or $\nu_{27} + \nu_{22}$ |
| 522.9 | 19 123 | 1874 | $\nu_{29} + \nu_{15}$ |
| | | | |
| 355.5 | 28 128 | 0 | $0_0^0$ |
| 343.8 | 29 086 | 958 | $\nu_{24/23}$ |
| 339.5 | 29 452 | 1324 | $\nu_{16/15}$ |
| 332.7 | 30 054 | 1926 | $2\nu_{24/23}$ |

### A.2.3 $C_9H_9^+$

In Figure A.7, the spectrum of *m*/*z* = 117 cations produced from an indane/helium vapour mixture and deposited with $CH_3Cl$ (trace a) is compared to that recorded without an electron scavenger (trace b); two cationic systems with onsets at 475.8 and 315.2 nm were identified. The same cationic absorptions with a similar intensity ratio (the relative band intensities are also same for the two systems) were seen in the spectrum obtained from an indene/ethanol mixture (not shown). Thus, these two cationic systems are assigned to the 2-protonated indene; it is the more stable isomer of the two of relevance.

As is seen from Figure A.7, neutrals and cations overlap, and their features can not everywhere be distinguished from each other, neither can zero-phonon lines (ZPLs) and side bands be separated. Also the position of the origin band of the visible system of 2-protonated indene was unclear. Due to such overlap of absorptions of neutral and cationic species, a complicated fluorescence pattern in the 470–580 nm spectral region has been observed and interpreted (Figure A.8).

In addition, it was found that irradiation of the „$117^+$" matrix with an mpHg lamp destroys all its discussed features; a system of 1-indenyl radical (*m*/*z*=115, section A.2.1) at 465 nm increases substantially. The process involved is $H_2$ loss, one of the lowest energy fragmentation channels of small PAHs. It was seen in matrices both with and without $CH_3Cl$, suggesting that the abstraction reaction involves neutral radical. Observing this photo-induced reaction provides further conformation of the assignments.

Absorption and fluorescence band maxima of electronic transitions of $C_9H_9^+$ cations and their neutrals observed in neon matrices are collected in Tables A.4 and A.5.

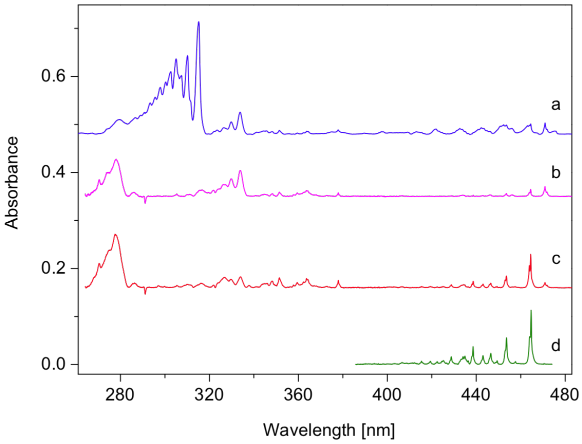

**Figure A.7:** Electronic absorption spectra recorded after mass-selective deposition of $C_9H_9^+$ ($m/z$ = 117) cations, produced from indane vapor in a discharge-type source, into a 6 K neon matrix (a) mixed with and (b) without $CH_3Cl$ as an electron scavenger, the latter scaled to the strength of the neutral absorption around 471 nm in trace a. Trace c was obtained after irradiating the matrix that corresponds to trace b. In (d) the visible part of the spectrum of neutral $C_9H_7$ ($m/z$ = 115) is shown.

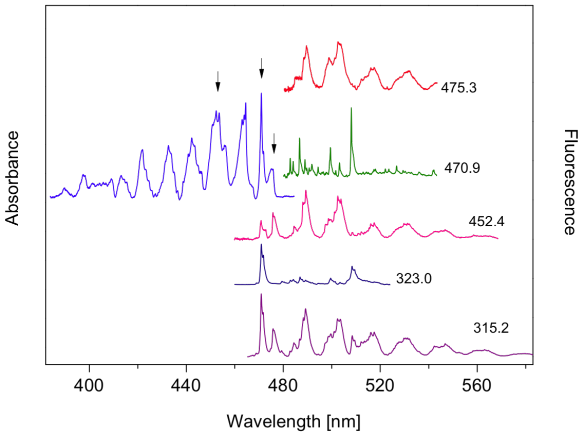

**Figure A.8:** The 400–470 nm system of overlapping absorptions of $C_9H_9^+$ and $C_9H_9$ species (left), and corresponding fluorescence spectra (right). Excitation wavelength for the recorded emission traces is given in nm and those in visible are marked with arrows.

**Table A.4** Absorption band maxima ($\lambda_{Ne}$ ± 0.1 nm) of electronic transitions of protonated indene $C_9H_9^+$cations and their neutrals observed in 6 K neon matrices.

| $\lambda_{Ne}$ /nm | $\tilde{\nu}$ /cm$^{-1}$ | $\Delta\tilde{\nu}$ /cm$^{-1}$ | Assignment |
|---|---|---|---|
| **117+** | | | |
| 475.8 | 21 017 | 0 | $0_0^0$ |
| 467.6 vw | 21 385 | 368 | $\nu_{31}$ |
| 463.0 | 21 597 | 580 | $\nu_{29}$ |
| 456.6 | 21 899 | 882 | $\nu_{26}$ |
| 452.3 | 22 109 | 1092 | $\nu_{22}$ |
| 450.8 | 22 185 | 1168 | $2\nu_{29}$ or $\nu_{21}$ |
| 443.6 | 22 545 | 1528 | $\nu_{10}$ |
| 442.2 | 22 614 | 1597 | $\nu_8$ |
| 440.8 | 22 688 | 1671 | $\nu_{29} + \nu_{22}$ |
| 433.8 | 23 051 | 2034 | |
| 432.5 | 23 119 | 2102 | $\nu_{29} + \nu_{10}$ |
| 431.3 | 23 184 | 2167 | $2 \times \nu_{22}$ or $\nu_{29} + \nu_8$ |
| 423.4 | 23 617 | 2600 | |
| 422.0 | 23 696 | 2679 | $\nu_{22} + \nu_8$ |
| | | | |
| 315.2 | 31 726 | 0 | $0_0^0$ |
| 311.6 | 32 096 | 370 | $\nu_{31}$ |
| 310.2 | 32 246 | 520 | $\nu_{30}$ |
| 307.4 | 32 529 | 803 | $\nu_{27}$ |
| 305.0 | 32 780 | 1054 | $2\nu_{30}$ or $\nu_{22}$ |
| 302.6 | 33 042 | 1316 | $\nu_{30} + \nu_{27}$ or $\nu_{16}$ |
| 300.3 | 33 296 | 1570 | $3\nu_{30}$ or $\nu_8$ |
| 298.0 | 33 563 | 1837 | $\nu_{30}$ + 1316 |
| 295.6 | 33 831 | 2105 | 2 × 1054 |
| 293.3 | 34 091 | 2365 | 1054 + 1316 |
| 290.7 | 34 395 | 2669 | |
| 286.6 | 34 895 | 3169 | |
| | | | |
| **117** | | | |
| 470.9 | 21 235 | 0 | $0_0^0$ |
| 456.2 | 21 918 | 683 | $\nu_{28}$ |
| 450.5 | 22 199 | 964 | $\nu_{24}$ |
| | | | |
| 333.8 | 29 960 | 0 | $0_0^0$ |
| 329.8 | 30 322 | 362 | $\nu_{31}$ |
| 327.3 | 30 556 | 596 | |
| or 326.6 | 30 623 | 663 | $\nu_{28}$ |
| 326.0 | 30 671 | 711 | $2\nu_{31}$ |
| 323.4 | 30 918 | 958 | $\nu_{31}$ + 596 |
| 322.1 | 31 042 | 1082 | $3\nu_{31}$ |

**Table A.5** Fluorescence band maxima ($\lambda_{Ne}$ ± 0.1 nm) observed for protonated indene $C_9H_9^+$ and its neutral in a neon matrix and the assignment.

| $\lambda_{Ne}$ /nm | $\tilde{\nu}$ /cm$^{-1}$ | $\Delta\tilde{\nu}$ /cm$^{-1}$ | Gas phase [a)] | Assignment |
|---|---|---|---|---|
| **117$^+$** | | | | |
| 475.74 | 21 020 | 0 | | $0_0^0$ |
| 484.38 | 20 645 | 375 | | $\nu_{31}$ |
| 488.02 | 20 491 | 529 | | $\nu_{30}$ |
| 489.19 | 20 442 | 578 | | $\nu_{29}$ |
| 497.22 | 20 112 | 908 | | $\nu_{25}$ |
| 498.53 | 20 059 | 961 | | |
| 500.95 | 19 962 | 1058 | | $\nu_{23/24}$ or $2\nu_{30}$ |
| 502.31 | 19 908 | 1112 | | $\nu_{22}$ |
| 503.60 | 19 857 | 1163 | | $\nu_{21}$ |
| 512.14 | 19 526 | 1494 | | $\nu_{10}$ |
| 513.45 | 19 476 | 1544 | | $\nu_9$ |
| 516.16 | 19 374 | 1646 | | $\nu_{22} + \nu_{30}$ |
| 517.54 | 19 322 | 1698 | | $\nu_{22} + \nu_{29}$ |
| 527.09 | 18 972 | 2048 | | |
| 528.35 | 18 927 | 2093 | | |
| 529.80 | 18 875 | 2145 | | |
| 530.56 | 18 848 | 2172 | | $\nu_{22} + \nu_{23/24}$ |
| 531.32 | 18 821 | 2199 | | |
| 532.08 | 18 794 | 2226 | | $2\nu_{22}$ |
| 545.20 | 18 342 | 2678 | | |
| 546.81 | 18 288 | 2732 | | |
| **117** | | | | |
| 471.08 | 21 228 | 0 | | |
| 479.62 | 20 850 ww | 378 | 377 | |
| 483.07 | 20 701 | 527 | 529 | |
| 484.28 | 20 649 | 579 | 583 | |
| 486.97 | 20 535 m | 693 | 700 | |
| 489.24 | 20 440 | 788 | 794 | |
| 490.97 | 20 368 | 860 | 865 | |
| 492.15 | 20 319 | 909 | 1006 | |
| 494.76 | 20 212 | 1016 | 1018 | |
| 496.87 | 20 126 ww | 1102 | -- | |
| 498.21 | 20 072 ww | 1156 | -- | |
| 499.90 | 20 004 m | 1224 | 1228 | |
| 502.13 | 19 915 | 1313 | -- | |
| 503.73 | 19 852 m | 1376 | 1378 | |
| 508.54 | 19 664 s | 1564 | 1570 | |
| 517.81 | 19 312 | 1916 | -- | |
| 522.49 | 19 139 | 2089 | 2096 | |
| 523.94 | 19 086 | 2142 | 2151 | |
| 527.15 | 18 970 | 2258 | 2267 | |
| 529.80 | 18 875 | 2353 | -- | |

---

[a)] Present matrix isolation fluorescence data are compared to the gas-phase LIF results available [17].

## A.3 $C_{10}H_7^+$

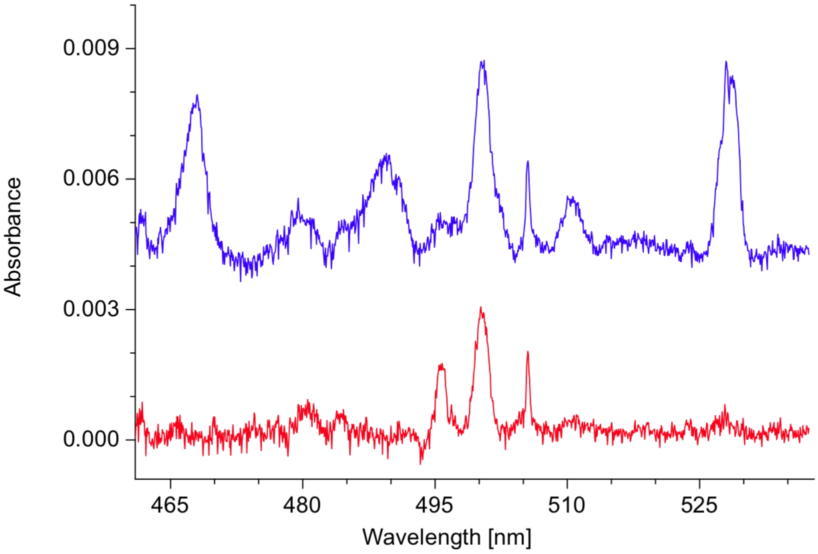

**Figure A.9:** Electronic absorption spectra of $C_{10}H_7^+$ ($m/e = 127$) cations, produced from 2-bromonaphthalene precursor, recorded after mass-selective deposition into a $CH_3Cl$/neon matrix (blue) and after subsequent irradiation of the matrix with medium-pressure Hg lamp (red). The absorption bands seen on the blue trace and disappear under irradiation conditions are of $C_{10}H_7^+$ cations.

# A.4 $TiO_2$

Chemical Physics 353 (2008) 115–118

Contents lists available at ScienceDirect

Chemical Physics

journal homepage: www.elsevier.com/locate/chemphys

## Electronic absorption spectrum of titanium dioxide in neon matrices

I. Garkusha, A. Nagy, Z. Guennoun *, J.P. Maier

*Department of Chemistry, University of Basel, Klingelbergstrasse 80, CH-4056 Basel, Switzerland*

ARTICLE INFO

*Article history:*
Received 25 June 2008
Accepted 8 August 2008
Available online 15 August 2008

*Keywords:*
Titanium dioxide
Electronic spectrum
Solid cryogenic matrix

ABSTRACT

Anions of titanium dioxide produced by sputtering $TiO_2$/graphite composite rods were trapped in 6 K neon matrices following mass selection. The electronic absorption spectrum of titanium dioxide has been measured subsequently, after exposing the matrices to UV radiation, revealing absorptions in the visible and UV regions. Bent and linear forms of $TiO_2$ have been observed with absorptions in the visible range.

Two electronic systems of the bent isomer, $^1B_2 \leftarrow X^1A_1$ and $^1B_1 \leftarrow X^1A_1$, are observed with origins at 524 and 368 nm in agreement with theoretical calculations. The electronic transition lying at 524 nm shows a long vibronic progression due to excitations of the symmetric stretching and bending modes of $TiO_2$. The linear form shows a transition at 628 nm for which a progression involving the symmetric stretching mode of $TiO_2$ is apparent. The spectral assignments have been supported by analysis of the vibrational structure associated with each electronic transition.

### 1. Introduction

Transition metals continue to be of special interest, partly due to the complexities associated with d shell electrons. The 3d-elements form a number of oxygen-containing clusters and compounds with variable oxidation states of the metal cation. Reactivity of these oxides is of interest to different chemistry areas: organometallic, surface science, catalysis, chemisorption processes, and interstellar matter. For these reasons, a large number of theoretical and experimental spectroscopic studies have been devoted to the monoxides and dioxides of the elements ranging from Sc to Zn, leading to reliable reference data about bond lengths, dissociation energies, dipole moments, and vibrational frequencies for both the ground and excited states of these oxides [1–4].

Titanium oxide (TiO), has been extensively studied spectroscopically due to its astrophysical interest [5–9]. Indeed, TiO is the main opacity source in the atmospheres of cool M-type stars in the visible and near infrared. In addition, owing to its importance in model atmosphere investigations and in quantum chemistry, a number of theoretical studies have been devoted to this species [10–13]. Its electronic structure is therefore well understood. In view of the high cosmic abundance of Ti and O [14], larger clusters of titanium oxides are believed to play an important role in dust formation processes from the gas-phase in circumstellar shells of oxygen-rich stars [15].

Titanium dioxide, is a technologically important material which has been widely studied as a prototypical transition metal oxide due to its rather simple electronic structure [16]. Compared to the TiO molecule, considerably less has been reported on $TiO_2$ [13,17–20]. The earliest work on $TiO_2$ was carried out in 1967 showing that this molecule has a dipole moment and therefore a bent structure [18]. Few years later, the emission spectrum of $TiO_2$ was measured for the first time reporting the origin emission band at 529 nm [19]. From these studies, the infrared spectrum of $TiO_2$ in neon matrices was also obtained. Two absorption bands were observed: a strong one at 934.8 $cm^{-1}$ and a weak one at 962.0 $cm^{-1}$, respectively assigned to the asymmetric stretch ($\nu_3$) and symmetric stretch ($\nu_1$). Similar works reported an infrared study on $Ti_nO_x$ species produced by reactions of laser-ablated Ti and $O_2$ in argon matrix at 10 K, confirming the $C_{2v}$ symmetry of the $^1A_1$ ground state of this closed shell molecule [20].

$TiO_n$ ($n = 1$–3) and $TiO_2(n)$ systems were also investigated by photoelectron spectroscopy (PES) to obtain vertical detachment energies [4]. For $TiO_2$, it was reported that both anion and neutral species have a bent structure. In addition, besides the vibrationally resolved ground state of $TiO_2$, two excited states were also observed at 1.96(10) and 2.4(2) eV, and assigned to the $A^3B_2$ and $a^1B_2$ excited states respectively [4]. Interestingly, they obtained for $TiO_2$ broad PES spectra indicating that large geometry changes occur between the anion and the two $B_2$ excited states of $TiO_2$. It was therefore suggested that these two states could be linear, which was found to be in agreement with SCF-CI calculations [17]. A large number of theoretical studies have been then devoted to titanium dioxide [21–26]. From these works, geometries, vibrational frequencies, electron affinities, and dissociation energies were obtained. In addition, different isomers of $TiO_2$, as the peroxo- and superoxo-ones, have also been considered and investigated. Recently, the electronic energy levels of $TiO_2$ have been calculated [27]. DFT adiabatic excitation energies as well as MRCI vertical

---

* Corresponding author. Tel.: +41 61 267 38 19.
*E-mail address:* zohra.guennoun@unibas.ch (Z. Guennoun).

0301-0104/$ - see front matter © 2008 Elsevier B.V. All rights reserved.
doi:10.1016/j.chemphys.2008.08.003

excitation energies were obtained for both the singlet and the triplet states. From these results, it is suggested that TiO$_2$ has a $C_{2v}$ structure in the $A_1$, $B_2$, $B_1$, and $A_2$ excited states which have similar geometries and excitation energies for both the singlet and the triplet multiplicities, with the latter lying 0.03 to 0.05 eV below the singlet ones. Similar results were obtained for the linear excited states which are predicted to be only 0.3 to 0.4 eV less stable than their bent counterparts.

All the results cited above make it a challenge to understand the electronic spectrum of titanium dioxide. The present article is a contribution to this understanding. The electronic absorption spectrum of TiO$_2$, using mass-selective neon matrix isolation spectroscopy, is presented for the first time. The spectral assignments will be discussed by comparison with experimental and calculated data previously reported.

## 2. Experimental

The electronic absorption spectra of titanium dioxide were recorded following mass-selective deposition in neon matrices using the described experimental set-up [28]. The anions were produced in a negative cesium ion sputter source from TiO$_2$/graphite composite rods in a ratio 2:1. The beam is then focused and directed into a quadrupole mass filter using a series of electrostatic optics. The TiO$_2^-$ anions were selected (m/e = 80) with a mass resolution of ±1 amu and the typical ion currents achieved were about 2–3 nA. The mass-selected anions, with a kinetic energy of $\sim$50 eV, were codeposited over a period of 4 h with an excess of neon onto a rhodium coated sapphire substrate held at 6 K.

After deposition, the electronic absorption spectra of the species embedded in neon were recorded with monochromatic light from halogen and xenon arc lamps with beams running parallel to the substrate surface. Absorption spectra were recorded between 220 and 1100 nm using photomultiplier and silicon diode detectors. The effective optical path of the light through the matrix using a waveguide technique is about 2 cm. Infrared spectra in the 4000–600 cm$^{-1}$ range were recorded by doubly reflecting light at an acute angle from a Fourier-transform infrared spectrometer through the matrix, of about 150 μm thickness, achieving a path length of about 1 mm. This method used to measure infrared spectra is an order of magnitude less sensitive than the waveguide approach.

The matrix samples were then exposed to a medium-pressure mercury lamp ($\lambda > 305$ nm) resulting in electron detachment. After each irradiation, a spectrum was recorded to distinguish the electronic transitions of neutral species from those of the ions.

## 3. Results

The trapping of the mass-selected TiO$_2$ anions in a neon matrix gave rise to a number of absorptions in the 220–1100 nm region. Fig. 1 shows the electronic absorption spectra measured in the visible range (400–650 nm). The lower trace corresponds to the deposition spectrum and the upper to the one recorded after irradiation and annealing of the matrix. According to the data in the literature, some of the absorption bands are easily assigned to titanium [29,30], titanium monoxide and its anion [19,31], as indicated in Fig. 1. TiO$^-$ is due to fragmentation of the mass-selected TiO$_2^-$ species hitting the matrix with a $\sim$50 eV kinetic energy. Besides these bands, several broad weak absorption bands, close to those of TiO, are observed in the visible range (Fig. 1). The vicinity of these bands to those of TiO complicates the identification. Nevertheless, the results of the photobleaching and annealing point out to neutral TiO$_2$ being responsible for these new electronic absorption bands. Warming the matrix sharpens the absorption bands of TiO and enhances the electronic and infrared absorption bands assigned to the TiO$_2$ neutral species. The presence of an absorption band at 935.6 cm$^{-1}$ in the infrared spectrum is due to the asymmetric stretching mode ($\nu_3$) of TiO$_2$ [19,20]. This is present after deposition and grows in intensity upon irradiation and annealing, as seen in Fig. 2, confirming the assignment. The fringe patterns in the infrared spectrum are due to interference of the light.

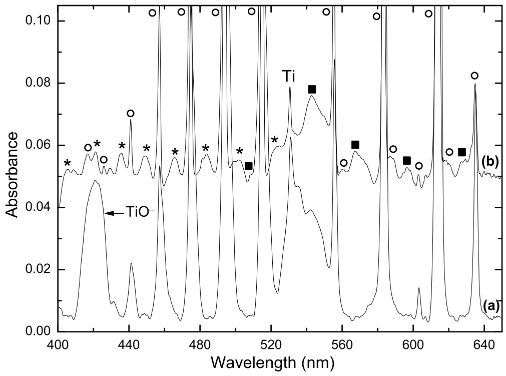

**Fig. 1.** Electronic absorption spectra recorded in a 6 K neon matrix: (a) after mass-selected deposition of TiO$_2^-$ produced from TiO$_2$/graphite composite rods in a cesium sputter ion source and (b) after subsequent UV irradiation and annealing of the matrix. Asterisks indicate the vibronic bands of the bent to bent electronic transition $^1B_2 \leftarrow X^1A_1$ of TiO$_2$, squares are for the vibronic bands of TiO$_2$ linear, and circles for the absorption bands of TiO.

In order to avoid misassignment of the absorption bands, which could be due to the species C$_4$O$_2$ with the same mass as TiO$_2$ (m/e = 80), experiments were also performed using TiO$_2$/silver composite rods which led to the same results.

Irradiation and annealing of the neon matrix reveal two band systems in the visible range. The first one shows a progression commencing at 628 nm with a maximum near 540 nm and a vibrational spacing of about 840 cm$^{-1}$ (Fig. 1). No absorption band was observed at higher wavelengths suggesting that the origin band of this system is at 628 nm. The overlap and the presence of absorptions of titanium (at 530 nm) and titanium oxide in the range 520–550 nm, as observed in Fig. 1, make it difficult to locate the origin

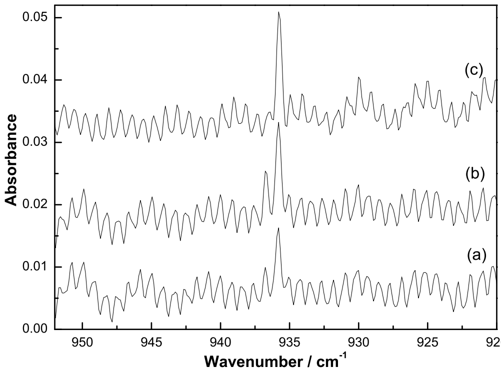

**Fig. 2.** Infrared spectrum recorded in a 6 K neon matrix: (a) after mass-selected deposition of TiO$_2^-$ produced from TiO$_2$/graphite composite rods in a cesium sputter ion source, (b) after UV irradiation ($\lambda > 305$ nm), and (c) after annealing of the matrix. The periodic structure in the baseline is an artefact (interference).

**Table 1**
Observed bands ($\tilde{\nu} \pm 5\ \mathrm{cm}^{-1}$) in the electronic absorption spectra of the $TiO_2$ species along with suggested assignments

| Species | $\lambda$ (nm) | $\tilde{\nu}$ (cm$^{-1}$) | $\delta$ (cm$^{-1}$) | Assignment | |
|---|---|---|---|---|---|
| $TiO_2$ linear | 628 | 15,924 | 0 | $0_0^0$ | |
| | 597 | 16,750 | 826 | $\nu_1$ | |
| | 568 | 17,606 | 1682 | $2\nu_1$ | |
| | 542 | 18,484 | 2560 | $3\nu_1$ | |
| | 509 | 19,646 | 3722 | $4\nu_1 + \nu_3$ | |
| $TiO_2$ bent | 524 | 19,084 | 0 | $0_0^0$ | $^1B_2 \leftarrow X^1A_1$ |
| | 502 | 19,920 | 836 | $\nu_1$ | |
| | 497 | 20,121 | 1037 | $\nu_1 + \nu_2$ | |
| | 485 | 20,619 | 1535 | $\nu_1 + \nu_2 + \nu_3$ | |
| | 481 | 20,790 | 1706 | $2\nu_1$ | |
| | 465 | 21,505 | 2421 | $3\nu_1$ | |
| | 461 | 21,692 | 2608 | $3\nu_1 + \nu_2$ | |
| | 448 | 22,321 | 3237 | $4\nu_1$ | |
| | 433 | 23,095 | 4011 | $5\nu_1$ | |
| | 419 | 23,866 | 4782 | $6\nu_1$ | |
| | 405 | 24,691 | 5607 | $7\nu_1$ | |
| | 368 | 27,174 | | $0_0^0$ | $^1B_1 \leftarrow X^1A_1$ |

and vibrational members of the second band system. However, based on the intensity distribution, the onset of this absorption might be at 524 nm. This system is characterized by a long vibronic progression showing an irregular pattern between 460 and 520 nm indicating that two fundamental modes are active in the excited state leading to overtones and combination bands. Vibrational spacings of about 850 cm$^{-1}$ and 180 cm$^{-1}$ are inferred. The assignment was complicated owing to the broadness and the vicinity of the absorptions of $TiO_2$ to those of TiO. The band position maxima and a vibrational analysis of the two electronic band systems are given in Table 1. In addition, a weak electronic absorption band was observed in the UV range at 368 nm. However, the presence of several absorption bands of titanium oxide in this region obscured observations of a vibrational progression. The overlap of the electronic absorption transitions of TiO and $TiO_2$ makes it also difficult to assign the $TiO_2^-$ bands. Nevertheless, by looking at the spectra in detail, an absorption band of the anion was found around 540 nm (Fig. 1).

## 4. Assignment and discussion

The electronic system at shorter wavelengths has an origin band at 524 nm (2.37 eV) as seen in Fig. 1. This system corresponds to that one observed by emission at 529 nm (2.34 eV) [19] and photoelectron spectroscopy at 516 nm (2.40 eV) [4]. The long progression observed for this system indicates that the equilibrium Ti–O bond length and/or OTiO angle in the excited state differ from those in the ground state. As reported in Table 1, vibrational spacings of about 180 cm$^{-1}$ are observed in this progression. These intervals are too small for any of the stretching modes of $TiO_2$ and could only be assigned to excitations of its bending mode $\nu_2$. The decrease of the bending frequency shows that the OTiO angle is smaller in the excited state. The larger vibronic spacings of about 850 cm$^{-1}$ observed for this electronic system are assigned to excitations of the symmetrical stretching mode $\nu_1$. The vibrational frequency being lower in the excited state than in the ground state is indicative that the bond length has increased.

Theoretical calculations carried out show that two of the bent excited states, $^1B_2$ and $^3B_2$, have a vertical excitation energy of 2.43 and 2.40 eV respectively at the MRCI level of theory, and 2.33 and 2.35 eV with DFT [27]. These values are close to our experimental result (2.37 eV). The transition to $^1B_2$ is in addition predicted to have a quite high oscillator strength. Furthermore, the reported DFT calculations provide information on the structures of the excited states and indicate an elongation of the bond length as well as a decrease of the angle for the $B_2$ excited states [27], in agreement with the observations. In addition, the $\nu_1$ and $\nu_2$ excitations observed in neon matrix (about 825 and 194 cm$^{-1}$, Table 1) are in good agreement with the harmonic vibrational frequencies calculated for the optimized $B_2$ states (about 880 and 195 cm$^{-1}$). In view of these comparisons, the electronic system is assigned to the dipole-allowed bent to bent electronic transition $^1B_2 \leftarrow X^1A_1$. Consequently, the weak absorption band observed in the UV range at 368 nm (27,174 cm$^{-1}$, 3.37 eV) is assigned to the $^1B_1 \leftarrow X^1A_1$ electronic transition in agreement with the vertical excitation energies of 3.57 and 3.66 eV calculated at the MRCI and DFT level of theory [27].

The electronic band system seen at longer wavelengths shows a vibronic progression with spacings of about 840 cm$^{-1}$. The origin band observed at 628 nm (1.97 eV) is consistent with the system at 632 nm (1.96 eV) observed by photoelectron spectroscopy [4]. However, none of the bent excited states of $TiO_2$ given in [27] have a vertical excitation energy lower than 2.40 eV. It is thus suggested that this electronic system is due to an other isomer of titanium dioxide.

Different isomers of titanium dioxide, as the linear OTiO, the peroxo (cyclic structure), and the superoxo (TiOO) ones, were investigated theoretically [21,23–27]. From these studies, the energetic ordering of these isomers is as follows: linear < peroxo < superoxo, with the bent one being the most stable. The linear isomer is found to lie 2 eV above the ground state of the bent one while the other two are much higher in energy at about 4.46 and 5.5 eV, respectively. The possibility to form the peroxo and superoxo isomers, being very high in energy, can be ruled out. Therefore, the only plausible isomer which could lead to the results obtained in neon matrix is the linear OTiO species. Photoelectron and solid matrices infrared studies of metal dioxides have shown that these species tend to have different structures [32–34] as the $FeO_2$ species which has been trapped in a low temperature argon matrix in three different structures, with two of the isomers being 2.12 and 2.55 eV higher in energy than the most stable one [34]. Consequently, we suggest that the electronic band system with an origin at 628 nm is due to the linear isomer of titanium dioxide, with a $^1\Sigma_g^+$ ground state. In addition, the vibrational interval observed in neon matrix for this electronic system (about 835 cm$^{-1}$) is consistent with the harmonic frequencies calculated for the $\nu_1$ and $\nu_2$ modes of the linear form (884 cm$^{-1}$ and 854 cm$^{-1}$ respectively) [27]. Because it is predicted that the $\nu_2$ mode has no oscillator strength, the observed vibronic progression is due to excitations in the symmetric stretching $\nu_1$ mode. No infrared absorption band of the linear isomer could be observed. Finally, it is worthwhile to note the persistence of the linear isomer after annealing of the matrix up to 8.5 K due to stabilization effects of the solid environment. Analogous observations were made for the high energy isomers of iron dioxide [34].

## 5. Conclusion

The electronic absorption spectrum of $TiO_2$ in 6 K neon matrices is reported for the first time. The transitions observed reveal that titanium dioxide exists in both bent and linear forms in the matrix environment with absorptions in the visible and UV regions. Two electronic band systems with origins at 524 and 368 nm were observed and assigned to the bent $^1B_2$ and $^1B_1$ excited states of $TiO_2$ whereas a transition with origin at 628 nm was found to be due to a linear isomer. As no higher excited states of the linear form have been calculated, assignment of the electronic transition has not been made. This opens the way for future theoretical calculations on the linear form of $TiO_2$.

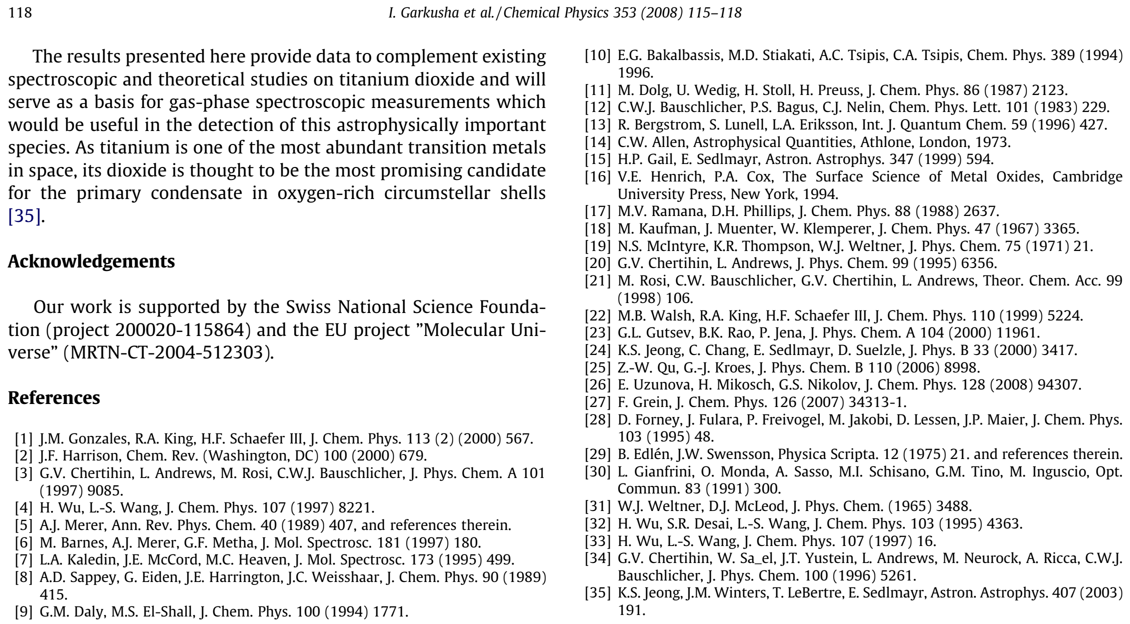

118 *I. Garkusha et al./Chemical Physics 353 (2008) 115–118*

The results presented here provide data to complement existing spectroscopic and theoretical studies on titanium dioxide and will serve as a basis for gas-phase spectroscopic measurements which would be useful in the detection of this astrophysically important species. As titanium is one of the most abundant transition metals in space, its dioxide is thought to be the most promising candidate for the primary condensate in oxygen-rich circumstellar shells [35].

**Acknowledgements**

Our work is supported by the Swiss National Science Foundation (project 200020-115864) and the EU project "Molecular Universe" (MRTN-CT-2004-512303).

**References**

[1] J.M. Gonzales, R.A. King, H.F. Schaefer III, J. Chem. Phys. 113 (2) (2000) 567.
[2] J.F. Harrison, Chem. Rev. (Washington, DC) 100 (2000) 679.
[3] G.V. Chertihin, L. Andrews, M. Rosi, C.W.J. Bauschlicher, J. Phys. Chem. A 101 (1997) 9085.
[4] H. Wu, L.-S. Wang, J. Chem. Phys. 107 (1997) 8221.
[5] A.J. Merer, Ann. Rev. Phys. Chem. 40 (1989) 407, and references therein.
[6] M. Barnes, A.J. Merer, G.F. Metha, J. Mol. Spectrosc. 181 (1997) 180.
[7] L.A. Kaledin, J.E. McCord, M.C. Heaven, J. Mol. Spectrosc. 173 (1995) 499.
[8] A.D. Sappey, G. Eiden, J.E. Harrington, J.C. Weisshaar, J. Chem. Phys. 90 (1989) 415.
[9] G.M. Daly, M.S. El-Shall, J. Chem. Phys. 100 (1994) 1771.
[10] E.G. Bakalbassis, M.D. Stiakati, A.C. Tsipis, C.A. Tsipis, Chem. Phys. 389 (1994) 1996.
[11] M. Dolg, U. Wedig, H. Stoll, H. Preuss, J. Chem. Phys. 86 (1987) 2123.
[12] C.W.J. Bauschlicher, P.S. Bagus, C.J. Nelin, Chem. Phys. Lett. 101 (1983) 229.
[13] R. Bergstrom, S. Lunell, L.A. Eriksson, Int. J. Quantum Chem. 59 (1996) 427.
[14] C.W. Allen, Astrophysical Quantities, Athlone, London, 1973.
[15] H.P. Gail, E. Sedlmayr, Astron. Astrophys. 347 (1999) 594.
[16] V.E. Henrich, P.A. Cox, The Surface Science of Metal Oxides, Cambridge University Press, New York, 1994.
[17] M.V. Ramana, D.H. Phillips, J. Chem. Phys. 88 (1988) 2637.
[18] M. Kaufman, J. Muenter, W. Klemperer, J. Chem. Phys. 47 (1967) 3365.
[19] N.S. McIntyre, K.R. Thompson, W.J. Weltner, J. Phys. Chem. 75 (1971) 21.
[20] G.V. Chertihin, L. Andrews, J. Phys. Chem. 99 (1995) 6356.
[21] M. Rosi, C.W. Bauschlicher, G.V. Chertihin, L. Andrews, Theor. Chem. Acc. 99 (1998) 106.
[22] M.B. Walsh, R.A. King, H.F. Schaefer III, J. Chem. Phys. 110 (1999) 5224.
[23] G.L. Gutsev, B.K. Rao, P. Jena, J. Phys. Chem. A 104 (2000) 11961.
[24] K.S. Jeong, C. Chang, E. Sedlmayr, D. Suelzle, J. Phys. B 33 (2000) 3417.
[25] Z.-W. Qu, G.-J. Kroes, J. Phys. Chem. B 110 (2006) 8998.
[26] E. Uzunova, H. Mikosch, G.S. Nikolov, J. Chem. Phys. 128 (2008) 94307.
[27] F. Grein, J. Chem. Phys. 126 (2007) 34313-1.
[28] D. Forney, J. Fulara, P. Freivogel, M. Jakobi, D. Lessen, J.P. Maier, J. Chem. Phys. 103 (1995) 48.
[29] B. Edlén, J.W. Swensson, Physica Scripta. 12 (1975) 21. and references therein.
[30] L. Gianfrini, O. Monda, A. Sasso, M.I. Schisano, G.M. Tino, M. Inguscio, Opt. Commun. 83 (1991) 300.
[31] W.J. Weltner, D.J. McLeod, J. Phys. Chem. (1965) 3488.
[32] H. Wu, S.R. Desai, L.-S. Wang, J. Chem. Phys. 103 (1995) 4363.
[33] H. Wu, L.-S. Wang, J. Chem. Phys. 107 (1997) 16.
[34] G.V. Chertihin, W. Sa_el, J.T. Yustein, L. Andrews, M. Neurock, A. Ricca, C.W.J. Bauschlicher, J. Phys. Chem. 100 (1996) 5261.
[35] K.S. Jeong, J.M. Winters, T. LeBertre, E. Sedlmayr, Astron. Astrophys. 407 (2003) 191.

## A.5 $TiO_3/TiC_4$

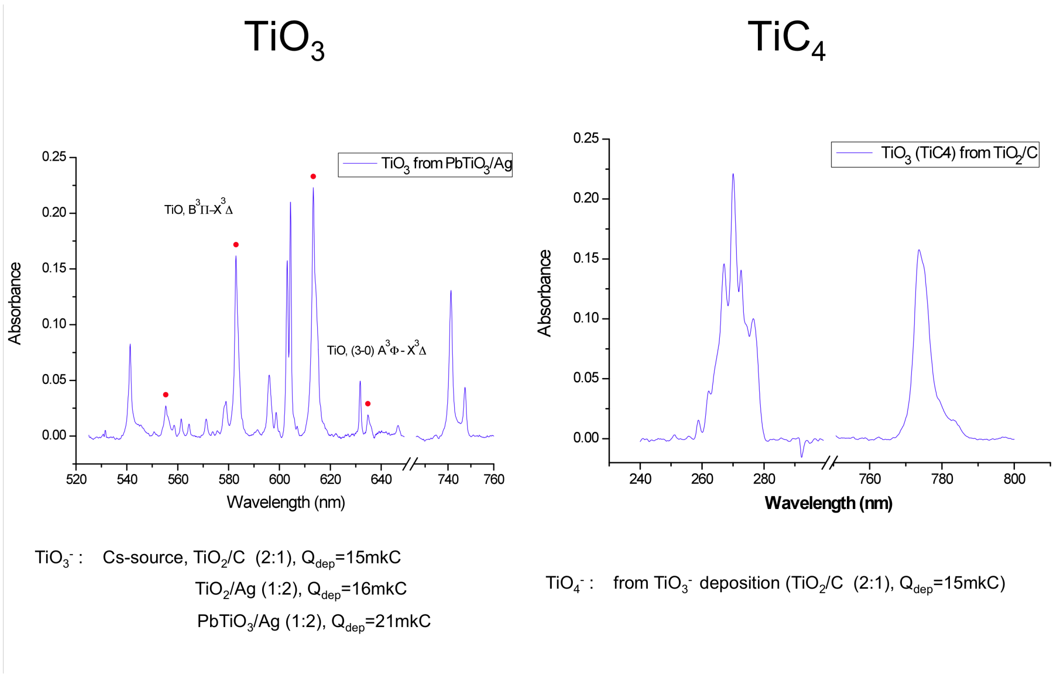

**Figure A.11:** Electronic absorption spectra recorded in 6 K neon matrices after mass-selected deposition of the m/z=96 nions produced from $PbTiO_3$/silver or $TiO_2$/C composite rods in a cesium sputter source.

# BIBLIOGRAPHY

[1] A.G.G.M. Tielens. Interstellar Polycyclic Aromatic Hydrocarbon molecules. *Annu. Rev. Astron. Astrophys.,* 46 (2008) 289-337.

[2] E. Herbst, V. Le Page. Do H atoms stick to PAH cations in the interstellar medium? *Astron. Astrophys.,* 344 (1999) 310-316.

[3] V. Le Page, Y. Keheyan, V.M. Bierbaum, T.P. Snow. Chemical constraints on organic cations in the interstellar medium. *J. Am. Chem. Soc.,* 119 (1997) 8373-8374.

[4] T.J. Millar, E. Herbst, R.P.A. Bettens. Large molecules in the envelope surrounding IRC+10216. *Mon. Not. Roy. Astron. Soc.,* 316 (2000) 195-203.

[5] K.-H. Homann. Fullerenes and soot formation – new pathways to large particles in flames. *Angew. Chem.,-Int. Ed.,* 37 (1998) 2434-2451.

[6] M.B. Bell, P.A. Feldman, J.K.G. Watson, M.C. McCarthy, M.J. Travers, C.A. Gottlieb, P. Thaddeus. Observations of long $C_nH$ molecules in the dust cloud TMC-1. *Astrophys. J.,* 518 (1999) 740.

[7] V.V. Kislov, N.I. Islamova, A.M. Kolker, S.H. Lin, A.M. Mebel. Hydrogen abstraction acetylene addition and Diels-Alder mechanisms of PAH formation: A detailed study using first principles calculations. *J. Chem. Theor. Comp.,* 1 (2005) 908-924.

[8] J. Appel, H. Bockhorn, M. Frenklach. Kinetic modeling of soot formation with detailed chemistry and physics: laminar premixed flames of $C_2$ hydrocarbons. *Comb. Flame,* 121 (2000) 122-136.

[9] P.M. Johnson, R. Anand, J.D. Hofstein, J.E. LeClaire. Reassessing the orbitals of pi systems using photoinduced Ryberg ionization spectroscopy. *J. El. Spec. Rel. Phenom.,* 108 (2000) 177-187.

[10] A. Nagy, J. Fulara, J.P. Maier. Formation of aromatic structures from chain hydrocarbons in electrical discharges: absorption and fluorescence study of $C_{11}H_9^+$ and $C_{11}H_9$ isomers in neon matrices. *J. Am. Chem. Soc.,* 133 (2011) 19796-19806.

[11] A. Nagy, I. Garkusha, J. Fulara, J.P. Maier. Electronic spectroscopy of fragment cations derived from small PAHs. *Gordon MIS Conf. Poster Pres.,* (2009).

[12] H. Xu, P.M. Johnson, T.J. Sears. Photoinduced rydberg ionization spectroscopy of phenylacetylene: Vibrational assignments of the *C* state of the cation. *J. Phys. Chem. A,* 110 (2006) 7822-7825.

[13] J. Fulara, M. Grutter, J.P. Maier. Higher excited electronic transitions of polyacetylene cations $HC_{2n}H^+$ (n=2–7) in neon matrixes. *J. Phys. Chem. A,* 111 (2007) 11831-11836.

[14] J. Fulara, A. Nagy, I. Garkusha, J.P. Maier. Higher energy electronic transitions of $HC_{2n+1}H^+$ (n=2–7) and $HC_{2n+1}H$ (n=4–7) in neon matrices. *J. Chem. Phys.,* 133 (2010) 024304.

[15] J.A. Stearns, T.S. Zwier. Infrared and ultraviolet spectroscopy of jet-cooled ortho-, meta-, and para-Diethynylbenzene. *J. Phys. Chem. A,* 107 (2003) 10717-10724.

[16] A.G. Robinson, P.R. Winter, C. Ramos, T.S. Zwier. Ultraviolet photochemistry of diacetylene: reactions with benzene and toluene. *J. Phys. Chem. A,* 104 (2000) 10312-10320.

[17] T.P. Troy, M. Nakajima, N. Chalyavi, R.G.C.R. Clady, K. Nauta, S.H. Kable, T.W. Schmidt. Identification of the jet-cooled 1-Indanyl radical by electronic spectroscopy. *J. Phys. Chem. A,* 113 (2009) 10279-10283.

# CONCLUSIONS

This thesis describes the results of experimental studies on production and spectroscopic characterization of protonated polycyclic aromatic hydrocarbons (H-PAH$^+$s) and other, PAH-related compounds which are of interest from an astrophysical as well as a fundamental point of view. The species have been produced in a hot-cathode discharge source and investigated by means of electronic absorption and fluorescence spectroscopy in 6 K neon matrices using a mass-selected ion beam. It has been shown, that H-PAH$^+$s are produced efficiently in proton transfer reactions of parent PAHs with suitable proton donors such as simple alcohols, when the donor's PA is ~50 kJ mol$^{-1}$ lower than the acceptor's for the reaction to proceed and for the H-PAH$^+$s to not dissociate due to high excess energy, as was tested on naphthalene and anthracene. These may not hold for larger PAHs, as they are able to dissipate higher reaction excess energies *via* internal vibrational relaxation. Such a protonation reaction route prefers production of the most stable H-PAH$^+$ isomers if a suitable proton donor is selected.

Dihydro-PAHs, if available, can also be used as a precursor; they easily get ionized and fragmented (H loss) in discharge-type sources, and form several structural isomers of the respective H-PAH$^+$. Thus, for example, the use of cyclohexadiene as a $C_6H_7^+$ precursor resulted not only in production of protonated benzene, but also of protonated fulvene, which has been characterized spectroscopically for the first time. The use of dihydronaphtalene resulted in detection and subsequent identification of three $C_{10}H_9^+$ isomers, α- and β-protonated naphthalenes and 2-indenylmethylium. For these, smaller H-PAH$^+$s and their structural isomers a photoinduced isomerization processes have been observed and stimulated their extended studies. As for the naphthalenes, the intermolecular proton transfer leading to the $\alpha \leftrightarrow \beta$ photoisomerization is of reversible character. Besides these, electronic spectra of several larger H-PAH$^+$s — protonated anthracene, phenanthrene, pyrene, corannulene and coronene — have been recorded. Their interpretation is based on the experimental observations and supported by computational data. For the majority of protonated species the correspondent neutrals have been also detected and characterized.

Protonated coronene is the largest PAH studied during this work and is of an especial interest in astrophysics. It is often considered as a model for studying PAH's possible presence and role in the ISM. Its strongest $S_1 \leftarrow S_0$ electronic transition detected in solid neon is in the visible 620–695 nm range, where a large number of narrow DIBs are present. Due to the uncertainties in the matrix to gas phase shift, it will be speculative to make some assumptions/conclusions, on whether it does or not contribute to some of them.

In general, the larger H-PAH$^+$s studied during this work (pyrene, coronene and corannulene) exhibit strong electronic absorption features in the visible range. These are characterized by strong narrow absorption origin bands followed by weaker, but complex, extended vibrational structure. These satisfy already several criteria, which must be met for a molecule to be accepted as a DIB carrier. Concerning the stability of H-PAH$^+$s, the calculated dissociation energies are rather low, with that for coronene being 4.4 eV. This is, however, only the thermodynamic threshold energy. Fast internal conversion and intramolecular vibrational energy redistribution may result in the remarkably enhanced photostability of PAH species. Another interesting point concerning protonated coronene is that it fluoresces, which is not necessary due to the matrix surrounding and, thus, contradicts the PAH hypothesis. According to this hypothesis, UIRs result from the electronic excitation of the PAHs (and their derivatives) and the subsequent nonradiative decay to vibrational levels of the electronic ground state. Thus, gas-phase LIF spectrum of protonated coronene or other/larger PAHs are of relevance. Another molecules of special interest would be corannulene and fullerene $C_{60}$ in their neutral, ionic and protonated forms.

Despite the great progress made in field of high-resolution gas-phase spectroscopy, matrix isolation technique in combination with mass selection remains a powerful tool for producing and investigating spectroscopic properties of free radicals and ions. It has proven to be successfully applicable to a large variety of species, differing in physical and chemical properties.

# CURRICULUM VITAE

NAME: Iryna Roth Garkusha

GEBURTSDATUM: 22. November 1981

GEBURTSORT: Kiew, Ukraine

## WERDEGANG:

| | |
|---|---|
| August 2006 – März 2012 | Doktorat in Physikalischer Chemie: *„Electronic spectroscopy of mass-selected protonated PAHs in neon matrices"*<br>Forschungsgruppe von Prof. John P. Maier<br>Departement Chemie, Universität Basel, Schweiz |
| August 2006 – Dezember 2011 | Assistentin: Praktikum in Physikalischer Chemie |
| November 2005 – März 2006 | Laborassistentin, Polyphor AG, Allschwill, CH |
| September 1998 – Juni 2003 | Studium im Fach Physik; Diplom eines Masters der Physik<br>Spezialisierung: Medizinische Physik<br>Qualifikation: Lehrerin der Physik<br>Departement Physik,<br>Staatliche Taras Schewtschenko Universität, Kiew, Ukraine |
| September 1988 – Juli 1998 | Primar- und Mittelschule, Kiew, Ukraine |

## KONFERENZEN:

| | |
|---|---|
| Juni 2011 | IAU Symposium 280: The Molecular Universe; Toledo, Spain |
| April 2011 | Frontiers in Spectroscopy: Faraday Discussion 150; Basel, Switzerland |
| August 2010 | 8th International Conference on Low Temperature Chemistry; Yerevan, Armenia |
| Juli 2009 | Gordon Conference on the Physics and Chemistry of Matrix Isolated Species; Oxford, United Kingdom |
| September 2008 | The 20th International Conference on High Resolution Molecular Spectroscopy; Prague, Czech Republic |

# LIST OF PUBLICATIONS

**Electronic transitions of $S_2^-$ and $S_3^-$ in neon matrixes**
Ivan Shnitko, Jan Fulara, Iryna Garkusha, Adam Nagy, John P. Maier
*Chem. Phys.*, **346**(1–3), 8–12, 2008.

**Electronic absorption spectrum of titanium dioxide in neon matrices**
Iryna Garkusha, Adam Nagy, Zora Guennoun, John P. Maier
*Chem. Phys.*, **353**(1–3), 115–118, 2008.

**Higher energy electronic transitions of $HC_{2n+1}H^+$ ($n$=2–7) and $HC_{2n+1}H$ ($n$=4–7) in neon matrices**
Jan Fulara, Adam Nagy, Iryna Garkusha, John P. Maier
*J. Chem. Phys.*, **133**(2), 024304/1–9, 2010.

**Electronic transitions of protonated benzene and fulvene, and of $C_6H_7$ isomers in neon matrices**
Iryna Garkusha, Jan Fulara, Adam Nagy, John P. Maier
*J. Am. Chem. Soc.*, **132**(42), 14979–14985, 2010.

**Identification of $H_2CCC$ as a diffuse interstellar band carrier**
J.P. Maier, G.A.H. Walker, D.A. Bohlender, F.J. Mazzotti, R. Raghunandan, J. Fulara, I. Garkusha, A. Nagy
*Astrophys. J.*, **726**(1), 41/1–9, 2011.

**On the benzylium/tropylium ion dichotomy: electronic absorption spectra in neon matrices**
Adam Nagy, Jan Fulara, Iryna Garkusha, John P. Maier
*Angew. Chem. Int. Ed.*, **50**(13), 3022–3025, 2011.

**Electronic absorption spectra of protonated anthracenes and phenanthrenes, and their neutrals in neon matrices**
Iryna Garkusha, Jan Fulara, Adam Nagy, John P. Maier
*Astrophys. J.*, **728**(2), 131/1–7, 2011.

**Electronic absorption spectra of protonated pyrene and coronene in neon matrices**
Iryna Garkusha, Jan Fulara, Peter J. Sarre, John P. Maier
*J. Phys. Chem. A*, **115**(40), 10972–10978, 2011.

**Fluorescence of protonated pyrene and coronene in neon matrices**
Iryna Garkusha, Jan Fulara, John P. Maier
*J. Mol. Struct.*, **1025**, 147–150, 2012

**Electronic spectra of $C_4H_3Cl^+$ isomers**
S. Chakrabarty, V. Rudnev, J. Fulara, R. Dietsche, A. Nagy, I. Garkusha, F. J. Mazzotti, C. A. Rice, J. P. Maier
*Mol. Phys.*, **110** (24), 3077-3084, 2012

**Electronic spectra and reversible photoisomerization of protonated naphthalenes in neon matrices**
I. Garkusha, A. Nagy, J. Fulara, M. F. Rode, A. L. Sobolewski, J. P. Maier
*J. Phys. Chem. A,* **117** (2), 351-360, 2013

**Electronic spectroscopy of transient species in solid neon: the indene motif polycyclic hydrocarbon cation family $C_9H_y^+$ (y=7–9) and their neutrals**
Adam Nagy, Iryna Garkusha, Jan Fulara, John P. Maier
*PCCP* **15**, 19091, 2013